UNIVERSITY OF SOUTHAMPTON

The Effect of Roughness and Inflow Unsteadiness on Turbine Flows

by

Florian Hammer

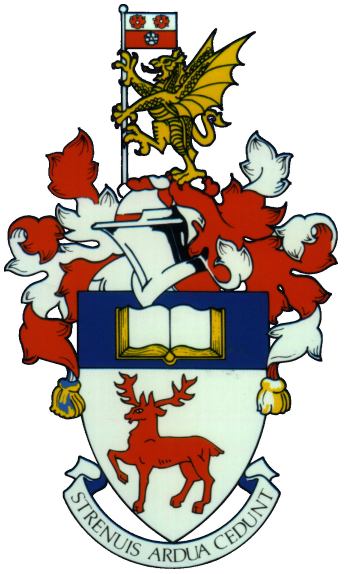

A thesis submitted for the degree of
Doctor of Philosophy

in the
Faculty of Engineering and the Environment
Aerodynamics and Flight Mechanics

February 2019

UNIVERSITY OF SOUTHAMPTON

ABSTRACT

FACULTY OF ENGINEERING AND THE ENVIRONMENT
AERODYNAMICS AND FLIGHT MECHANICS

Doctor of Philosophy

THE EFFECT OF ROUGHNESS AND INFLOW UNSTEADINESS ON TURBINE FLOWS

by Florian Hammer

The aim of this work is to characterise the effects of unsteady incoming wakes with different wake profiles and roughness on the turbine blade and loss mechanisms of a linear low-pressure turbine (LPT) cascade. The main focus lies on the boundary layer development as well as the profile and overall losses, which are affected by periodically incoming wakes and surface roughness due to boundary layer interactions.

Large eddy simulations with the WALE model of the T106A linear LPT cascade at Reynolds number $Re = 100{,}000$ were carried out for the investigations within this work. At this Reynolds number, the highly loaded blade profile is prone to a large separation bubble on the suction surface in an unperturbed environment. Unsteady wakes and surface roughness can exert a beneficial effect by minimising, and in some cases preventing, unwanted laminar separation.

Within this work three different incoming wake profiles, generated by means of upstream bars and the Magnus effect, are investigated. It has been found that it is paramount to simulate the correct incoming wake strength compared to actual blade row wakes. The combined effects of wake-blade boundary layer interaction and the wake distortion losses within the turbine passage mutually affect the overall turbine losses.

Additionally to the interaction between incoming wakes and the blade's boundary layer, surface roughness and its implications on the profile and overall losses is considered. In order to do so, a simple roughness model was used and a set of different roughness parameters was simulated. The model, which keeps the computational costs low compared to fully resolved roughness surfaces, was able to reproduce the behaviour observed in the literature in terms of the onset of transition and the effect on the laminar and turbulent boundary layer. For comparison, and for a more detailed analysis of flow mechanisms, a real as-cast roughness patch, scaled down to match representative roughness parameters, was simulated by means of an immersed boundary method. The roughness height definition of the roughness model corresponds well to the roughness height of the as-cast roughness based on the evaluation of the onset of transition, boundary layer development and losses.

Contents

List of Figures

List of Tables

Nomenclature

Abbreviations

TKE	turbulent kinetic energy
APG	adverse pressure gradient
API	application programming interface
BL	boundary layer
CFD	computational fluid dynamics
DNS	direct numerical simulation
FPG	favourable pressure gradient
GPU	graphics processing unit
HiPSTAR	high performance solver for turbulence and aeroacoustic research
HPC	high performance computing
LES	large eddy simulation
LPT	low pressure turbine
MPI	message passing interface
WALE	wall-adapting local eddy-viscosity

Greek letters

α	angle of attack, bar rotation rate
α_i	parametric forcing roughness factor
ΔU^+	roughness function, velocity deficit
δ	channel half height, Dirac function
δ_h	discretised distribution function
δ_{ij}	Kronecker delta
γ	ratio of specific heat
Γ_b	boundary of an immersed body Ω_b
κ	von Kármán constant
λ	wave-length
$\left\langle \widetilde{\Phi} \right\rangle$	time and spatially averaged flow quantity
μ	kinematic viscosity, molecular viscosity
$\mu_0^{\epsilon,F}$, $\mu_1^{\epsilon,F}$	interpolation functions
Ω	total pressure loss
Ω_b	immersed body domain
Ω_f	fluid domain
ω_i	vorticity component
ω_M	mixed-out loss

ω_{wake}	wake mixing loss
$\overline{\Phi}$	Reynolds averaged flow quantity
Φ	flow coefficient, flow quantity
ϕ	angle between the blade surface tangent and the x-axis
Φ'	Reynolds fluctuation of flow quantity
Φ''	Favre fluctuation of flow quantity
Φ^+	nondimensional wall unit
Φ_∞	reference quantity
Φ_{is}	isentropic quantity
Φ_M	mixed-out quantity
Φ_{ref}	reference quantity
Φ_{rms}	root mean square of quantity
Φ_t	stagnation quantity
ρ	density
τ_w	skin friction
τ_{ij}	Reynolds stress component
$\widetilde{\Phi}$	Favre averaged flow quantity
ζ, η	generalised coordinates
u_τ	friction velocity
$-\overline{\rho u_i'' u_j''}$	Reynolds stresses

Latin letters

c	nominal chord length
c	speed of sound
C_D	drag coefficient
C_L	lift coefficient
c_p	pressure coefficient
c_{ax}	axial chord length
c_{sut}	nondimensional Sutherland temperature
D	bar diameter
d	signed distance, pipe diameter
e	inner energy
e_t	total energy
e_{kin}	kinetic energy
F	roughness shape function, wake distortion loss
f	frequency
F_{red}	reduced frequency
H	shape factor
h_{ij}	discrete surface height
h_i	parametric forcing roughness height, grid spacing
J	Jacobian matrix
K_ϵ	nascent delta kernel
$k_{eq,s}$	equivalent sand-grain roughness parameter
k_{rms}	rms roughness
$k_{s,adm.}$	admissible sand-grain roughness

k_s	sand-grain size
M	Mach number
M_{is}	isentropic Mach number
n	wall-normal direction
P	blade pitch
P	production of turbulent kinetic energy
p	static pressure
p_t	total pressure
Pr	Prandtl number
q_i	heat flux vector
Ra	average roughness height
Re	Reynolds number
Re_τ	friction Reynolds number
Re_{is}	isentropic Reynolds number
Re_k	roughness Reynolds number
S	total surface length
s	surface length
S_{ij}	strain rate tensor
$S_{z,5\times5}$	mean peak-to-trough height
T	temperature, total time, bar passing period
t	time
t_{ij}	viscous stresses
t_{TE}	trailing edge thickness
Tu	turbulence intensity
u, v, w	streamwise, pitchwise and spanwise velocity components
u_c	centre line velocity in streamwise direction
u_i	velocity component
U_{bar}	bar sliding velocity
U_{def}	velocity deficit of bar wake
V_{ax}	axial inlet velocity
V_{pitch}	inlet velocity in pitchwise direction
X_i	Lagrangian coordinates
x_i	Cartesian coordinates
z, r	streamwise and pitchwise coordinates in curvilinear system
$\dot{m}$	mass flow rate

Miscellaneous symbols

$\mathbb{1}$	indicator function

Declaration of Authorship

I, Florian Hammer, declare that this thesis entitled The Effect of Roughness and Inflow Unsteadiness on Turbine Flows and the work presented in it are my own and has been generated by me as the result of my own original research.

I confirm that:

1. This work was done wholly or mainly while in candidature for a research degree at this University;
2. Where any part of this thesis has previously been submitted for a degree or any other qualification at this University or any other institution, this has been clearly stated;
3. Where I have consulted the published work of others, this is always clearly attributed;
4. Where I have quoted from the work of others, the source is always given. With the exception of such quotations, this thesis is entirely my own work;
5. I have acknowledged all main sources of help;
6. Where the thesis is based on work done by myself jointly with others, I have made clear exactly what was done by others and what I have contributed myself;
7. Either none of this work has been published before submission, or parts of this work have been published as: Florian Hammer.

Signed:

Date:

Acknowledgements

First of all I would like to thank Prof. Neil Sandham for his great support, advice and for giving me direction during my PhD. I would also like to thank Prof. Richard Sandberg for sharing his knowledge and valuable inputs. My time here in Southampton would not have been so rewarding without my great colleagues, who were always there for long discussions and brainstorming sessions. A special thanks goes to Jake and Markus for being great motivators and supporters during this journey. I would like to thank my previous supervisors in Germany, Prof. Thomas Carolus and Prof. Holger Foysi, who introduced me to the fields of turbomachinery and computational fluid dynamics, which inspired me to undertake this challenge. I also thank Stéphanie for the great support and all the patience during long working days.

The simulations within this work have been carried out on the supercomputer of the UK National Supercomputing Service ARCHER and the resources were provided by the UK Turbulence Consortium funded by the EPSRC. I also gratefully acknowledge the Supercomputing facility (IRIDIS) of the University of Southampton.

Ich danke ganz besonders meinen Eltern, Angelika und Michael, für die großartige Unterstützung all meiner Pläne und die dieses Vorhaben überhaupt ermöglicht haben.

Chapter 1

Introduction

1.1 Motivation

Today aeroplanes are common means of transportation. The main aims of today's research are lowering the fuel consumption, minimising noise production, reducing the exhaust of hazardous substances as well as more detailed design aspects. In order to achieve these goals, a sound understanding of the physics of aeroplanes is needed, and especially the jet engine. It drives the aeroplane and consists of expensive components, which are exposed to high temperatures and forces. Thus, the design process of such an engine is of great importance. Numerical flow simulations are a valuable tool that are used in the very first stages of the design of an engine. In particular, RANS simulations are widely used in the industry and serve as a design tool for prototypes, which are then experimentally tested. However, to gain deeper insight into the physical phenomena of flows large eddy simulations (LES) or direct numerical simulations (DNS) are needed. In direct numerical simulations the Navier-Stokes equations are directly solved without a model or simplification, whereas in large eddy simulations the smaller flow scales are modelled. A drawback of DNS, however, is the higher computational cost and memory consumption. Additionally, the Reynolds number is another limiting factor, as it is related to the computational cost. The higher the Reynolds number, the more flow details have to be resolved. As a consequence, high performance computing is inevitable. In this work numerical simulations of the compressible Navier-Stokes equations with an in-house flow solver, called HiPSTAR, are carried out. The solver has been validated for massively parallel high-performance simulations on several HPC clusters.

A jet engine consists of different types of components, including compressors, fans and turbines. The turbine of a jet engine can be further distinguished between high- and low-pressure turbines (LPT). As low-pressure turbines operate in a Reynolds number range where DNS and LES simulations are more feasible in terms of cost and time consumption, this work is focused only on this type of turbine. The aim and motivation is to further enhance the flow physical understanding of LPTs.

1.2 Linear Low-Pressure Turbine Cascade

1.2.1 General Overview

In figure 1.1 a two-shaft high-bypass turbofan is depicted. As can be seen, the engine comprises of different stages. The fan as well as the high- and low-pressure compressors give the thrust. They use mechanical energy in order to compress the fluid. The mechanical energy is provided by the high- and low-pressure turbines, which in turn are driven by the compressed and combusted fluid. The fan and the low-pressure compressor are directly connected to the low-pressure turbine by a shaft (green) and the high-pressure compressor is connected to the high-pressure turbine (purple).

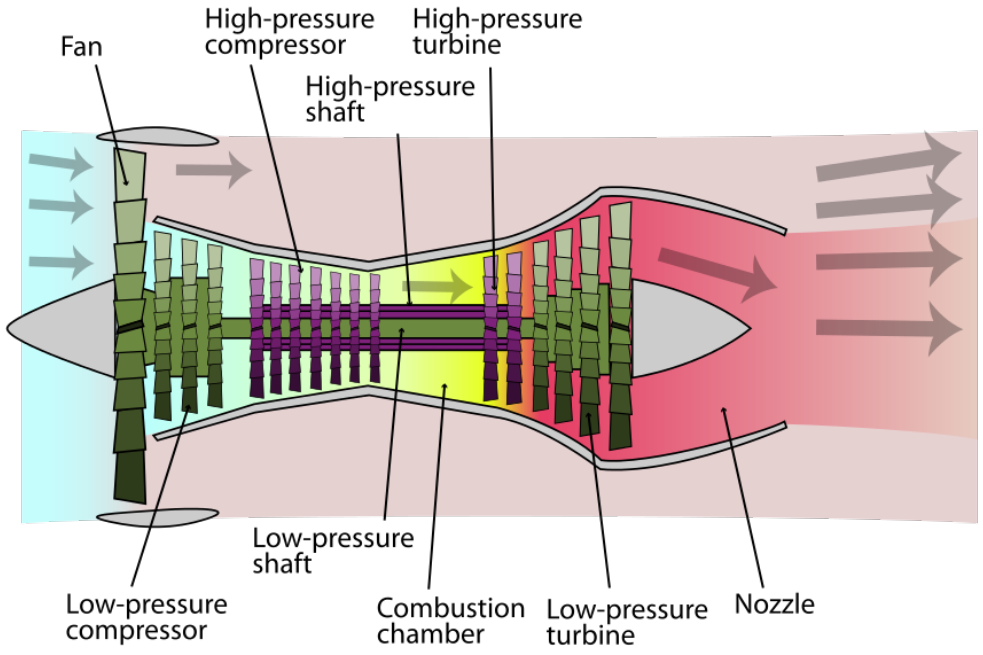

FIGURE 1.1: Two-shaft high-bypass turbofan engine; LP turbine connected to the fan and LP compressor; reproduced from Aainsqatsi (2008)

As already mentioned, the focus in this work is on the low-pressure turbine, see figure 1.2, in which the cross section of an LP turbine is depicted. It can be seen that the turbine has several stages in order to gradually expand the flow, i.e. a reduction in static pressure. Each stage consists of a stator and a rotor blade row.

A low-pressure turbine in a jet engine makes up 20-30% of its total weight. Its dimension is restricted by the diameter of the jet engine casing as can be seen in figure 1.1. The rotational speed of the LPT and hence the prevalent flow velocities are bounded to the operational range of the fan and the low-pressure compressor due to its direct connection with the shaft. Thus, typical Reynolds number range from 0.5×10^5 to 5.0×10^5 (Hodson and Howell 2005b).

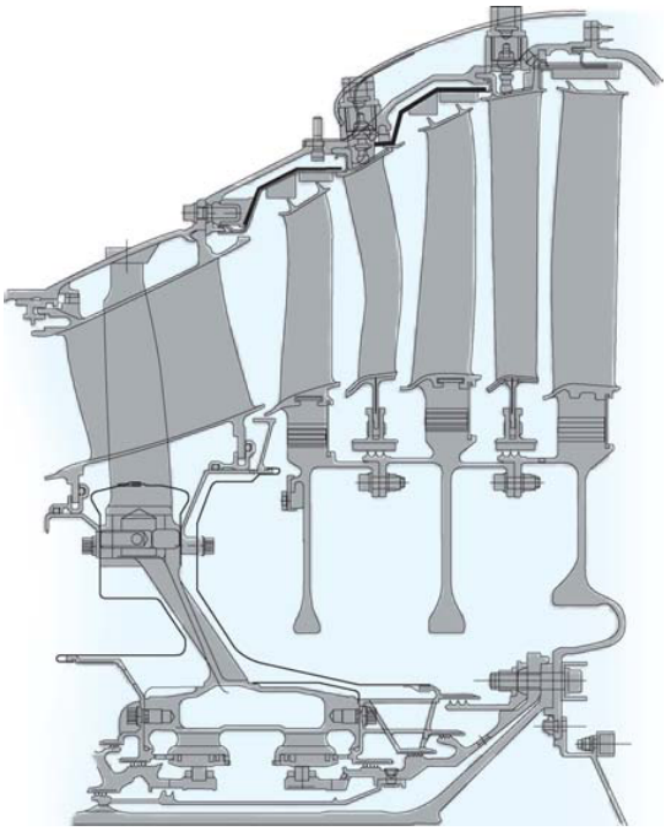

FIGURE 1.2: LP turbine cross section reproduced from Cobley et al. (1997)

In order to reduce operational costs the fuel consumption can be lowered by increasing the efficiency of the turbine. Another possibility is to increase the lift of the blades, which allows the number of blades and thus weight to be reduced (Hodson and Howell 2005b). Because of the decreased blade count each blade is now required to carry higher loadings, which renders the blade's boundary layer more sensitive to disturbances and prone to laminar and turbulent separation, depending on the Reynolds number. Consequently, a balance between the loadings, i.e. blade count and overall weight, and the reduction in aerodynamic efficiency - or increase in aerodynamic loss generation - has to be found. This requires an understanding of the loss generation in turbomachines. The term loss means that the efficiency is negatively affected and the main aim in the designing process is to reduce those losses. Denton (1993) uses the definition of the isentropic efficiency in a turbomachine to be able to quantify the loss. Only deviations from the isentropic state of the flow influence the isentropic efficiency. The flow conditions in a machine are commonly adiabatic and the only measure that can cause this deviation is the generation of entropy (Denton 1993). According to the author, a turbomachine has three main loss components where entropy is generated, which are

1. the profile loss,
2. the endwall loss and
3. the tip-leakage loss.

The profile loss includes the loss generated in the boundary layer and by the trailing edge due to viscous friction (Denton 1993). Furthermore, it is mentioned that even though the flow in a turbomachine is three-dimensional, the profile losses can be investigated in the two-dimensional frame in order to help understand the flow physics. The endwall losses originate from the shaft and the casing of the jet engine. Tip-leakage losses occur owing to the small gap between the rotor tip and the casing, where flow is able to leak through. The interaction with the leakage-flow and the mainstream causes entropy generation and thus a reduction in efficiency (Denton 1993). Each of the three main loss sources contribute about 1/3 to the total loss and hence a sound understanding of the physical phenomena of the flow within turbomachines is required (Denton 1993).

Within this work the profile losses of the low-pressure turbine are investigated. Direct numerical flow simulations of complex three-dimensional turbomachines with rotating blades are not feasible. However, as only the profile losses are investigated and two-dimensional results give reasonable insights into the flow phenomena, some simplification can be made. By unwrapping a single stage of a turbomachine, a linear cascade with constant blade sections in spanwise direction can be created, see figure 1.3.

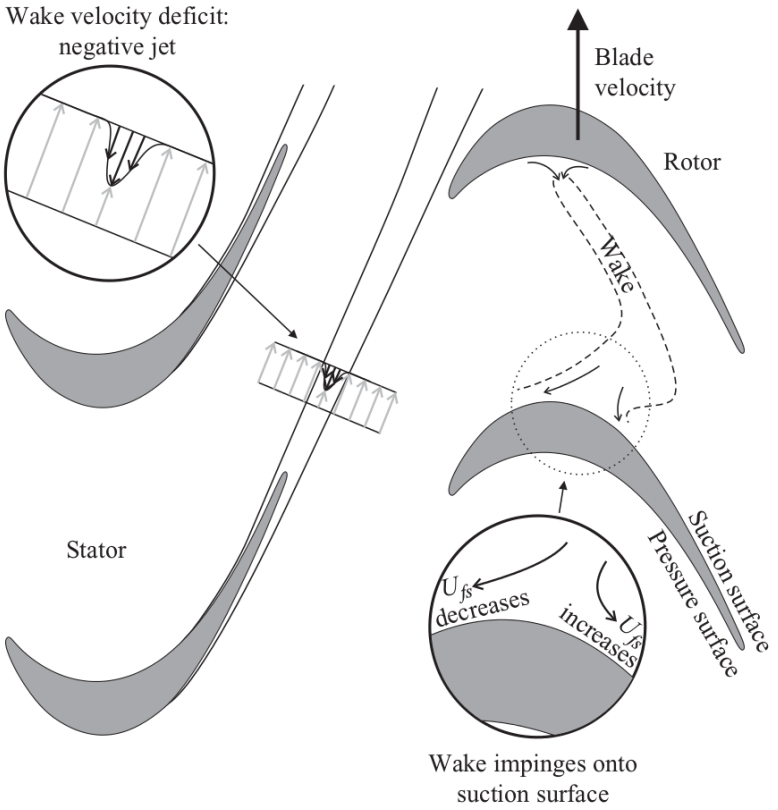

FIGURE 1.3: Single stage linear low-pressure turbine cascade with stator and rotor

Linear cascades can be used for both experimental and numerical investigations of profile losses (Denton 1993). Instead of a rotational motion a linear motion in the pitchwise direction is achieved. Even though rotation in a real turbine influences the flow through turbomachine stages, it is still possible to gain reasonable insights into the fundamentals of the flow (Hodson and Howell 2005a). Tip-leakage losses can now be easily prevented by attaching the blades

directly to the wall on both sides. As for simulations periodic boundary conditions can be applied in the spanwise direction. The mean gradients of the flow in this direction is zero, which allows for quasi two-dimensional simulations (Wu and Durbin 2001).

1.2.2 The Unsteady Environment in Turbines

In the previous section the concept of the linear low-pressure turbine cascade was introduced, which is the basis for the numerical simulations in this work. A review of the research into linear low-pressure turbine cascade, that has been done so far, is given in the following.

Disturbances and Unsteadiness:

The flow in a turbomachine is characterised by disturbances and unsteadiness that are generated due to several effects. The unsteadiness is on account of the relative motion between the stator and rotor (Hodson and Howell 2005b; Korakianitis 1993). The stator, which is upstream of the turbine rotor, gives rise to viscous velocity wakes that interact with the rotor. Another disturbance is the potential flow field induced because of the lift (circulation) generation of both the stator and the rotor blades. These potential flow fields can be seen as changes in the static pressure field. Both forms of periodic unsteady effects make up the primary and most important disturbance generators. However, the potential flow field interactions between the stator and the rotor are weaker than the effect of the generated wake and only affect boundary layers that are close to separation (Hodson and Howell 2005b). Pichler et al. (2018) found that the effect of the potential field on an upstream stator increases for smaller stator-rotor gap sizes, but did not observe a change in the profile losses.

Korakianitis (1993) investigated the effect of the potential field in a linear LPT cascade. Based on experimental measurements they found that the pressure variation in the pitchwise direction is almost sinusoidal. The amplitude of the pressure reaches a maximum at the leading edge of the stator and decays very fast with the downstream distance. Both the stator and the rotor create a potential field that interact and influence each other. His investigations revealed that as the stronger potential field of the stator reaches the rotor plane the potential flow field is cut by the weaker pressure field of the rotor. This results into a separation of the pressure field. The downstream part of the potential flow field then travels through the cascade and interacts with the boundary layers of the blades.

In addition to the potential field investigations Korakianitis (1993) also examined the effect of velocity wakes. Based on experimentally obtained data he concluded that the wake is similar to a Gaussian distribution. Furthermore, in most cases the width of the wake of the pressure side is narrower than the suction side width of the wake due to the thinner boundary layer on the pressure side. Meyer (1958) studied the effect of the velocity wake in form of a van Kármán vortex street on a stationary blade. The velocity wake is also referred to as a 'negative jet' which travels towards its origin in a uniform flow, see figure 1.3. Hodson and Howell (2005b) did LDA measurements of a wake passing through a linear cascade. Figure 1.4 shows a time series of snapshots as the wake of the stator passes the cascade. They observed a simultaneous bowing, elongation and stretching motion that concur with the suggestions of Smith (1966).

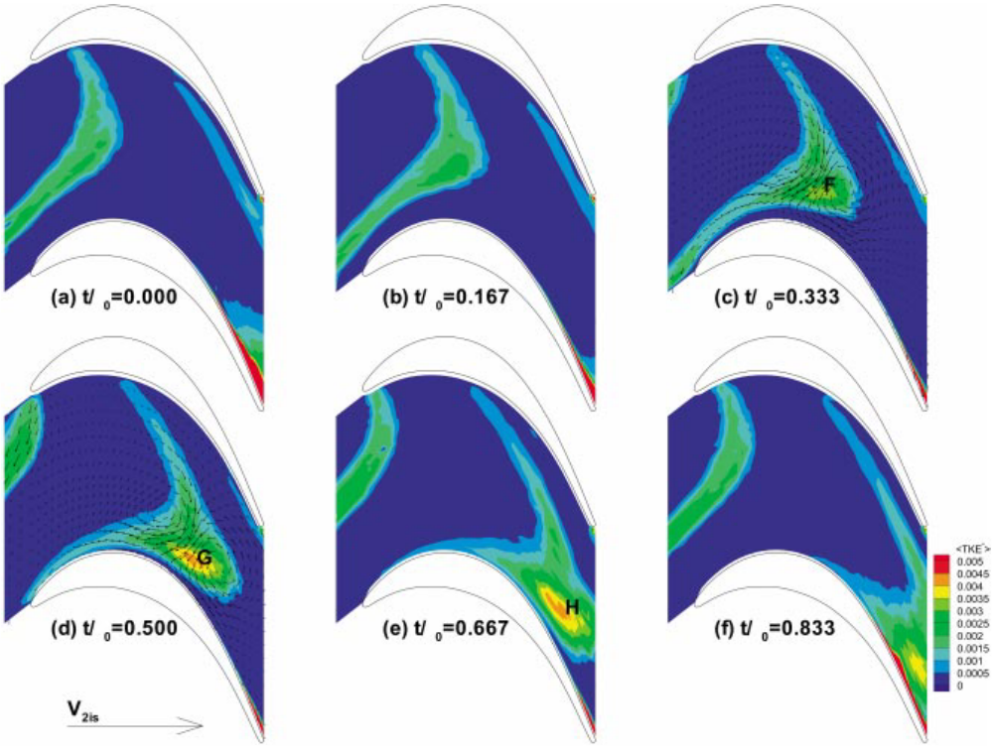

FIGURE 1.4: LDA measurements of wake passing blade cascade (Hodson and Howell 2005b)

The periodically incoming wakes interact with the boundary layers of the blades, which is discussed in more detail in a later section.

On account of the relative motion between the stator and the rotor the wake and the freestream flow can be viewed in different reference frames. Figure 1.5 shows the absolute and the relative frame of the flow velocities of the wake and the freestream.

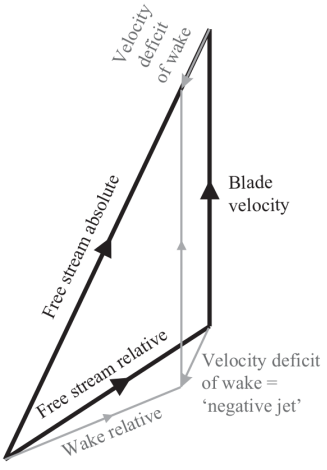

FIGURE 1.5: Velocity triangle (Coull and Hodson 2011)

The rotor, which moves with a given 'blade velocity', sees the wake and the free stream velocities in the relative frame as opposed to the stator which refers to the absolute frame. It should be

noted that due to the wake deficit ('negative jet') the freestream and the wake have a different angle in the relative frame. Thus, care has to be taken when setting up experiments and simulations.

In order to simplify both experiments and simulations, a setup with moving bars upstream of the rotor is commonly used to generate velocity wakes (Engber and Fottner 1995; Ladwig and Fottner 1993; Michelassi et al. 2003, 2015; Pfeil and Eifler 1976). Pfeil and Eifler (1976) conducted measurements of pitchwise-rotating cylinder bars to investigate the turbulent behaviour in the wake. According to them, the wake velocity profile of a cylinder is similar to that of an actual stator blade cascade when a similar drag is achieved. Liu and Rodi (1994) investigated the effect of unsteadiness on a turbine cascade. They used circular cylinder bars arranged in a squirrel cage to generate incoming wakes. Based on this experimental setup Wu et al. (1999) carried out DNS of the effect wakes on the boundary layer transition of turbine blades. However, instead of a circular arrangement of the cylinders they used a linear arrangement. Coull and Hodson (2011) investigated the unsteady boundary layer transition mechanisms in a turbine cascade due to incoming wakes. In their experimental setup they designed a moving bar cascade to generate these wakes. The moving bar design is based on results of turbulence and wake measurements in a three-stage research turbine conducted by Halstead (1997). In order to mimic the wakes of an upstream rotor within the LES and DNS simulations of a linear LPT in this work, moving cylinder bars are incorporated as well.

Boundary-Layer Transition induced by Wakes:

In the Reynolds number range in which an LP turbine operates, boundary layer transition and separation play an important role and have to be taken into account in the design process. As already mentioned earlier, in order to reduce the operational cost of a jet engine the weight of a turbine can be decreased by reducing the blade count. As a consequence each blade has to generate more lift and thus experiences a higher loading, which can be described by the Zweifel number

$$Zw = 2\frac{P_{Blade}}{c}\cos^2\alpha_2\left(\tan\alpha_2 - \tan\alpha_1\right). \tag{1.1}$$

Here P_{Blade}, c, α_1 and α_2 are the blade pitch, the chord length, the inlet and the exit flow angle, respectively. Higher loadings mean that the boundary layers on the suction and the pressure side of the blade are exposed to larger adverse pressure gradients leading to unsteady transitional boundary layers (Sandberg et al. 2015). Hodson and Howell (2005b) state that, as the flow on the pressure side still accelerates fairly fast in the direction of the trailing edge, the boundary layer remains laminar in most cases. Thus, the boundary layer on the suction surface of the blade takes the main contribution of the two-dimensional profile loss. A laminar separation bubble develops on the suction surface on the rear part of the blade due to the adverse pressure gradient. The separation bubble is highly sensitive to the unsteady and disturbed flow in the LP turbine and the effect of the upstream wakes play an important role (Hodson and Howell 2005b).

In an extensive study Halstead et al. (1997b) exposed three forms of boundary layer transition on blades in a turbine cascade caused by incoming wakes:

1. Attached flow transition
2. Transition in the laminar separated shear layer

3. A mix between transition in attached and separated flow

Attached flow transition can occur because of two reasons. Either the Reynolds number is high enough, which causes the attached flow to be transitional before it can separate, or else a low adverse pressure gradient allows the flow to remain attached and transition is induced by the turbulent wakes and/or freestream turbulence (Hodson and Howell 2005b). In case of a low Reynolds number and with a stronger adverse pressure gradient the laminar flow separates and transition is eventually induced by the turbulent wake in the shear layer of the separated bubble (Hodson and Howell 2005b). Depending on the wake passing frequency at mid-level Reynolds numbers separation can occur during wake impinging events. After separation, transition is then induced by the incoming wakes. If the passing frequency of the wakes is high enough, transition due to the wakes is triggered in the attached laminar boundary layer (Hodson and Howell 2005b). Unsteady wakes have a great impact on the state of the boundary layer and the size of the separation bubble. Hodson and Howell (2005b) found in their experimental investigations that wakes impinging on the blade increase the skin-friction and thus create more losses. Several authors (Hodson and Howell 2005a; Montomoli et al. 2010) ascertained that the incoming wakes can prevent laminar separation and the development of a separation bubble due to the induction of early transition. This means that, since the size of the separation bubble is related to the loss of efficiency (Coull and Hodson 2011), wakes can reduce the overall loss compared to a case without wakes. The effect is strongest for highly loaded blades where a large separation bubble is present in steady cases without incoming wakes.

Wake Mixing and the Effects on the Turbine:

In order to shed more light on the influence of the wake passing frequency, Michelassi et al. (2015) conducted an extensive DNS study of a linear low-pressure turbine cascade. Simulations with different reduced frequencies F_{red} of the wake generating bars were carried out. For the simulations two different isentropic Reynolds numbers ($Re_{2,is} = 60,000$ and $100,000$) and a range of different levels of background turbulence were chosen. The spacing between the bars in pitchwise direction is related to the reduced frequency as follows

$$F_{red} = f\frac{c}{V_{2,is}} = \frac{U_{bar}}{P_{bar}}\frac{c}{V_{2,is}}, \tag{1.2}$$

with the bar passing frequency f, the tangential bar velocity U, the bar pitch P_{bar} and the isentropic exit velocity $V_{2,is}$. The authors also found that the effect of incoming wakes, combined with background turbulence, can shorten the separation bubble and in some cases even prevent laminar separation.

Another effect on the loss generation is due to the mixing of the wakes generated by the upstream bars, which was already investigated by Smith (1966). The DNS simulations carried out by Michelassi et al. (2015) confirm that wake mixing plays an important role in the loss generation. For a high reduced frequencies, e.g. $F_{red} = 1.2$, the wakes of the bars are mixed out before reaching the rotor passage, whereas for lower reduced frequencies the separated wakes pass the leading edge of the cascade and the mixing process takes place within the passage and thus causes extra loss generation.

Michelassi et al. (2016) further investigated the combined effect of reduced frequency F_{red} and the flow coefficient Φ on a linear LPT turbine cascade by carrying out large eddy simulations.

The flow coefficient Φ is defined by

$$\Phi = \frac{V_{ax}}{U_{bar}}, \tag{1.3}$$

where V_{ax} and U_{bar} are the axial flow velocity in the absolute frame and the tangential bar velocity, respectively. In the study they found that for different combinations of the flow coefficient and reduced frequency a distorted and weakened wake can be achieved before reaching the blade passage and thus improving performance.

Wake generation and Gap Sizes:

As already mentioned, moving bars upstream of the rotor are used instead of actual stator blades in order to simplify both experiments and numerical simulations. A van Kármán vortex street is generated when flow passes a bluff body (Kármán 2013). Behind an aerofoil with a blunt trailing edge the formation of a vortex street can also be noticed. Vortices are shed in an alternating fashion from the upper and lower part of the cylinder and produce circulation (lift). Due to the fact that the cylinder is symmetric each vortex generates the same amount of lift and thus the mean net lift equals zero.

One of the aims of this work is to investigate the effect of different wake profiles on the linear low-pressure turbine cascade, which can be seen as a change of axial gap size between a stator and a rotor blade in a turbine stage (Pichler et al. 2018). The stator-rotor gap size is an important design parameter, as it not only affects the turbine flow itself, but also the overall size and weight (Pichler et al. 2018). However, to keep things as simple as possible a moving bar cascade is used instead of actual stator blades. There are four possibilities in order to simulate different wake profiles.

1. Imposing wake profiles as inlet conditions
2. Different bar diameters
3. Different gap sizes, i.e. increasing or decreasing the distance between the bars and the rotor blades
4. Using the Magnus effect (Prandtl 1925)

The first option is the simplest and the computationally least expensive method of simulating and investigating different incoming wake profiles. Based on prior simulations or a mathematical model wake profiles can be extracted or calculated and then imposed as inlet conditions. However, as mentioned above, there are interaction between the rotor and the stator due to the generated potential field, which influences the rotor as well as the stator (Hodson and Howell 2005b; Korakianitis 1993; Pichler et al. 2018). Hence, by just imposing wakes as inlet conditions would not account for the interaction between the stator and the rotor. For this reason, the decision to simulate an actual stator - in form of bars - was made.

The second and the fourth option are based on the statement of Pfeil and Eifler (1976), who claimed that the velocity deficit of a bar is similar to that of a blade when the drag is the same. Possibility 2 was used by Halstead et al. (1997a), who changed the rod diameters in order to generate different "wake-turbulence intensities". However, they found that in terms of wake-boundary layer interaction it is more important to consider the wake intensity and not

the produced velocity deficit, as opposed to the claims of Pfeil and Eifler (1976). The stronger the wakes, the more effective the emerging streaks in the boundary layer and the stronger the calmed region. Furthermore, the authors noted that for similar velocity deficits between a bar wake and an actual blade wake the intensity levels are considerably higher for the bar.

The third option is to directly change the distance between the wake generating bars and the turbine blade. Pichler et al. (2018) conducted large eddy simulations of a full stage stator-rotor turbine cascade. They found that for smaller gap sizes the incoming wakes were stronger, by considering the TKE values, and were able to completely prevent the separation bubble that was still present in the case with a larger gap. Even though the profile losses were reduced due to the absence of the separation bubble, the overall turbine losses were increased due to stronger wake mixing effects.

However, options 2 and 3 require re-meshing every time a different configuration is used. This is prone to introducing unnecessary errors, caused by the different meshes and domain sizes. In order to keep as many parameters as possible unchanged, option four was used within this work, where the bars were set into rotation around their axis generating lift and drag forces. Figure 1.6 shows an illustration of a clockwise rotating cylinder in a uniform flow.

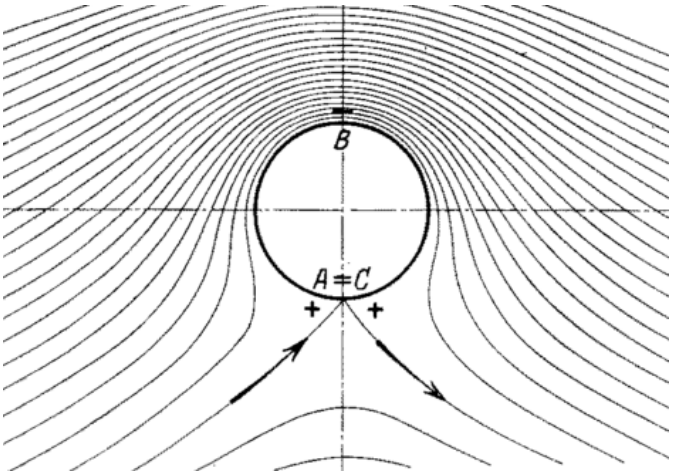

FIGURE 1.6: Rotating cylinder creating lift due to Magnus effect

The flow above the cylinder is accelerated and on the bottom side it is decelerated. Furthermore, at a certain rotation rate the two stagnation points A and C that are located at the leading and the trailing edges in the non-rotating case move downwards along the cylinder surface and eventually merge to a single stagnation point. The static pressure at this position is above the freestream pressure, p_∞, whereas the pressure on the upper surface, denoted by point B, is below p_∞. Thus a net lift is generated due to the pressure difference between the top and the bottom part of the cylinder . Moreover, the cylinder wake is now asymmetric similar to a real stator blade wake as stated by Korakianitis (1993). Changing the rotation rate is a very effective and convenient way to change the incoming wake characteristics, which requires neither an alteration of the grid nor the computational domain.

1.2.3 Surface Roughness in Turbines

General Overview of Surface Roughness:

During the operation cycle of a turbine the blade surface becomes rough due to numerous effects. Operational factors like combustion particles and natural factors like aerosols, dust, sand, ashes etc. damage and wear the surface of the blades Bons 2010. Bons et al. (2001) summarised four distinct roughness mechanisms within turbines. First, airborne particles can settle on the blade leading to small local spikes. Second, there may be corrosion pitting which, in contrast to airborne particles, causes small local holes. Third, the combination of particles and corrosion can lead to erosion, causing more irregular surfaces. The last type is spallation, where due to the concentration of stresses small parts of the material break off. Spallation is also the most significant roughness mechanism, causing the most irregular and rough surfaces. These mechanisms happen on any part of the blade leading to 4-8 times higher roughness values compared to a new blade.

Nikuradse (1933) was the first to conduct an extensive study on the effects of roughness on fluid flow by means of an experimental investigation of water flow through a roughened pipe. The pipe was coated with sand grains, leading to the iconic and popular roughness parameter, k_s, which describes the actual size of the grain. For pipe flow a resistance factor was introduced and is defined by

$$\lambda = \frac{dp}{dx}\frac{d}{\frac{1}{2}\rho\overline{u}^2}, \tag{1.4}$$

which describes the pressure drop per unit length, $\frac{dp}{dx}$, in a pipe with diameter, d, and the dynamic pressure, $\frac{1}{2}\rho\overline{u}^2$, based on the average flow velocity, $\overline{u}$, and density, ρ. Nikuradse (1933) categorised three different ranges for the different trends and behaviours of the resistance factor.

1. The hydraulically smooth regime
2. The transitionally rough regime
3. The fully rough regime

For very low Reynolds numbers, $Re_d = \overline{u}d/\nu$, the sand-grain roughness, k_s, shows no effect on the pipe flow and the resistance factor, λ, follows the same trend as pipe flow with smooth walls. Hence, the flow problem is said to be hydraulically smooth. If the ratio between the boundary layer thickness and the sand grain roughness decreases, i.e. by increasing the Reynolds number, Re_d, the roughness begins to affect the flow and is classified as transitionally rough. In the fully rough regime, the resistance factor is completely independent of the Reynolds number, Re_d.

These regimes can also be denoted by the non-dimensional sand grain roughness parameter

$$k^+ = \frac{u_\tau k_s}{\nu}, \tag{1.5}$$

where u_τ is the skin friction velocity and ν the dynamic viscosity. For the "transitionally rough" region a range of $5 < k^+ < 70$ was observed. Once k^+ exceeds a threshold of 70, the resistance factor becomes only a function of the non-dimensional sand grain parameter.

One major finding made by Nikuradse (1933) was that the well known velocity profile

$$U^+(z^+) = \frac{1}{\kappa}\ln(z^+) + A \tag{1.6}$$

for turbulent boundary layers was still observable in the presence of roughness. With the difference, however, that the constant A now depends on k^+. Common values for the the Kárman constant and the additive constant in the fully rough regime are $\kappa \approx 0.4$ and $A \approx 5.1$, respectively (Jiménez 2004).

Based on these observations Schlichting (1936) conducted experiments with different kinds of roughness elements and correlated his findings with those of Nikuradse (1933). He came up with the equivalent sand grain roughness parameter, k_s, which has since been used throughout the literature for roughness related investigations. The equivalent sand grain roughness, k_s, allows the classification of different roughness types that have a similar (equivalent) effect on the skin friction as actual sand grain roughness.

Another important contribution is the observation and definition of the Hama roughness function, ΔU^+ (Hama 1954; Perry et al. 1969). By comparing the mean streamwise velocity profiles between a smooth and a rough wall case, a velocity deficit of the velocity in the logarithmic region due to the increased skin friction can be observed, which was then termed as ΔU^+. Furthermore, combining the roughness function with the law of the wall equation for smooth wall cases yields

$$U^+(z^+) = \frac{1}{\kappa}\ln(z^+) + A - \Delta U^+(k^+). \tag{1.7}$$

Here $\Delta U^+(k^+)$ acts as a correction term in the presence of surface roughness.

These equations are based on k-type roughness as opposed to d-type roughness. The classification into k-type and d-type roughness is based on the ratio between the height of the roughness peaks, k, to their distance, w, from each other. E.g. for $2D$ bars in a channel k-type roughness is assumed when the distance between each element is larger than its height, $k/w < 1$ (Leonardi et al. 2007). Leonardi et al. (2007) further investigated the distinct effects of both roughness types and found that "a d-type behavior ensues when the frictional drag dominates over the pressure drag, whereas for a k-type roughness the pressure drag is large."

For more complex types of roughnesses, e.g. real rough surfaces in turbomachinery or irregular combinations of simple elements, it is common to characterise the surfaces by parameters like the averaged centreline roughness height, Ra, and its root mean square value, k_{rms}, which are defined as

$$Ra = \frac{1}{N}\sum_{i=1}^{N}|h_i - h| \tag{1.8}$$

and

$$k_{rms} = \frac{1}{N}\sqrt{\sum_{i=1}^{N}(h_i - h)^2}. \tag{1.9}$$

Here h_i is the height of the roughness at a discrete point i of the overall amount of discrete points, N, and h is the mean roughness height defined by

$$h = \frac{1}{N} \sum_{i=1}^{N} h_i. \tag{1.10}$$

These parameters are then correlated with the equivalent sand-grain roughness parameter, k_s. When investigating real roughness surfaces, however, Bons et al. (2001) found a wider range of correlations between Ra and k_s than was commonly observed for more simplified roughness geometries and arrays. Throughout the literature of turbomachinery research, many authors proposed different convertion factors between Ra and k_s, resulting in a large range $1 < k_s/Ra < 10$ (Bons 2010).

Effects of Surface Roughness on the Turbine:

The wide range of roughness correlations makes it hard to obtain definitive results. Bons (2010) stated that there are two universally defined parameters serving as guidelines (Harbecke et al. 2002; Hummel et al. 2005). The first is the admissible roughness height

$$\frac{k_{s,adm.}}{c} \leq \frac{100}{Re_c}, \tag{1.11}$$

where Re_c is the Reynolds number based on the chord length, c. Roughness has no influence on the turbulent boundary layer, i.e. hydraulically smooth, as long as equation 1.11 holds true (Bons 2010; Schlichting 1936). The second parameter is the roughness Reynolds number

$$Re_{k_s,\infty} = \frac{U_\infty k_s}{\nu} < 100, \tag{1.12}$$

which is also extensively used in literature (Blair 1992; McIlroy et al. 2003). The admissible roughness height and the roughness Reynolds number thresholds are based on the assumption that a turbulent boundary layer is present. Bons (2010) noted that for transition to turbulence the relation is less clear, with values found to be between $Re_{k_s,\infty} \approx 120$ (Feindt 1957) for low Reynolds numbers at low freestream disturbance levels and $Re_{k_s,\infty} = 600$ for a single roughness element at elevated freestream turbulence levels (White and Corfield 2006), which are common in turbomachinery.

Furthermore, there are various effects of surface roughness on turbine flows. The overall trend is that roughness negatively affects the efficiency of a low-pressure turbine. This is owing to a higher boundary layer momentum thickness, a shift in the boundary layer transition further upstream and turbulent flow separation (Boyle and Senyitko 2003). These negative aspects were identified in particular for operation points at high Reynolds numbers. However, in the low Reynolds numbers operating range, where laminar separation bubbles can be prevented or reduced due to earlier transition, a positive effect was observed (Montomoli et al. 2010; Vera et al. 2007). Roughness induced transition in free shear layers was also found to be able to reduce the size of separation bubbles (Roberts and Yaras 2005). Stripf et al. (2009) noted that roughness had no effect on the flow characteristics of the laminar boundary layer before transition has occurred, but enhanced the profile loss and heat transfer in turbulent boundary layers. Bons (2010) also noted the additive and "synergetic effects" of roughness and freestream turbulence, which both increased profile losses at high Reynolds numbers. One further effect was mentioned by Tsikata

and Tachie (2013), who found in their rod roughened channel case that the addition of adverse pressure gradients (APG) "significantly increased turbulence production and Reynolds stresses" slightly above the roughness.

Another important area is film cooling in turbines. Being exposed to very high temperatures, efficient cooling and convection of heat from the blades need to be guaranteed. Rutledge et al. (2006) found that roughness decreases the adiabatic effectiveness of film cooling. Because roughness also enhances the heat transfer, a combined effect was observed resulting in a $30\% - 70\%$ higher heat flux toward the blade surface.

As mentioned above, the suction surface is in general the main contributor to profile losses due to the stronger APGs and its sensitivity to disturbances. Several studies have confirmed that the suction surface is also more strongly affected by surface roughness including Bons 2010; Rao et al. 2014b; Stripf et al. 2009.

Numerical Investigation of Surface Roughness:

Roughness research to date has mainly been done by means of experiments owing to the complexity of rough surface geometries and the lack of computational power (Busse and Sandham 2012). When computational power increased it was finally also possible numerically investigate roughness. However, the research was still mainly constrained to channel and boundary layer flows with simple roughness elements, e.g. $2D$ bars, isolated elements or array configurations (Kind et al. 1996; Leonardi et al. 2003; Rao et al. 2017; Redford et al. 2010; Stripf et al. 2004; Tsikata and Tachie 2013; White and Corfield 2006). More recently the focus has also shifted to real rough surface simulations in channel flows (Licari and Christensen 2011; Rao et al. 2014b; Roberts and Yaras 2005). For example, Forooghi et al. (2017), Thakkar (2017), and Thakkar et al. (2017b) conducted a extensive DNS studies of channel flow with several different surface roughness samples, providing a large database for surface correlations.

Numerical simulations of roughness on actual low-pressure turbine blades still pose a difficulty in terms of computational power. This is even more so considering real rough surfaces, which require a much higher resolution. Hence, it is common to use channel flows with imposed pressure distributions that were obtained from actual turbine blade simulations or experiments. This is usually achieved by a curved no slip wall at the top of the channel and allows for a turbine blade-like environment. Rao et al. (2014b) conducted LES simulations of real roughness in the mentioned channel setup. The authors found the same benefits due to surface roughness as previous low Reynolds number studies (Bons 2010; Montomoli et al. 2010; Vera et al. 2007), namely the reduction in the size of separation bubbles and thus lower profile losses. Joo et al. (2016) carried out large eddy simulations of an actual linear low-pressure turbine cascade but with 'artificial' roughness, consisting of homogeneously distributed little squares on the blade surface, and confirmed the findings about the negative effects.

There are three basic principles in order to represent or model roughness in numerical simulations (Bons 2010; Busse and Sandham 2012). Firstly, adjusting the wall boundary conditions to account for the effects of roughness (Fiala and Kügeler 2011; Flores and Jimenez 2006; Tucker 2013). Tucker (2013) noted that an adjustment of the "law of the wall constants" was commonly used. Secondly, roughness can be modelled by additional terms in the governing equations that account for the form drag and blockage effects of roughness (Anderson and Meneveau 2010;

Busse and Sandham 2012; Taylor et al. 1985); this is termed the "discrete element approach" (DEM). Lastly, the rough surfaces can be fully resolved by means of body-fitted grids (Chan et al. 2015; Choi et al. 1993) or immersed boundary methods (IBM) (Bhaganagar et al. 2004; Busse et al. 2015; Mittal and Iaccarino 2005; Peskin 2002; Tseng and Ferziger 2003). The choice between body-fitted grids and immersed boundary methods depends mainly on the complexity of the surface and the available computational power. For more complex geometries immersed boundary methods are more suitable, as usually only a simple mesh is required. However, due to this a much higher grid resolution is needed as well (Busse and Sandham 2012). Cui et al. (2003) combined the discrete element method with an immersed boundary method. The authors represented the larger roughness features by means of an IBM, whereas the smaller features were modelled by the DEM.

For all roughness representations method, however, it is paramount that the prediction of the right transition location in the presence of roughness is guaranteed, as the change in heat transfer and boundary layer momentum in the turbulent boundary layer is strongly affected by roughness (Stripf et al. 2009).

1.3 Research Objectives

This work is based on the numerical setup and main parameters of the large eddy simulations of Sandberg et al. (2015) and Michelassi et al. (2015). There are two important aspects that will be investigated. Firstly, the influence of different wake profiles on the linear low-pressure turbine cascade.

1. Based on the statement of Halstead et al. (1997a), what is the relation between the velocity deficit and the turbulent kinetic energy of bars with different drag coefficients?
2. What are the effects of different wakes on the boundary layer of the blade and the overall losses of the turbine?
3. Do simple bars, by using the Magnus effect, show similar trends to a full turbine stage regarding different gap sizes?

Another aspect of this work is the investigation of the effect of surface roughness on the boundary layer of a turbine blade and losses within a cascade as well as the suitability of a roughness model for transitional boundary layers.

4. Can a simple roughness model, namely the Parametric Forcing Approach (PFA) (Busse and Sandham 2012), be used for transitional cascade flows?
5. What are the effects of surface roughness on the blade's boundary layer and loss mechanisms?
6. Is it feasible to carry out large eddy simulations of a real surface roughness patch, represented by an immersed boundary method (Schlanderer et al. 2017), on a turbine blade with periodically incoming wakes?

1.4 Thesis Layout

The thesis is divided into six main chapters. Chapter 1 has presented the motivation and the key objectives of this work as well as a literature review of the linear low-pressure turbine cascade concerning the unsteady turbine environment and surface roughness effects.

The numerical methods for the simulations are laid out in chapter 2, including the governing equations (section 2.1). In section 2.2, the boundary data immersion method (BDIM) and its extension for handling complex three dimensional geometries are explained, which is followed by a validation case. Furthermore, the used parametric forcing approach for roughness modelling is introduced (section 2.2.3).

Chapter 5 presents the two roughness representation methods, the boundary data immersion method and the parametric forcing approach, within turbulent channel flow at Reynolds number, $Re_\tau = 180$. Firstly, results for a streamwise wavy channel flow and grit blasted roughness using the BDIM are presented. The effect of the PFA in laminar-turbulent transitional channel flow is investigated in section 3.3. In section 3.4 results of the parametric forcing approach and the boundary data immersion method are compared. This chapter also serves as a basis for chapter 5, which is concerned with roughness in the linear cascade.

In chapter 4 the influence of different wake profiles on the linear low-pressure turbine cascade is investigated. The chosen cascade setup is shown and a validation case for the boundary data immersion method, representing the wake generating bars, is presented. After that the relation between the different drag coefficients of the rotating bars with the velocity deficit and the turbulent kinetic energy is shown. Finally, the effects of incoming wakes with different strengths on the blade's boundary layer and overall turbine losses are examined.

Surface roughness and its effects on the low-pressure turbine are considered in chapter 5. Firstly, a grid convergence and validation case for the surface roughness patch using the boundary data immersion method is presented. Then the effects on both the boundary layer of the turbine blade and the overall turbine losses are examined. A parameter study of the modelled surface roughness, where the roughness height, density and length were varied, is laid out in section 5.3.

In chapter 6 the findings are summarised and an outlook for future work and projects is given.

Chapter 2

Numerical Methods

In this chapter the numerical methods used within this work are introduced as well as the initial, boundary and characteristic boundary conditions including the incorporated immersed boundary method and roughness forcing model. The in-house code HiPSTAR - High Performance Solver for Turbulence and Aeroacoustic Research - was used, which is written in Fortran 95. In HiPSTAR the compressible Navier-Stokes equations with an ideal gas assumption are solved. The reason for solving the compressible rather than the incompressible equations is due to the turbine environment, which is exposed to higher temperatures and Mach numbers exceeding the common threshold of $M > 0.3$ under which compressible flow effects are negligible.

2.1 Governing Equations of Compressible Viscous Flow

The nondimensional compressible Navier-Stokes equations with ideal gas assumption are given in Cartesian coordinates by

$$\frac{\partial \mathbf{Q}}{\partial t} + \frac{\partial \mathbf{E}}{\partial x_1} + \frac{\partial \mathbf{F}}{\partial x_2} + \frac{\partial \mathbf{G}}{\partial x_3} = \mathbf{S}_V, \tag{2.1}$$

in terms of the conservative flow quantities

$$\mathbf{Q} = [\rho,\, \rho u_1,\, \rho u_2,\, \rho u_3,\, \rho e_t]^T \tag{2.2}$$

and the fluxes

$$\begin{aligned} \mathbf{E} &= [\rho u_1,\, \rho u_1 u_1 + p,\, \rho u_1 u_2,\, \rho u_1 u_3,\, u_1(\rho e_t + p)]^T, \\ \mathbf{F} &= [\rho u_2,\, \rho u_1 u_2,\, \rho u_2 u_2 + p,\, \rho u_2 u_3,\, u_2(\rho e_t + p)]^T, \\ \mathbf{G} &= [\rho u_3,\, \rho u_1 u_3,\, \rho u_2 u_3,\, \rho u_3 u_3 + p,\, u_3(\rho e_t + p)]^T. \end{aligned} \tag{2.3}$$

Here, ρ is the density, u_i are the components of the velocity vector $\mathbf{u}$, e_t is the total energy and p is the static pressure. The nondimesnional pressure, p, is calculated by the equation of state for an ideal gas

$$p = \frac{\rho T}{\gamma M^2}. \tag{2.4}$$

Furthermore, the total energy, e_t, is defined as

$$\begin{aligned} e_t &= e(T) + e_{kin} \\ &= \frac{T}{\gamma(\gamma-1)M^2} + \frac{1}{2}u_i u_i \end{aligned}$$

with the inner energy, $e(T)$, the kinetic energy, e_{kin}, the nondimensional temperature, T, and the ratio of specific heat, γ. The viscous flux derivatives are contained in the viscous source term $\mathbf{S_v}$, which is defined as

$$\mathbf{S_v} = \frac{\partial \mathbf{E_v}}{\partial x_1} + \frac{\partial \mathbf{F_v}}{\partial x_2} + \frac{\partial \mathbf{G_v}}{\partial x_3}, \tag{2.5}$$

with

$$\begin{aligned} \mathbf{E_v} &= \left[0, t_{11}, t_{12}, t_{13}, u_1 t_{11} + u_2 t_{12} + u_3 t_{13} - q_1\right]^T, \\ \mathbf{F_v} &= \left[0, t_{12}, t_{22}, t_{23}, u_1 t_{12} + u_2 t_{22} + u_3 t_{23} - q_2\right]^T, \\ \mathbf{G_v} &= \left[0, t_{13}, t_{23}, t_{33}, u_1 t_{13} + u_2 t_{23} + u_3 t_{33} - q_3\right]^T. \end{aligned} \tag{2.6}$$

t_{ij} denote the components of the viscous stresses and are defined by

$$t_{ij} = 2\mu S_{ij} - \frac{2}{3}\mu \frac{\partial u_k}{\partial x_k}\delta_{ij} \tag{2.7}$$

for Newtonian fluid, where the nondimensional molecular viscosity μ is calculated by Sutherland's law

$$\mu = T^{\frac{3}{2}} \frac{1 + c_{sut}}{T + c_{sut}}, \tag{2.8}$$

with the nondimensional Sutherland temperature, c_{sut}, which takes the value $c_{sut} = 0.3686$ for air at a reference temperature of $T_{ref} = 300K$ (Schlichting and Gersten 2006). The strain rate tensor is given by

$$S_{ij} = \frac{1}{2}\left[\frac{\partial u_i}{\partial x_j} + \frac{\partial u_j}{\partial x_i}\right]. \tag{2.9}$$

The equation for the heat flux vector is

$$q_i = \frac{1}{\gamma - 1} \frac{-\mu}{Re_\infty Pr_\infty M_\infty^2} \frac{\partial T}{\partial x_i}, \tag{2.10}$$

with the reference Reynolds number Re_∞, the reference Mach number M_∞ and the reference Prandtl number Pr_∞, which are expressed as follows:

$$\begin{aligned} Re_\infty &= \frac{\rho_\infty u_\infty a}{\mu_\infty}, \\ M_\infty &= \frac{u_\infty}{c_\infty}, \\ Pr_\infty &= \frac{\mu_\infty c_p}{\kappa_\infty}. \end{aligned}$$

The superscript ∞ denotes the reference location of the flow quantity. For the nondimensionalisation flow quantities located within in the freestream are used and a reference length, a, is denoted. Depending on the flow problem, the reference length can be the radius, in the case of pipe or cylinder flow, the half height or length of a channel or the chord length of aerofoils etc. The Prandtl number is set to a constant value of $Pr = 0.72$.

2.1.1 Generalised Coordinates

The flow problems that are tackled are fairly complex and require non-uniform curvilinear meshes. However, the order of accuracy of finite difference methods for these kinds of meshes is lower compared to uniform ones (Moin 2010). Thus, to allow for more complex geometries without sacrificing numerical accuracy the compressible Navier-Stokes equations 2.1 are transformed from an (x_1, x_2) coordinate system into a generalised coordinate system (ζ, η). In the generalised coordinate frame the physical domain is represented by an equidistant uniform domain. The resulting coordinates have the following dependencies:

$$\begin{aligned} \zeta &= \zeta(x_1, x_2) \\ \eta &= \eta(x_1, x_2) \\ x_3 &= x_3 \end{aligned} \tag{2.11}$$

The azimuthal direction (x_3) is equidistant and discretised by means of a Fourier spectral method.

The derivatives in the generalised coordinate system are given by

$$\begin{aligned} \frac{\partial}{\partial x_1} &= \frac{1}{|J|}\left[\frac{\partial x_2}{\partial \eta}\frac{\partial}{\partial \zeta} - \frac{\partial x_2}{\partial \zeta}\frac{\partial}{\partial \eta}\right] = x^*_{2,\eta}\frac{\partial}{\partial \zeta} - x^*_{2,\zeta}\frac{\partial}{\partial \eta}, \\ \frac{\partial}{\partial x_2} &= \frac{1}{|J|}\left[\frac{\partial x_1}{\partial \zeta}\frac{\partial}{\partial \eta} - \frac{\partial x_1}{\partial \eta}\frac{\partial}{\partial \zeta}\right] = x^*_{1,\zeta}\frac{\partial}{\partial \eta} - x^*_{1,\eta}\frac{\partial}{\partial \zeta}, \end{aligned} \tag{2.12}$$

with

$$x^*_{1,\zeta} = \frac{1}{|J|}\frac{\partial x_1}{\partial \zeta}, \quad x^*_{1,\eta} = \frac{1}{|J|}\frac{\partial x_1}{\partial \eta}, \quad x^*_{2,\zeta} = \frac{1}{|J|}\frac{\partial x_2}{\partial \zeta} \quad \text{and} \quad x^*_{2,\eta} = \frac{1}{|J|}\frac{\partial x_2}{\partial \eta}. \tag{2.13}$$

The determinant of the Jacobian is given by

$$|J| = \begin{vmatrix} \frac{\partial x_1}{\partial \zeta} & \frac{\partial x_1}{\partial \eta} & 0 \\ \frac{\partial x_2}{\partial \zeta} & \frac{\partial x_2}{\partial \eta} & 0 \\ 0 & 0 & 1 \end{vmatrix}. \tag{2.14}$$

These transformations can be used to express the Navier-Stokes equations in a generalised form

$$\frac{\partial \mathbf{Q}}{\partial t} + \left[x^*_{2,\eta}\frac{\partial \mathbf{E}}{\partial \zeta} - x^*_{2,\zeta}\frac{\partial \mathbf{E}}{\partial \eta}\right] + \left[x^*_{1,\zeta}\frac{\partial \mathbf{F}}{\partial \eta} - x^*_{1,\eta}\frac{\partial \mathbf{F}}{\partial \zeta}\right] + \frac{\partial \mathbf{G}}{\partial x_3} = \mathbf{S}_{\mathbf{v},\mathbf{g}}, \tag{2.15}$$

where $\mathbf{S}_{\mathbf{v},\mathbf{g}}$ is the generalised viscous source vector

$$\mathbf{S}_{\mathbf{v},\mathbf{g}} = \left[x^*_{2,\eta}\frac{\partial \mathbf{E}_\mathbf{v}}{\partial \zeta} - x^*_{2,\zeta}\frac{\partial \mathbf{E}_\mathbf{v}}{\partial \eta}\right] + \left[x^*_{1,\zeta}\frac{\partial \mathbf{F}_\mathbf{v}}{\partial \eta} - x^*_{1,\eta}\frac{\partial \mathbf{F}_\mathbf{v}}{\partial \zeta}\right] + \frac{\partial \mathbf{G}_\mathbf{v}}{\partial x_3}. \tag{2.16}$$

2.1.2 Discretisation

For the spatial discretisation in the streamwise and lateral directions two different schemes can be chosen. A five-point stencil standard central finite difference scheme and a compact finite difference scheme were introduced by Kim and Sandberg (2012). Both schemes have fourth-order accuracy, but the compact scheme has lower numerical dissipation and dispersion error.

In HiPSTAR the spanwise direction is discretised by a Fourier transformation as it is assumed periodic. This is done by means of an FFTW library (Frigo and Johnson, 2005). The time discretisation is done by a five-step fourth-order Runge-Kutta scheme introduced by Kennedy et al. (2000). In order to increase the numerical stability a skew-symmetric splitting of the non-linear terms in the NS equations is applied (Kennedy and Gruber 2008).

2.2 Initial, Boundary and Interface Conditions

In order to be able to solve the discretised NS equations, initial and boundary conditions have to be applied. As a starting point for a simulation, initial conditions are set in the whole fluid domain at each grid point. The better the initial assumption, the quicker the simulation reaches a fully developed state.

2.2.1 Immersed Boundary Method

As already mentioned the NS equations are typically solved for high-fidelity turbomachinery applications on body-fitted grids using a generalised coordinate system.

However, another possibility to define a geometry, one that only requires a uniform Cartesian grid, is the Immersed Boundary Method (IBM) (Mittal and Iaccarino 2005; Peskin 2002), which was introduced by Peskin (1972) in 1972. In the context of the present study, this approach is attractive to represent rough surfaces. The boundary (Γ_b) of the body (Ω_b) is represented by a set of Lagrangian points $\mathbf{X}(s_i, t)$ and the fluid domain (Ω_f) is represented by the cells on a Cartesian grid $\mathbf{x}_{i,j}$ (see fig. 2.1).

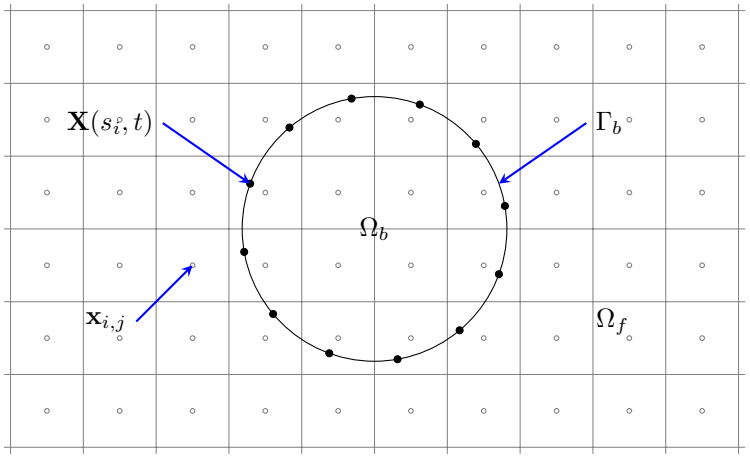

FIGURE 2.1: Circular cylinder represented by a set of Lagrangian points $\mathbf{X}(s_i, t)$ on the Cartesian grid defined by the cell points $\mathbf{x}_{i,j}$.

In order to impose the boundary conditions the NS equations have to be modified in the vicinity of the obstacle boundary Γ_b. This is done by means of a forcing function either in a continuous or a discrete manner (Mittal and Iaccarino 2005), which is discussed later.

There are advantages and disadvantages of the immersed boundary method compared to body-conformal grid simulation. One of the disadvantages is that a suitable forcing function is necessary. However, the impact on the accuracy of the numerical scheme and the influence on the correct physical behaviour is not as clear as when using body-conformal grids. Furthermore, the assessment of the grid in terms of resolution based on the wall normal distance is not as easy (Mittal and Iaccarino 2005).

On the other hand, the creation of a Cartesian grid for immersed boundary methods is fairly simple compared to the generation of a body-conformal mesh. In addition, when moving bodies are incorporated within a simulation the IBM shows another advantage, in that there is no need to rebuild and adapt the mesh at every timestep.

As mentioned earlier there are two different ways to impose the boundary conditions. In the following these two different forcing approaches are discussed.

Continuous forcing:

In the continuous approach the analytical NS equations on the Cartesian grid are modified by an additional forcing term. After that, the modified equations are discretised and then solved in both the fluid domain Ω_f and the body domain Ω_b.

The velocity of the Lagrangian point $\mathbf{X}(s_i, t)$ is related to the local fluid velocity by

$$\frac{\partial \mathbf{X}(s_i, t)}{\partial t} = \mathbf{u}(\mathbf{X}(s_i, t), t). \tag{2.17}$$

The force $\mathbf{f}(\mathbf{x}_{i,j}, t)$ exerted on the fluid at any Cartesian point by the immersed body can be obtained by

$$\mathbf{f}(\mathbf{x}_{i,j}, t) = \sum \mathbf{F}(\mathbf{X}(s_i, t))\delta_h(\mathbf{x}_{i,j} - \mathbf{X}(s_i, t))h^{ndim}, \tag{2.18}$$

where $\mathbf{F}(\mathbf{X}(s_i, t))$ is the force on the Lagrangian point, h is the grid spacing and $\delta_h(\mathbf{x}_{i,j})$ is a discretised distribution function. The discretised distribution function $\delta_h(\mathbf{x})$ is used for the 'interpolation' and 'spreading' operations between the Lagrangian points and the fluid domain and is the essential part of the immersed boundary method. Peskin (2002) introduced some postulates for the distribution function. The main purpose of these postulates is to get a continuous and computationally cost efficient function that conceals the structure of the Cartesian grid as much as possible. Furthermore, the function has to approach the Dirac function $\delta(\mathbf{x}_{i,j})$ for $h \to 0$ (Peskin 2002).

The resulting δ_h function is able to interpolate a linear function exactly and the interpolation of smooth functions is of second order. However, the normal velocity derivative of an immersed elastic boundary with a thickness of zero is not smooth and thus the interpolation accuracy is only of first-order (Peskin 2002)

The forcing terms are based on a relation between the deformation and a respective constitutive law for the elastic body. As for rigid bodies, where no elastic behaviour is assumed and the boundary does not undergo a deformation, the forcing terms are not sufficient and have to be modified or simplified. This, however, leads to accuracy and stability issues (Mittal and Iaccarino 2005).

Discrete forcing:

In contrast to the continuous approach, in the discrete approach the NS equations are discretised first and then modified by a discrete forcing term. As a result, the forcing term has to be adapted according to the discretisation scheme. This has the advantage that the stability and the accuracy can be directly influenced (Mittal and Iaccarino 2005). The forcing itself is directly obtained and related to the local result of the simulation in the vicinity of the boundary. The boundary conditions are then imposed by 'spreading' the values from the Lagrangian points to the Cartesian points by the distribution function δ_h. These kind of methods are referred to as direct forcing methods (Guy and Hartenstine 2010).

When conducting simulations at higher Reynolds numbers the smoothing due to the distribution function δ_h is not desirable, as the boundary layer is potentially not sufficiently resolved. In order to overcome this issue and to retain higher-order accuracy so called sharp-interface methods were proposed. The step of 'spreading' the values from the Lagrangian points to the Cartesian grid is cancelled and instead the local numerical stencil or operators are modified (Mittal and Iaccarino 2005). The boundary conditions are then applied on the immersed boundary rather than only on the Lagrangian points.

2.2.2 Boundary Data Immersion Method

A major drawback of sharp-interface methods is that the simplicity of the immersed boundary method disappears. As far as direct forcing methods are concerned, the generation of spurious pressure fluctuations in the vicinity of the immersed body can occur and are not desirable. Furthermore, these methods are only first-order accurate in the L_∞ norm (Weymouth and Yue 2011).

The boundary data immersion method (BDIM) was proposed by Weymouth and Yue (2011) in order to keep the simplicity of continuous forcing approaches and also retain the high accuracy achieved by sharp-interface methods. In the following, a brief description of the methodology of the boundary data immersion method is given, but a more detailed explanation can be found in (Maertens and Weymouth 2013).

Figure 2.2 shows a body Ω_b immersed in a fluid domain Ω_f. The fluid domain is described by the compressible Navier-Stokes equations $f(\Phi)$ and the body domain is prescribed by a set of fixed values for each velocity component and temperature $\mathbf{b}$. The set of equations can be expressed as a meta equation, which has the form

$$\Phi(\mathbf{x},t) = \begin{cases} \mathbf{b}, & \text{if } \mathbf{x} \in \Omega_b \\ f(\Phi), & \text{if } \mathbf{x} \in \Omega_f \end{cases}. \tag{2.19}$$

By means of the indicator functions $\mathbb{1}_{\Omega_f}(\mathbf{x})$ and $\mathbb{1}_{\Omega_b}(\mathbf{x})$ equation 2.19 can be written as

$$\Phi(\mathbf{x},t) = f(\Phi,\mathbf{x},t)\mathbb{1}_{\Omega_f}(\mathbf{x}) + \mathbf{b}(\mathbf{x},t)\mathbb{1}_{\Omega_b}(\mathbf{x}). \tag{2.20}$$

Convolving the equation with a nascent delta kernel K_ϵ yields the smoothly coupled equation

$$\Phi_\epsilon(\mathbf{x},t) = \int_\Omega \Phi(\mathbf{x}',t)K_\epsilon(\mathbf{x},\mathbf{x}')\,\mathrm{d}\mathbf{x}' = f_\epsilon(\Phi_\epsilon,\mathbf{x},t) + \mathbf{b}_\epsilon(\mathbf{x},t), \tag{2.21}$$

with ϵ being the size of the smoothing region as indicated in figure 2.2 and the terms

$$f_\epsilon(\Phi_\epsilon,\mathbf{x},t) = \int_{\Omega_f} f_\epsilon(\Phi_\epsilon,\mathbf{x}_f,t)K_\epsilon(\mathbf{x},\mathbf{x}_f)\,\mathrm{d}\mathbf{x}_f \tag{2.22}$$

$$\mathbf{b}_\epsilon(\mathbf{x},t) = \int_{\Omega_b} \mathbf{b}_\epsilon(\mathbf{x}_b,t)K_\epsilon(\mathbf{x},\mathbf{x}_b)\,\mathrm{d}\mathbf{x}_b. \tag{2.23}$$

The fluid and solid domains are merged into a single domain $\Omega = \Omega_f \cup \Omega_b$. Furthermore, Weymouth and Yue (2011) demonstrated that $\Phi_\epsilon = \Phi + \mathcal{O}(\epsilon^2)$. The next step is the discretisation of the above equation. After applying a Taylor expansion and replacing the nascent delta kernel by a one-dimensional kernel, the final meta equation reads

$$\Phi_\epsilon = f(\Phi,\mathbf{x},t)\mu_0^{\epsilon,F} + b(\Phi,\mathbf{x},t)(1-\mu_0^{\epsilon,F}) + \mu_1^{\epsilon,F}\frac{\partial}{\partial\mathbf{n}}\left(f(\Phi,\mathbf{x},t) - b(\Phi,\mathbf{x},t)\right). \tag{2.24}$$

Here $\mu_0^{\epsilon,F}$ and $\mu_1^{\epsilon,F}$ are interpolation functions (see fig. 2.2 right) that only depend on the signed distance d from the body's surface. They are defined by

$$\mu_0^{\epsilon,F}(d) = \begin{cases} 0.5\left[1 + \frac{d}{\epsilon} + \frac{1}{\pi}\sin\left(\frac{d}{\epsilon}\pi\right)\right], & \text{if } |d| < \epsilon \\ 0, & \text{if } d \le -\epsilon \\ 1, & \text{if } d \ge \epsilon \end{cases} \tag{2.25}$$

$$\mu_1^{\epsilon,F}(d) = \begin{cases} \epsilon\left[\frac{1}{4} - \left(\frac{d}{2\epsilon}\right)^2 - \frac{1}{2\pi}\left(\frac{d}{\epsilon}\sin\left(\frac{d}{\epsilon}\pi\right) + \frac{1}{\pi}\left(1+\cos\left(\frac{d}{\epsilon}\pi\right)\right)\right)\right], & \text{if } |d| < \epsilon \\ 0, & \text{if } |d| \ge \epsilon \end{cases}, \tag{2.26}$$

with $\mu_0^{\epsilon,B}(d) = 1 - \mu_0^{\epsilon,F}(d)$ and $\mu_1^{\epsilon,B}(d) = -\mu_1^{\epsilon,F}(d)$. The third term on the right hand side of equation 2.24 is a higher order term that enhances the original BDIM method in order to tackle the discontinuity issues of the velocity gradient at the boundary (Maertens and Weymouth 2013).

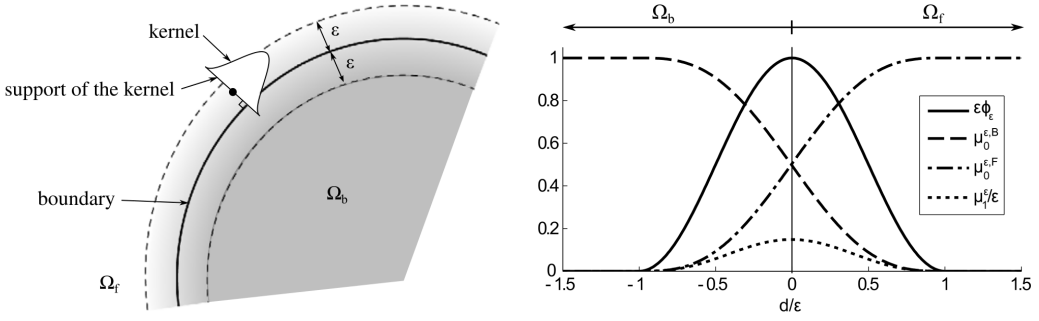

FIGURE 2.2: BDIM domain reproduced from (Maertens and Weymouth 2013); Right: Interpolation function μ

The method was tested and validated by the authors for an incompressible flow solver. Prior to the current work, a compressible formulation of the BDIM was also implemented into HiPSTAR

by Schlanderer et al. (2017). Simulations of Tollmien-Schlichting waves and aero-vibro-acoustic systems were carried out in order to validate the implementation for compressible flows.

However, the implementation of the BDIM in HiPSTAR was only capable of representing 2D and 2.5D geometries, i.e. geometries like bars that are extruded in spanwise direction without any spanwise variation. Thus, to be able to carry out surface roughness simulations the method had to be extended in the present work to three dimensions. Furthermore, surface roughness elements are complex geometries, which are composed of concave and convex elements in a numerical sense. As a consequence, special treatments need to be taken into account that so far have not been necessary for simple geometries like boxes, cylinders, aerofoils etc. (Senocak et al. 2015). These treatments are outlined and discussed in the following section.

2.2.2.1 Extension for Three-Dimensional Geometries

In the scope of this work a new pre-processor for the BDIM was implemented in order to be able to cope with the difficulties of simulating arbitrarily complex geometries like surface roughness. There are four points that will be addressed in this section to describe the procedure of the extension to arbitrarily complex geometries.

1. Body representation
2. Distance between the grid points and the body surface
3. Determination of grid points in the vicinity of the body surface
4. File format

For $2D$ and $2.5D$ simulations line segments are used to represent the immersed boundary. Given that the code has been extensively validated within this framework, no change was made with regard to the mentioned four points for those kinds of simulations. The new pre-processing routine will only be used for full 3D simulations, i.e. where the represented body has variations in the spanwise direction. In the three-dimensional case the body surface is composed of small triangles - surface triangulation - instead of simple line segments, see figure 2.3. Each triangle can be described by three vertices (A,B,C) and three edges ($\overline{AB}$ ($\vec{u}$), $\overline{AC}$ ($\vec{v}$), $\overline{BC}$), see figure 2.4. These are then connected to form the complex immersed boundary surface, where each vertex is share by six adjacent triangles and each edge is shared by two adjacent triangles.

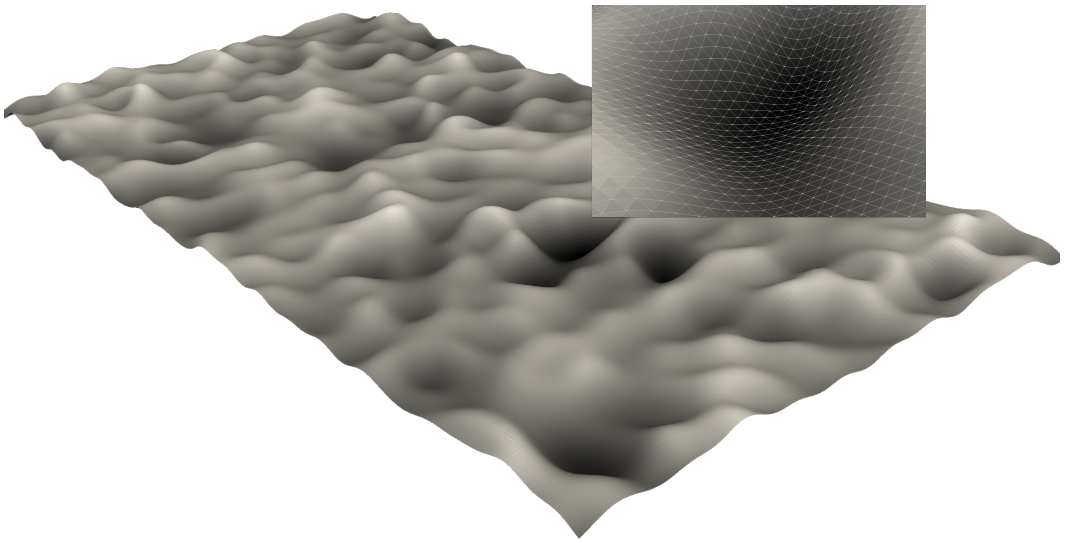

FIGURE 2.3: Surface roughness patch and its triangulation.

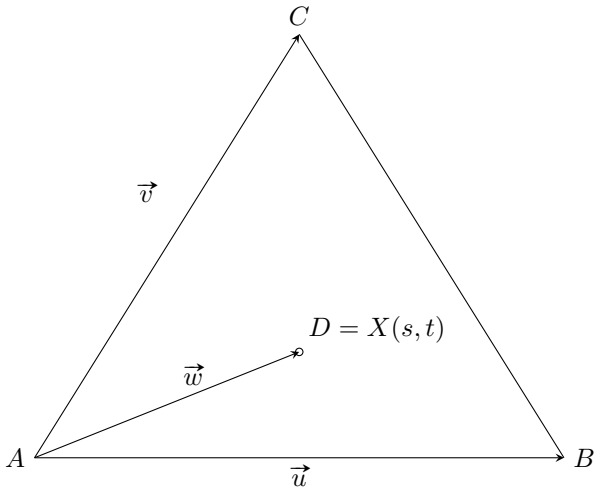

FIGURE 2.4: Surface triangle with vertices A, B, and C and edges $\overline{AB}$ ($\vec{u}$), $\overline{AC}$ ($\vec{v}$) and $\overline{BC}$. Here the intersection point D lies within the surface triangle and is described by the parameters s and t.

The second step is the calculation of the closest signed distance, d, between grid points and the surface of the body. More precisely, this is the closest signed distance between each grid point and each individual triangle. A grid point is related to a triangle by constructing the vector $\vec{w}$ on the line $\overline{AG}$; see figures 2.4 and 2.5. Since a triangle describes a surface and consists also of edges as well as vertices, it has to be determined which of these three elements the grid point is closest to. In order to do so, a line normal to the triangular surface - unity normal vector $\vec{n_0}$ - is drawn through the grid point. Then it has to be determined whether this line intersects with

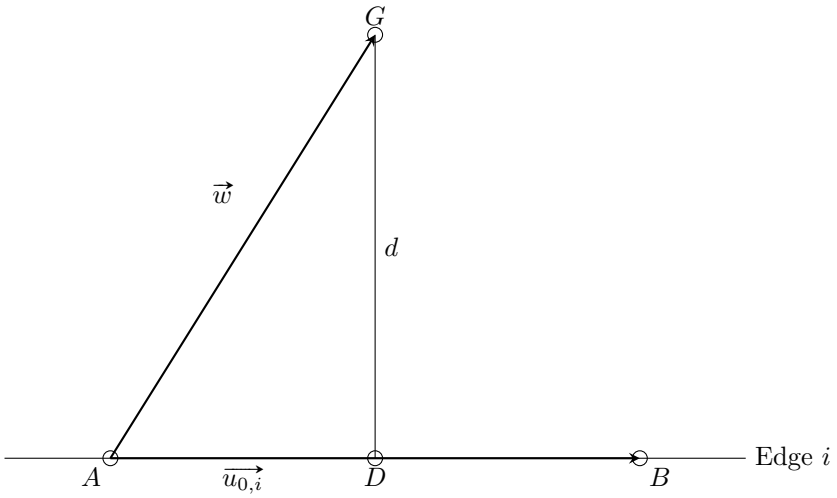

FIGURE 2.5: Minimum distance d between point G and the i-th edge - defined by the unity edge and normal vectors $\vec{u_{0,i}}$ and $\vec{n_{0,i}}$ - of a surface element.

the triangular surface. This is done with an algorithm by Sunday (2001), based on defining

$$s = \frac{(\vec{u}\cdot\vec{v})(\vec{w}\cdot\vec{v}) - (\vec{v}\cdot\vec{v})(\vec{w}\cdot\vec{u})}{(\vec{u}\cdot\vec{v})^2 - (\vec{v}\cdot\vec{v})(\vec{u}\cdot\vec{u})}, \tag{2.27}$$

$$t = \frac{(\vec{u}\cdot\vec{v})(\vec{w}\cdot\vec{u}) - (\vec{u}\cdot\vec{u})(\vec{w}\cdot\vec{v})}{(\vec{u}\cdot\vec{v})^2 - (\vec{v}\cdot\vec{v})(\vec{u}\cdot\vec{u})}. \tag{2.28}$$

In case the inequalities

$$\begin{aligned} s &\geq 0, \\ t &\geq 0 \text{ and} \\ s + t &\leq 1 \end{aligned} \tag{2.29}$$

are true, the intersection point, D (fig. 2.4), exists and the distance to the surface can be easily obtained by taking the scalar product of the unity normal vector, $\vec{n_0}$, of the triangular surface and the vector, $\vec{w}$. If there is no intersection point, the next step is to check whether the grid point is closest to one of the edges or vertices. For this, the scalar products of $\vec{w}$ and the unity edge vectors, $\overrightarrow{u_{0,i}}$, are calculated (fig. 2.5). If the result is either a negative value or greater than the respective length of the triangle edge, the grid point is bound to the nearest vertex and the calculation of the distance d between both points is trivial. Otherwise, the closest signed distance to the three edges, with unity vectors $\overrightarrow{u_{0,i}}$, is obtained from the scalar product of vector, $\vec{w}$, and the unity normal vectors, $\overrightarrow{n_{0,i}}$, of the three edges. This procedure is done for all adjacent triangles as well in order to determine the overall closest signed distance. According to results of Senocak et al. (2015) for a triangulated terrain geometry, in 74.4% of the cases grid points were closest to a triangular surface. The likelihood that a grid point was closer to one of the edges was 25% and only 0.6% were closer to a vertex.

An important point to note is that during the triangulation process the triangles need to be defined in a way such that the surface normals point outwards. This ensures that scalar products for the distance calculations give the correct sign and hence tell us whether the grid points lie

within the body or the fluid domain. The calculated signed distances, d, are then used for the interpolation functions (eqs. 2.25 and 2.26) of the meta equation 2.24.

So far it was assumed that an arbitrary grid point was chosen in order to determine the closest distance. However, the bigger and more complex the geometries, the more grid points and triangles are necessary. Hence, it is advantageous to only determine the grid points within the smoothing region close to the immersed surface to keep the computational effort minimal. In the current $2D$ implementation of the boundary data immersion method this is done by looping over the line segments and only flagging grid points within a set radius to the line segment as "interface nodes", i.e. grid points within the smoothing region. The signed distances, based on the description above, are then calculated for each line segment and the pre-processing is finished. As the available algorithm has been proven to be efficient and reliable in the mentioned validation case (Schlanderer et al. 2017) for $2D$ geometries, it will also be used for the extension for three-dimensional geometries.

In order to do so, the $3D$ body is cut into n spanwise slices, where the number of the slices, n, corresponds to the number of grid points in the spanwise direction. The algorithm is then executed for each slice and the "interface nodes" are flagged. The resulting grid points are then looped and the signed distances, d, to the surface triangles are calculated, where only triangles in a given bounding box around the grid point are considered, to reduce the execution time. After that the interpolation functions are updated and the pre-processing step is finished. An important point to remember is that further steps need to be taken when moving bodies are involved, as that would require the re-computation of the signed distances for every timestep. However, in the scope of this work only surface roughness elements are considered and the extension to moving geometries is left for future work.

The triangulated surface is stored in the stereo lithography file format (STL), where the three triangle vertices together with the unity surface normal vector are given. This file format is used by many conventional CAD and data visualisation (e.g. ParaView) softwares and offers data storage in ASCII and binary formats.

2.2.2.2 Validation

In order to check and verify the implementation of the extension of the BDIM for three dimensional geometries, a wavy cylinder at Reynolds number $Re_m = 100$, based on the mean cylinder diameter D_m, was simulated. The test case is based on one of the simulations of Lam and Lin (2009) and is periodic in the spanwise direction. The change of the diameter in the spanwise direction is given by

$$D_z = D_m + 2a\cos\left(\frac{2\pi z}{\lambda}\right), \tag{2.30}$$

with the wave-length λ, the amplitude a and the spanwise coordinate z in the interval $[0, 1]$. One simulation with $\lambda/D_m = 2$ and $a/D_m = 0.3$ was carried out and compared to the reference. A steady solution is expected for this pair of parameters, which could be confirmed by the time history of the velocity components (fig. 2.6). As can be seen in table 2.1, the drag and the lift coefficients compare well to the reference data. It has to be noted, that the simulations were carried out at a Mach number of $M = 0.2$, whereas Lam and Lin (2009) used an incompressible

flow solver. Hence, the slight differences might be attributed to compressibility effects. Furthermore, a time snapshot of the z-vorticity, ω_z (fig. 2.7), at $z = 0.0$ (left) and 0.5 (right) shows a steady wake several cylinder diameters downstream. An iso-surface of ω_z, contoured by the absolute velocity, U, is also shown in figure 2.7 (bottom) and reveals the wavy cylinder geometry and the symmetrical flow profile.

TABLE 2.1: Comparison of lift and drag coefficients.

	C_D	C_L
HiPSTAR	1.223	$-3.252 \cdot 10^{-6}$
Lam and Lin (2009)	1.250	0.0

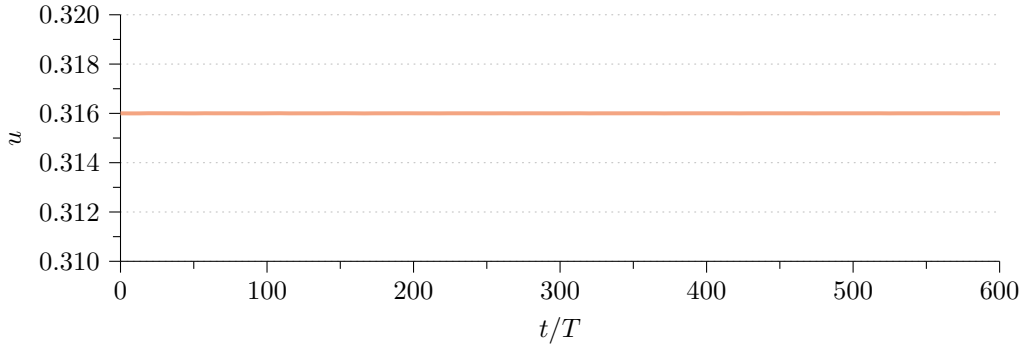

FIGURE 2.6: Time history of the streamwise velocity component.

2.2.3 Parametric Forcing Approach

Another approach to representing surface roughness - instead of using immersed boundary methods or body-fitted grids - is to incorporate a surface roughness model. This can be achieved by either modifying the wall-boundary conditions or by altering the Navier-Stokes equations close to the wall (Busse and Sandham 2012). The benefit is the lower computational cost relative to the full simulation of rough surfaces, as the number of required grid points can be significantly smaller.

Within the scope of this work the parametric forcing approach, introduced by Busse and Sandham (2012), has been implemented into HiPSTAR, where an additional forcing term is added to the Navier-Stokes equations. More precisely, the extra terms

$$-\alpha_i F_i(z, h_i) u_i |u_i| \quad \text{and} \quad -u_i \alpha_i F_i(z, h_i) u_i |u_i| \tag{2.31}$$

are added to the momentum equation and the energy equation, respectively. It has to be noted that there is no summation on repeated indices for this formulation. Here α_i denotes the roughness factor in the respective flow direction and is a representation of the overall drag coefficient of a roughness element. The roughness shape function $F_i(z, h_i)$ scales the strength of the forcing term based on the surface distance z and the height of the roughness element h_i. An important point to remember is that the height parameter h_i is not an exact description of an actual

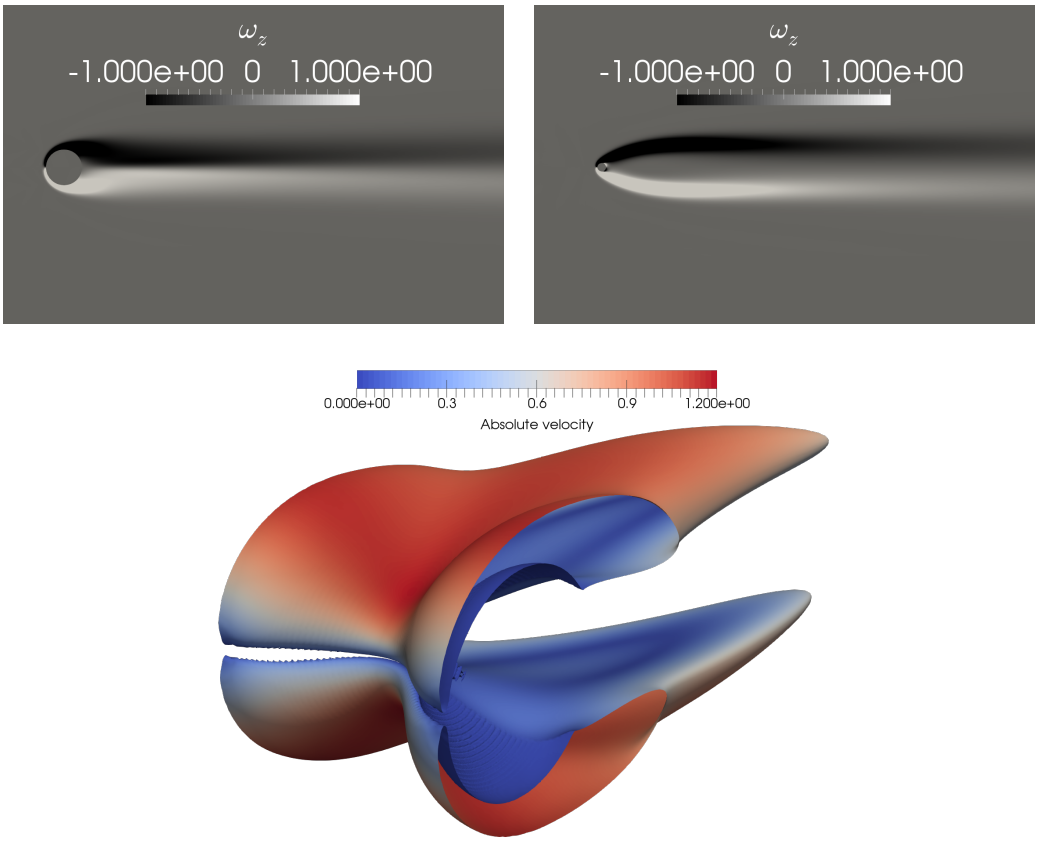

FIGURE 2.7: Snapshot of the spanwise vorticity, ω_z, at $z = 0.0$ (left) and 0.5 (right). Isosurface of ω_z, contoured by the absolute velocity, U. (bottom)

physical height or sand grain roughness. It is defined as the mean profile height

$$h = \frac{\int_0^\infty F(z,h) z \, \mathrm{d}z}{\int_0^\infty F(z,h) \, \mathrm{d}z} \tag{2.32}$$

in case of a boundary layer or

$$h = \frac{\int_0^\delta F(z,h) z \, \mathrm{d}z}{\int_0^\delta F(z,h) \, \mathrm{d}z} \tag{2.33}$$

in case of a channel flow. Busse and Sandham (2012) defined six different shape functions in order to describe different types of roughnesses. The maximum of all the different shape functions is set to 1 in order to normalise them. In this work a simple box profile

$$F(z,h) = \begin{cases} 1, & \text{if } z \leq \eta(h) \\ 0, & \text{if } z > \eta(h) \end{cases} \tag{2.34}$$

and a Gaussian profile

$$F(z,h) = \exp\left(-\frac{z^2}{\eta(h)^2}\right) \tag{2.35}$$

have been used. $\eta(h)$ is an auxiliary parameter, which is obtained from equation 2.33 by setting $\eta(h)$ as the limit. For the box profile $\eta(h)$ equals $2h$ and denotes a discontinuous end of the forcing region. In contrast, the Gaussian profile gradually decreases for an increasing distance,

z, with $\eta(h) = 1.77h$.

Busse and Sandham (2012) undertook an exhaustive study of fully turbulent rough channel flow with an incompressible flow solver and the parametric forcing term. They found that the forcing term was capable of capturing turbulence characteristics in the near-wall region. Especially, mean profile variations and anisotropy effects above roughness elements could be successfully represented. Furthermore, apart from extremely rough cases, where $\Delta U^+ > 10$, outer-layer similarity was achieved by the additional forcing and a comparison with the equivalent sand grain roughness graph of Nikuradse (1933) showed good agreement.

In order to use the roughness model for more complex flows, the forcing term needs to be calibrated first. This can possibly be done by tweaking the three parameters in a way that they match fully resolved DNS or experiments of a simple flow problem. After that the calibrated parameters can be used in more elaborate flow simulations (Busse and Sandham 2012). As already mentioned, the parametric forcing term was implemented into HiPSTAR in this work. A validation case was simulated and the results will be presented in section 3.3.

2.2.4 Characteristic Interface Conditions

In HiPSTAR characteristic boundary and interface conditions are used that are based on the quasi-linear characteristic wave equation 2.36, which for the ζ-direction reads

$$\frac{\partial \mathbf{R}}{\partial t} + \underline{\Lambda}\frac{\partial \mathbf{R}}{\partial \zeta} = \underline{\mathbf{P}}\mathbf{S}_{char}. \tag{2.36}$$

The characteristic variables are represented by $\mathbf{R}$ and $\mathbf{S}_{char}$ is the modified source term. The eigenvalues are defined by

$$\underline{\Lambda} = \left[U, U, U, U + c\sqrt{\zeta_z^2 + \zeta_r^2}, U - c\sqrt{\zeta_z^2 + \zeta_r^2}\right], \tag{2.37}$$

with the speed of sound c and the velocity

$$U = \zeta_z u + \zeta_r v \tag{2.38}$$

The equation is derived from the non-conservative form of the NS equations in generalised form and is used to determine the direction of transport at boundaries and block-interfaces (Kim and Lee 2000). Based on this, appropriate boundary and interface conditions can be applied in order to reduce reflections. A detailed definition can be found in Kim and Lee (2000).

Characteristic Boundary Condition:

By assuming local one-dimensional inviscid (LODI) behaviour at boundary points, i.e. neglecting the source term $\mathbf{S}_{char}$ in equation 2.36, Kim and Lee (2000) introduced soft inflow and non-reflecting outflow boundary conditions. These boundary conditions are used for the simulations within this project.

Characteristic Interfaces:

For flow problems where complex geometries are employed, e.g. turbine or compressor aerofoils, it is advantageous to decompose the whole domain into smaller block domains. One advantage, given the large grid sizes of today's simulations, is that the decomposed domain can be more easily distributed on multiple processing cores for parallel computing. Another advantage is that the grid generation is more flexible and more suitable meshes can be obtained. In the cascade cases, an O-grid is used around the aerofoil, while in the outer regions, where the inflow, outflow and periodic pitchwise boundary conditions are applied, an H-type grid is employed.

However, with the adopted domain-decomposition approach the metrics of the grid are no longer continuous at the connection points and interfaces between blocks. When higher-order finite difference schemes in generalised coordinates are used to solve the NS equations in conservative form this potentially leads to numerical oscillations (Kim and Lee 2003). In order to overcome these issues, interface conditions introduced by Kim and Lee (2003) are used in the flow solver. The conditions are applied at the interface of the blocks and ensure the communication between the blocks without introducing any oscillations.

Sliding characteristic interface condition:

Based on the characteristic interface method for block-structured grids, Johnstone et al. (2015) introduced a sliding boundary condition. With this boundary condition it is possible to set blocks into relative motion. It is used to simulate rotor-stator interaction cases, e.g. a moving bar upstream of a turbine cascade, where the moving bars are used to generate wakes.

2.3 Parallel Performance

The demand for more complex and more memory consuming simulations and calculations is increasing. Thus, in order to solve the problem in a sufficient way, the whole problem domain needs to be decomposed into smaller parts. The parts can be distributed among only a few or up to tens of thousands of compute nodes and processors within high performance computing (HPC) clusters depending on the size of the calculation. As each node/processor only contains information of a part of the whole domain, relevant data needs to be exchanged among the corresponding nodes/processors. This is realised through the "Message Passing Interface" (MPI) standard, which was proposed to set specifications for library developers. Today there are many free and commercial MPI implementations (libraries).

In general, a grid is decomposed into N domains. Each domain has additional layer of cells at the outside edges of its boundaries, called halo layers. Furthermore, the layers of cells at the inside egdes of the domain are marked as window cells. During the simulation the values on the window cells are sent to the halo cells of the corresponding neighbour domains. The number of required layers of halo and window points can dependent on the incorporated numerical scheme and its stencil size for discretisation.

The process of sending and receiving data is called communication. Communication is classed as either point-to-point or collective communication. The former describes data transfer between

only two processes as opposed to the latter that involves data transfer between all processes within a group.

Another multiprocessing API is OpenMP, which is used for shared memory architectures, where all the threads/cores share the same memory. OpenMP incorporates parallel loop directives and scheduling options, which can be easily and quickly implemented in order to parallelise do/for loops and improve the performance of the flow solver. The latest trend is the usage of graphics processing units (GPU) for CFD simulations. One readily available API for porting the flow solver to GPUs is the OpenACC library, which works similar to OpenMP by using directives for Fortran and C++ codes.

Owing to the immense grid sizes required for DNS and LES simulations, HiPSTAR incorporates the message passing interface (MPI), the OpenMP API and the OpenACC API. A combination of the three allows for heterogeneous high performance computing on different kinds of architectures. In HiPSTAR, MPI is used for the decomposition of the $2D$ domain, which is distributed among different compute nodes. When using the FFTW routine for the discretisation of the third dimension, shared memory is required for the collocation points. Thus, OpenMP is ideal for this parallelisation task. In terms of heterogeneous computing, the decomposed block of the combined MPI/OpenMP construct can be substituted by a single GPU using OpenACC. It has to be noted, however, that within the current work only MPI and OpenMP were used for the linear low-pressure turbine simulations, which is mainly due to the missing OpenACC implementation for the extended boundary data immersion method for complex geometries.

Sandberg et al. (2015) showed that the MPI/OpenMP implementation has very good weak scaling ($> 90\%$) capabilities. Moreover, Pichler (2016) tested the strong scaling and found that the combination of MPI and OpenMP is always beneficial to only using MPI. In general, the strong scaling was found to be good for a large number range of processors.

2.4 Data Output and Post-processing

During the runtime of a simulation in HiPSTAR, several output files are generated and written out in the binary format. For given timesteps part or even the whole $2D/3D$ flow field can be written out storing the nondimensional temperature, T, the velocities, u_i, and the density, ρ. Furthermore, due to the immense amount of generated data the gathering of the flow statistics needs to be done on the fly. As the compressible Navier-Stokes equations are solved, the flow quantities are Favre averaged, where the variable Φ is decomposed into a mean quantity, $\widetilde{\Phi}$, and a fluctuation quantity, Φ''.

$$\Phi = \widetilde{\Phi} + \Phi'' \text{ with} \tag{2.39}$$

$$\widetilde{\Phi} = \frac{\overline{\rho\Phi}}{\overline{\rho}} \tag{2.40}$$

The classical Reynolds average is indicated by the overbar. Moreover, the relation between the Reynolds average and the fluctuation quantity is

$$\overline{\Phi''} \neq 0 \text{ and } \overline{\rho\Phi''} = 0. \tag{2.41}$$

The collected data is post-processed by means of the in-house Python library called PLATUS and the parallel post-processing software FAT, which allows for the analysis of instantaneous flow fields and time series.

2.5 Validation and Verification of the linear Low-Pressure Turbine Cascade Simulations

Before running eddy resolving simulations of a linear low-pressure turbine cascade with incoming wakes and surface roughness it is important to validate the flow solver (HiPSTAR) by means of experimental data. To that end, Sandberg et al. (2015) conducted direct numerical simulations, with HiPSTAR, of an LPT at an isentropic exit Reynolds number of $Re_{2,is} = 60{,}000$ and an isentropic exit Mach number of $M_{2,is} = 0.4$. They compared the results to experiments of Stadtmüller (2001) and found that the pressure coefficient, c_p, on the turbine blade and the total pressure loss, Ω, of the turbine blade wake compared well to the experimental data, see figure 2.8.

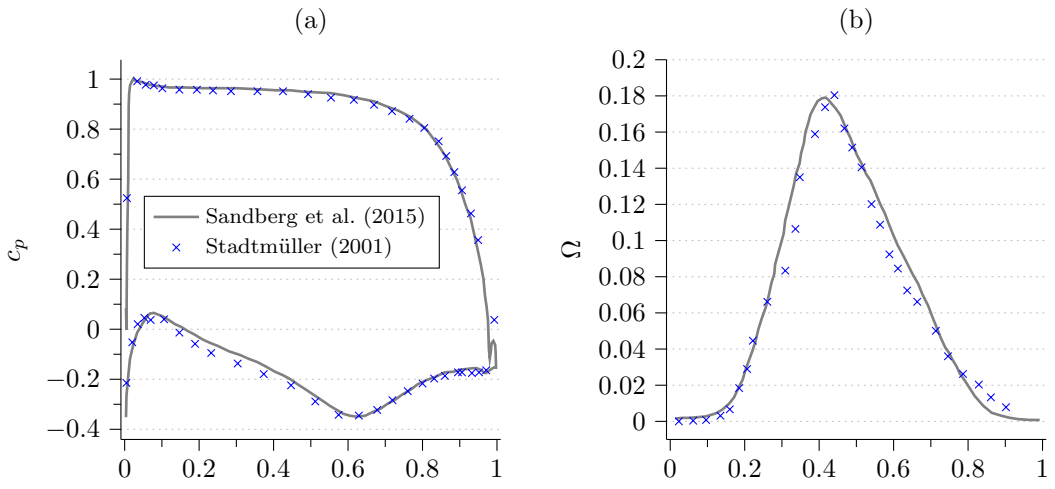

FIGURE 2.8: Comparison of the pressure coefficients, c_p, on the turbine blades and the total pressure losses, Ω, of the turbine blade wakes between the DNS of Sandberg et al. (2015) and the experiments of Stadtmüller (2001).

Based on this validation, Michelassi et al. (2016), who used HiPSTAR as well for a study on the effect of reduced frequency and flow coefficient, carried out DNS and LES simulations of an LPT with upstream bars at an isentropic exit Reynolds number of $Re_{2,is} = 100{,}000$ and an isentropic exit Mach number of $M_{2,is} = 0.4$. The results of the direct numerical simulation were used to verify the large eddy simulations, which saved around a factor of 10 of computational time. Within this work a simulation with the same grid and simulation setup was conducted and compared in order to verify the current version of the flow solver. A comparison of the bar and blade wakes as well as the pressure coefficient, c_p, the skin friction, τ_w, the total pressure loss, Ω, and the mixed out loss, ω, between the LES (R_0) and the DNS and LES of Michelassi et al. (2016) is shown in figure 2.9. As can be seen, there is a reasonable agreement between the results of the DNS and LES simulations. This gives confidence in the results obtained with

HiPSTAR version v5.4, which was used for the linear low-pressure turbine cascade simulations throughout this work.

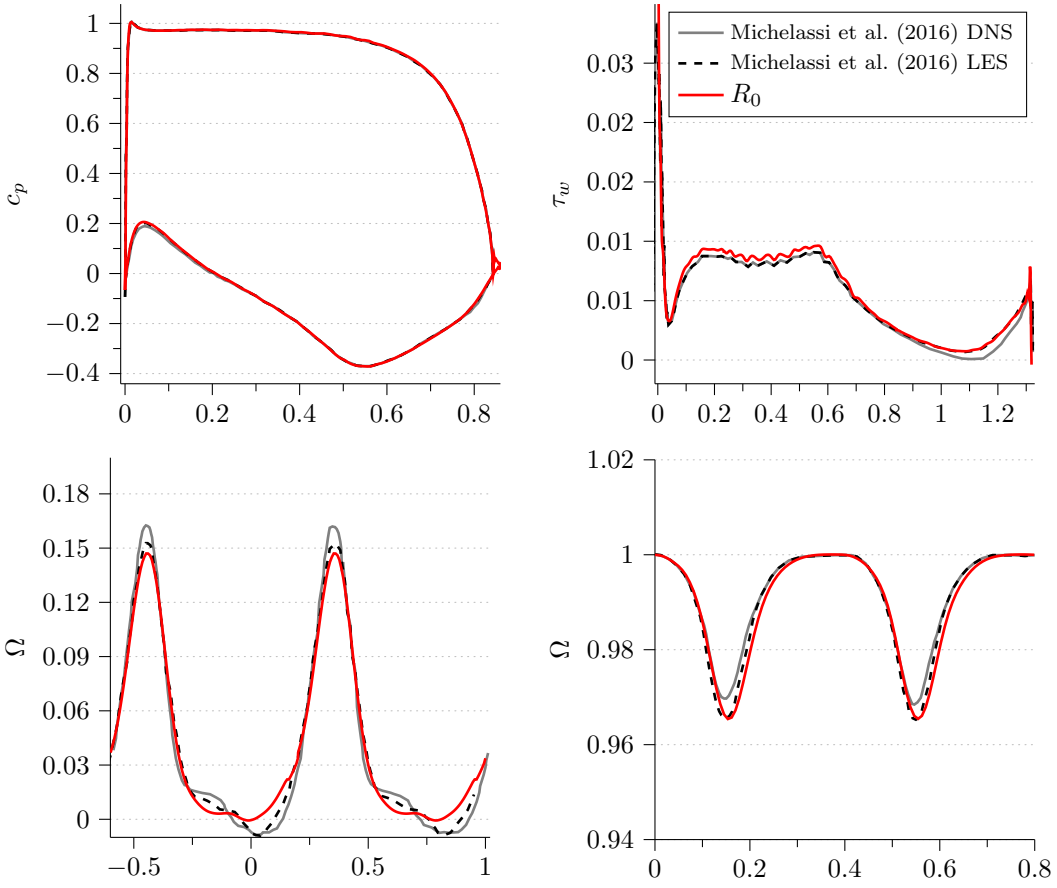

FIGURE 2.9: Comparison between HiPSTAR v5.4 (LES) and the DNS as well as LES of Michelassi et al. (2016).

2.6 Summary

The compressible flow solver HiPSTAR has been extensively used and validated for different kinds of flow problems. The applications include turbine and compressor flows (Leggett 2018; Leggett et al. 2018; Pichler 2016; Pichler et al. 2018; Sandberg et al. 2012; Sandberg et al. 2015), aeroacoustics of compliant trailing-edges (Schlanderer and Sandberg 2018; Schlanderer et al. 2017), adjoint-based flow control (Otero et al. 2017; Otero 2017), evolutionary algorithms (Schoepplein et al. 2018; Weatheritt 2015), fluid-structure interaction of membrane aerofoils (Galiano 2016; Serrano-Galiano et al. 2018) and turbulent boundary layer flows (Bechlars 2015; Bechlars and Sandberg 2017). Further validation cases for the parametric forcing approach and the extended boundary data immersion method for complex three dimensional geometries will appear in the following chapters.

Chapter 3

The Representation of Surface Roughness

One aim of this work is to investigate the effect of surface roughness on linear-low pressure turbine cascades. For that, the incorporated roughness patches will be represented by two different approaches. Firstly, a roughness modelling term, namely the parametric forcing approach, is used, which has been implemented into the flow solver as part of this work (section 2.2.3) and allows for a more simple grid in terms of resolution in the wall region. Secondly, the boundary data immersion method will be used allowing a full representation of the main roughness features of the surface roughness patch, see section 2.2.2.1.

The aim of this chapter is to compare and cross-correlate both approaches. The added advantage of using the two chosen and very different approaches is a reduction of computational cost within the design and investigation process. Using a simple roughness modelling term within the very first stages of the turbine design process enables to gain valuable insight at a low cost. It also opens the possibility for a roughness parameter study. After that, a more sophisticated approach, here the boundary data immersion method, can be used to simulate distinct roughness features to get deeper insights into the physical phenomena. This, however, requires a highly resolved grid in order to sufficiently represent the surface roughness.

Before using both approaches for the linear-low pressure turbine, they first will be verified by means of rough channel simulations. Channel cases can be readily set up and simulations from hydraulically smooth over transitionally rough to fully rough can be carried out. These simulations will then be used to compare and correlate the parametric forcing term and the boundary data immersion method. The possibility of tuning the values of the modelling term with channel simulations for later use in other simulations will be elaborated. Possible shortcomings will be given as well.

In order to test the suitability of the boundary data immersion method for surface roughness simulations, channel flows with two different stages of roughness complexity were conducted. Firstly, a case with wall waviness only in streamwise direction was investigated, see section 3.2.1. This case served as a first functionality test of the extension of the BDIM. Secondly, a real rough wall channel case, as presented in Thakkar (2017), was carried out.

In section 3.3 results of the implemented parametric forcing approach in a channel is presented and compared to the incompressible results of Busse and Sandham (2012). The next step is the investigation of the behaviour of the forcing term in hydraulically smooth and transitionally rough channel flows. For this, results of hydraulically smooth and transitionally rough channels, with a real rough surface taken from Thakkar et al. (2017a), are used. Based on the comparison and the resulting parameters for the forcing approach, a fully rough channel simulation at $Re_\tau = 180$ is carried out.

Section 3.4 deals with the comparison of both approaches in the channel case. First, common statistical data, like centre-line velocities and *rms*-values, will be consolidated to draw conclusions about limitations of the forcing model. Furthermore, the relation between the forcing parameters and a real rough surface will be examined. Then, in the light of the above findings and the computational cost for both methods, advantages and disadvantages for the usage of either one of them will be given. This finally leads to the question on the proper application of the parametric forcing approach and the boundary data immersion as means of roughness representation methods in linear low-pressure turbine cascade simulations.

3.1 Smooth Wall Channel Flow

Before moving on to the rough wall channel cases, a smooth wall channel case at

$$Re_\tau = \frac{u_\tau \delta}{\nu} = 180 \tag{3.1}$$

was simulated as a reference case, with the skin friction velocity, u_τ, and the channel half height, δ. A sketch of the channel domain is given in figure 3.1

FIGURE 3.1: Domain of smooth wall channel flow, which serves as a reference case.

The results will be compared to classical references (Kim et al. 1987; Vreman and Kuerten 2014) in order to verify the flow solver and to obtain needed reference values. The skin friction Reynolds number, Re_τ, is based on the skin friction velocity, u_τ, which can be related to the mean streamwise pressure gradient by

$$-\frac{\delta}{\rho}\frac{\mathrm{d}P}{\mathrm{d}x} = u_\tau^2 = 1.0, \tag{3.2}$$

which drives the flow through the channel that is defined by the half height δ. The mean pressure gradient was kept constant throughout the simulation and chosen in a way such that

the skin friction velocity remains $u_\tau = 1.0$ for all channel simulations within this work. The Mach number, based on the centre-line velocity, u_c, was set to $M = 0.3$ in order to ensure an "incompressible"-like solution and giving a reasonable simulation time. The domain size was chosen to be $11\delta \times 2\delta \times 4\delta$ in the streamwise, the wall-normal and the spanwise direction, respectively, comparable to Kim et al. (1987). An important point to note is that periodic boundary conditions with 98 equidistantly distributed points in the spanwise direction were used, allowing a Fourier spectral method with 48 Fourier modes for the spatial discretisation. 140 points in the wall-normal direction were spatially distributed by means of the function

$$y = \frac{\tanh(bx)}{\tanh(b)}\delta, \tag{3.3}$$

with constant $b = 1.5$. Furthermore, 100 equidistantly spaced points were used for the streamwise direction, resulting in a total number of 1,372,000 grid points.

The time and spatially averaged streamwise velocity $\tilde{u}^+$ and the Reynolds stresses $\widetilde{u'^2}$, $\widetilde{v'^2}$, $\widetilde{u'v'}$ and $\widetilde{w'^2}$ - all normalised by u_τ and u_τ^2, respectively - are shown in figure 3.2. The results from Kim et al. (1987) and Vreman and Kuerten (2014), where case FD1 was chosen based on the grid resolution, are shown as well for verification purposes. As can be seen, the slopes of the averaged streamwise velocities, $\tilde{u}^+$, are identical for all cases. When looking at the Reynolds stresses in the streamwise direction, $\widetilde{u'^2}$, slight differences in the peak value at around $y^+ = 15$ can be noticed. However, towards the middle of the channel, $y^+ = 180$, the values match very well. A similar trend can be observed for the stresses in the wall-normal direction, $\widetilde{v'^2}$, with the values being closer to Kim et al. (1987). The shear stresses, $\widetilde{u'v'}$, match very well until $y^+ = 80$ and then start to diverge slightly from the results in the references. A good agreement with Vreman and Kuerten (2014) was achieved for the stresses in the spanwise direction, $\widetilde{w'^2}$, with only a minor deviation in the peak values.

Furthermore, in table 3.1 the flow and grid values are summarised and compared to the references.

TABLE 3.1: Summary of the smooth channel flow results compared to the references.

	Re_τ	u_c	Δx^+_{max}	Δy^+_{max}	Δz^+_{max}	u_{rms}	v_{rms}	w_{rms}
HiPSTAR	181.5	18.33	11.16	4.4	6.05	0.7822	0.6048	0.5947
Kim et al. (1987)	178.1	18.3	17.7	4.4	5.9	0.8140	0.6118	0.5893
Vreman and Kuerten (2014)	180	18.42	8.8	4.4	5.9	0.7976	0.6154	0.6103

In the wall-normal and the spanwise direction the maximum grid spacings are the same for all three simulation. The streamwise resolution lies between the two reference cases. As can be seen, the skin friction Reynolds number, $Re_\tau = 181.5$, is slightly above the goal values of 180. This might be due to some compressibility effects, as the Mach number based on u_c is very close to a value of 0.3, which was necessary to reduce the simulation time.

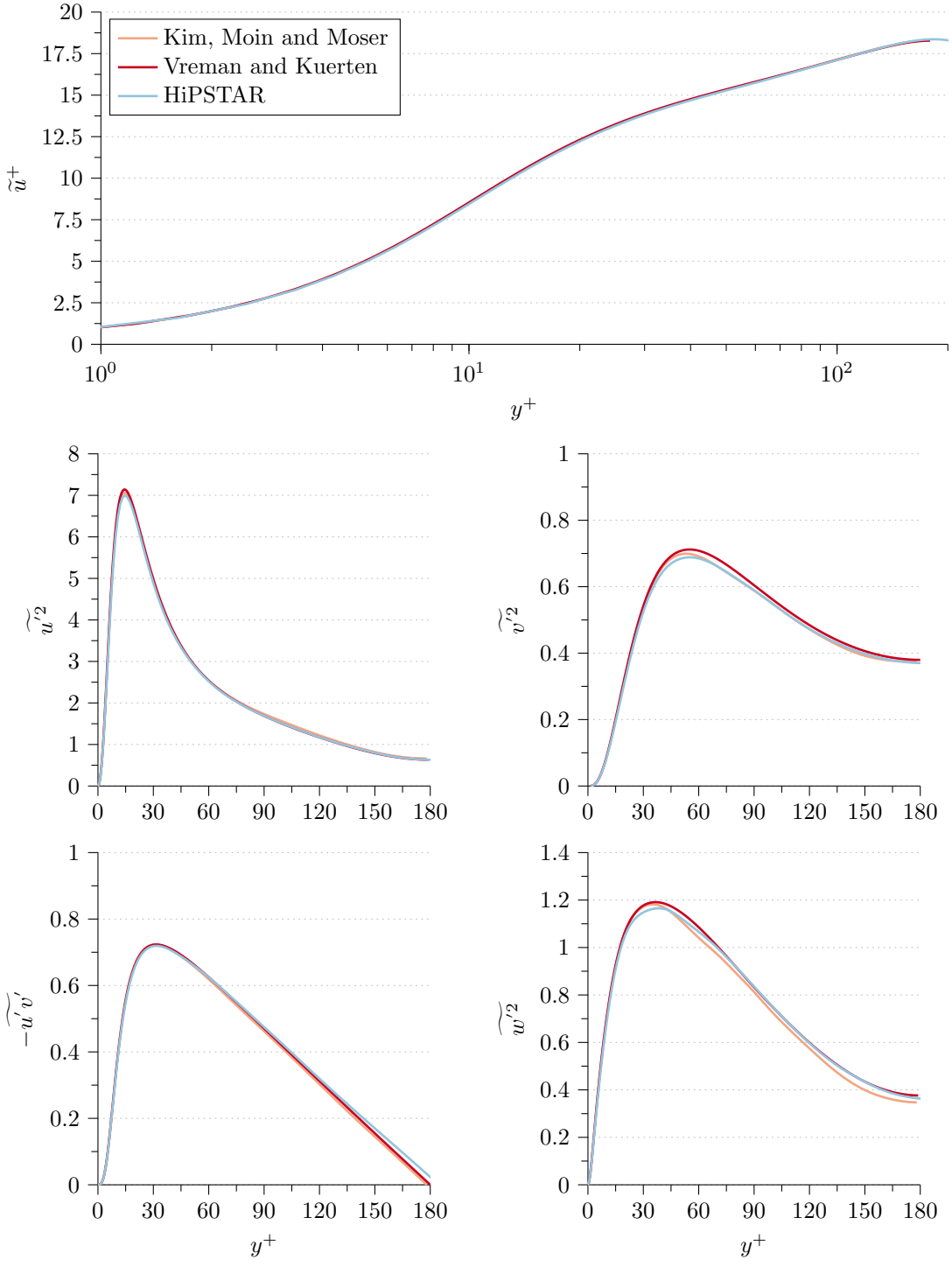

FIGURE 3.2: Time and spatially averaged streamwise velocity $\tilde{u}^+$ and Reynolds stresses $\widetilde{u'^2}$, $\widetilde{v'^2}$, $\widetilde{u'v'}$ and $\widetilde{w'^2}$ are shown for HiPSTAR as well as the results of Kim et al. (1987) and Vreman and Kuerten (2014)

The centre line velocities, u_c, are very similar for all cases and the root mean square values, taken at the centre line and which are defined by

$$\Phi_{rms} = \sqrt{\widetilde{\Phi'^2}}, \tag{3.4}$$

lie within an error range of around 4.0%.

Given the very small differences for all three cases, it can be concluded that the smooth wall channel reference case is sufficiently resolved and hence can be used for the normalisation of the following rough wall cases.

3.2 Roughness Represented by the Boundary Data Immersion Method

In the following sections, the boundary data immersion method will be tested by means of simple and cost effective channel cases before moving to cascade simulations. Firstly, turbulent channel cases with wavy bottom and top walls were simulated, where the waviness of the channel walls was restricted to the streamwise direction. The boundary data immersion method case will be compared to a bodyfitted case. Secondly, a channel simulation with a grit blasted surface profile was carried out in order to test the suitability of the BDIM for the representation of complex rough surface geometries. The grit blasted surface profile was taken from Thakkar et al. (2017a) and Thakkar et al. (2017b) and the results will be compared to the results in the mentioned article.

3.2.1 Channel with Streamwise Waviness

Firstly, in order to test the functionality of the implementation of the extended 3D boundary data immersion method, a wavy wall channel was chosen as a test case. This test case serves as an initial step for the follow-up simulations with a real rough surface.

In figure 3.3 the domain dimensions of the wavy channel case is shown.

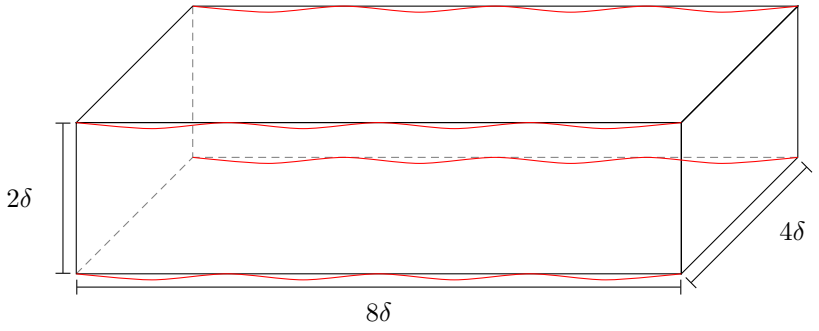

FIGURE 3.3: Domain of the streamwise wavy channel case.

The bodyfitted grid consists of $240 \times 187 \times 98$ gird points, whereas the BDIM grid has a resolution of $240 \times 210 \times 98$. The wavy wall is defined by

$$y(x) = y_{wall} + \alpha \cdot \cos\left(2\pi \frac{n_x}{L_x} x\right) \tag{3.5}$$

with the mean wall locations $y_{wall}^{bot} = -1.0$ and $y_{wall}^{top} = 1.0$, the amplitude $\alpha = 0.04$, the number of waves $n_x = 4$ and the length of the domain $L_x = 8.0$. The same Reynolds and Mach numbers ($Re_\tau = 180$, $Ma_c = 0.3$) as in the reference simulation were used.

Figure 3.4 shows the velocity profiles and the Reynolds stresses of the smooth reference case and the two wavy-wall cases.

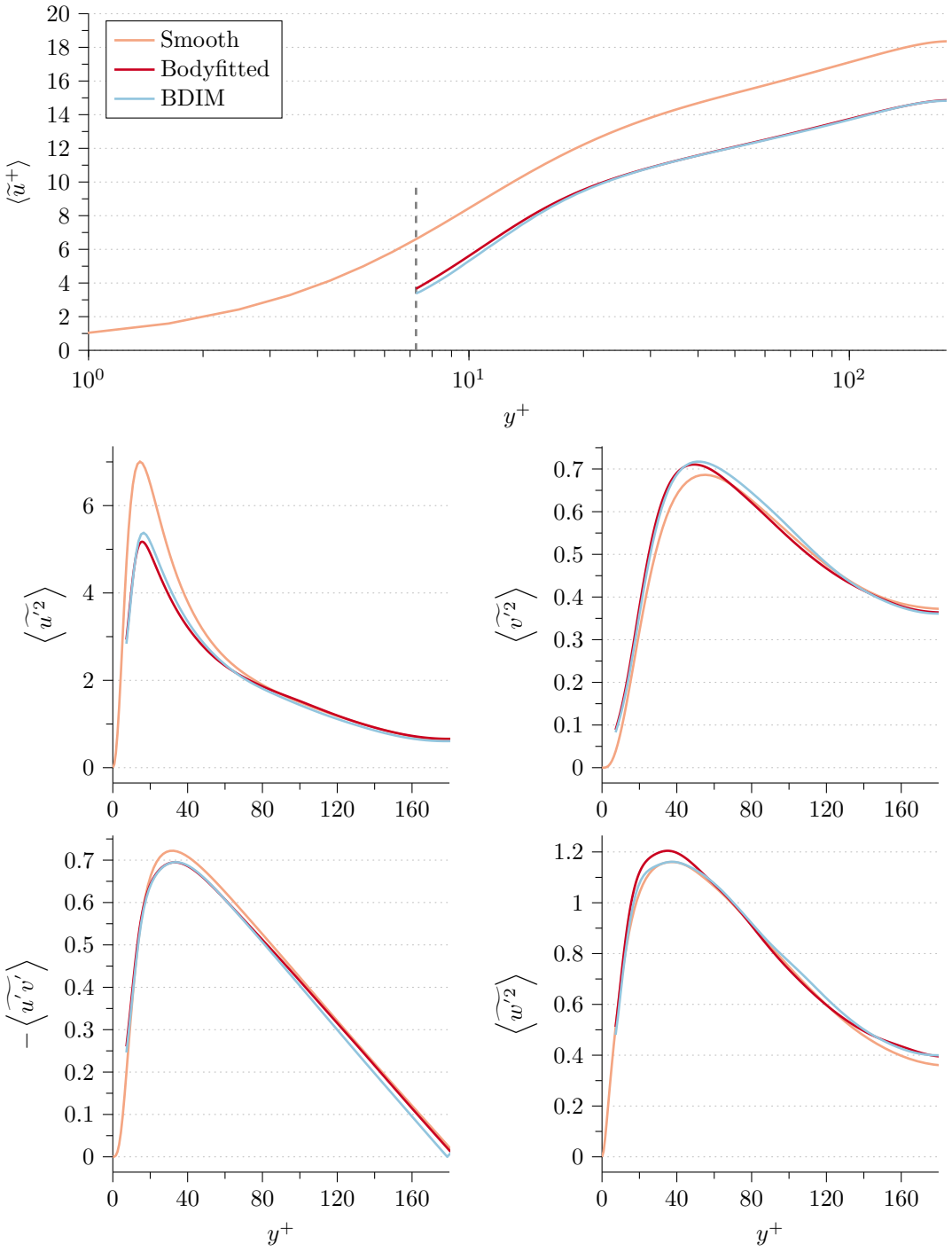

FIGURE 3.4: Time and spatially averaged streamwise velocity $\tilde{u}^+$ and Reynolds stresses $\langle\widetilde{u'^2}\rangle$, $\langle\widetilde{v'^2}\rangle$, $\langle\widetilde{u'v'}\rangle$ and $\langle\widetilde{w'^2}\rangle$ are shown for HiPSTAR.

The profiles were extracted along the channel and then averaged in the spanwise and the streamwise directions, denoted by $\langle\cdot\rangle$ notation. The top position of the wavy wall, i.e. $y/\delta = 0.04$ ($y^+ = 7.26$), is indicated by the vertical grey dashed line. As can be observed, the streamwise velocity, $\langle\widetilde{u}^+\rangle$, for the body-fitted and the BDIM case match very well and only small deviations towards the top wavy wall position occur. A fairly good agreement for the $\left\langle\widetilde{u'^2}\right\rangle$ Reynolds stresses were obtained, with a slight overestimation of the peak value for the BDIM case. The same is true for $\left\langle\widetilde{v'^2}\right\rangle$, where the immersed boundary overestimates the stresses. In case of the shear stresses, the near wall and peak values match very well. However, towards the centre line of the channel the stresses are slightly underestimated in case of the BDIM.

In table 3.2 the velocity deficit, ΔU^+, which is defined by

$$\Delta U^+ = \widetilde{u}^+_{c,smooth} - \left\langle\widetilde{u}^+_{c,wavy}\right\rangle, \tag{3.6}$$

and the peak TKE for both wavy wall cases are shown. As can be seen, the velocity deficits due to the wavy walls match very well. The same is true for the peak TKE values, defined by

$$TKE_{max} = \left.\frac{\left\langle\widetilde{u'_i u'_i}\right\rangle}{2}\right|_{max}, \tag{3.7}$$

which differ by around 3.6%.

TABLE 3.2: Velocity deficit, ΔU^+, and peak TKE values for the wavy channel flow.

	Bodyfitted	BDIM
ΔU^+	3.47	3.50
Peak TKE	3.51	3.63

Based on the results of this initial test it can be concluded that, firstly, the domain dimensions, the initial and boundary conditions for the boundary data immersion method were chosen appropriately. Secondly, fairly reliable results with the BDIM were obtained compared to a bodyfitted case and hence gives confidence for the following simulation of a much more complex geometry.

3.2.2 Channel with Grit Blasted Roughness

In this section the extension of the boundary data immersion method will be tested by representing a complex rough surface geometry. A grit blasted roughness patch, using case s8 provided by Thakkar et al. (2017a) and Thakkar et al. (2017b), was used in a periodic turbulent channel flow at $Re_\tau = 180$. The heightmap of the surface is presented in figure 3.5. The roughness height is $k = \delta/6$, and denotes the mean peak-to-trough height, $S_{z,5\times5}$. $S_{z,5\times5}$ is obtained by decomposing the roughness patch into 5×5 smaller regions, for each of which the minimum and maximum heights are determined and then averaged. The difference between the averaged maxima and minima denotes the mean peak-to-trough height. This results in a non-dimensional roughness height of

$$k^+ = \frac{k u_\tau}{\nu} = 30, \tag{3.8}$$

which falls into the transitionally rough regime according to the authors (Thakkar et al. 2017b).

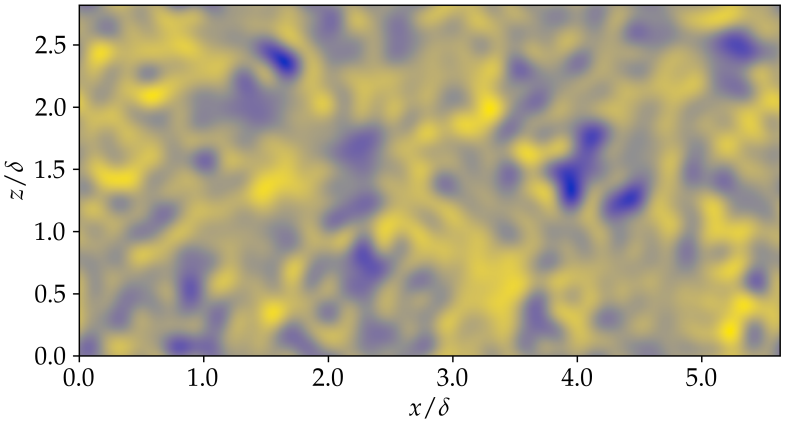

FIGURE 3.5: Height map of the grit blasted roughness patch, where the peaks and troughs are denoted by the colours yellow and blue, respectively.

The domain dimensions are shown in figure 3.6 and were based on the case of Thakkar et al. (2017b). According to the authors' meshing criteria, a uniform grid in the streamwise and the spanwise direction were chosen, with 320 and 162 grid points, respectively. This resulted in dimensionless wall units of $\Delta x^+ = \Delta y^+ \approx 3.3$. For the wall-normal direction a uniform grid from the outer walls to slightly above the highest roughness peak was used. After the peak, the grid spacing was gradually increased towards the centre line of the channel. The spacing for the uniform portion of the grid resolving the roughness is $\Delta z^+ < 0.92$. In the middle of the channel, the maximum spacing is below $\Delta z^+ < 2.6$.

Firstly, the roughness was applied to the bottom wall, where the average roughness height, defined by

$$h = \frac{1}{MN} \sum_{i,j}^{M,N} |h_{i,j}| = 0.0, \tag{3.9}$$

is on the level of $y/\delta = 0.0$. Here the discrete number of roughness points in the streamwise and the spanwise direction are denoted by N and M, respectively. $h_{i,j}$ is the roughness height at the respective discrete point. The roughness on the top wall is first mirrored and then shifted in the streamwise and the spanwise direction by $L_x/2$ and $L_z/2$. The averaged roughness height is located at $y/\delta = 2.0$. Hence, the effective channel half height between the bottom and the top rough surfaces is 2δ. The grey areas in figure 3.6 represent the extent of the surface roughness.

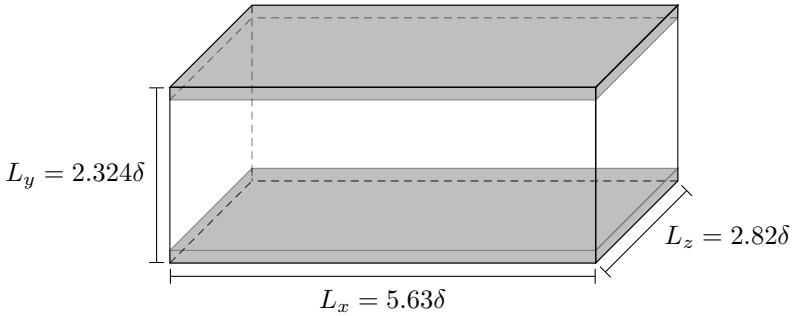

FIGURE 3.6: Domain of the grit blasted rough surface channel flow.

The resulting channel with grit blasted walls is shown in figure 3.7 and the highly irregular, complex surface geometry is apparent.

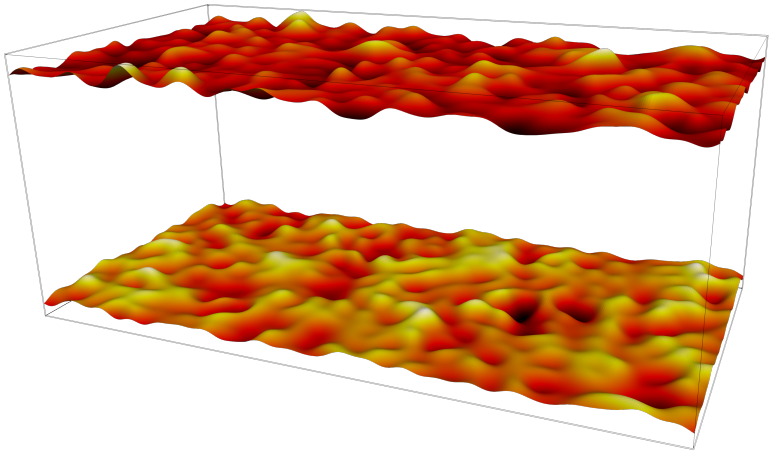

FIGURE 3.7: Grit blasted walls for the transitionally rough channel flow simulation. The top roughness was mirrored and shifted by $L_x/2$ and $L_z/2$ in the streamwise and the spanwise directions.

The results for the time and spatially averaged streamwise velocity and Reynolds stresses are shown in figure 3.8. For the spatial averaging ($\langle\cdot\rangle$) profiles in the time averaged ($\widetilde{\cdot}$) flow field at randomly chosen locations were extracted and then averaged by only considering the fluid part outside of the boundary data immersion region. The results are compared to Thakkar et al. (2017b), who used an incompressible DNS flow solver with an immersed boundary method (Busse et al. 2015) to represent the roughness. The top of the roughness is denoted by the grey dashed line at $y^+ = 30$. As can be seen, the streamwise velocity profiles match very well above the roughness towards the channel centre line.

As to the Reynolds stresses, larger differences are evident. For $\left\langle \widetilde{u'^2} \right\rangle$ HiPSTAR slightly overestimates the peak value, whereas towards the channel centre a marginal underestimation can be observed. The wall-normal and the spanwise stresses show the opposite trend, where the peak stress values are lower compared to Thakkar et al. (2017b). The same is true for the stress values towards the channel centre.

As can be seen in table 3.3, the velocity deficits, ΔU^+, compared to the smooth reference case match fairly well. Furthermore, the peak TKE for HiPSTAR is slightly higher by around 5.5% compared to the reference. This is due to the relatively higher streamwise Reynolds stresses, as seen in figure 3.8.

TABLE 3.3: Velocity deficits, ΔU^+, compared to the smooth reference case and peak TKE values.

	HiPSTAR	Thakkar et al. (2017b)
ΔU^+	4.32	4.36
Peak TKE	3.24	3.06

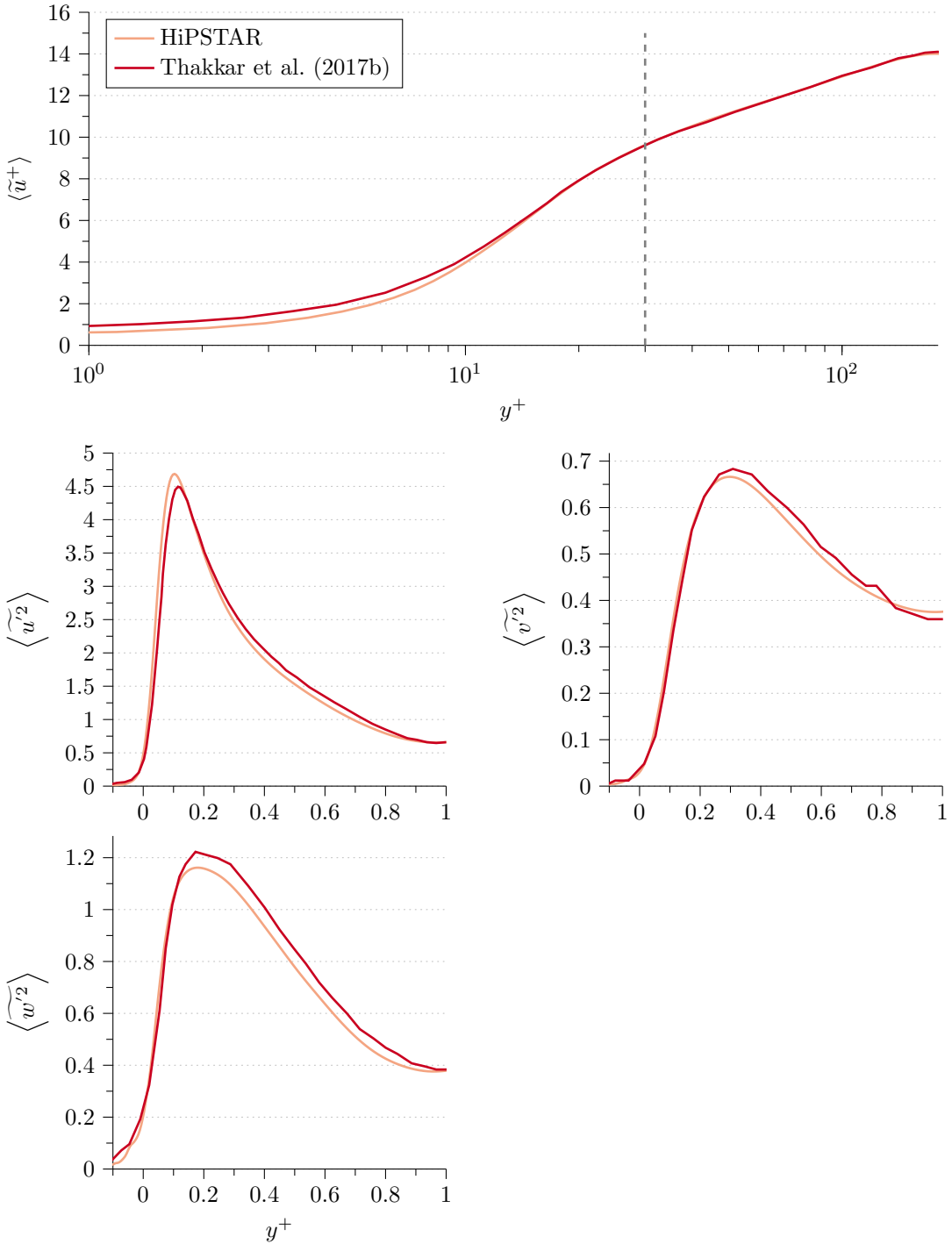

FIGURE 3.8: Time and spatially averaged streamwise velocity, $\langle \widetilde{u}^+ \rangle$, and Reynolds stresses, $\langle \widetilde{u'^2} \rangle$, $\langle \widetilde{v'^2} \rangle$ and $\langle \widetilde{w'^2} \rangle$.

In figure 3.9 the Reynolds shear stresses, $-\left\langle \widetilde{u'v'} \right\rangle$, are compared. The spanwise-normal plane at $z/\delta = 1.44$ is shown, with the greyed out area representing the grit blasted surface geometry. Qualitatively the flow fields look very similar and shows the same trends in the vicinity of the rough surface. Furthermore, the roughness peaks and troughs are well represented by the BDIM. At around $x/\delta \approx 2.3$ the shear stresses are slightly lower compared to Thakkar et al. (2017b), whereas higher values of $-\left\langle \widetilde{u'v'} \right\rangle$ at the end of the channel can be observed, which enter into the start of the domain.

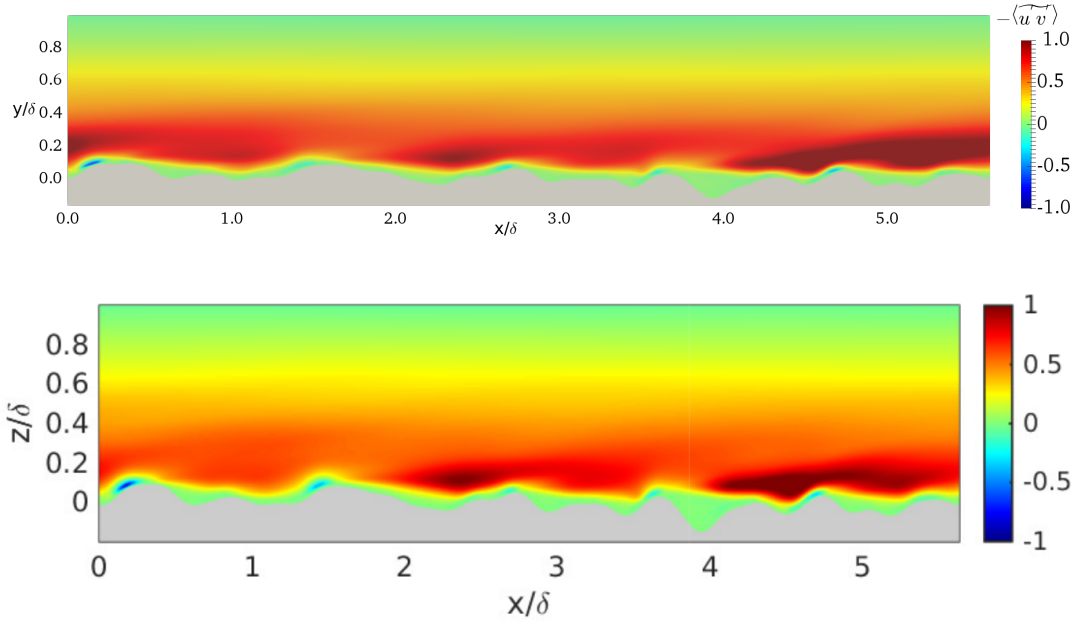

FIGURE 3.9: Reynolds shear stresses, $-\left\langle \widetilde{u'v'} \right\rangle$, in the spanwise-normal plane at $z/\delta = 1.44$. Note the different axis denotations for the wall-normal directions.

Based on the presented results it can be concluded that the extended boundary data immersion method is suitable for representing complex geometries like surface roughness. Hence, it will be used for the linear low-pressure turbine cascade simulations in chapter 5, where an as-cast roughness patch is mapped onto the suction surface of the turbine blade.

3.3 Modelling Roughness by Means of the Parametric Forcing Approach

In this section the implementation of the parametric forcing approach will be verified by comparing DNS results of a fully rough channel at a friction Reynolds number of $Re_\tau = 180$ with results of Busse and Sandham (2012), obtained by an incompressible flow solver. After that the behaviour of the forcing model in terms of transition will be investigated by looking at a laminar-turbulent transitional channel flow at $Re_\tau = 80$. The resulting forcing parameters will be used in a transitionally rough channel case at $Re_\tau = 180$ and compared to the results of the grit blasted channel.

3.3.1 Verification of the Parametric Forcing Approach

Firstly, the implementation of the parametric forcing approach into HiPSTAR will be verified by means of the results of Busse and Sandham (2012). An important point to remember is that, as opposed to the simulations done by Busse and Sandham (2012), HiPSTAR uses the compressible Navier-Stokes equations, which required an additional forcing term in the energy equation; see section 2.2.3. Hence, a proper verification is needed before moving to the roughness parameter studies and applying the roughness term to an actual linear low-pressure turbine cascade. For this, a fully rough channel case at $Re_\tau = 180$ was simulated. The same Reynolds number, Mach number and streamwise pressure gradient as for the smooth reference channel case were used for the verification case. The domain size (see figure 3.10) of the channel is $7\delta \times 2\delta \times 3.5\delta$ and the grid consists of $128 \times 128 \times 128$ (streamwise, wall-normal, spanwise) grid points, which was chosen according to Busse and Sandham (2012). Grid stretching in the wall-normal direction was applied, resulting in $\Delta z^+ < 0.9$ at the wall and $\Delta z^+ < 4.8$ in the centre of the channel.

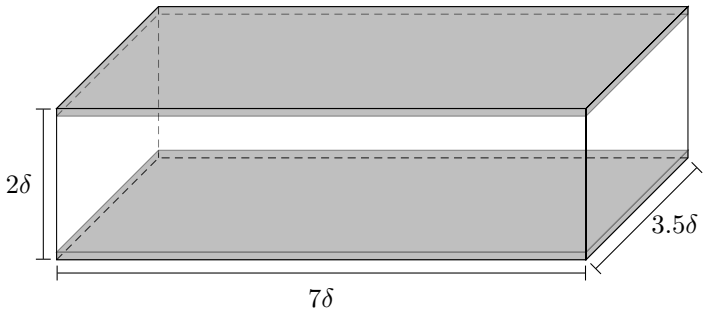

FIGURE 3.10: Domain of the verification case for the parametric forcing approach.

For the verification simulations, the forcing factor was set to $\alpha_x = \alpha_z = \alpha = 1.0$ for the streamwise and the spanwise direction and to $\alpha_y = 0.0$ for the wall-normal direction. The box shape function

$$F(z,h) = \begin{cases} 1, & \text{if } z \leq \eta(h) \\ 0, & \text{if } z > \eta(h) \end{cases} \tag{3.10}$$

was used, with $\eta(h) = 2h$, which can be determined by equation 2.33. The height parameter, h, denotes the mean roughness height in wall-normal direction from the channel wall. Hence, the top of the box profile roughness is at $2h$, which was chosen to be 0.111 for this verification case. In the simulation of Busse and Sandham (2012) these parameters resulted in a roughness function of $\Delta U^+ = 8.0$, which indicates that the channel flow is in the fully rough regime. The reasons for using a box profile instead of other profiles are two-fold. Firstly, the definition of the roughness height is simpler and a distinct region can be defined where the forcing is applied. Busse and Sandham (2012) found a dampening of the velocity fluctuations for shape functions extending too far into the flow. Secondly, based on channel flow simulations of Chung et al. (2015), the transition behaviour of the box shape function closely matched that of sand-grain roughness.

The comparison between the results of Busse and Sandham (2012) and the parametric forcing implementation in HiPSTAR are presented in figure 3.11. The streamwise velocity profiles, $\langle \widetilde{u}^+ \rangle$, show good agreement close to the wall. However, from $y^+ = 20$ towards the middle of the channel

marked differences can be observed, where the profile from the reference shows higher values. This leads to a velocity deficit of

$$\Delta U^+ = \langle \widetilde{u}_{c,smooth} \rangle - \langle \widetilde{u}_{c,pfa} \rangle = 8.55, \tag{3.11}$$

compared to $\Delta U^+ = 8.0$ obtained by Busse and Sandham (2012), representing a difference of $\approx 6.5\%$ in ΔU^+. It should be noted that there is almost no density variation between the wall ($\rho_w = 1.006$) and the centre line ($\rho_c = 0.999$) of the channel and thus non-density weighted profiles are compared in this case. A kink in the profile at $y^+ = 20$, stemming from the top edge of the box profile, is apparent for the incompressible case, but not for the compressible one.

The streamwise Reynolds stresses match fairly well towards the centre of the channel. On top of the forcing region, however, the peak values are overestimated compared to Busse and Sandham (2012). The same can be observed for the wall-normal stresses, $\left\langle \widetilde{v''^2} \right\rangle$, and the spanwise stresses, $\left\langle \widetilde{w''^2} \right\rangle$, where the values in the roughness region are slightly higher. Interestingly, a very good agreement for the shear stresses, $-\left\langle \widetilde{u''v''} \right\rangle$, are apparent.

The first derivative of the streamwise velocity in wall-normal direction, $\partial \langle \widetilde{u}^+ \rangle / \partial y$, and the velocity defect, $\left\langle \widetilde{u_c}^+ \right\rangle - \langle \widetilde{u}^+ \rangle$, are shown in figure 3.12. The first thing to notice is the discontinuity in the derivative due to the sharp box shape function. Compared to the reference case $\partial \langle \widetilde{u}^+ \rangle / \partial y|_{wall}$ at the wall is slightly higher. The behaviour, however, is opposite on top of the roughness region, where the peak values are markedly lower. Furthermore, a plateau rather than a peak is apparent, which might be due to the additional filtering that is needed for the stability of compressible flow simulations. The sharp edge induces wavenumbers in the flow field that are filtered out, leading to the observed plateau and might also explain the differences in the Reynolds stresses. The differences in the streamwise velocity derivative diminish towards the centre of the channel. As can be seen, the slopes of the velocity defect along the wall-normal direction match well, indicating that outer similarity is preserved.

To summarise, the results of the implemented parametric forcing approach in HiPSTAR compare well to the results of Busse and Sandham (2012). The observed differences might be attributed to the fairly different flow solvers, i.e. compressible vs. incompressible, additional forcing term in the energy equation as well as the needed additional filtering for numerical stability.

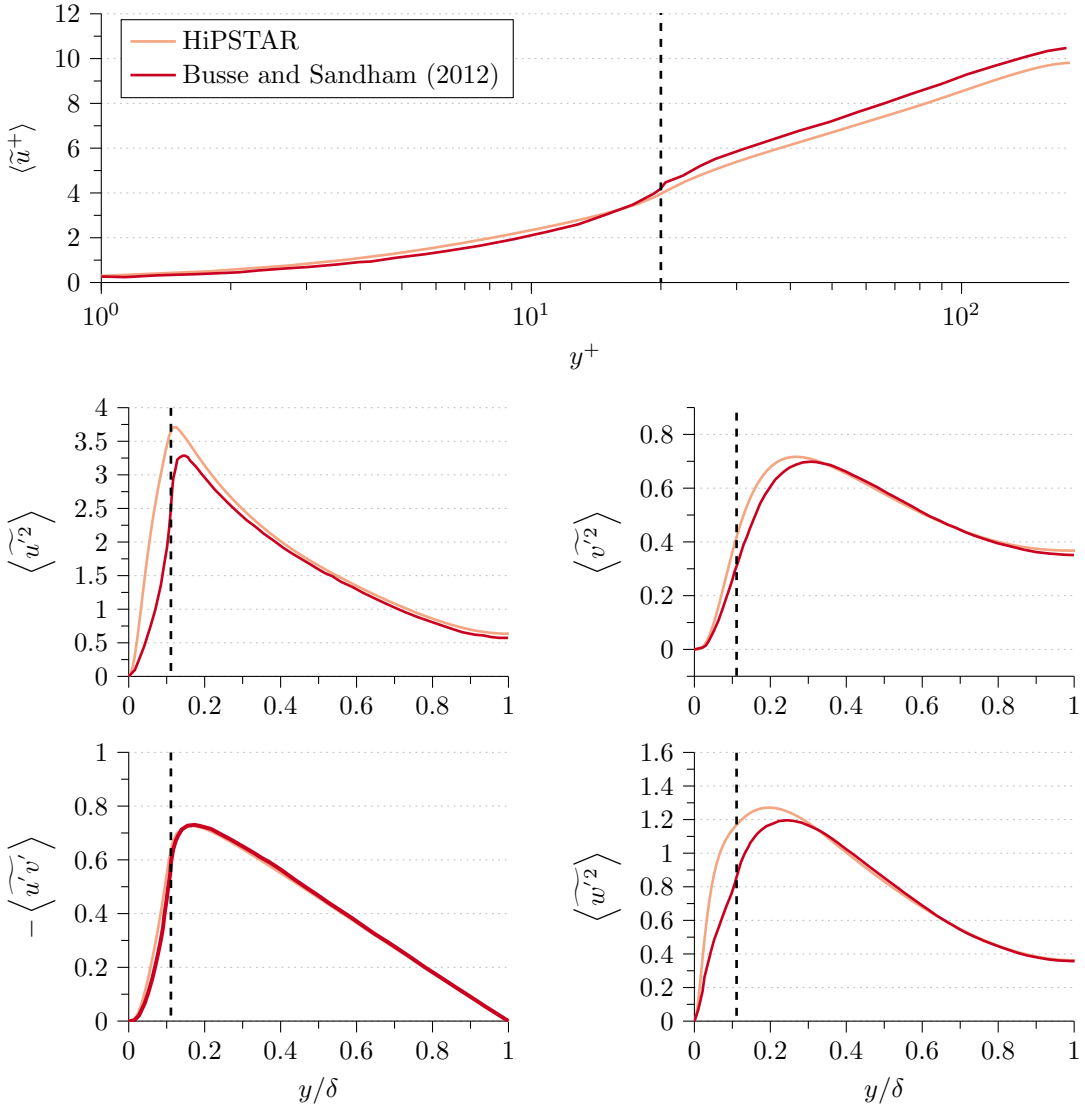

FIGURE 3.11: Comparison of the implemented parametric forcing approach in HiPSTAR with the reference case at $Re_\tau = 180$. The vertical dashed line at $y^+ = 20$ denotes the top of the box shape function.

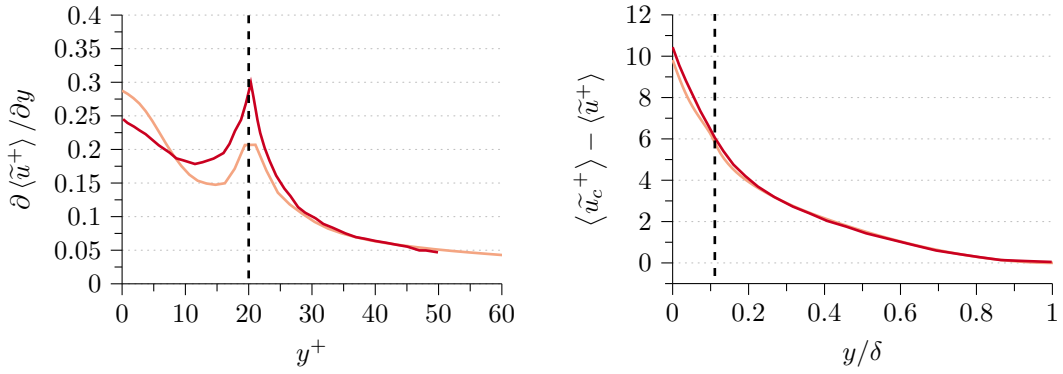

FIGURE 3.12: First derivative of the streamwise velocity in wall-normal direction, $\partial \langle \widetilde{u}^+ \rangle / \partial y$, and velocity defect, $\langle \widetilde{u_c}^+ \rangle - \langle \widetilde{u}^+ \rangle$ for HiPSTAR and the reference case.

3.3.2 Laminar-turbulent Channel Flow with the Parametric Forcing Approach

The boundary layer on the low-pressure turbine blade in the linear cascade transitions from a laminar to a turbulent state (Halstead et al. 1997b). However, so far the behaviour of the parametric forcing approach has only been investigated in the turbulent boundary layer regime (Busse and Sandham 2012). Hence, in this section laminar-turbulent channel cases with the roughness model are examined. For this, the transition study of Thakkar (2017) was replicated by using the forcing term instead of a real rough wall. The domain dimensions are shown in figure 3.13 and were chosen according to the reference case of Thakkar (2017), who used grit blasted walls; see also section 3.2.2 for roughness specifications.

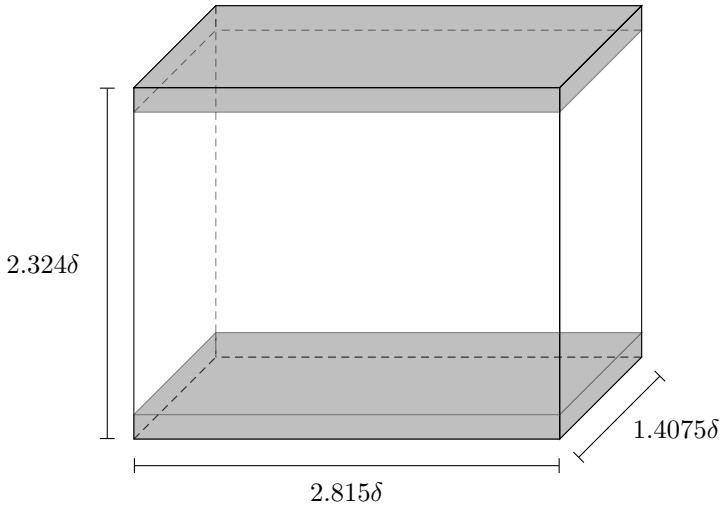

FIGURE 3.13: ChannelCasePFALaminar

The domain was discretised by $96 \times 112 \times 48$ grid points in the streamwise, the wall-normal and the spanwise direction. With grid stretching in the wall-normal direction, the resulting spacing at the wall was $\Delta z^+ < 1.3$ and at the channel centre $\Delta z^+ < 3.1$. Moreover, the box profile with a height of $2h = 0.324$ was used, because, as mentioned above, the transition behaviour of this shape function was found to be similar to that of sand-grain roughness (Chung et al. 2015). The reason for using an extended wall-normal length of 2.324δ instead of 2δ is the aforementioned blockage effect of the box shape function in Busse and Sandham (2012).

Thakkar et al. (2017b) used grit blasted wall channel flow at different Reynolds numbers ranging from $Re_\tau = 45$ to 95. They found that the grit blasted roughness caused laminar-turbulent transition at a Reynolds number of $Re_\tau = 89.5$. For the transition study of the parametric forcing approach only one case at $Re_\tau = 80$ was chosen. The flow field was initialised with a turbulent channel solution and the forcing parameter, α, was decreased from a high value, $\alpha = 1.0$, until the flow turned from a turbulent to a laminar flow state. The forcing parameter was applied in the streamwise and the spanwise direction. A monitor point at the centre of the channel was used to track the streamwise velocity, u_c, in order to check the state of the flow field.

Figure 3.14 shows the time history of u_c for three different roughness densities, close to laminar-turbulent transition.

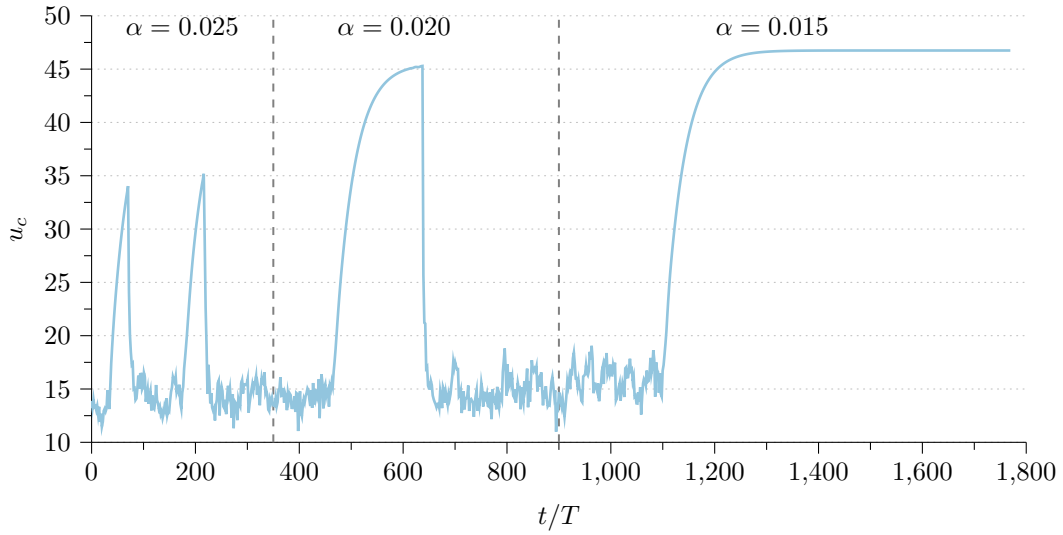

FIGURE 3.14: Channel flow at $Re_\tau = 80$, where the roughness density, α, was decreased until a laminar state was achieved.

As can be seen, the α values are relatively low, compared to $\alpha = 1.0$ used in the turbulent flow study in the previous subsection. For $\alpha = 0.025$ two peaks are apparent, indicating that the flow is close to the critical transition point. By further decreasing the roughness density the flow slowly becomes laminar, but then suddenly and rapidly recovers to a turbulent state again. The time span of the this process is almost $200t/T$ time units. After $250t/T$ time units and without any indication of sudden transition peaks the roughness density was further reduced to $\alpha = 0.015$. Eventually, the flow transitions to a laminar state and remains so for more than $400t/T$ time units, after which the simulation was stopped as no further changes were to be expected.

The transition study proves the capability of the parametric forcing approach to successfully model transition behaviour. Furthermore, the resulting roughness density, $\alpha = 0.015$, can be regarded as a model representation of the grit blasted wall used in (Thakkar et al. 2017b) and section 3.2.2. The next step is to compare the parametric forcing approach with a real rough surface in a turbulent channel flow at a skin friction Reynolds number of $Re_\tau = 180$.

3.4 Comparsion between the Parametric Forcing Approach and the Boundary Data Immersion Method in a Grit Blasted turbulent Channel Flow

In this section the implemented parametric forcing approach and the extended boundary data immersion method for complex geometries are compared by means of turbulent channel flow at a skin friction Reynolds number of $Re_\tau = 180$. The aim is to further test the capabilities of the PFA to model a real rough surface, which will then later be used for the linear low-pressure

turbine simulations. The results of the grit blasted channel flow in section 3.2.2 were used, where the BDIM compared well to the reference case. For the parametric forcing approach the roughness density value $\alpha = 0.015$ was used, based on the transition study in the previous section.

The domain is shown in figure 3.15, which is the same as for the grit blasted grid presented in section 3.2.2. Furthermore, the roughness height was chosen to be $2h = 0.324$ and thus covering the same flow area as the grit blasted surface patch, denoted by the grey area in figure 3.15. This will also clarify whether the blockage effect due to the forcing model is sufficient to reproduce a similar effect as the real roughness. The grid resolution and stretching are the same for both cases, with $320 \times 288 \times 162$ grid points in the streamwise, the wall-normal and the spanwise directions, respectively, in order to obtain grid independent results.

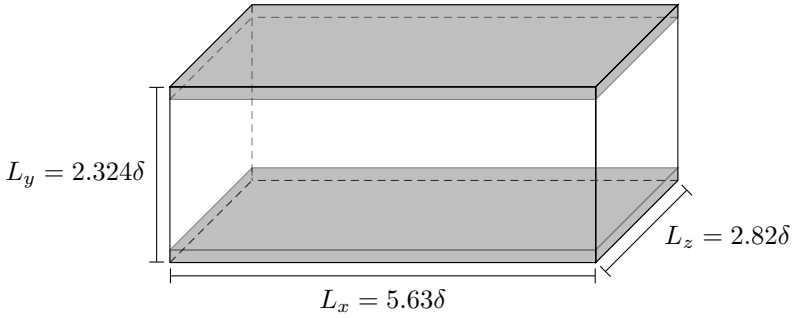

FIGURE 3.15: Domain of the grit blasted and parametric forcing rough surface channel flow.

Figure 3.8 shows the time and spatially averaged streamwise velocity $\langle \widetilde{u}^+ \rangle$ and the Reynolds stresses $\left\langle \widetilde{u'^2} \right\rangle$, $\left\langle \widetilde{v'^2} \right\rangle$, $\left\langle \widetilde{u'v'} \right\rangle$ and $\left\langle \widetilde{w'^2} \right\rangle$ for the PFA, the grit blasted and the smooth reference cases. Looking at the streamwise velocity component it is evident that the parametric forcing approach with the fairly low roughness density of $\alpha = 0.015$ is not able to reproduce the results of the grit blasted walls and rather follows the trend of the smooth wall case. The streamwise Reynolds stresses reveal that the peak values even exceed the values of the reference case. Furthermore, the peak is within the forcing region, rather then outside and slightly above the top peak, as observed for the grit blasted case. This is a very good indication that the roughness density value is too low for simulations in the turbulent flow regime and does not exert a sufficient blockage effect. The wall-normal, the shear and the spanwise stresses show the same behaviour. Moreover, the outer similarity was not achieved, as is apparent from the offset in the stresses at the centre of the channel. The reason for this is the missing blockage effect in the larger wall-normal domain size 2.324δ. Because the same pressure gradient,

$$-\frac{\delta}{\rho}\frac{\mathrm{d}P}{\mathrm{d}x} = u_\tau^2 = 1.0, \tag{3.12}$$

was applied, with $\delta = 1.0$ based on the smooth reference case rather than $\delta = 1.162$ for driving the channel flow, the resulting skin friction velocity increased and hence a higher Reynolds number, $Re_\tau = 225$, was obtained for the larger domain. This could already be observed in the transition study in figure 3.14, where the centre line velocity of $u_c > 45$ in the laminar region exceeded $u_c = 40$, which is obtained for a smooth laminar channel at $Re_\tau = 80$.

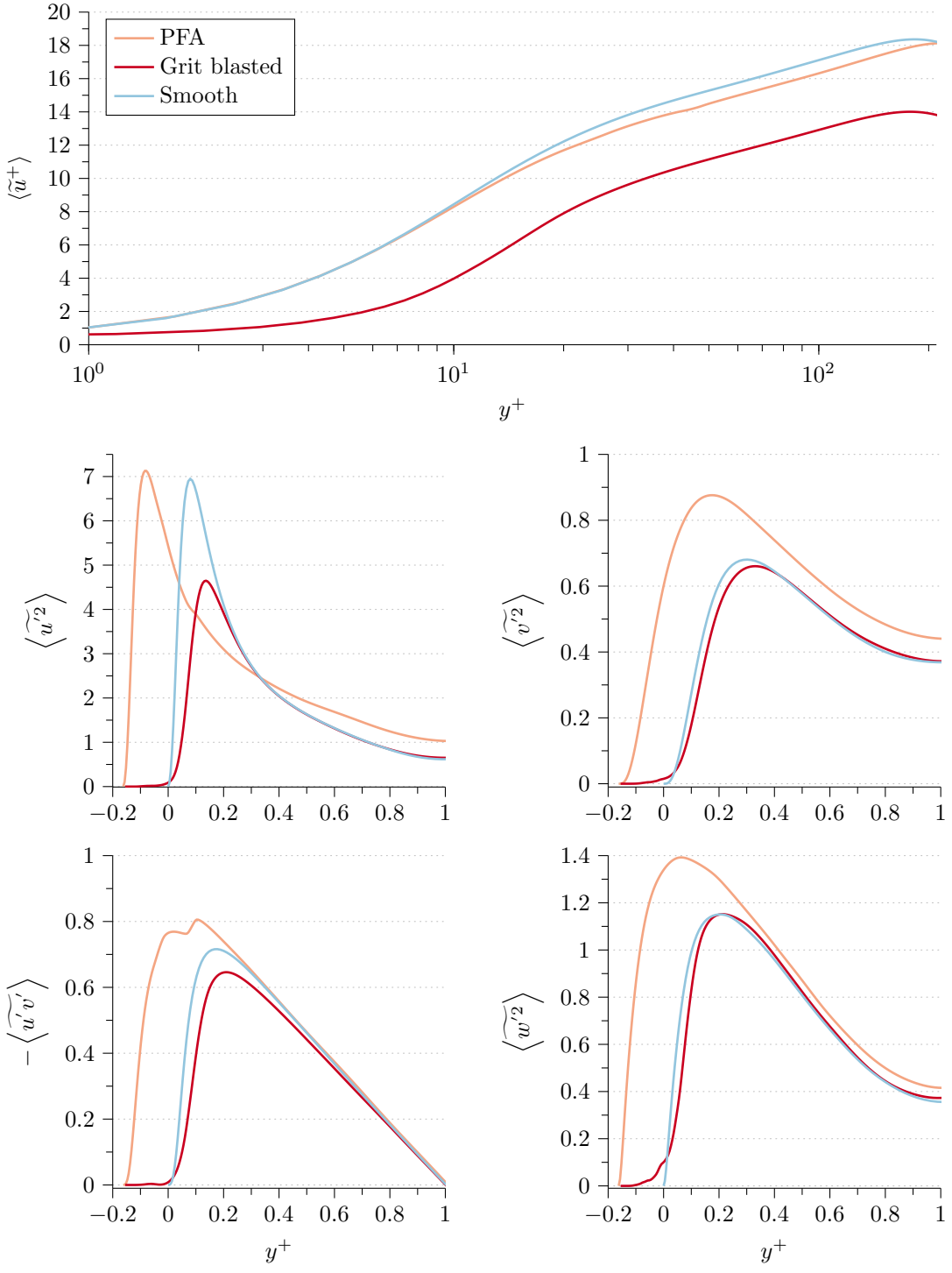

FIGURE 3.16: Time and spatially averaged streamwise velocity $\langle \widetilde{u}^+ \rangle$ and Reynolds stresses $\langle \widetilde{u'^2} \rangle$, $\langle \widetilde{v'^2} \rangle$, $\langle \widetilde{u'v'} \rangle$ and $\langle \widetilde{w'^2} \rangle$ for the PFA, the grit blasted and the smooth reference cases.

Figure 3.17 shows the time and spatially averaged streamwise velocity derivative in the wall-normal direction, $\partial \langle \widetilde{u}^+ \rangle / \partial y$, for the PFA and the smooth reference cases. The vertical black line at $y/\delta = 0.0$ denotes the wall for the reference case.

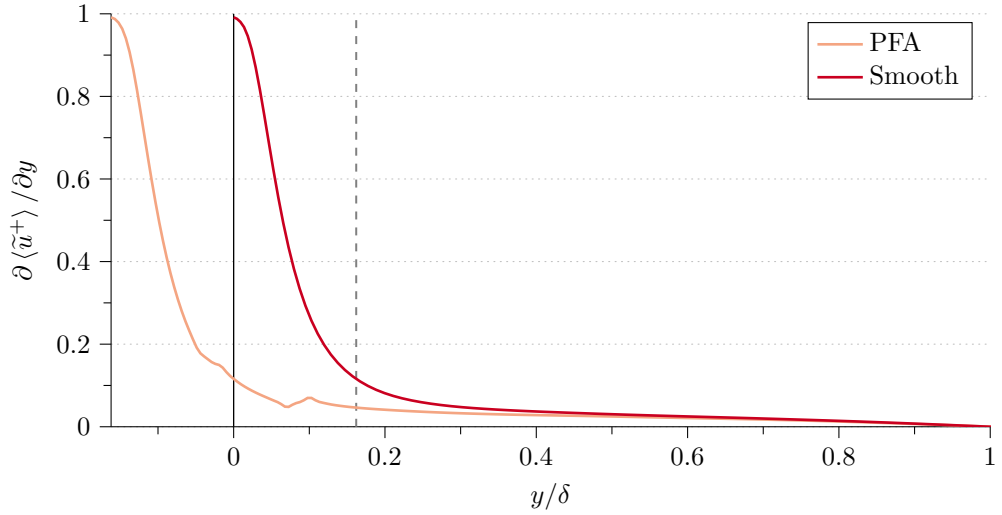

FIGURE 3.17: Time and spatially averaged streamwise velocity derivative in the wall-normal direction, $\partial \langle \widetilde{u}^+ \rangle / \partial y$, for the PFA and the smooth reference cases.

As can be seen, the forcing only has a marginal effect on $\partial \langle \widetilde{u}^+ \rangle / \partial y$ within the roughness region and even reaches the same wall value, $\partial \langle \widetilde{u}^+ \rangle / \partial y|_{wall}$, as the smooth case, indicating the insufficiency of the low roughness density value.

In order to further investigate why the parametric forcing at a low roughness density level of $\alpha = 0.015$ was able to induce transition at the current Re_τ, but had no real effect in the turbulent channel flow, the laminar and turbulent states of the transition study case in section 3.3.2 are compared. Figure 3.18 shows the time and spatially averaged streamwise velocity derivative in the wall-normal direction, $\partial \langle \widetilde{u}^+ \rangle / \partial y$, in the laminar and turbulent channel flow at $Re_\tau = 80$.

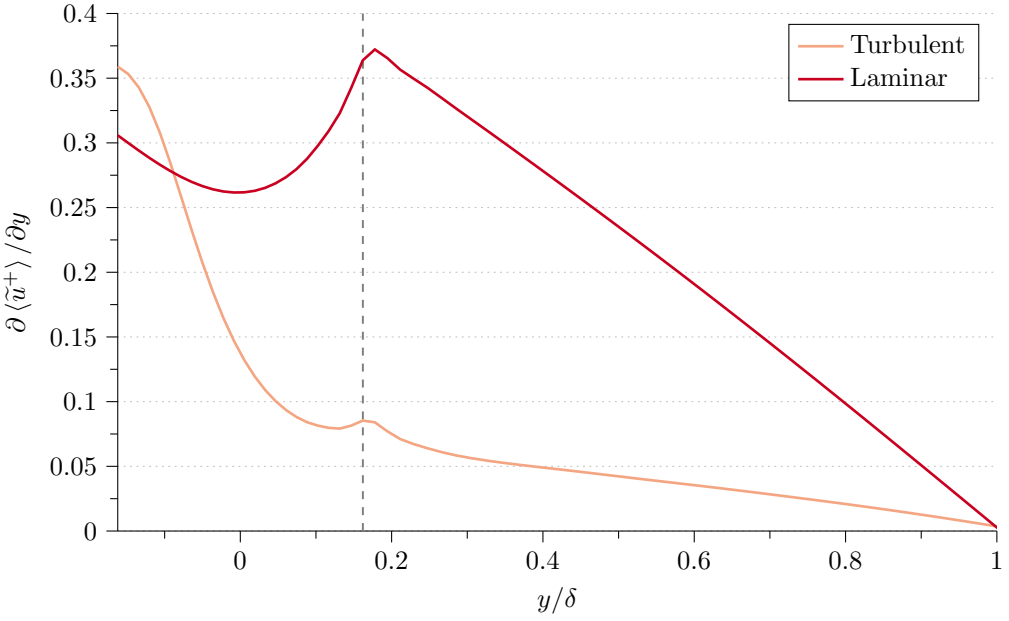

FIGURE 3.18: Time and spatially averaged streamwise velocity derivative in the wall-normal direction, $\partial \langle \widetilde{u}^+ \rangle / \partial y$, in the laminar and turbulent channel flow of the transition study case at $Re_\tau = 80$ or rather $Re_\tau = 100$ when based on the real channel half height $\delta = 1.162$.

It has to be noted, however, that due to the marginal blockage effect the channel half height is also larger than δ for the transition study case, resulting in an effective Reynolds number of $Re_\tau = 100$ when based on the real channel half height $\delta = 1.162$; see equation 3.12. For the laminar state the flow in the time range of $t/T \leq 1{,}400$ was averaged. In order to get statistical data in the turbulent state, the flow solution was averaged between $923 \leq t/T \leq 1{,}097$ time units. Again, in the turbulent state the forcing only has a very weak effect on $\partial \langle \widetilde{u}^+ \rangle / \partial y$, explaining why the flow in the middle of the channel is barely influenced. Moreover, this allowed the channel flow to transition to the laminar state. The forcing effect in the laminar state, however, is only apparent in the forcing region itself for $y/\delta < 2h$ and hence is neither able to force the flow back to a turbulent state nor reduce the centre line velocity. For the slightly higher roughness densities, $\alpha \geq 0.02$, this forcing effect must have been strong enough to cause transition to a turbulent boundary layer.

This was confirmed by a laminar parameter study at $Re_\tau = 45$ in a minimal channel, see figure 3.19, with $10\delta \times 112\delta \times 10\delta$ grid points in the streamwise, the wall-normal and the spanwise direction.

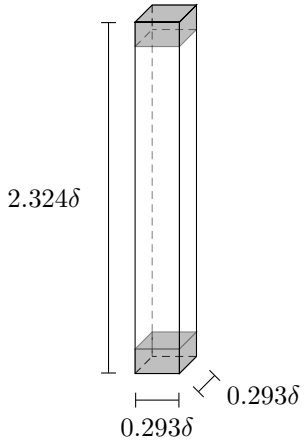

FIGURE 3.19: ChannelCasePFALaminar

As can be seen in figure 3.20, only with the highest $\alpha = 1.0$ value the forcing model was able to have a considerable effect on the streamwise velocity, u, in the laminar channel compared to the analytical solution. For the lowest roughness density no effect is noticeable for u and barely any effect is seen for $\partial u/\partial y$.

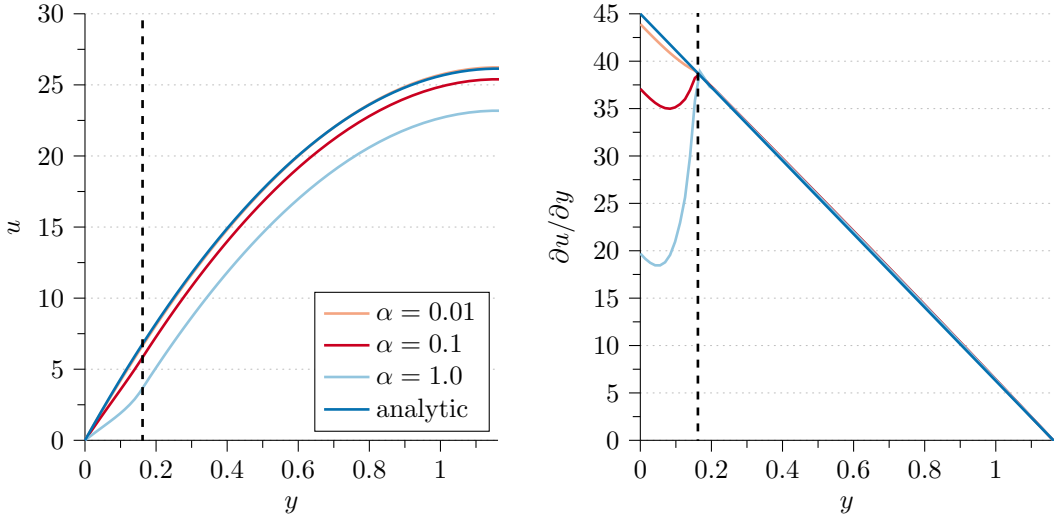

FIGURE 3.20: Time and spatially averaged streamwise velocity; $2\delta = 2.324$

To summarise, the parametric forcing approach is able to induce transition at very low roughness density values. However, these values are too low to have an actual effect on the channel flow outside the roughness region due to the marginal blockage effect. In order to gain more insight, a further parameter study with different domain sizes needs to be carried out. To circumvent this problem for the linear low-pressure turbine simulations in the later chapters, much higher roughness densities, $\alpha \geq 1$, will be used, appropriate to the turbulent flow regime. This makes the comparison between the roughness forcing model and a real rough surface in terms of transition difficult, but valuable insights in the turbulent boundary layer region can be gained. It can be concluded that a 'tuning' of the roughness parameters to a real rough surface in a simple channel regarding the roughness function ΔU^+ is possible, but meaningful only in the fully rough flow regime. Regarding the turbine design stage, the parametric forcing could be used as an inexpensive and readily implementable means for transition control. Furthermore, during the time span of this work a modified version of the PFA was proposed by Forooghi et al. (2018), who added an additional linear term to the formulation in order to account for the viscous drag. They achieved satisfactory results compared to a fully resolved geometry, but application to transition were not considered.

3.5 Summary

In this chapter the extended boundary data immersion method for complex geometries and the compressible formulation of the parametric forcing approach were investigated and verified by means of simple channel flow. This serves as the foundation for the linear low-pressure turbine cascade simulations in the later chapters, where both approaches are incorporated. The boundary data immersion method will be used to represent the wake generating bars as well as real surface roughness patches on the turbine blade. However, real roughness simulations in turbines are computationally expensive, rendering this approach less appropriate for the turbine designing phase. For this reason, a simple roughness model, namely the parametric forcing approach can be

used, allowing for roughness parameter studies in order to gain first insights during the designing process.

Firstly, a smooth wall turbulent channel flow at $Re_\tau = 180$ was simulated in order to obtain reference values and to verify the current version of HiPSTAR. The reference values were used for the normalisation of the results of the roughness simulations within this chapter. It has been shown that the results compared well to the reference cases in the literature (Kim et al. 1987; Vreman and Kuerten 2014).

The next step was the verification of the extended boundary data immersion method. In order to do so turbulent channel flow at $Re_\tau = 180$ with wavy walls in streamwise direction and grit blasted walls were simulated. The wavy channel case compared very well to the bodyfitted fitted case. A very good agreement with the results of Thakkar et al. (2017b), who also used an immersed boundary method (Busse et al. 2015), for the grit blasted wall case was obtained, giving confidence in the suitability of the boundary data immersion method for the later roughness simulations in the low-pressure turbine.

After that the compressible formulation of the parametric forcing approach was also verified for turbulent channel flow at $Re_\tau = 180$. The results were compared to Busse and Sandham (2012) and a good agreement was observed. However, differences in the Reynolds stresses and the wall-normal derivative of the streamwise velocity were apparent as well. These might be attributed to the fairly different flow solvers, i.e. compressible vs. incompressible, additional forcing term in the energy equation as well as the needed additional filtering for numerical stability.

As the boundary layer on the low-pressure turbine blade in the linear cascade transitions from laminar to turbulent, the parametric forcing approach had to be tested in laminar-turbulent channel flow, which had not been done yet. Hence, a transition study based on grit blasted channel flow of Thakkar et al. (2017b) was carried out. An initially turbulent channel at $Re_\tau = 80$ was simulated with different roughness density values, α. The values were decreased until the flow transitioned from a turbulent to a laminar state.

The obtained roughness density, $\alpha = 0.015$ of the transition study was then used for turbulent channel flow at $Re_\tau = 180$. A comparison between the grit blasted roughness, represented by the BDIM, and the forcing model revealed that the roughness density was too low to sufficiently affect the flow at the centre of the channel due to the marginal blockage effect. This led to the conclusion that a further parameter study with different domain dimension is necessary. For the linear low-pressure turbine simulations higher roughness density values, $\alpha \geq 1$, will be used, which makes the comparison to a real rough surface in terms of transition difficult. However, the PFA is still thought to be a valuable approach for the turbine design process in order to gain first insights of roughness effects on the turbine flow.

Chapter 4

Influence of different Wake Profiles in a linear Low-Pressure Turbine Cascade[†]

In this chapter the research questions, given in section 1.3, i.e. whether a simple bar setup is capable of representing an actual blade wake profile and whether the drag coefficient is reliable as a design parameter for bars, as stated by Pfeil and Eifler (1976), are addressed. In order to do so, the effect of different wake profiles, generated by bars with different rotation rates, on the boundary layer of the T106A low-pressure turbine blade, as well as the overall linear LPT losses are investigated. A total of ten large eddy simulations of the linear low-pressure turbine cascade with the T106A blade profile were carried out. The numerical scheme, the bar rotation rate, the boundary data immersion method - for representing the upstream bars - as well as the grid size were varied. The wall-adapting local eddy-viscosity (WALE) model of Ducros et al. (1999) was used, which has proven to be reliable and viable in previously conducted simulations. Wake profiles of both the bars and the T106A turbine blade at different downstream positions were gathered for comparison.

The structure of the chapter is as follows. First of all, the linear low-pressure turbine setup including domain size, grid metrics and numerical methods is presented in section 5.1. An explanation of the ten different cases and the reasons for choosing them are given. After that, in section 4.1.1, the boundary data immersion method and the grids for the complete LPT setup are validated. The results are compared with a simulation carried out by Michelassi et al. (2015), where a discrete momentum forcing approach, proposed by Goldstein et al. (1993a), was used for representing the wake generating bars. Additionally, a case with bodyfitted bars was simulated for validation purposes. As mentioned in section 2.1.2, there is the option of two different spatial discretisation schemes. A brief note on why the compact discretisation scheme was preferred within this work is given. The characterisation of the bar wakes and the method of extraction are discussed in section 4.2. This is followed by the comparison of the different bar wakes with an actual turbine blade wake. The implications of the different wakes on the boundary layer of the

[†]This chapter is an extended form of the work published of Hammer et al. (2018b)

blade, the wake distortion itself and the loss mechanisms on the linear LPT are demonstrated in section 4.3. This is the most crucial section, where the major conclusion are drawn.

4.1 Linear Low-Pressure Turbine Cascade Setup

In this section and the following subsection the linear low-pressure turbine cascade setup and the simulation parameters are introduced. Furthermore, the boundary data immersion method, which was used for the representation of the wake generating bars throughout this work, is validated by means of simulation results of a different immersed boundary approach and a body-fitted case.

The complete cascade-bar setup is depicted in figure 5.1. Two wake-generating bars are located 0.7 chord-lengths c upstream of the blade's leading edge ($x_{LE} = 0.0$). The diameters of the bars were chosen according to the round trailing edge diameter, $D = 0.02c$, of the blade, which has been a common design choice in the literature (Engber and Fottner 1995; Ladwig and Fottner 1993; Michelassi et al. 2003, 2015; Pfeil and Eifler 1976). Characteristic inlet and outlet conditions (section 2.2) were used as well as periodic conditions for the pitchwise and spanwise directions (section 2.1.2). The grid for the cascade itself was generated by means of a multi-block Poisson grid generator for cascade simulations (Gross and Fasel 2008). The blade is surrounded by an O-type mesh that, in turn, is connected to an H-type mesh. In order to achieve a relative motion between the bars and the blade the two upstream blocks are connected to the cascade grid via a sliding interface (section 2.2.4). Using 32 Fourier modes, i.e. 66 collocation points, for the spanwise discretisation and 181,632 grid points in the 2D plane, results in a total grid node count of 11,987,712 for the 3D simulation. With a distance of $\Delta y/c \approx 3.5 \cdot 10^{-4}$ for the first grid point from the blade surface, a value of $\Delta y^+_{min} \approx 2$ was achieved. However, in the aft region of the blade where flow transition and separation occurs, Δy^+_{min} drops well below 1, ensuring DNS-like resolution. Furthermore, the wall-adapting local eddy-viscosity (WALE) sub-grid model of Nicoud and Ducros (1999) was used for all simulations. Data was captured across 'Measurement plane 1' ($x_1 = -0.3c$) and 'Measurement plane 2' ($x_2 = 1.26c$) in order to calculate the different losses.

The inlet velocities, Mach number and Reynolds number for all simulations are presented in table 5.2. They were chosen such that the isentropic Reynolds and Mach numbers, which are defined based on the exit velocity $V_{is,2}$ at $x_2 = 1.26c$ (denoted 'Measurement plane 2' in figure 5.1) and the true chord length c, are around $Re_{is,2} = 100{,}000$ and $M_{is,2} = 0.4$, respectively. In order to fully describe the compressible Navier-Stokes equations with the ideal gas assumption, the Prandtl number Pr and the Sutherland constant S are also given in the table.

Table 4.1: Inlet parameters for the cascade simulations.

Re	M	V_{ax}	U_{bar}	Pr	S/T_{ref}
62707	0.24357	0.697	0.41	0.72	0.3686

In order to be able to investigate the influence of impinging wakes on the turbine blades, it is desirable to chose inflow conditions that allow for distinct and pronounced bar wake development and convection throughout the turbine cascade. There are two important parameters that

determine the state of the incoming wakes. Firstly we have the flow coefficient

$$\Phi = \frac{V_{ax}}{U_{bar}}, \tag{4.1}$$

which gives us the ratio between the axial flow velocity V_{ax} and the bar sliding velocity U_{bar}. The axial velocity also determines the mass flow rate of the turbine, whereas the bar sliding velocity sets the relative velocity between the bars and the blades, which causes the periodic nature of the flow problem. Secondly, we have the reduced frequency

$$F_{red} = \frac{U_{bar}}{P_{bar}} \frac{c}{V_{2,is}}, \tag{4.2}$$

which reveals more about the periodic behaviour within turbomachinery. Within this work the pitch between the two bars was set to $P_{bar} = P_{blade}/2 = 0.4995$. Both parameters contribute to the unsteadiness, wake mixing and turbulence levels in the low-pressure turbine cascade.

Based on the study of Michelassi et al. (2016) the flow coefficient and the reduced frequency were set to $\Phi = 1.7$ and $F_{red} = 0.6$, respectively. For configurations with bar counts of two or less, distinct wakes enter the cascade passage with almost no wake mixing prior to the leading edge of the turbine blade. Furthermore, two wake generating bars (rather than one bar) were chosen to give the advantage of a lower wake passing time, which reduces the simulation time needed for gathering time-averaged statistical data. Given these parameters, an equivalent background turbulence level, due to the wake mixing within the blade passage, of $Tu \approx 5\%$ was found.

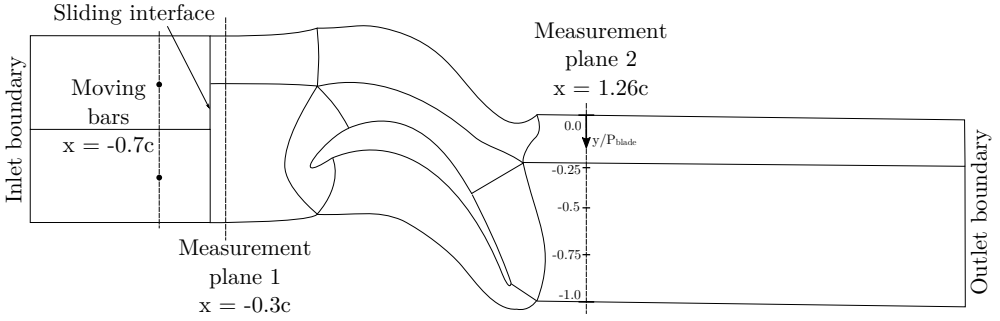

FIGURE 4.1: Setup of the linear low-pressure turbine with two wake generating bars upstream.

In order to establish wakes with different profiles and intensities, the bars rotate around their axis with different rotation rates. The rotation rate

$$\alpha = \frac{\omega D}{2U_\infty} \tag{4.3}$$

is defined by the angular velocity ω, the bar diameter D and the free stream velocity U_∞. In the following, the simulation cases are denoted by R_a with $a \in \mathbb{R}$. $a = 0$ denotes the non-rotating bar setups, which are commonly used in the experimental and numerical works throughout the literature. The bars for cases with $a \neq 0$ rotate in the counter-clockwise direction if positive and in the clockwise direction if negative, with a tangential velocity of $u_t = a \cdot U_\infty$. Counter-clockwise rotating bars correspond more closely to the LPT configuration, creating a lift force, owing to the Magnus effect, that points in the opposite direction relative to the blade motion. A clockwise rotation setup was simulated as well in order to provide a range of different wake properties.

Additionally, a simulation without upstream bars was carried out, serving as a reference case. Validation cases for the boundary data immersion method of isolated rotating cylinders cases at low Reynolds numbers are given in the appendix A.2.

Table 4.2 shows a summary of all simulated cases, which, in the following, are referred to by the notation given in the reference column. For the spatial discretisation two different schemes, the standard central difference scheme and the compact scheme (see section 2.1.2), were used in order to draw a comparison and to see possible differences. Additionally, a case with body-fitted bars was simulated to highlight the differences between the immersed boundary scheme and a fully resolved wall. The previously mentioned Poisson grid generator was used in order to generate the bar grids, resulting in a setup with 27 blocks in total. The $2D$ plane has 189,992 nodes, resulting in 12,539,472 points for the 3D simulations; also based on 32 Fourier modes in spanwise direction.

Table 4.2: Summary of the simulation cases

Method	**Scheme**	**Rotation Rate α**	**Reference**
No wakes	Compact	-	R_{ref}
Discrete Forcing	Standard	0.0	$R_{0s,FF}$
BDIM	Compact	-1.0, 0.0, 1.0, 1.0	R_{-1}, R_0, R_1, $R_{1,corr.}$
	Standard	0.0, 0.5, 1.0, 2.0	R_{0s}, R_{05s}, R_{1s}, R_{2s}
Body-fitted	Compact	0.0	$R_{0,bf}$

4.1.1 Validation of the Boundary Data Immersion Method

In this section the boundary data immersion method, used with both numerical schemes (R_{0s} and R_0), is validated with results of simulations by Michelassi et al. (2016), who used the feedback forcing method of Goldstein et al. (1993b) for representing the wake generating bars ($R_{0s,FF}$), and the body-fitted case $R_{0,bf}$. Only the non-rotating configurations were used for the validation. At the inlet boundary, the inflow angle amounts to 46.05° and was kept constant for the simulations.

Figure 4.2 shows the bar wake data for the different cases obtained at position $x_{bar} = -0.5c$. The wakes show a similar level of turbulent kinetic energy, apart from the compact BDIM case, which produces slightly higher peak values. When looking at the velocity deficit $U_{def} = u(y) - U_\infty$, it can been seen that the feedback forcing method compares best to the body-fitted case, whereas the cases R_0 and R_{0s} show a slightly lower and a slightly larger deficit, respectively. The same can be observed for the spanwise vorticity component, ω_z.

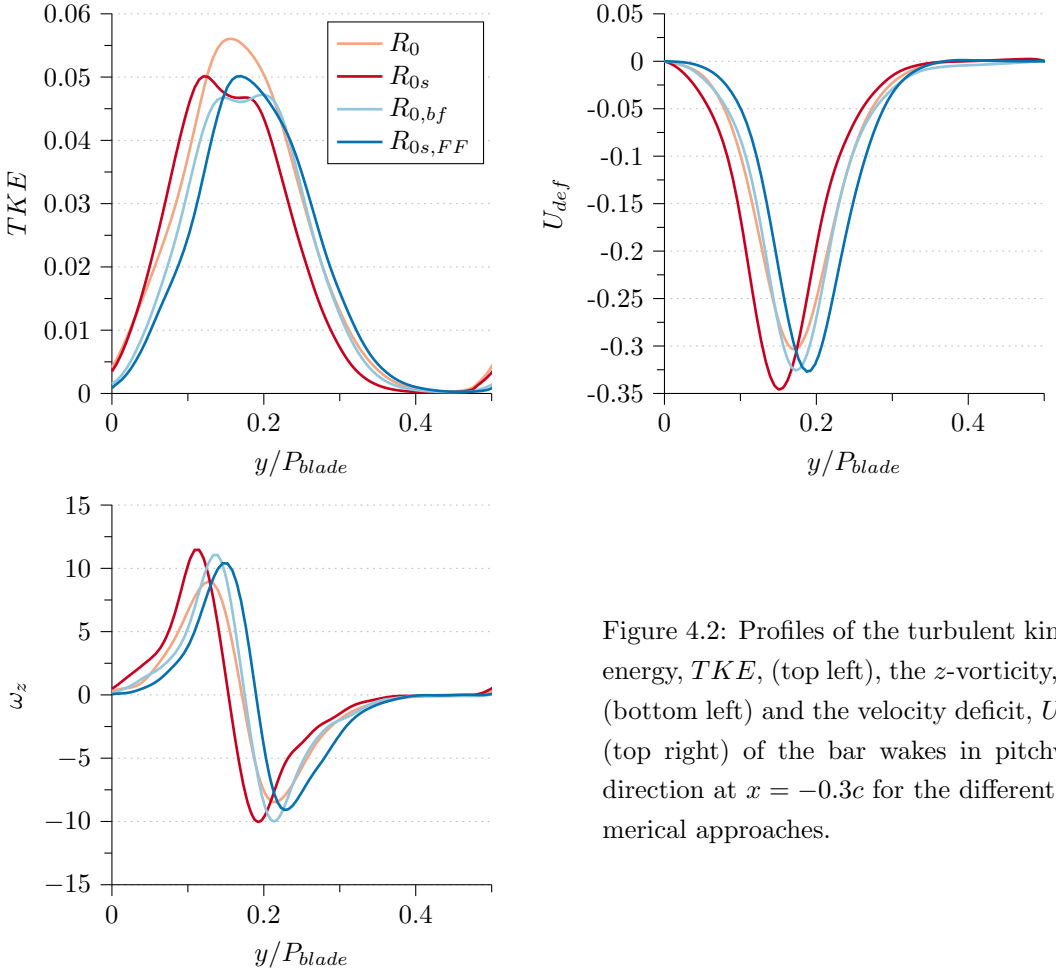

Figure 4.2: Profiles of the turbulent kinetic energy, TKE, (top left), the z-vorticity, ω_z, (bottom left) and the velocity deficit, U_{def}, (top right) of the bar wakes in pitchwise direction at $x = -0.3c$ for the different numerical approaches.

In order to see possible differences with regard to the cascade blade downstream, the pressure coefficient C_p is depicted in figure 4.3.

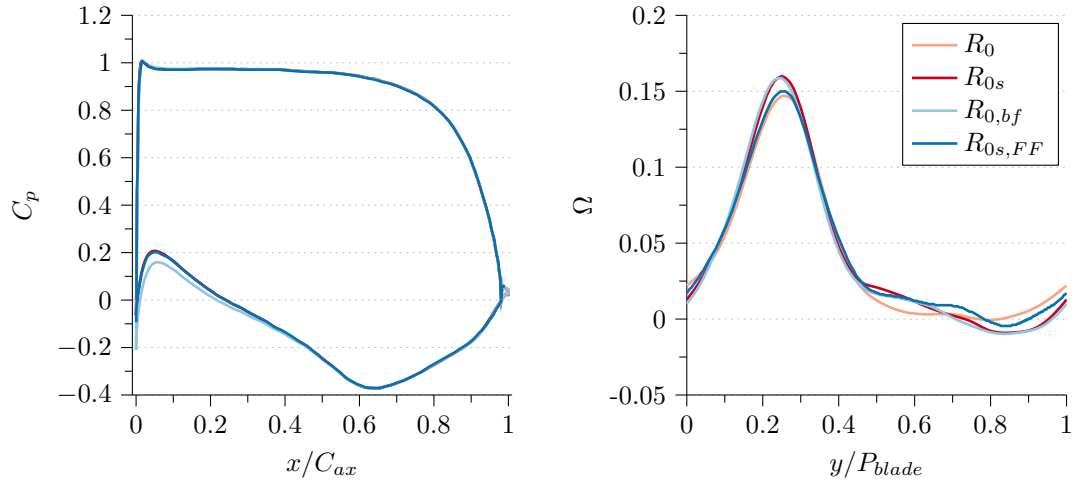

FIGURE 4.3: Pressure coefficient C_p (left) of the four non-rotating bar cases and kinetic loss profile Ω (right) at $x = 1.26c$.

Interestingly, the only case that does not match with the other cases is the body-fitted one; even though the wakes of $R_{0s,FF}$ and $R_{0,bf}$ match best. However, a marked difference can only be observed on the pressure side close to the blade's leading edge. This might be due to the somewhat increased angle of attack α_1 of the blade, as listed in table 4.3. Furthermore, the isentropic Reynolds and Mach numbers obtained at 'Measurement plane 2' as well as the outlet angles α_2 ('Measurement plane 2') are shown. A measure of loss, namely the mixed out loss ω_M (Prasad 2005) is also listed and is defined by

$$\omega_M = \frac{p_{t,1,M} - p_{t,2,M}}{p_{t,1,M} - p_{2,M}}, \tag{4.4}$$

where M denotes flow variables at a mixed-out state, i.e. a state of complete equilibrium.

TABLE 4.3: Summary of the results for the cases without rotating bars.

	$Re_{is,2}$	$M_{is,2}$	$\alpha_1[^\circ]$	$\alpha_2[^\circ]$	ω_M
R_{0s}	$\approx 98,000$	0.4059	42.91	-63.44	0.04085
R_0	$\approx 98,000$	0.4058	42.89	-63.45	0.04039
$R_{0,bf}$	$\approx 98,000$	0.4069	43.36	-63.50	0.04255
$R_{0s,FF}$	$\approx 98,000$	0.4030	43.00	-63.44	0.04536

As can be seen, the isentropic Reynolds and Mach numbers $Re_{is,2}$ and $M_{is,2}$, respectively, approximate the expected values mentioned earlier and do not vary much for the different cases. Also almost no differences in the in- and outflow angles of the blade can be observed. On the contrary, marked variations in the mixed out losses are clearly evident. For the case with the feedback forcing method, the loss is much higher compared to the body-fitted and especially for the BDIM cases.

Another measure of loss is the so called total pressure loss or kinetic loss profile Ω, which is defined by

$$\Omega = \frac{p_{t,1} - p_{t,2}(y)}{p_{t,1} - p_2}, \tag{4.5}$$

where $p_{t,1}$ and p_2 are the mass averaged stagnation and static pressure, respectively, and $p_{t,2}(y)$ is the stagnation pressure along the non-dimensional pitchwise direction y/P_{blade} at "Measurement plane 2". The results for the 4 cases are shown in figure 4.3 (right), where the portion on the left side of the peak corresponds to the suction side of the blade and the right side portion to the pressure side. The profiles of the standard scheme case R_{0s} and the body-fitted case $R_{0,bf}$ fit quite well and show a higher stagnation pressure defect at the peak compared to the other two cases. Apart from that, R_0 gives the lowest defect on the pressure side part, whereas there are no major differences for the other simulations. However, the profile of the feedback forcing method configuration starts departing in the suction part resulting in higher losses. Here, the BDIM together with the compact scheme show the highest defect. The negative values for Ω can be attributed to changing inlet values in the pitch-wise direction caused by the bars, as was shown by Leggett et al. (2018).

In figure 4.4 the phase-lock averaged skin friction on the suction side is presented, where the white spots indicate separated flow. Twelve phases per bar passing period were gathered and then averaged over 15 flow-through times. The results of the $R_{0s,FF}$ case can be found in

(Michelassi et al. 2015). The main differences are slightly different separation bubble sizes and the duration of reattachment per period. Another detail to point out is the marginally lower skin friction in the fore- to mid-portion of the blade for the body-fitted case (right).

Even though there are some differences between the BDIM cases and the feedback forcing method as well as the body-fitted case, it is not clear whether the results can be assessed as better or worse, especially as there is an additional dependency on the numerical discretisation scheme that is used. The main advantage of the boundary data immersion method over the feedback forcing method is that there is no additional timestep constraint. For large simulations this is paramount and the timestep can be solely chosen based on the grid resolution of the blade. The same holds true for the body-fitted case. Additionally, the BDIM is more flexible and convenient with regards to geometry alterations, e.g. changes in diameter, and to the computational setup, as the body-fitted case requires a cascade like grid per bar. Therefore, the BDIM was used for the simulations that are presented in the following sections. As to the differences between the numerical discretisation schemes, more simulations were conducted with both the compact and the standard scheme and a final assessment is made in the following section.

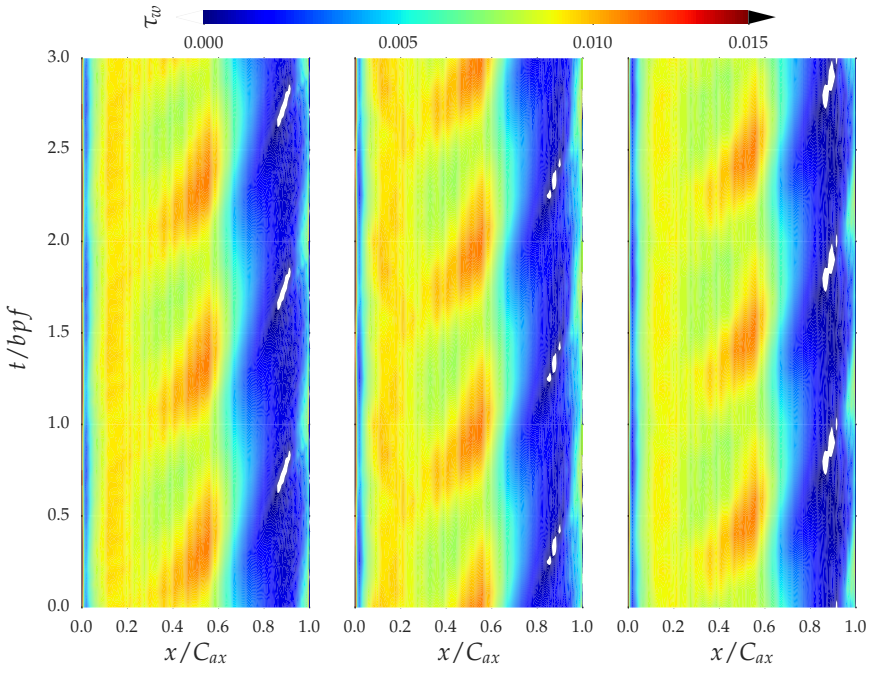

FIGURE 4.4: Phase-locked averaged skin friction on the suction surface of the blade; Left: R_0; Middle: R_{0s}; Right: $R_{0,bf}$

4.2 Rotating Bar Wakes

As already mentioned in section 1.3, the question is whether it is possible to compute wakes that better resemble the wake of an actual turbine blade - here a T106A - by means of a rotating bar, which creates circulation due to the Magnus effect.

In this section, the results of the bar wakes for all cases are presented and discussed. After that the wakes of the bars are compared to an actual blade wake. Firstly, the wake extraction process

- along the wake centre lines - at different downstream positions is briefly explained. Then the wake shapes and development are compared to a turbine blade wake. In the conclusion section a final assessment of the two numerical discretisation schemes is made.

4.2.1 General Considerations: Flow Turning

Before jumping to the comparison between the bar wakes and an actual blade wake the focus in this section is on the general considerations that are needed for the following sections. When applying rotating bars to the cascade setup the flow that enters the cascade passage is altered due to flow turning. However, in order to make a meaningful comparison between different incoming wake profiles it must be ensured that

1. the angle of attack of the blade, α_1, and
2. the mass flow rate, $\dot{m}$,

are approximately the same for all cases.

In order to see the effect of the flow turning, the domain inflow angle, before the bars, was set to $\theta = 46.05°$ except for cases R_{ref}, $R_{1,corr.}$ and R_{-1}, where Θ was adjusted in order to account for the flow turning and to achieve similar angle of attack values. The results are listed in table 4.4 and as can be observed, owing to the rotation of the bars, the wakes are deflected and thus the velocity triangles upstream of the cascade changes; see angle of attack, α_1.

TABLE 4.4: Results of the angle of attack, the drag and lift coefficients as well as the mixed out loss of the rotating bars.

	R_{ref}	R_0	R_{0s}	R_{05s}	R_1	R_{1s}	R_{2s}	$R_{1,corr.}$	R_{-1}
α_1	43.04	42.91	42.89	44.06	46.53	45.68	48.58	42.64	42.76
C_D	-	0.728	0.687	1.236	2.166	2.005	3.588	2.205	-0.412
C_L	-	1.041	1.061	0.594	-0.338	-0.024	-1.072	-0.636	1.664
$C_{D,\zeta}$	-	1.271	1.264	1.166	0.832	1.033	0.870	0.684	1.224
$C_{L,\eta}$	-	-0.042	0.005	-0.723	-2.028	-1.719	-3.643	-2.191	1.200
ω_M	-	0.1317	0.1298	0.1214	0.0936	0.1090	0.1012	0.0748	0.1434

Additionally, the drag, C_D, and lift, C_L, coefficients in the streamwise and the pitchwise direction, respectively, are shown. By means of the rotation matrix

$$A_\phi = \begin{bmatrix} \cos[\phi(s)] & -\sin[\phi(s)] & 0 \\ \sin[\phi(s)] & \cos[\phi(s)] & 0 \\ 0 & 0 & 1 \end{bmatrix} \tag{4.6}$$

the drag and lift coefficients in the flow direction $C_{D,\zeta}$ and $C_{L,\eta}$ are calculated. As can be seen, the drag and lift coefficients of the non-rotating bar cases are very similar. For increasing rotation rates in counter-clockwise direction both the streamwise drag and α_1 increase as well. The lift coefficient, on the other hand, decreases and eventually changes sign for the two highest rotation rates.

Looking at the drag and lift coefficients in the rotated coordinate system, $C_{D,\zeta}$ and $C_{L,\eta}$, respectively, one sees the same results and trends as were already observed for the $2D$ rotating cylinder validation cases in section A.2.1. Having large changes in the lift for increasing rotation rates, the drag shows much more moderate changes. Furthermore, by setting the bars into rotation the mixed out losses ω_M are reduced, which might be due to the lower shedding frequency and the narrowing of the wakes. The mixed out losses also show a strong correlation with the drag coefficients.

In order to account for the deflection for cases R_{ref}, $R_{1,corr.}$ and R_{-1} with the compact scheme, the velocity component in pitchwise direction, V_{pitch}, was changed in order to achieve the same cascade inflow angle, α_1, as for the non-rotating bar configurations. The streamwise velocity component, V_{ax}, was kept the same in order to maintain the same mass flow rate, flow coefficient and reduced frequency. This resulted in very similar angle of attacks for these cases, as can be seen by the grey-shaded entries in table 4.4. Here R_{ref} is the reference case without bars, $R_{1,corr.}$ has counter-clockwise rotating bars and the bars for case R_{-1} rotate in clockwise direction. For case $R_{1,corr.}$ a reduction of drag, $C_{D,\zeta}$, and mixed out losses compared to the uncorrected case R_1 can be observed. The reason for this is the lower absolute velocity - in the bar reference frame - as the streamwise velocity component was not altered to keep a constant mass flow rate. The opposite is true for case R_{-1}.

The reduction in losses and the narrowing can also be observed from the kinetic loss profiles shown in figure 4.5 for the standard and compact scheme cases. The profiles were extracted $0.2c$ ($10D$) downstream of the centre of the bars in pitchwise direction. Here the deflection of the wakes, leading to different α_1 values due to the rotation is apparent.

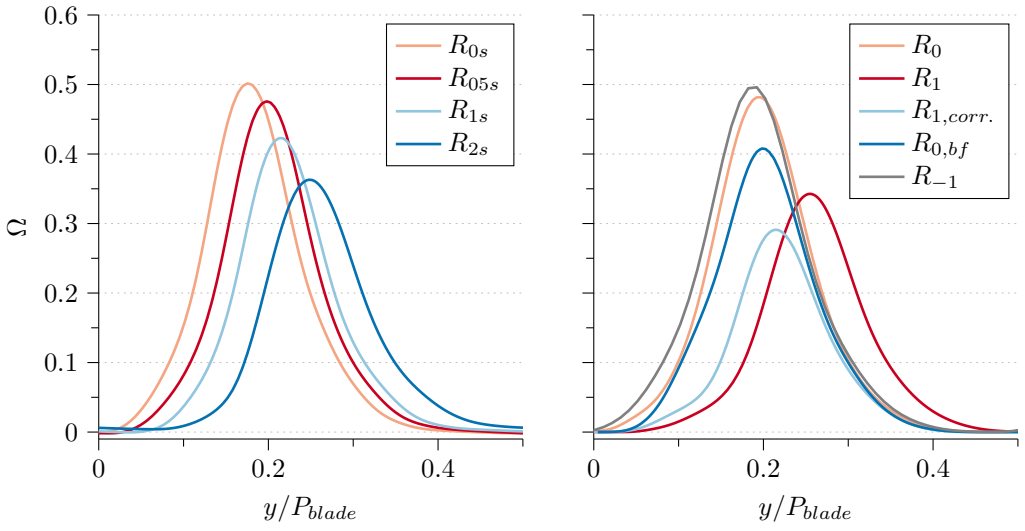

FIGURE 4.5: Kinetic loss profiles, Ω, of the standard (left) and the compact (right) scheme cases at $0.2c$ downstream of the rotating bars.

Thus, for the investigation of the effect of different wakes on a low-pressure turbine cascade it is paramount to take the flow turning due to the rotation into account. However, this does not affect the comparison of the bar wakes with an actual blade wake, as a different reference frame is used, which is explained in more detail in the next subsection.

4.2.2 Comparison with a T106A Blade Wake

In this section the different bar wakes for the boundary data immersion method, given in table 4.2, are compared to an actual blade wake. As mentioned above, the deflection due to the rotation does not matter for this comparison. The differences between the bar wakes and the actual blade wake are first shown by means of time-averaged statistics. In order to do so, wake profile data perpendicular to the wake centre lines at three different positions $5.5D$ ($6.0D$), $11D$ ($11D$) and $16.5D$ ($17D$), based on the bar diameter D, downstream of the bars and blade, were extracted, see figure 4.6; with positions for the standard scheme given in the brackets. The centre of the extracted lines were determined by the peak velocity deficit locations in the wakes. Flow axes x_ζ and x_η denote the streamwise and pitchwise direction in the bar reference frame, respectively. Moreover, the results were split up for the standard scheme and the compact scheme in the following. Based on the findings, a brief note on why the compact scheme was preferred is given at the end.

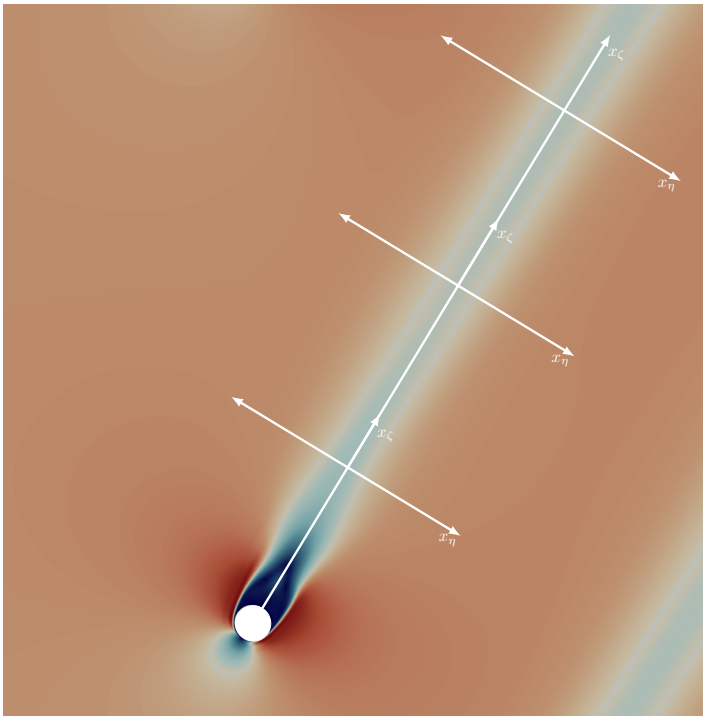

FIGURE 4.6: Wake extraction positions $5.5D$ ($6.0D$), $11D$ ($11D$) and $16.5D$ ($17D$).

4.2.2.1 Compact Scheme

The turbulent kinetic energy, TKE (top) and the velocity deficit, U_{def} (bottom) profiles for the three different positions are shown in figure 4.7.

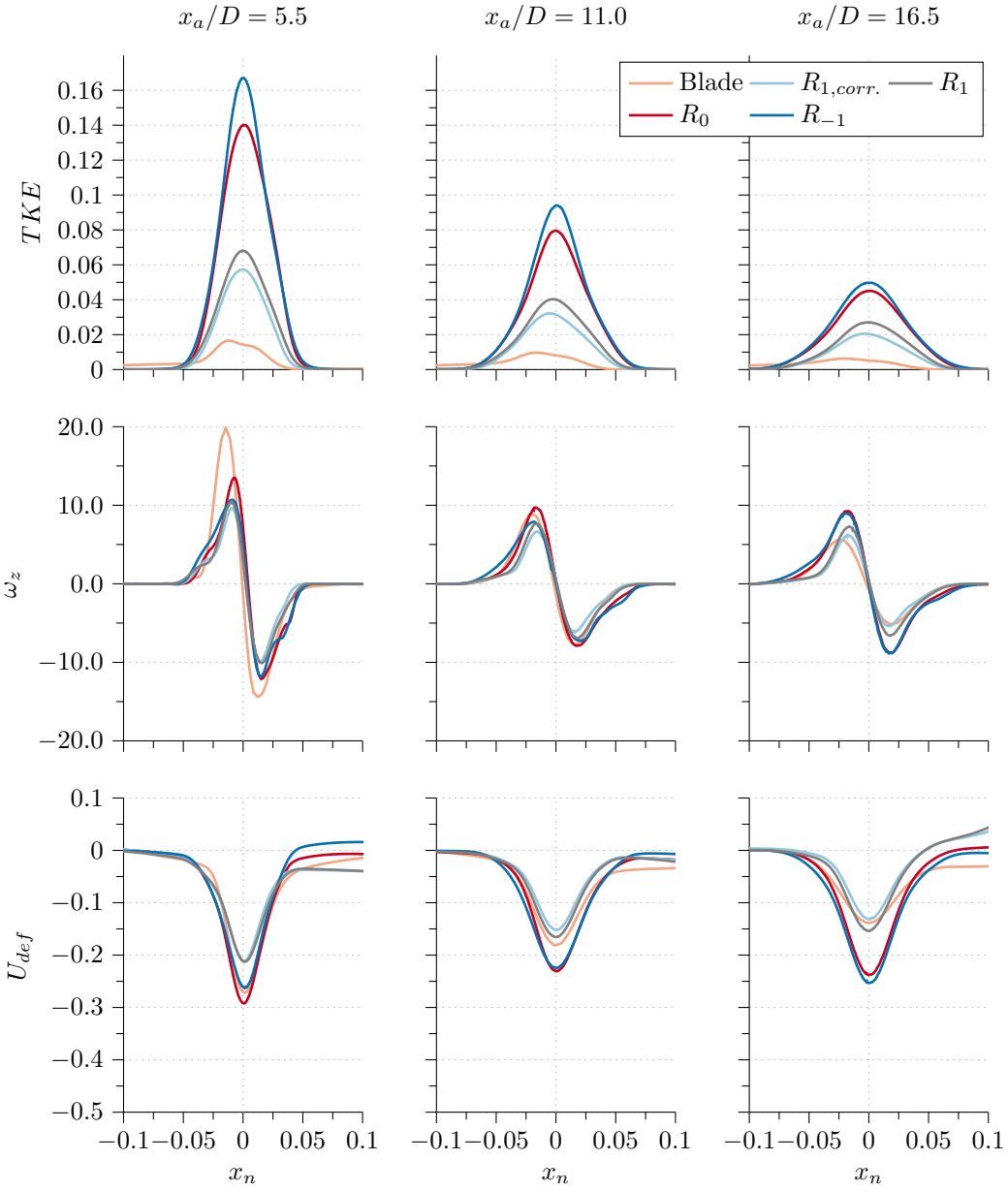

FIGURE 4.7: Comparison of the normalised turbulent kinetic energy, TKE, (top), the z-vorticity, ω_z, (middle) and the velocity deficit, U_{def}, (bottom) of the bar and blade wakes for different downstream positions. x_a and x_n denote the axes parallel and perpendicular to the wakes, respectively. The non-rotating bar case is denoted by R_0, the counter-clockwise rotating bar cases by R_1 and $R_{1,corr.}$, the clockwise rotating bar case by R_{-1} and the wake of a low pressure turbine (LPT) blade by 'Blade'.

These quantities were normalised by u_{ref}^2 and u_{ref}, respectively, with the local velocity, u_{ref} obtained outside the wakes. A fairly rapid mixing of all the wakes, indicated by the decreasing TKE and widening of the profiles while moving downstream, is evident. The clockwise rotating bars, R_{-1}, generate wakes with the highest levels of turbulent kinetic energy, followed by the stationary bar case. Slightly skewed and much weaker wake profiles are achieved by the counter-clockwise rotating bars, which are more similar in shape to an actual blade wake. However, the turbulent kinetic energy is still a factor of three higher. The fact that the bars generate

much higher levels of turbulent kinetic energy is in agreement with the experimental findings of Halstead et al. (1997b, p. 442).

The different wake profiles, in the rotating bar cases, at a given position can also be seen as a change in distance to the given position with respect to a non-rotating bar setup. For example, in order to obtain similar TKE values for cases R_0 (non-rotating bars) and $R_{1,corr.}$ (rotating bars) at position a fixed position, the bars in case R_0 would have to be either located much further upstream in order to give the wakes more time to dissipate or the measurement position would have to be moved further downstream. This means that the lower the given values of TKE at a particular position, the larger the distance or "gap" size if one were to use non-rotating bars.

The velocity deficits of the bar wake profiles, aligned at point $x_n = -0.1$, for the cases R_0 and R_{-1} are quite similar for all three downstream positions. In the R_1 case, the amplitude of the velocity deficit is markedly lower and decays in a similar manner to the blade wake. Interestingly, the profiles of the bar wakes compare better to the blade wake profiles, as opposed to the TKE profiles.

4.2.2.2 Standard Scheme

The different profiles for the standard scheme cases are depicted in figure 4.8. The first thing that can be seen is that by increasing the rotation rate the velocity deficit reduces. This is apparent especially for the R_{2s} case. Compared to the blade wake (blue) this rotation case comes closest, but does not quite match the growth rate.

The same can be observed in the vorticity plot. The kinks in the profiles are due to the sliding interface, as the profiles further downstream partly reach over the domain boundary. Interestingly, some similarities between the blade wake and the R_{2s} are the shape - especially for the downstream position $x/D = 6$ at around $x_\eta = -0.05$ - and the asymmetry, which is indicated by the different magnitudes of the positive and the negative peaks of the profile.

Again, figure 4.8 reveals that the bars create wakes with much more turbulent kinetic energy than the blade.

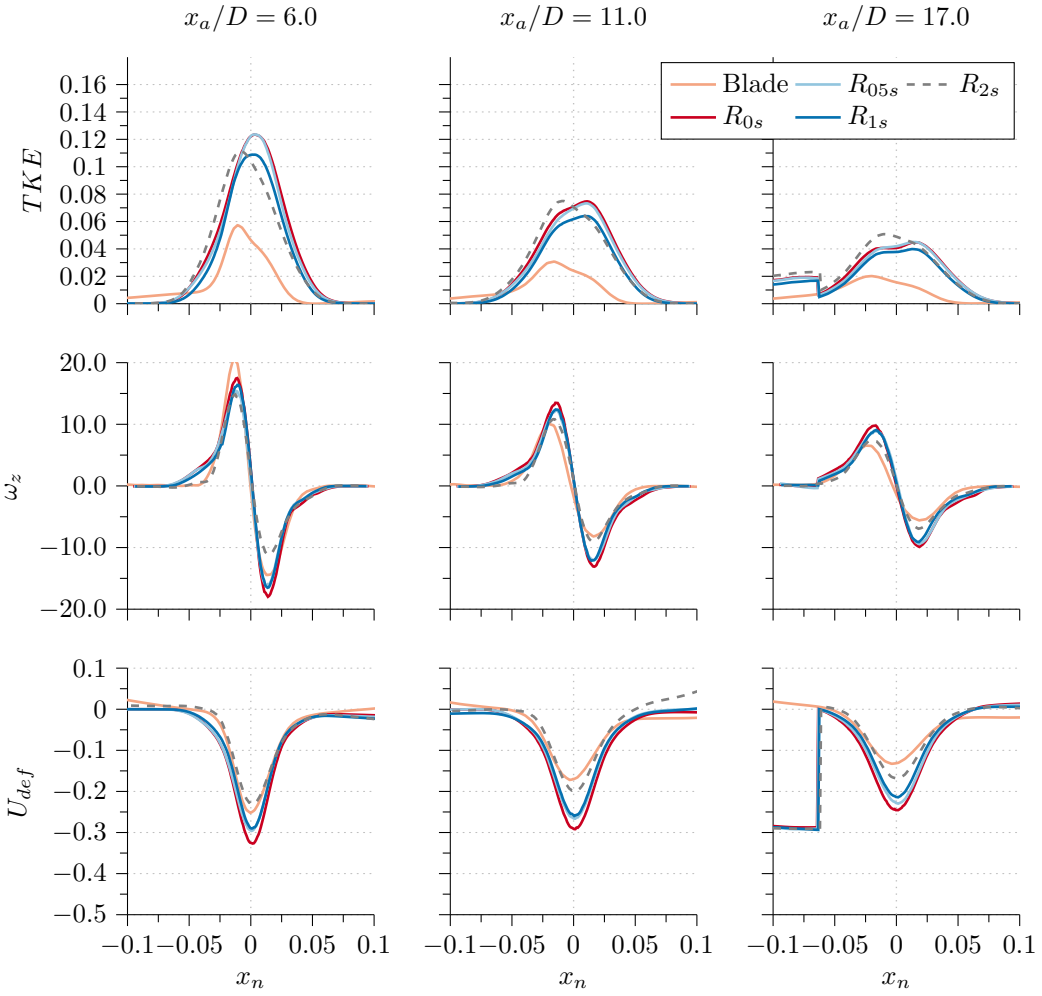

FIGURE 4.8: Comparison of the normalised turbulent kinetic energy, TKE, (top), the z-vorticity, ω_z, (middle) and the velocity deficit, U_{def}, (bottom) of the bar and blade wakes for different downstream positions. x_a and x_n denote the axes parallel and perpendicular to the wakes, respectively. The non-rotating bar case is denoted by R_{0s}, the different counter-clockwise rotating bar cases by R_{05s}, R_{1s} and R_{2s} and the wake of a low pressure turbine (LPT) blade by Blade.

However, the TKE profile shape itself of the R_{2s} case shows a remarkable resemblance compared to the blade wake.

4.2.2.3 Conclusions

Given the results from the previous sections, no conclusive assessment between the standard and the compact scheme can be made. However, due to the fact that the compact scheme theoretically has a lower numerical dissipation and dispersion error, see section 2.1.2, this scheme was used for the remainder of this work. Furthermore, only the cases with the adjusted angle of attack, α_1, given in table 4.4 in the gray coloured cells were considered. Case $R_{1,corr.}$ was renamed to R_1 for the following sections.

4.3 Effect of Different Wakes on the Low-Pressure Turbine

In this section the effects of the different bar wake profiles on the linear low-pressure turbine cascade are investigated. As mentioned in the literature review in chapter 1, the state of the blade wakes is dependent on the state of the boundary layers, which in turn are influenced by the bar wakes passing through the blade passage. A mutual dependence between the bar wakes and the blade wakes is the result, which will be investigated more deeply in the following sections. In order to do so, firstly, the influence of the bar wakes on the blade itself is presented. After that, the combined effects of the merged blade and bar wakes in terms of loss quantification are examined. Lastly, the question whether simple bars, by using the Magnus effect, show similar trends to a full turbine stage regarding different gap sizes is answered.

Both time and phase-locked averaged statistics were gathered in order to investigate the flow field. All simulations were restarted based on an initial simulation and then run for more than 15 non-dimensional time units in order to go past the transient, where one non-dimensional time unit corresponds to the time it takes for the flow with unit velocity to convect over one chord length, c. After that, data over another 16 non-dimensional time units were collected for the averaged statistics. The periodicity in the spanwise direction allowed for a spatial averaging in this direction while the simulation was running, reducing the costs for I/O. The already spatially averaged data were then averaged over time.

For the phase-locked averaging, each bar passing period, defined by

$$T = \frac{P_{blade}}{n_{bar} U_{bar}}, \tag{4.7}$$

with the bar count n_{bar}, was divided into 24 phases and each phase was then averaged over 16 bar passing periods T.

4.3.1 Effect on the Boundary Layer

Table 4.5 shows the cases with the correction angle α_{inlet} that was needed in order to compensate the flow turning and establish a constant angle of attack α_1. This also ensured that the same turbine conditions, determined by the isentropic Reynolds, $Re_{is,2}$ and Mach numbers, $M_{is,2}$, could be achieved. Hence, the differences shown in the results section can be solely attributed to the different bar wake properties. As can be seen, the correction only has a small effect on the bar Reynolds number, Re_{bar}.

TABLE 4.5: Resulting low-pressure turbine flow conditions.

	$Re_{is,2}$	$M_{is,2}$	Re_{bar}	$\alpha_1(°)$	$\alpha_{inlet}(°)$	$C_{D,\zeta}$	$C_{L,\eta}$	ω_M
R_{ref}	≈98,000	0.4074	-	43.04	40.00	-	-	0.0001
R_0	≈98,000	0.4059	1663	42.91	46.05	1.5503	−0.0914	0.1317
R_1	≈98,000	0.4074	1714	42.64	37.45	0.9307	−2.8347	0.0748
R_{-1}	≈98,000	0.4053	1545	42.76	50.15	1.6730	1.6400	0.1434

Isentropic Reynolds number $Re_{is,2}$, isentropic Mach number $M_{is,2}$, bar Reynolds number Re_{bar}, angle of attack α_1, flow correction angle, α_{inlet}, at the domain inlet, drag $C_{D,\zeta}$ and lift $C_{L,\eta}$ coefficients, mixed out loss ω_M

The drag, $C_{D,\zeta}$, and lift, $C_{L,\eta}$, coefficients will allow us later to check whether the drag coefficient is a reliable parameter as a design criterion for bars.

Phase-locked averaged results enable the tracking of the wakes passing through the cascade at different time instants. As already mentioned, one bar passing period was divided into 24 phases, which were averaged over a total of 16 periods. The phase-lock averaged turbulent kinetic energy, TKE, for the three different bar wakes at two different phases is shown in Figure 4.9.

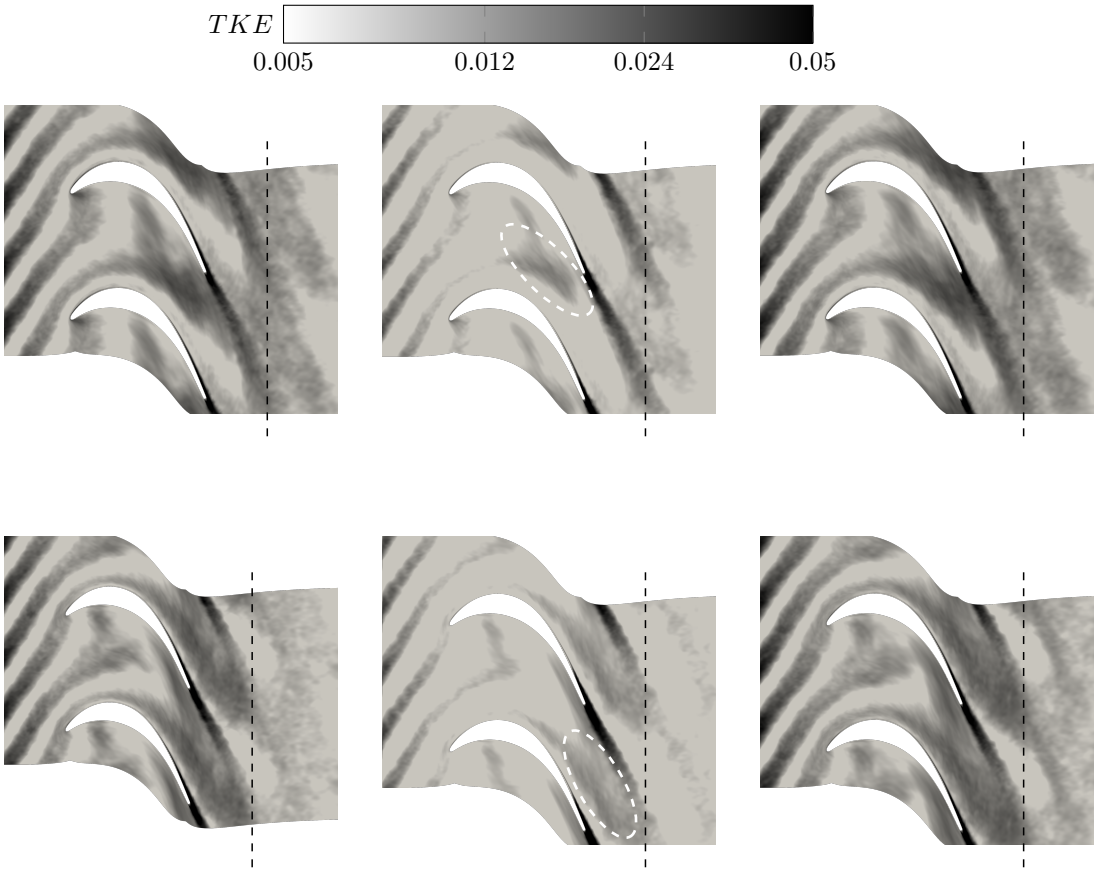

FIGURE 4.9: Phase-lock averaged turbulent kinetic energy (TKE) at different phases for the non-rotating bar case R_0 (**a**,**d**), the counter-clockwise rotating bar case R_1 (**b**,**e**) and the clockwise rotating bar case R_{-1} (**c**,**f**).

As can be seen, the wakes of the cases R_0 (a,d) and R_{-1} (c,f) passing through the turbine passage are much more pronounced than the wake of case R_1 (b,e). The typical wake distortion, as described by Smith (1966), and an increase in turbulent kinetic energy in the passing wake close to the suction surface, as observed by other authors (Michelassi et al. 2003; Stieger and Hodson 2005), were apparent for all cases. Furthermore, the levels of TKE of the blade wakes are substantially higher compared to the bar wakes, but merge with them further downstream.

Given a clearer picture of the strength and development of the incoming wakes, the effect on the blade can now be examined. Time-averaged plots of the pressure coefficient C_P over the whole blade surface and the wall shear stress τ_w on the suction surface are shown in figure 4.10 (a,c).

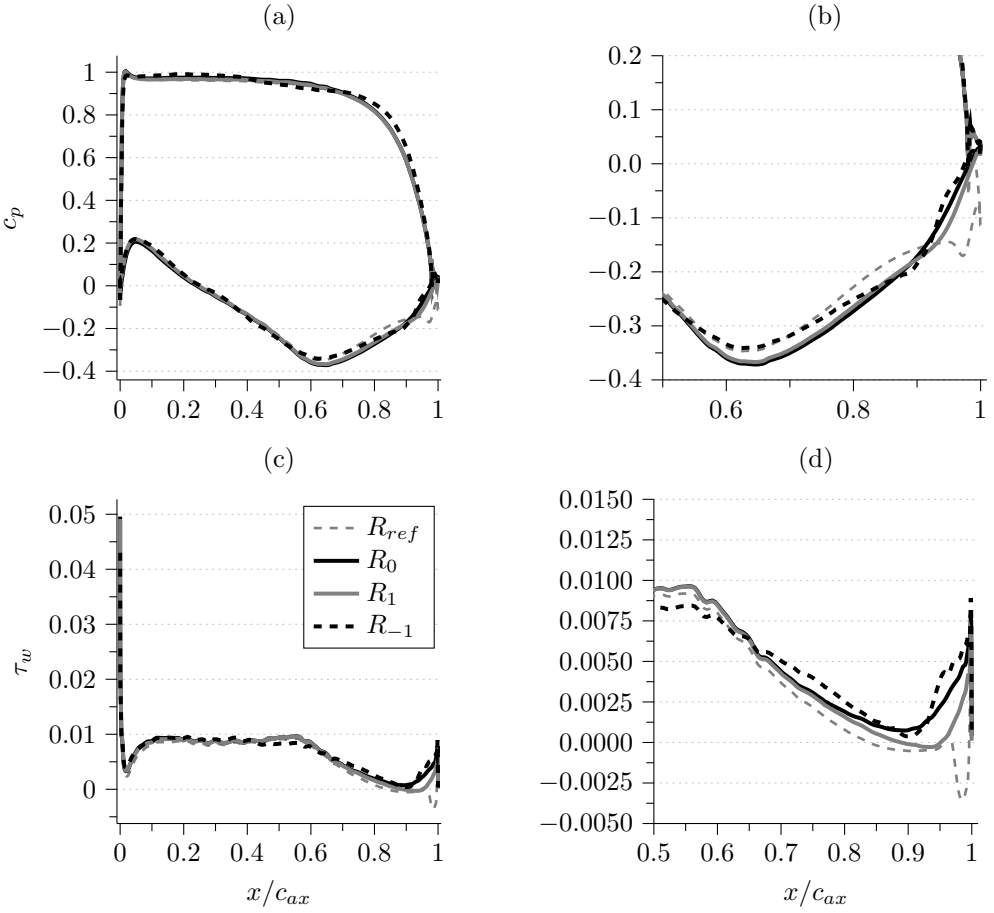

FIGURE 4.10: Comparison of the time-averaged pressure coefficient C_P (a,b) and the wall shear stress τ_w (c,d) for the four cases. With the non-rotating bar case R_0, the counter-clockwise rotating bar case R_1, the clockwise rotating bar case R_{-1} and the reference case R_{ref} without bars.

For all cases, there are virtually no differences in C_P for most of the blade surface. The portion most affected by the bar wakes is restricted to the aft region of the suction surface of the blade. The strongest wakes, case R_{-1}, slightly increase the pressure on both the suction and the pressure surface compared to the other cases. A separation bubble for the R_1 case, which starts at around $x/c_{ax} \approx 0.89$ and reattaches near $x/c_{ax} \approx 0.95$, can be observed (fig. 4.10 (b,d)). The reference case R_{ref} shows a marked difference from $x/c_{ax} \approx 0.58$ up to the trailing edge, indicating an even larger separation bubble.

The wall shear stress, τ_w, on the suction surface is identical for cases R_0 and R_1 up to $x/c_{ax} \approx 0.73$. After that point, τ_w drops for R_1 and goes below zero, but then rapidly recovers. The wall shear stress for the R_{-1} case drops at around $x/c_{ax} \approx 0.4$ and then increases at $x/c_{ax} \approx 0.67$, yielding the highest values. These differences correlate with the strength of the bar wakes, where the strongest wakes R_{-1} produce the highest τ_w due to the mixing with the turbulent boundary layer in the aft portion, whereas the weakest wakes R_1 are not able to prevent the separation bubble. Furthermore, the wall shear stress level for the reference case R_{ref} is marginally lower from the leading edge up to $x/c_{ax} \approx 0.65$. Towards the trailing edge, τ_w is significantly lower compared to the cases with bars, leading to a large separation bubble. This large separation bubble decreases the peak velocity on the blade and hence results in the aforementioned reduction of τ_w before $x/c_{ax} \approx 0.65$. The latter bubble, indicated by a sharp dip in wall shear stress, closes again at the trailing edge. The kink in the C_P and τ_w slopes is caused by an additional small separation region behind the trailing edge.

Phase-locked averaged data are used in order to further investigate the effects on the cascade blade. A space-time diagram of the wall shear stress on the suction surface along the blade surface s, normalised by the total suction surface length S, for three bar-passing periods t/T is shown in figure 4.11. Additionally, the time-averaged free stream velocities are plotted on top of the contours, where the peak velocity is aligned with the peak τ_w location at $s/S \approx 0.4$. The white spots denote wall shear stress levels below zero, i.e. flow separation. Qualitatively, the cases with bars are fairly similar for the majority of the blade, as already observed for the time-averaged results. The wall shear stress levels at the mid-chord, where the wakes hit the blade surface, seem to be slightly lower for case R_1. This is consistent with the experimental results of Halstead et al. (1997b), who found increasing levels of wall shear stress for stronger wakes impinging on the blade. However, as already observed in figure 4.10, the wakes in case R_{-1} cause slightly lower stress levels compared to case R_0 in the mid-chord region.

Looking at the aft section of the blade, a large separation bubble for most of the time period can be observed for R_1. The size, the start and end point, as well as the duration of the bubbles markedly vary over the bar passing periods. At some time instants, two distinct separation bubbles occur. In the case of R_0, the size and the duration of the bubbles are substantially reduced. For case R_{-1}, the separation bubbles are almost completely suppressed. Owing to the absence of incoming wakes, the reference case R_{ref} does not show much variation over time, although there is clearly unsteadiness. Looking at a highly resolved time signal close to the bubble, the frequency and period of this unsteadiness could be calculated, yielding $f = 6.9531/T$ and $0.144T$, respectively. The values correspond to the vortex shedding frequency at the trailing edge and do not necessarily correlate with the frequencies of the instabilities that eventually lead to transition, as was also found by Wheeler et al. (2016), although for a high-pressure turbine blade.

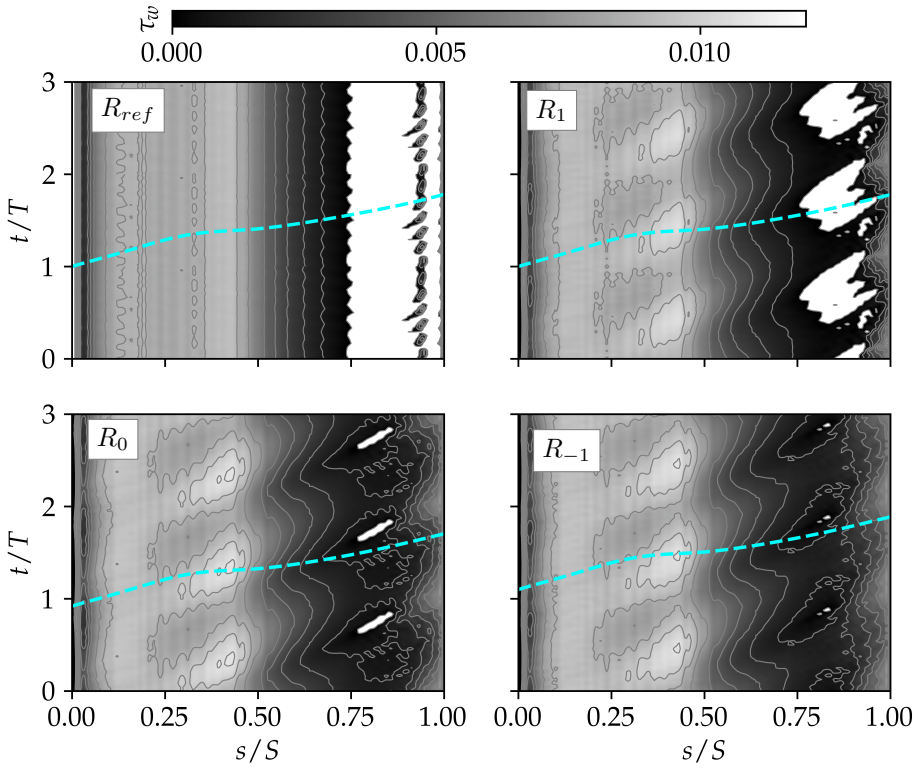

FIGURE 4.11: Space-time diagram of the suction side wall shear stress τ_w along the streamwise direction for three bar passing periods, for cases R_{ref} (no bars), R_1 (counter-clockwise), R_0 (non-rotating) and R_{-1} (clockwise).

The reason for the larger separation bubble for case R_1 can be explained by looking at the incoming wakes passing through the blade passage; see figure 4.9. Due to the sensitivity of the separated flow to inflow disturbances, like incoming wakes, the weaker wakes of the R_1 case seem to be less effective at reducing the size of the bubble, whereas the wakes for case R_{-1}, which have the highest TKE levels, are most effective. As can be seen, this results in larger calmed regions, yielding a reduced separation bubble. This is also consistent with the experimental results of Halstead et al. (1997b) and the simulation results of Sarkar (2009).

As the size of the separation bubble is related to the loss generation (Coull and Hodson 2011), the largest overall loss values are to be expected from the reference case R_{ref}, whereas the resulting loss values for the bar cases depend on both the incoming wakes and the size of the separation bubble. Furthermore, time varying losses for all cases should be linked to unsteadiness, which was even observed for the case without bars.

4.3.2 Effect on Loss Mechanisms

The total pressure loss profiles (eq. 4.5) for all cases are shown in figure 4.12. The profile peaks, denoting the total pressure loss due to the blade wake, of R_0 and R_{-1} are very similar. The slightly lower peak loss value might be explained by the smaller separation bubble, only observed in the phase-lock averaging, for case R_{-1}. For the bar case with the largest separation bubble, R_0, the peak loss value is the lowest, and the blade wake is slightly shifted, as well. The reference

case shows a significant deflection and widening of the blade wake, which is the result of the large separation bubble. Interestingly, the peak value of Ω is lower than for the bar cases and the total pressure losses are more distributed along the wide wake.

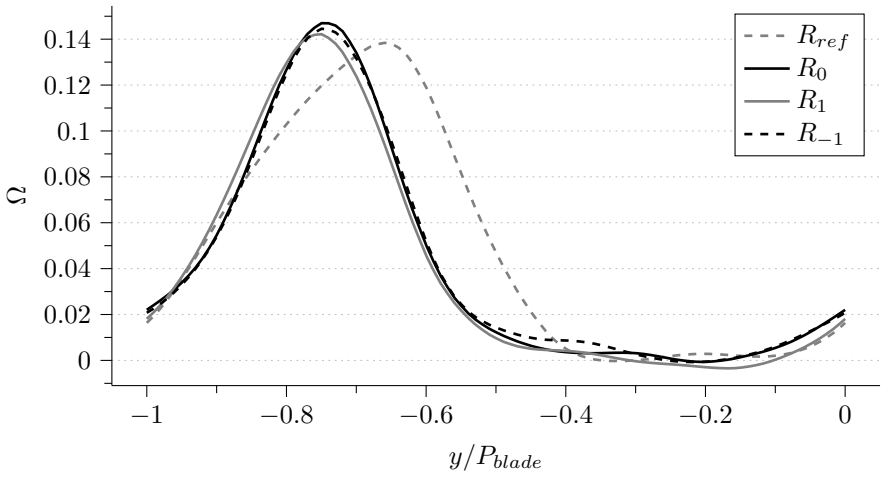

FIGURE 4.12: Time-averaged total pressure loss profile Ω extracted at 'Measurement Plane 2' (1.26c) for cases R_{ref} (no bars), R_1 (counter-clockwise), R_0 (non-rotating) and R_{-1} (clockwise).

The losses in the region of the profile away from the peak values can be attributed to the passing wakes or rather to the losses generated in the turbine passage. At around $y/P_{blade} = -0.4$, the losses are most elevated for case R_{-1} with the clockwise rotating bars, which produced the most pronounced wakes and hence had the strongest wake distortion. For case R_1, with the weakest incoming bar wakes, the smallest amount of pressure loss in the blade passage can be seen. The negative loss between $-0.3 < y/P_{blade} < -0.1$ is due to varying inlet values in the pitch-wise direction caused by the bars (Leggett et al. 2018).

Denton (1993) identified three sources accounting for the overall profile loss, which will be referred to as Denton loss ζ;

$$\zeta = \frac{C_{pb}(\delta^*_{TE} + t_{TE})}{P_{blade}\cos\alpha_2} + \frac{2\theta_{TE}}{P_{blade}\cos\alpha_2} + \left(\frac{\delta^*_{TE} + t_{TE}}{P_{blade}\cos\alpha_2}\right)^2. \tag{4.8}$$

The first term of the right-hand side is the base pressure loss (A) consisting of the base pressure coefficient C_{pb} and the displacement thickness, δ^*_{TE}, at the trailing edge with thickness t_{TE}. The losses due to the momentum and the displacement thickness at the trailing edge are given by the second (B) and the third (C) term, respectively.

The total Denton losses, ζ (D), and the respective terms (A, B and C), the overall mixed-out losses (E; see eq. 4.4) and the wake distortion losses (F^*), where only the part of the profile outside the blade boundary layer is taken into account, are shown in figure 4.13. For the latter, only values less than roughly 10% of the peak total pressure loss of the respective profile were considered.

*not to be confused with the roughness shape function introduced in the previous chapter

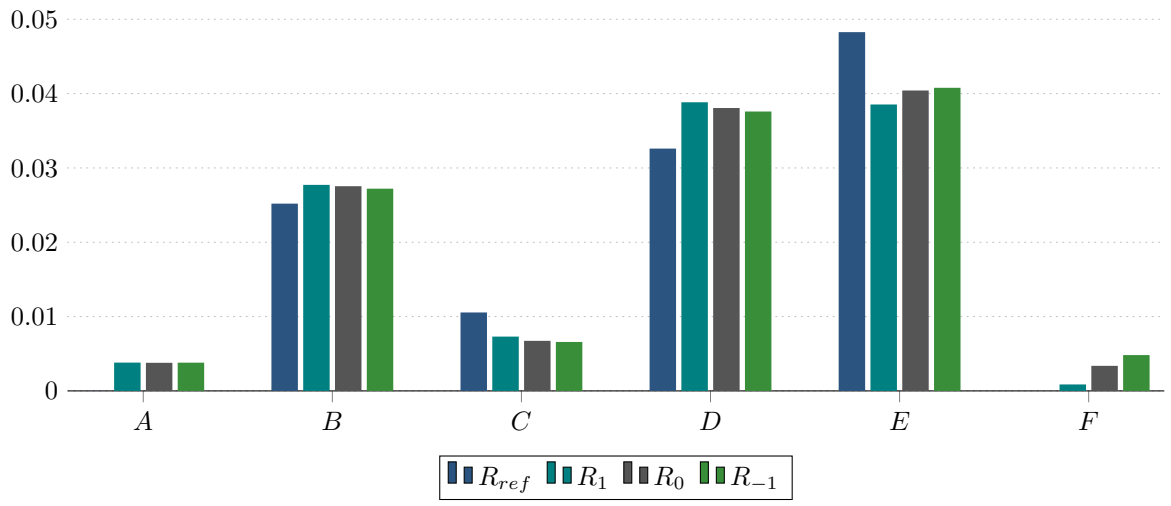

FIGURE 4.13: Denton loss terms, A–D, where $D = A + B + C$, overall mixed-out losses, E, and wake distortion losses, F.

There are no apparent differences in the base pressure losses, A, for the three bar cases. The same observation can be made for the losses due to the momentum thickness, B. Owing to the larger separation bubble and hence a larger displacement thickness for case R_1, the displacement thickness loss term, C, is increased. This is due to blockage effects, leading to a higher overall Denton loss, D, compared to the other cases. For the reference case, a negative base pressure was obtained due to a small second separation region behind the trailing edge. Furthermore, the momentum loss, B, is lower compared to the bar cases. The very large separation bubble causes a marked increase in the displacement loss, C; however, a significantly lower overall Denton loss, D, is achieved.

The highest mixed out loss, E, is produced in the reference case R_{ref}, as was already expected due to the large separation bubble. The bar case R_1, which led to the largest bubble, generated the lowest loss, whereas for case R_{-1} with the almost non-existent separation bubble, the highest loss out of the three bar cases is obtained. Another reason for this can be found by looking at the wake distortion losses F. As can be seen, the wakes with the lowest TKE levels, as well as the lowest drag coefficient and mixed out loss (table 4.5) in case R_1, also produce the least loss as opposed to the case with the most pronounced wakes, R_{-1}. The TKE production term, defined by

$$P = -\overline{\rho}\widetilde{u_i'' u_j''}\frac{\partial \tilde{u}_i}{\partial x_j}, \tag{4.9}$$

explains this behaviour, as already pointed out by Stieger and Hodson (2005). The higher the turbulent stresses $\overline{\rho}\widetilde{u_i'' u_j''}$, as is the case for R_{-1}, the higher the production of turbulent kinetic energy and hence an increase in wake distortion losses. A comparison between the Denton losses, D, and the mixed out losses, E, in combination with the wake distortion losses, F, reveals the importance of wake mixing effects. Stronger incoming wakes are able to further reduce the size of the separation bubble, which leads to decreasing Denton losses. However, the higher wake mixing losses diminish this beneficial effect in terms of the overall mixed-out losses. This is in line with the findings of Pichler et al. (2018), who conducted large eddy simulations of a full turbine stage with two different stator-rotor gap sizes. They found that a smaller gap size resulted in

the suppression of a separation bubble, but the overall mixed-out losses were increased due to higher wake mixing losses. The reference case represents a special case, where due to the strong widening of the blade wake, the highest overall mixed out loss is achieved, but with the lowest profile loss, as a result of the second separation bubble behind the trailing edge.

The phase-lock averaged mixed-out losses for one bar passing period are presented in figure 4.14. A distinct minimum and maximum peak loss for all bar cases is evident. Furthermore, all bar cases reach a similar minimum loss at around $t/T = 0.333$. Considering the TKE contours in figure 4.9a–c (the black dashed line denotes the loss accounting plane) and the space-time diagram (figure 4.11) for $t/T < 0.333$, it is clear that the minimum loss occurs at the time without a separation bubble on the blades and when the bar wake has not mixed with the blade wake yet. The opposite effect can be seen from $t/T = 0.6$ onwards, where a separation bubble occurs for all cases, and the bar wakes mix with the blade wake. Lower losses are generated in the R_1 case, whereas cases R_0 and R_{-1} reach a similar maximum loss. The deviation between the cases from $t/T = 0.1$ to 0.25 can be attributed to the influence of the larger separation bubble in the R_1 bar case. This again demonstrates that the absence or reduction of a separation bubble in a low-pressure turbine does not necessarily lead to reduced overall losses, since wake distortion and combined effects play an important role.

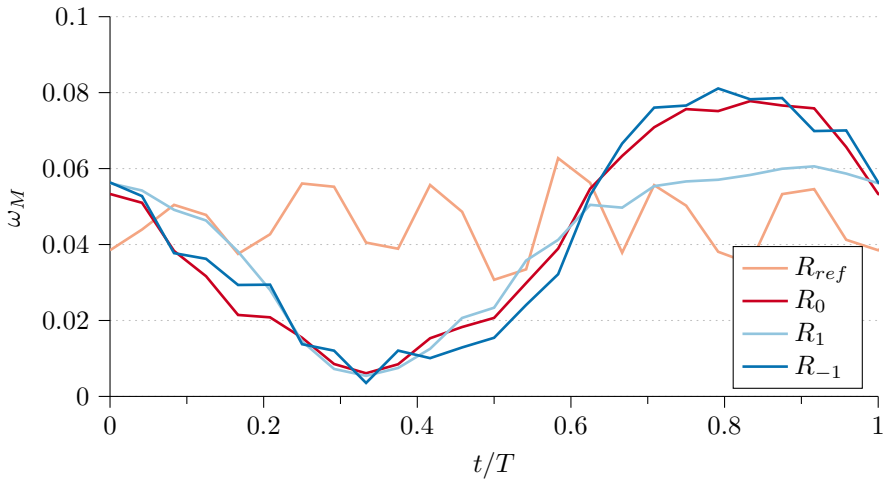

FIGURE 4.14: The variation of the mixed-out losses ω_M for one bar passing period.

As already expected from the space-time diagram in figure 4.11, the reference case shows an unsteady loss behaviour, with a period related to the vortex shedding frequency of the blade, but has a smaller amplitude due to the absence of the bar wakes. Hence, in this case, the time varying mixed-out losses can be solely attributed to the large separation bubble and the vortex shedding at the trailing edge.

In conclusion, the interaction between the weaker incoming wakes in case R_1 and the blade wake leads to considerably lower overall and maximum losses, even though a much larger separation bubble is present, leading to higher profile losses. The consideration of the TKE levels is important when choosing wake-generating bars in the design process. This can be realised by using rotating bars and changing the drag coefficient, as already stated by Pfeil and Eifler (1976); it has been proven to be a viable alternative to using different bar diameters. The very different lift coefficients did not contribute to any observable effect in our simulations.

As mentioned, the reduced frequency was chosen such that distinct wakes enter the blade passage. For higher reduced frequencies, the strength of the wakes might no longer be as important, as wake mixing occurs before the blade's leading edge (Michelassi et al. 2016). Moreover, added inlet turbulence and higher Reynolds numbers can positively affect the losses (Michelassi et al. 2015), and hence, the importance of the wake strength might change, as well. Coull et al. (2010) have shown that for higher Reynolds numbers, the wakes dominate the profile loss generation due to the increase of the momentum thickness of the turbulent boundary layer.

4.4 Summary

Large eddy simulations of the T106A linear low-pressure turbine cascade were carried out. The bar representation by means of the boundary data immersion method achieved comparable results to the feedback forcing method and body-fitted bars. Moreover, the BDIM allows for quick changes in the geometry, e.g. increasing or decreasing the diameter, without the need for creating a new grid. The timestep independence that comes with the BDIM is another reason for choosing this approach within the scope of this work.

Three different bar wakes, generated by means of different bar rotation rates, and a blade wake were investigated. By setting the wake-generating bars into rotation, it was possible to achieve similar wakes compared to an actual blade wake in terms of wake width. It has been shown that the TKE levels of the wakes for the non-rotating bars, which are commonly used, are several times higher compared to a turbine blade wake. In the experimental study of Halstead et al. (1997b), who used different bar diameters, the authors came to the same conclusion.

The effect of the three different bar wake profiles on the loss mechanisms of the low-pressure turbine was also considered, as incoming wakes have a profound effect on the profile losses (Hodson and Howell 2005a). Mean pressure and wall shear stress profiles of the blade differed only in the rear part of the blade's suction surface, where a separation bubble could be observed in the R_1 case with the weakest incoming wakes. A space-time diagram of the wall shear stress on the suction surface revealed a markedly bigger and longer-lasting separation bubble per blade passing period for R_1. For case R_{-1}, with clockwise rotation, the bubble could be almost completely prevented. A reason for the larger separation bubble is due to the weaker wake boundary-layer interaction and thus the positive effects of earlier transition and calmed regions are less pronounced. It was also shown that the maximum and overall loss was lower for the clockwise rotating bar case, even though a larger and longer-lasting separation bubble was present. Both mechanisms, the strength of the incoming wakes and the size of the separation bubble, and the combined effect on the overall loss generation have to be considered in the design process. Hence, it is paramount to choose a bar setup that generates reasonable wakes in terms of TKE levels. The results are also in line with the large eddy simulations of a full turbine stage of Pichler et al. (2018), who investigated two different stator-rotor gap sizes.

Chapter 5

Influence of Surface Roughness in a linear Low-Pressure Turbine Cascade[†]

As mentioned in section 1.2.3 surface roughness plays an important role in low-pressure turbines. It can have a profound effect on the onset of transition, on the turbulent boundary layer development on the blade and the turbine losses in general. Thus, an attempt was made to further investigate the influence of surface roughness in a linear low-pressure turbine cascade with the T106A profile by means of large eddy simulations. This chapter is partly based on, and has to be understood in the light of the results of the previous chapter (Ch.). In particular the laminar, transitional and fully rough behaviour of the flow over roughness are important, as all three regimes play an important role on a blade in a low-pressure turbine.

The chapter starts with a presentation of the numerical setup and the simulation parameters and then moves on to the surface roughness cases with the boundary data immersion method. An as-cast patch representing surface roughness, introduced in the previous chapter for the channel cases, was used. After that the grid convergence is checked followed by the investigation of the roughness effects on the boundary layer and the loss mechanisms.

Next is an investigation of the parametric forcing approach and its usage as well as its suitability as a roughness model for low-pressure turbine simulations. In order to do so, different roughness parameters - densities and heights - were chosen and the effects on the boundary layer development and the loss mechanisms are explored. Furthermore, different roughness patch sizes - in terms of length, i.e. covering the blade's suction surface - are considered as well. In the final section the findings of this chapter are summarised.

[†]This chapter is an extended form of the work published of Hammer et al. (2018a)

5.1 Numerical Setup and Simulation Parameters

The setup and domain decomposition of the linear low-pressure turbine with two wake generating bars is shown in figure 5.1.

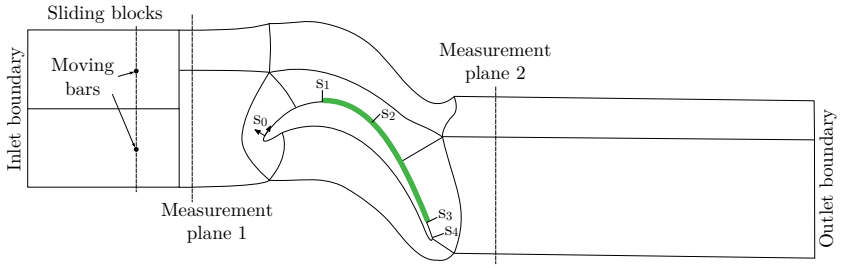

FIGURE 5.1: Setup of the linear low-pressure turbine with two wake generating bars upstream. The green line depicts the region where the roughness patch and the roughness forcing are applied.

The region where the roughness patches and forcing equations were applied is denoted by the green line. Interface, boundary, inlet and outlet conditions are identical to the ones used in chapter 4. However, the grids for all roughness simulations were refined in the wall-normal direction, where the number of points was increased by a factor of 1.5. Furthermore, the grid stretching was reduced to achieve a higher resolution for both the as-cast and the parametric forcing surface roughnesses. The resulting Δy^+ values at the blade surface and in the vicinity of the surface roughness is below 1. This ensures DNS-like resolution in the critical regions and eliminates the need to rely on the LES model. A comparison between the old (red lines) and the refined mesh (black lines) close to the blade surface, where the roughness is applied, is shown in figure 5.2.

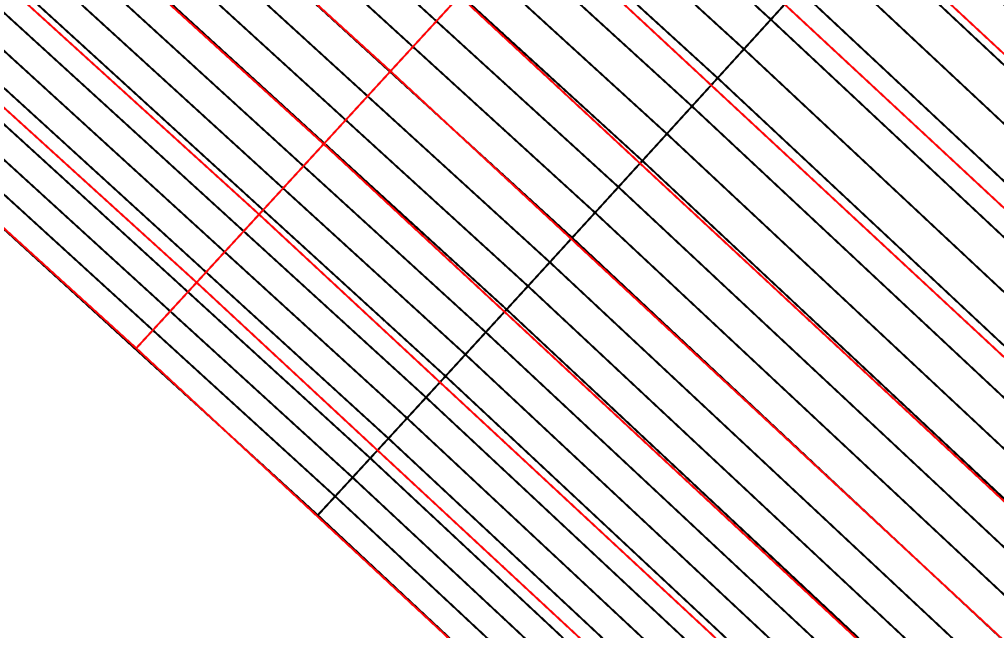

FIGURE 5.2: Comparison between the old grid (red lines) used in chapter 4 and the refined grid (black lines) for the roughness simulations.

In table 5.1 the simulation cases are listed. Using 9 to 11 blocks for the cases without and with wake generating bars as well as 32 to 64 Fourier modes - equivalent to 66 and 130 collocation points - for the spanwise discretisation depending on the different cases, resulted in grid sizes ranging from 12,539,472 to 27,256,320 points in $3D$.

TABLE 5.1: Summary of the roughness simulation cases.

Case	No. of blocks	Spanwise modes (Collocation points)	No. of grid points $2D$ / $3D$	Reference
BDIM as-cast without wakes	9	48 (98)	154,368 / 15,128,064	$AC_{c,nw}$
BDIM as-cast without wakes	9	64 (130)	154,368 / 20,067,840	AC_{nw}
BDIM as-cast	11	64 (130)	209,664 / 27,256,320	AC
Parametric Forcing Approach	11	32 (66)	209,664 / 13,837,824	$F_{\alpha \mathbf{x} h \mathbf{y}}$
Reference case without wakes	11	32 (66)	189,992 / 12,539,472	R_{ref}*

Similar to the simulations in chapter 4, the inlet velocities, based on the reference velocity $u_{ref} = 1.0$, Mach and Reynolds numbers for all simulations were chosen such that the isentropic Reynolds number is around $Re_{is,2} = 100{,}000$ and the isentropic Mach number approximates $M_{is,2} = 0.4$, see table 5.2.

TABLE 5.2: Inlet parameters for the cascade simulations.

Re / $Re_{2,is}$	M / $M_{2,is}$	V_{ax}	V_{pitch}	α_{inlet} [°]	Pr	c_{sut}/T_{ref}
62,707 / 100,000	0.24357 / 0.4	0.697	1.13	46.05	0.72	0.3686

The flow coefficient and the reduced frequency were kept the same as well, with values of $\Phi = 1.7$ and $F_{red} = 0.6$, based on the bar sliding velocity $U_{bar} = 0.41$. Statistically converged time-statistics were gathered over 16 bar passing periods, where the data were first spatially averaged in the spanwise direction before performing the time-averaging. The simulations were restarted from a fully converged simulation that had been previously conducted and run a further 5 bar passing periods, allowing the flow to pass through a short transient period due to the added roughness, after which time-statistics were collected.

*The reference case without bars consists of 11 blocks, because the two blocks for the incoming bars were still used in this simulation in order to check the sliding interface. Since the obtained results proofed reliable, the case was used as a reference case.

5.2 Surface Roughness with the Boundary Data Immersion Method

In this section surface roughness is added to the T106A turbine blade and the flow is investigated. The chosen roughness patches are represented by the boundary data immersion method, see sections 2.2.2 and 2.2.2.1.

The structure of the section is as follows. Firstly, the particular surface roughness used in the simulations is introduced and the relevant parameters are presented. Contrary to the channel cases, the roughness samples for the low-pressure turbine simulations need to be scaled and mapped onto the blade surface. The procedure to do so is explained in some detail. After that a grid resolution test is undertaken, where the clean setup without bars was used. This is followed by the results sections, where the effect of the roughness with and without combined incoming wakes on the boundary layer and the aerodynamic losses are investigated.

5.2.1 As-cast Roughness on the linear Low-Pressure Turbine Blade

An as-cast roughness patch, using case (s1) provided by Thakkar et al. (2017b), was used for the roughness patch simulations. The roughness patch is periodic in the streamwise and spanwise directions and has a distinct peak (yellow spot) as can be seen in the height map shown in figure 5.3.

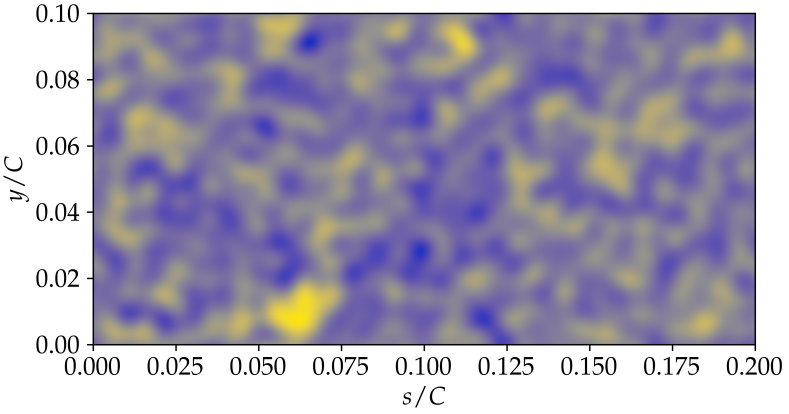

FIGURE 5.3: Height map of the as-cast roughness patch, where the peaks and troughs are denoted by the colours yellow and blue, respectively. The as-cast patch has a distinct roughness peak at around $s/C = 0.6$ and $y/C = 0.1$.

The patch had to be scaled down first to fit on the blade surface on the one hand, and to obtain the desired roughness parameters on the other hand. The procedure, also used in literature (Licari and Christensen 2011; Rao et al. 2014b), is illustrated in figure 5.4.

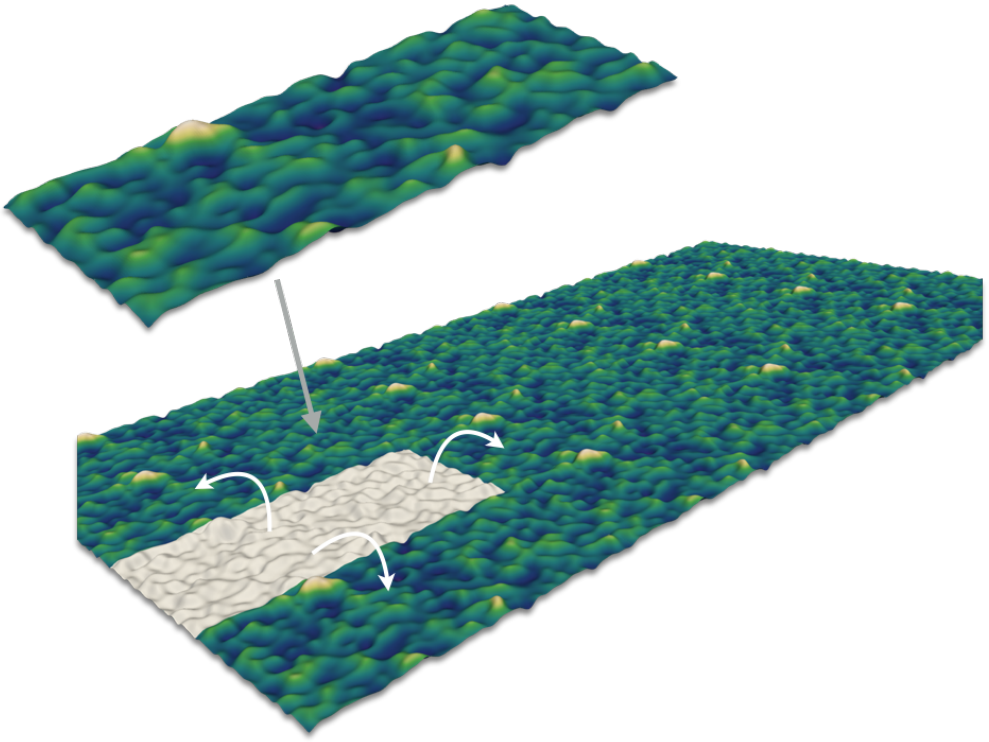

FIGURE 5.4: Scaling, attaching and distribution of the as-cast roughness patches before mapping onto the turbine blade.

After the scaling several patches were attached to each other, resulting in a larger patch. Before mapping the obtained large patch onto the blade surface, the Hann window function was applied at the beginning and end region of the patch in order to achieve a smooth transition between the blade surface and the roughness. After that the mapping onto the turbine blade along the green line depicted in figure 5.1 was performed. The suction surface starts at $s_0 = 0.0c$ ($s_0/S = 0.0$) and ends at $s_4 = 1.294c$ ($s_4/S = 1.0$), having a total suction surface length of $S = 1.294c$. The point $s_2 = 0.647c$ ($s_2/S = 0.5$) denotes the middle of the suction surface. The patch ranges from $s_1/S = 0.31$ to $s_3/S = 0.94$, covering around 63.32% of the blade's suction surface. Various authors (Bons 2010; Rao et al. 2014b) noted that this is the critical region where the boundary layer is most sensitive to roughness. The mapping was done by means of a rotation matrix,

$$A_\phi(s) \cdot \vec{k}(s) = \begin{bmatrix} \cos[\phi(s)] & -\sin[\phi(s)] & 0 \\ \sin[\phi(s)] & \cos[\phi(s)] & 0 \\ 0 & 0 & 1 \end{bmatrix} \cdot \begin{bmatrix} k_x(s) \\ k_y(s) \\ 1 \end{bmatrix}, \tag{5.1}$$

where $\vec{k}(s)$ is the vector pointing from the blade surface, s to a discrete surface roughness point. ϕ gives the angle between the blade surface tangent and the x-axis. The obtained low-pressure turbine blade with the added as-cast patch is depicted in figure 5.5.

FIGURE 5.5: T106A turbine blade with multiple patches mapped onto the blade's suction surface by means of a rotation matrix.

In table 5.3 the roughness parameters of the final as-cast patch are presented together with a typical range of roughness values for turbine blades, including a clean surface and a surface covered by deposits. Furthermore, common values used in the literature, and that mainly serve for research purposes only, are displayed as well. Here h/c denotes the average roughness height, defined by

$$h/c = \frac{1}{MN} \sum_{i,j}^{M,N} |h_{i,j}| \,, \tag{5.2}$$

with the discrete number of roughness points in the spanwise, M, and streamwise direction, N. The roughness height at the respective discrete point is given by $h_{i,j}$. The mean peak-to-trough height, $S_{z,5\times5}$, is denoted by k/c and is obtained by first segmenting the roughness patch into 5×5 smaller areas. For each area the minimum and maximum height is determined and the mean values for both are calculated. The difference between the mean maximum and minimum height is the mean peak-to-trough height, $S_{z,5\times5}$.

TABLE 5.3: Roughness parameters of roughness patches based on chord length $c = 1.0\,m$.

	$Ra\ [\mu m]$	$k_{rms}\ [\mu m]$	Sk	Ku	$h/c\ [\cdot 10^{-4}]$	$k/c\ [\cdot 10^{-3}]$
As-cast	467	596	0.6	4.0	4.7	4.5
Surface B (Rao et al. (2014b))	417	520	-0.72	3.3	5	-
Deposit (Bons et al. (2001))	3.7	4.8	0.72	4.15	0.04	-
Clean surface (Bons et al. (2001))	1.1	1.3	-0.4	3.0	0.01	-
Typical (Bons et al. (2001))	1.1 - 41.3	1.3 - 52.5	-4.1 - 2.18	3.0 - 36.0	0.01 - 0.41	-
Hydraulically smooth (Hummel et al. (2005))	0.38	-	-	-	-	-
Ceramic sprayed rough (Hummel et al. (2005))	11.78	-	-	-	-	-

As can be seen, the values of the centerline average roughness, Ra, and the rms roughness, k_{rms}, are up to two orders of magnitudes higher compared to typical surface roughness values found in real applications. However, the main purpose of this work is to test the viability of the extended immersed boundary method for surface roughness simulations in turbine flows as well as more fundamental flow mechanisms and for this it is important to be in a roughness regime where effects can be observed. The chosen values are in line with the more research-oriented literature, where many researchers used elevated surface roughness values or even isolated roughness elements, protruding into and in some cases through the boundary layer (Bons 2010; Montomoli et al. 2010; Redford et al. 2010; Roberts and Yaras 2005; Tsikata and Tachie 2013). Furthermore, the larger roughness values do not require such fine grids and hence allow for more simulation cases.

Before moving on, another important parameter has to be defined, namely the admissible roughness height, $k_{s,adm.}$, which is widely used in industry for turbomachinery applications (Bons 2010). Roughness is expected to have no influence on the turbulent boundary layer as long as

$$\frac{k_{s,adm.}}{c} \leq \frac{100}{Re_c} \tag{5.3}$$

holds true, where Re_c is the Reynolds number based on the chord length, c. In order to calculate the admissible roughness height for the setup within this work, Re_c was chosen to be the isentropic Reynolds number, $Re_{is,2} = 100{,}000$. The chord length for the simulation setup is $c = 1.0$, which results in $k_{s,adm.} \leq 1.0 \cdot 10^{-3}$. This correlates to another often-mentioned parameter, namely the roughness Reynolds number, $Re_{k_s,\infty}$, which is defined by

$$Re_{k_s,\infty} = \frac{U_\infty k_s}{\nu}, \tag{5.4}$$

where U_∞ denotes the free stream velocity and k_s the equivalent sandgrain roughness.

However, as Bons (2010) noted, in order to obtain the equivalent sandgrain roughness, k_s, for real surface roughness, i.e. the as-cast patch used within this work, a correlation between the measurable roughness parameter, Ra, and k_s has to be determined. This is not an easy task, as the wide range of different correlations used throughout the literature suggests (Bons 2010). Bons (2010) stated a current range of $1 < k_s/Ra < 10$, which results in equivalent sandgrain roughness values for the chosen as-cast roughness of $4.7 \cdot 10^{-4} < k_s < 4.7 \cdot 10^{-3}$. Hence, the roughness Reynolds number for the present surface roughness lies in between $Re_{k_s,\infty} = 47 - 474$.

The admissible roughness height and the roughness Reynolds number thresholds are based on the assumption that a turbulent boundary layer is present. Bons (2010) noted that for triggering transition the relation is less clear, with values found to be $Re_{k_s,\infty} \approx 120$ for low Reynolds number at low freestream disturbance levels and $Re_{k_s,\infty} = 600$ for a single roughness element at elevated freestream turbulence levels, which is common in turbomachinery. With cases AC_{nw} and AC it is hoped to shed more light on this aspect.

5.2.2 Grid Convergence and Verification of the LES Simulation

Before moving on to the result sections, the grid convergence for the as-cast patch, represented by the boundary data immersion method, is examined. In order to do so, two cases with as-cast patches and without incoming wakes were used, see tables 5.1 and 5.3 for the number of grid points and the roughness parameters. The absence of incoming wakes serves two purposes. Firstly, two additional blocks could be saved and thus significantly reduce the overall grid count by approximately 7,000,000 – 12,000,000 grid points for the normal, AC_{nw}, and the coarse case, $AC_{c,nw}$, respectively, compared to the as-cast roughness case, AC, with incoming wakes. Secondly, the periodicity due to the relative motion between the bars and the blade is removed, allowing for a shorter simulation time to obtain converged statistical data. The absence of additional free stream turbulence, also caused by the incoming wakes, does not affect the validity and accuracy of the convergence test, as a grid convergence study concerning this had already been done (see chapter 4).

For the grid convergence study for the roughness simulations, both grids have the same number of points in the $2D$ plane and only the number of spanwise modes was changed. Decreasing the number of modes from 64 (130 collocation points) to 48 (98 collocation points) increased the spanwise cell size by a factor of about 1.3. As acceptable results were obtained with these two configurations there was no need to run further cases for the convergence study.

The following results mainly serve to highlight the similarities and differences between the two cases. Thus, the discussion is only done in a qualitative rather than a quantitative way. A more thorough analysis, however, is done in the coming sections.

Figure 5.6 shows the displacement thickness, δ^*, the momentum thickness, Θ, and the shape factor, $H = \delta^*/\Theta$, along the blade's suction surface.

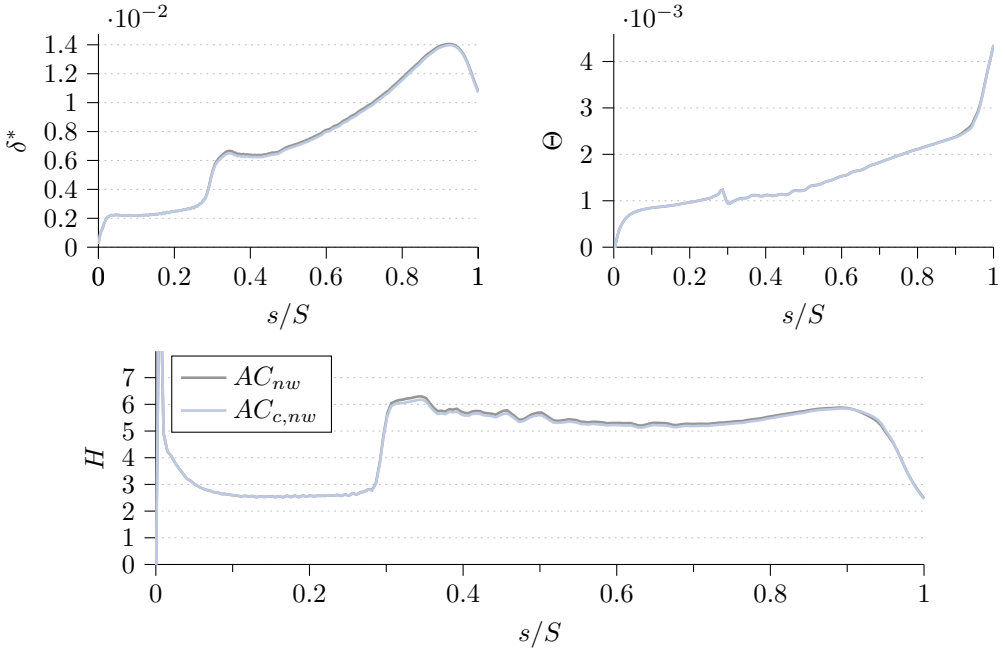

FIGURE 5.6: Lines of the displacement thickness, δ^*, the momentum thickness, Θ, as well as the shape factor H along the blade surface.

As can be seen, there is only a marginal difference for the displacement thickness in the mid-section of the blade, whereas the momentum thickness is identical. The shape factor shows the same marginal difference owing to the displacement thickness. This is a good indication for a reasonable grid resolution.

Turbulence levels, Tu, at different wall normal positions along the suction surface are shown in figure 5.7. The different wall normal positions along the blade are denoted by the subscripts max (maximum Tu level position), bl (Tu levels at boundary layer height) as well as 04 and 08, which are constant heights above the surface at $n = 0.004C$ and $n = 0.008C$, respectively. For the Tu levels taken at the height of the boundary layer (bl), the coarse case reveals markedly lower values. However, both slopes still show very similar characteristics. The same behaviour can be observed for the values of Tu_{08}, where the differences between the two cases, however, are less significant. For case Tu_{04} almost no differences can be observed, where the Tu levels were captured closer to the roughness surface at $n = 0.004C$. As is evident from the bottom plot of figure 5.7, the maximum turbulence levels, Tu_{max}, lie around $n = 0.004C$ up to a blade position of $s/S \approx 0.68$ and hence show similar results. For turbulence levels taken at different positions - apart from bl - past $s/S \approx 0.68$ no significant discrepancies are apparent.

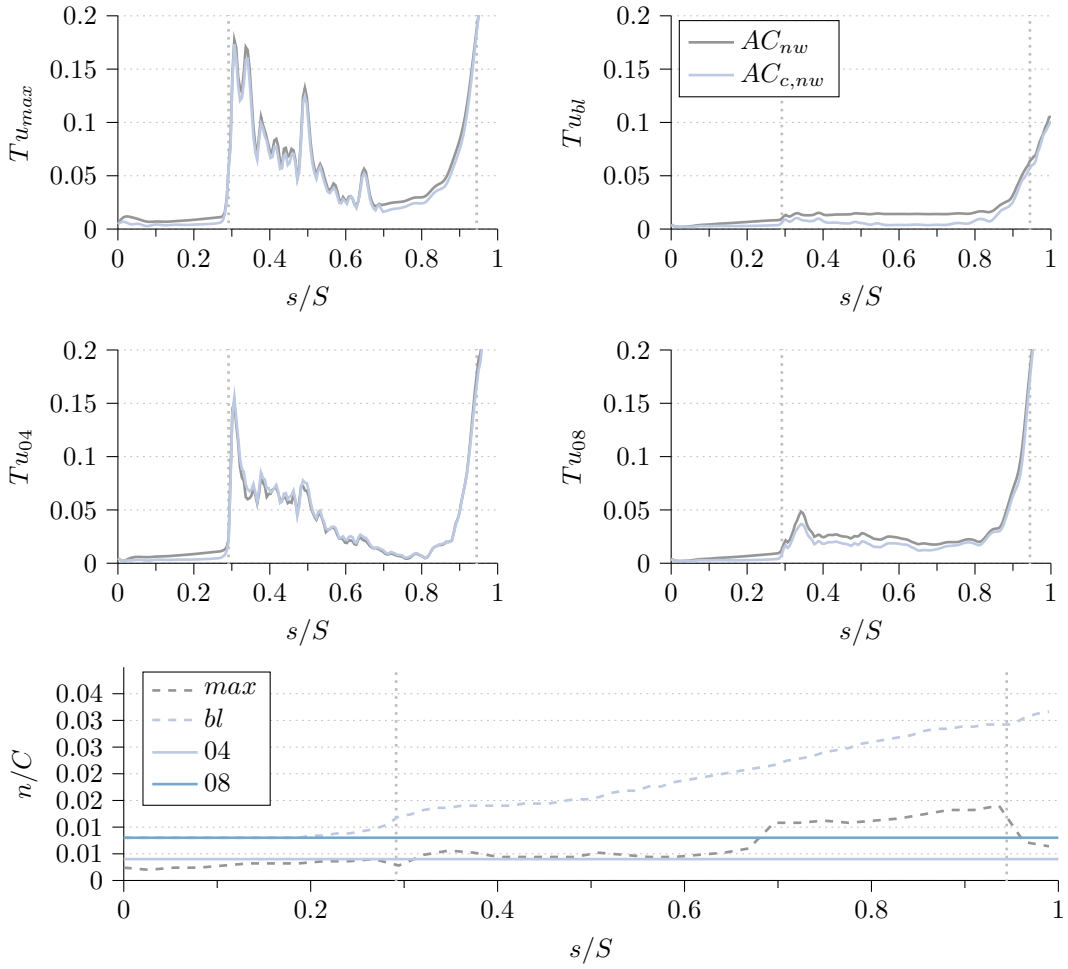

FIGURE 5.7: Turbulence levels, Tu, at different wall-normal heights along the blade surface indicate the onset of transition for the fine and coarse roughness cases.

In order to check the influence of the grid resolution on the losses, the profile and the mixed-out loss quantities were calculated and are shown in figure 5.8.

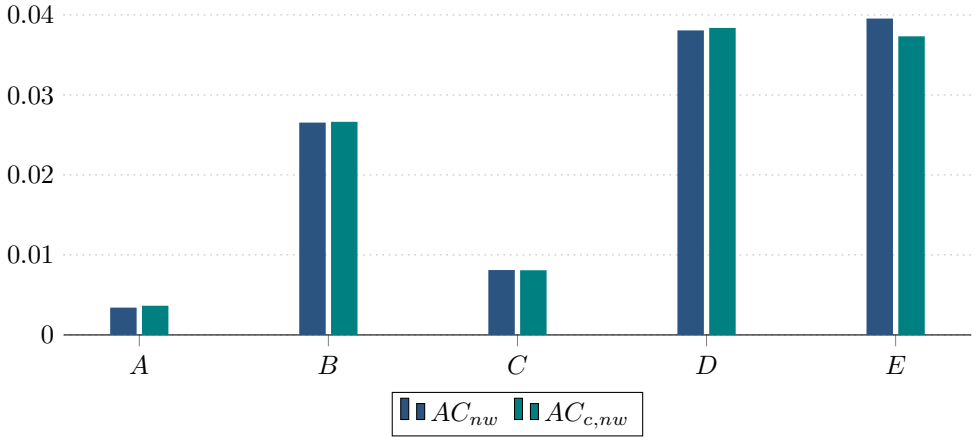

FIGURE 5.8: The Denton losses and its different contribution terms (A–D) as well as the overall mixed-out losses (E).

As can be seen, the profile losses, D, and its three contribution terms A – C are nearly the same. However, a marked difference for the mixed-out loss, E, which takes the blade wake into account, is evident. The reason for this might be the mixed-out loss accounting plane, which is located at a distance of $40\%c$ behind the trailing edge. Thus, the coarse grid seems to be sufficient for resolving the as-cast patch and the resulting profile losses, but insufficient in terms of blade wake resolution.

To summarise, both grids have almost no differences in the flow quantities and characteristics close to the as-cast patches. This gives high confidence in a sufficient mesh resolution for case AC_{nw}, which serves as a basis for all following roughness simulations.

5.2.3 Effects of an As-cast Roughness Patch on the linear Low-Pressure Turbine Cascade

In this section the effects of the chosen as-cast patch configuration, see section 5.2.1, on the boundary layer and the loss mechanisms are investigated. For this purpose, cases R_{ref}, $F_{\alpha 0 h 0}$, AC_{nw} and AC, given in table 5.1, were chosen. This allows for an analysis of several important questions:

1. What happens when roughness is added in a clean case setup, i.e. R_{ref} and AC_{nw}?
2. What is the combined effect of incoming wakes and surface roughness, i.e. cases $F_{\alpha 0 h 0}$, AC_{nw} and AC?

The analysis of these questions is split into two part. Firstly, the effect on the boundary layer development is investigated. After that, the impact on different loss quantities is examined.

5.2.3.1 Effect of Added As-cast Roughness on the Boundary Layer

In this section the questions above are addressed with respect to the effects on the boundary layer of the low-pressure turbine blade.

In figure 5.9 contour plots of the time-averaged and normalised tangential velocity, U_t, for the different cases are presented, where negative velocities, $U_t < 0.0$, are denoted by white contours. The contours are plotted along the suction surface, s/S, and the wall normal distance, n, which is normalised by the chord length, c. The thick black, white and red dashed lines show the boundary layer edge, the displacement thickness, δ^*, and the momentum thickness, Θ, respectively. An important point to note is that, due to the strong curvature of the blade and the changing pressure gradients - from favourable to adverse - along the suction surface, it was difficult to obtain a reliable boundary layer edge by means of the 99% approach. Hence, instead of using the $U_t = 0.99U_\infty$ as a threshold, the derivative of the tangential velocity in wall-normal direction, $\partial U_t/\partial n$, was used. Owing to the pronounced wake regions in the boundary layer profiles under adverse pressure gradients (APG), this approach has been found to be more consistent and reliable. The position where the derivative is minimal, i.e. $\min(\partial U_t/\partial n)$, or crosses a given value

$$\min\left(\frac{\partial U_t}{\partial n}\right) < \epsilon = 0.01 \left.\frac{\partial U_t}{\partial n}\right|_{wall} \tag{5.5}$$

denotes the edge of the boundary layer. This formulation is still not perfect and in particular the definition is problematic near the trailing edge.

For cases AC_{nw} and AC the mean peak-to-trough roughness heights are denoted by the thin white dashed line. As mentioned in section 5.2.1, the start and end of the as-cast patch was smoothed by means of a Hann window, resulting in the observed "ramps". It has to be noted that this is just a simplified representation of the smooth transition between the blade surface and the roughness patch. The roughness case therefore includes a step in the surface, but as will be shown later, the transition is due to the roughness rather than then the step.

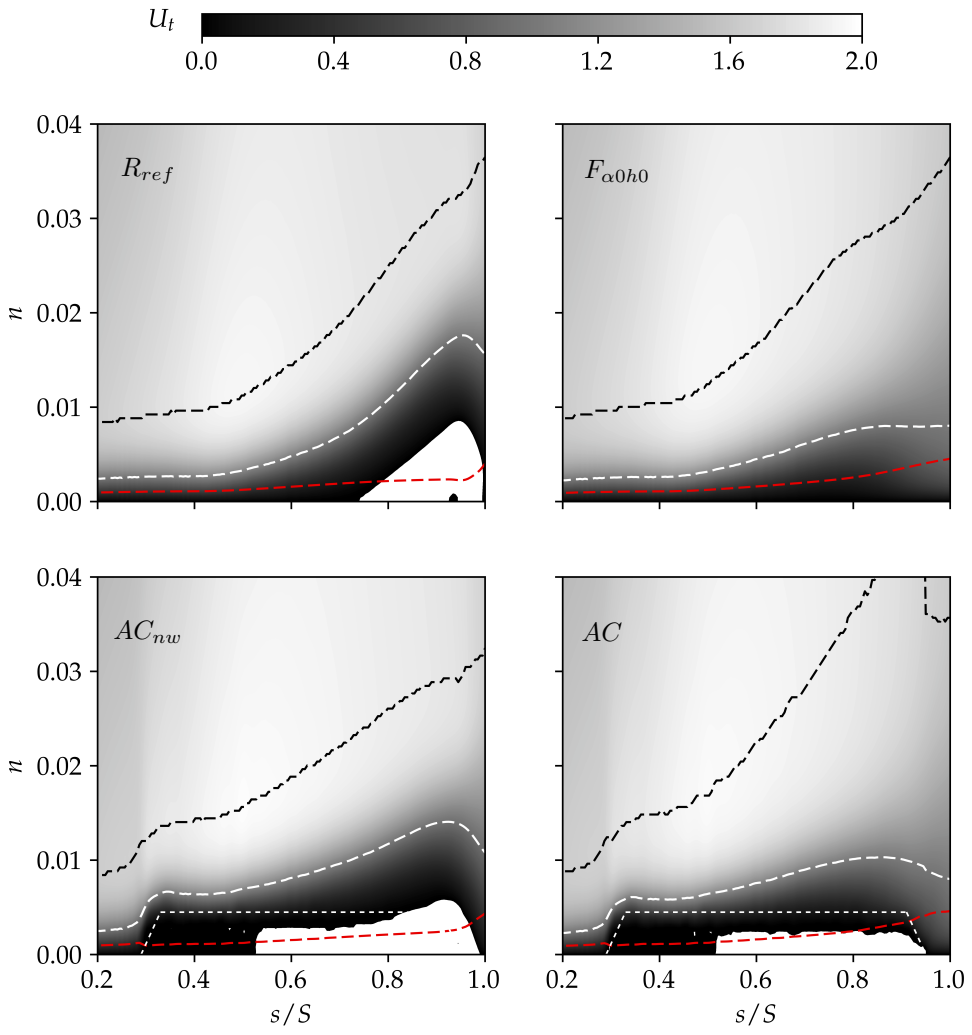

FIGURE 5.9: Tangential velocity, U_t, contours along the blade suction surface, s/S. The dashed black, white and red lines depict the boundary layer edge, the displacement thickness, δ^*, and the momentum thickness, Θ, are denoted by the dashed black, white and red lines, respectively. The thin white dashed line in the roughness cases denotes the mean peak-to-trough heights, k/c.

As already observed in chapter 4, there is a large separation bubble for the reference case, R_{ref}, resulting in a rapid and considerable increase of the displacement thickness, δ^*. The momentum thickness, Θ, starts growing after the transition to a turbulent boundary layer at

around $s/S \approx 0.98$. Furthermore, for the two roughness cases AC_{nw} and AC sudden increases in the boundary layer and displacement thickness are apparent, which was to be expected as the blade becomes thicker due to the added roughness. Hence, the actual displacement thickness has to be regarded relative to the surface roughness patch itself, i.e. the thin white dashed lines. The sudden thickening causes an abrupt rise in U_t indicated by a vertical contour line sightly before $s/S = 0.3$. However, the displacement and boundary layer slopes start to differ as of $s/S = 0.5$, with AC_{nw} following a laminar trend similar to R_{ref} and AC resembling similar behaviour of the incoming wake case without roughness, $F_{\alpha 0 h 0}$. Moreover, the roughness in case AC_{nw} is not able to completely suppress a separation bubble, as transition does not seem to be triggered by the as-cast roughness.

In order to check whether a detached shear layer is caused by the as-cast roughness, the z-vorticity, ω_z, in the $x-y$ and $y-z$ planes for AC_{nw} is shown in figure 5.10, ranging between $-300 \leq \omega_z \leq 300$.

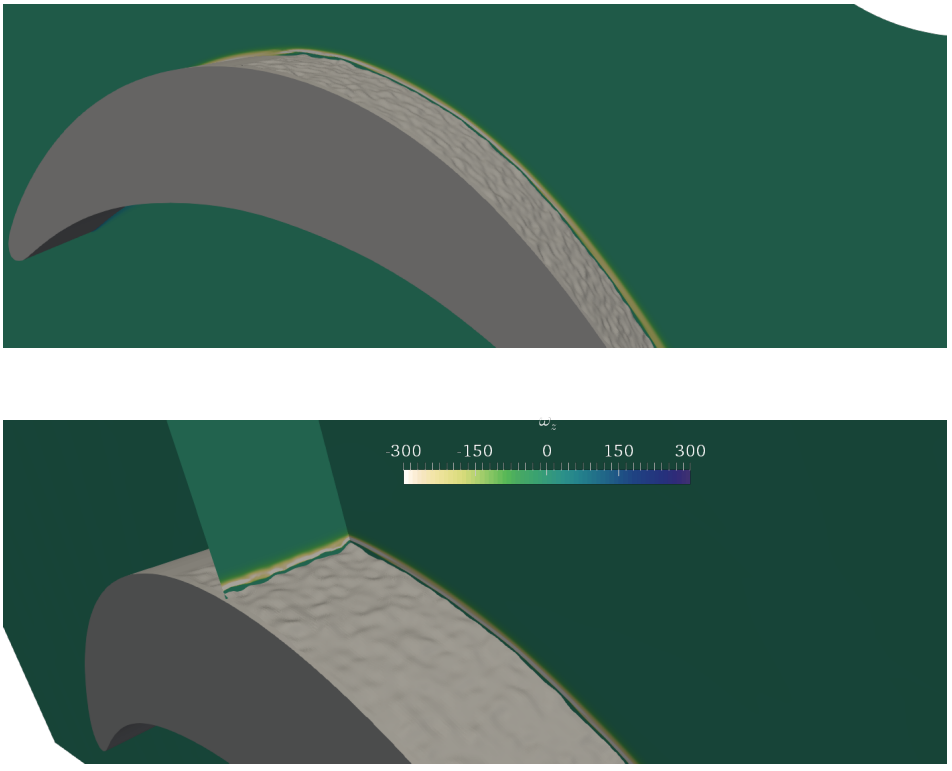

FIGURE 5.10: Instantaneous z-vorticity contours, ω_z, in the $x-y$ and $y-z$ planes for case AC_{nw}. The vorticity ranges between $-300 \leq \omega_z \leq 300$.

As can be seen, the flow stays attached and remains laminar along the blade surface. Given the results of the velocity contours and the fact that the boundary layer in case AC_{nw} is laminar for a large portion of the blade indicates two important things. Firstly, as mentioned above, the roughness Reynolds number, Re_k, based on the peak-to-trough roughness height k is around $Re_k \approx 370$. According to Redford et al. (2010), who investigated an isolated roughness element in a compressible boundary layer, for roughness Reynolds number values $Re_k > 300$ the single element was able to trigger transition at very low Mach numbers. The reason that the as-cast patch did not induce transition right at the beginning, even though this threshold was exceeded, is

probably due to the slight ramp between the blade surface and the roughness surface, obtained by means of the Hann window. Secondly, given that the as-cast patch does not seem to trigger earlier transition compared to the no-roughness case and considering the findings presented by Bons (2010), with the given transition threshold for turbomachinery applications of $Re_{k_s,\infty} > 120$ for the equivalent sand-grain roughness, k_s, the above mentioned critical roughness Reynolds number range for the used as-cast patch can be reduced to $Re_{k_s,\infty} = 47 - 120$, with regard to the rest of the roughness surface. It will be evident later from the instantaneous flow fields that $Re_{k_s,\infty}$ for the roughness patch is around the critical threshold of 120.

The displacement, δ^*, and the momentum thickness, Θ, as well as the shape factor, $H = \delta^*/\Theta$, along the suction surface are shown in figure 5.11, in order to obtain a clearer picture of the boundary layer development.

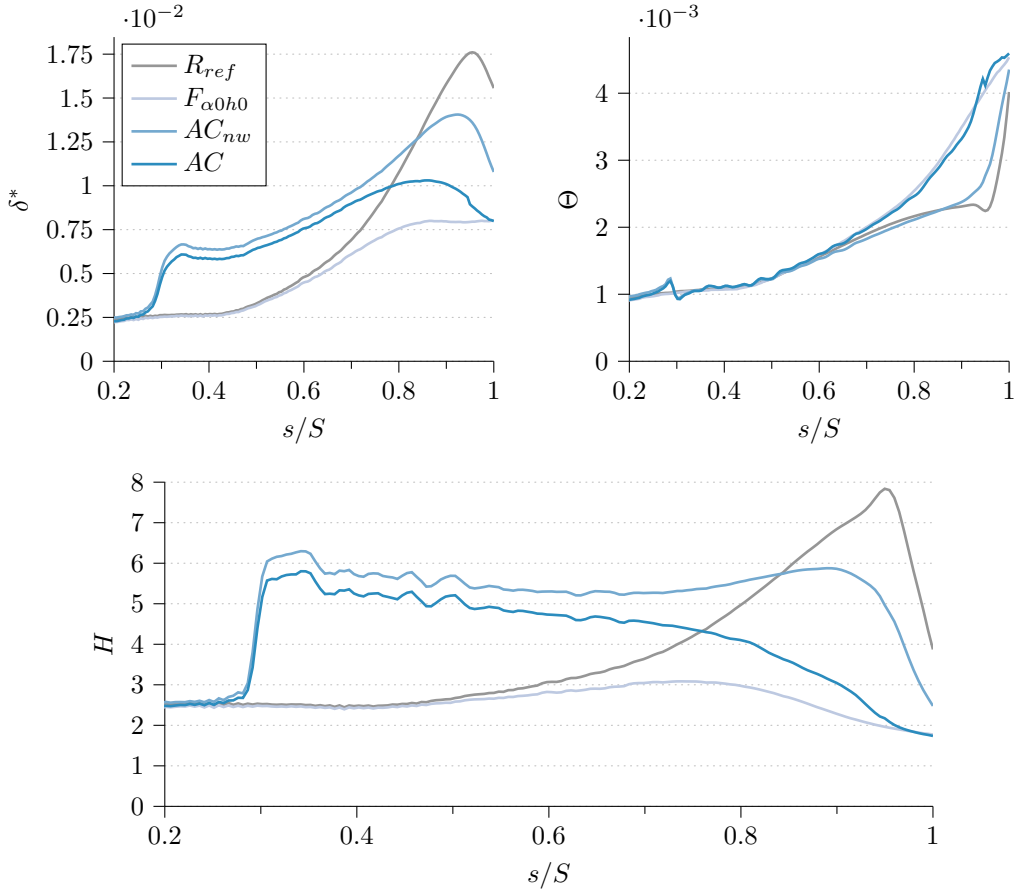

FIGURE 5.11: Lines of the displacement thickness, δ^*, the momentum thickness, Θ, as well as the shape factor H along the blade surface.

Again, the sudden jump for δ^* due to the roughness patches is apparent. A slightly higher displacement thickness for the roughness case without incoming wakes can be observed. At around $s/S \approx 0.68$ the slopes start to diverge, following a laminar development for case AC_{nw} and a turbulent development for case AC, when compared to R_{ref} and $F_{\alpha 0 h 0}$. This behaviour is especially evident when looking at the momentum thickness. Cases $F_{\alpha 0 h 0}$ and AC show very similar results, indicating a negligible roughness effect on Θ. The same can be seen for cases R_{ref} and AC_{nw}, which only reveal a difference towards the trailing edge due to the different

separation bubble sizes, highlighted by δ^*. Interestingly, the momentum thickness is very similar for all cases until transition for AC and $F_{\alpha 0 h 0}$ occurs at about $s/S \approx 0.6$, which means that the incoming wakes play the major role in terms of boundary layer transition.

The abrupt increases in displacement thickness for both roughness cases lead to high shape factor values. For AC_{nw} these values remain fairly high until shortly before the trailing edge, where a sharp drop is evident. Whereas for case AC, H starts to decrease as of $s/S \approx 0.6$ to a value of $H = 1.8$, which is common for a turbulent boundary layer for turbine flows and matches the results of Rao et al. (2014a).

Furthermore, AC and AC_{nw} expose the same characteristics indicated by the small bumps in the slopes. Both cases also show a kink in the momentum thickness slightly before the start of the as-cast patches due to the higher effective blade thickness. When compared to R_{ref} and $F_{\alpha 0 h 0}$ the roughness seems to slightly increase Θ in the laminar boundary layer and then causes a sudden decrease once the flow reaches the roughness elements.

In order to further investigate the roughness effects on the boundary layer transition, the maximum turbulence intensity levels, Tu_{max}, along the blade surface are analysed, see figure 5.12.

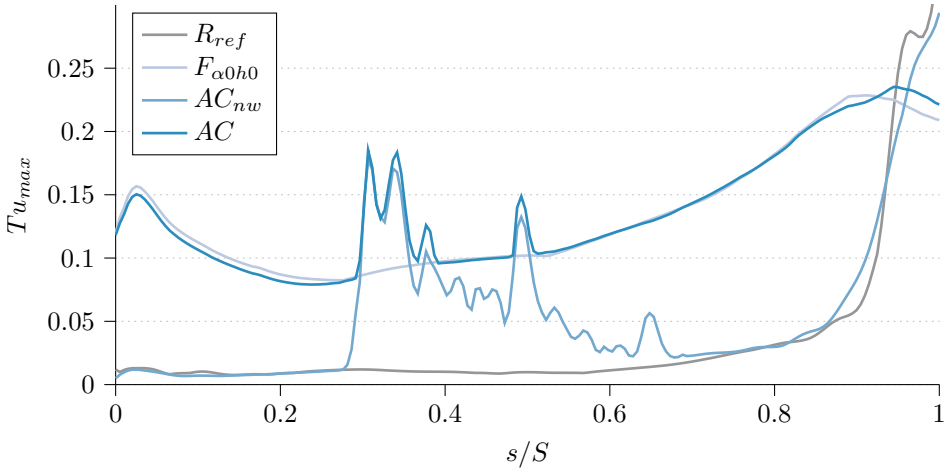

FIGURE 5.12: Maximum turbulence levels, Tu_{max}, along the blade indicate the onset of transition. A rapid increase denotes the start of the transition process.

The turbulence levels were not normalised in order to be able to compare the disturbance free cases with the incoming wake cases.

The first thing to notice is the large difference in turbulence levels due to the presence or absence of the incoming wakes. Furthermore, the laminar and turbulent boundary layer developments are apparent. Apart from the four peaks in case AC shortly after the beginning of the as-cast patch, the slope is very similar to the one of $F_{\alpha 0 h 0}$, indicating the dominant influence of the bar wakes. Case AC_{nw} shows much higher turbulence levels along the surface roughness with respect to R_{ref}, but does not quite reach the levels of AC and $F_{\alpha 0 h 0}$. The slope then follows again the behaviour of the reference case in the aft section of the blade. This means that the chosen roughness heights are not high enough to cause earlier transition, no matter if incoming wakes are present or not. Interestingly, the cases AC and AC_{nw} reveal similar features indicated

by the apparent peaks and thus can be solely attributed to roughness effects rather than to a combined effect of bar wakes and roughness.

Turbulent kinetic energy, TKE, contours for the four cases are presented in figure 5.13. For all cases the TKE levels outside of the boundary layer remain very low. At the trailing edge a rapid increase of turbulent kinetic energy can be observed for R_{ref} and AC_{nw}, after turbulent reattachment of the large separation bubbles. The increase of TKE for the incoming wake cases is more gradual and a larger elevated region is evident due to the earlier transition induced by the wakes and hence resulting in a longer turbulent boundary layer. The as-cast roughness patches in both cases, however, slightly shift and "clip" the TKE regions, owing to the higher effective blade thicknesses.

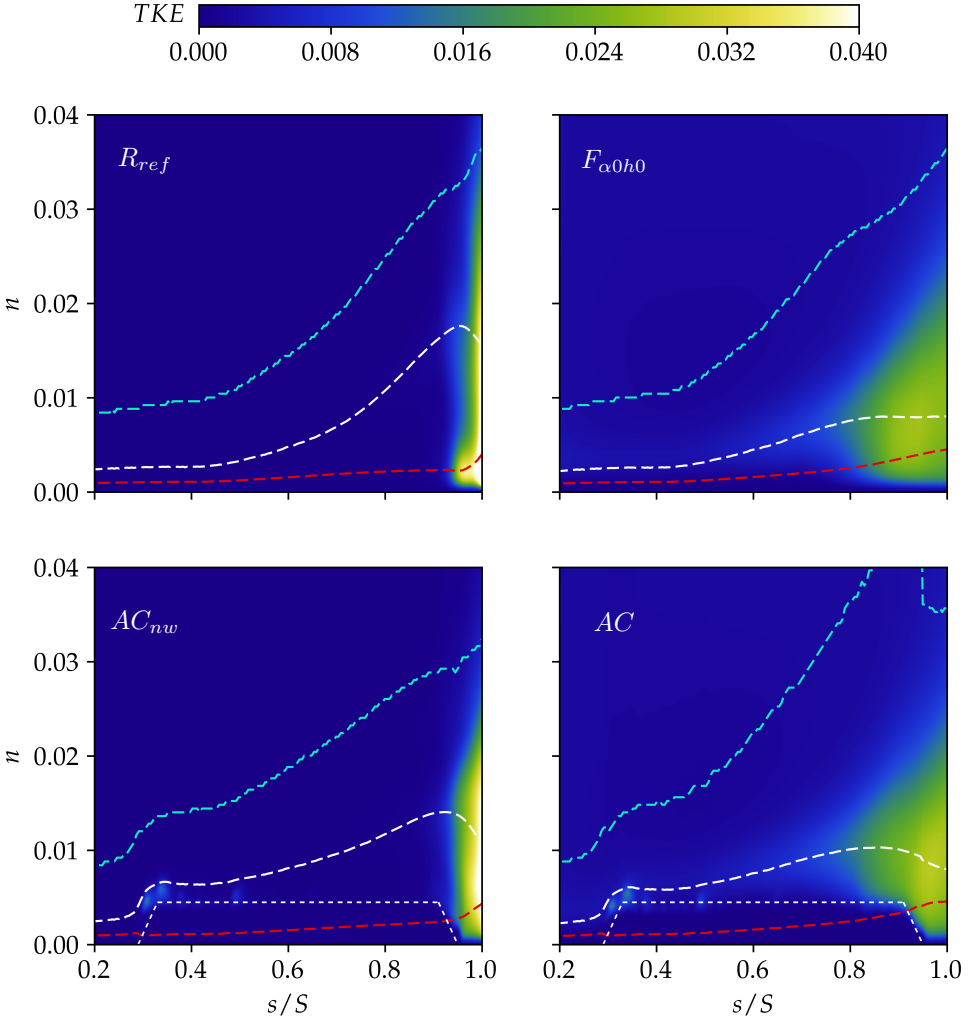

FIGURE 5.13: Contour plots of the normalised turbulent kinetic energy, TKE, along the blade's suction surface, s/S.

This further explains the observed sudden jumps in the momentum thicknesses, Θ. Moreover, two small TKE spots at the start of the patch and a third one at around $s/S \approx 0.5$ can be observed, but neither grow nor influence the boundary layer downstream.

The highest peak TKE is achieved by R_{ref} due to the large separation bubble, followed by AC_{nw} with a significantly lower value, see table 5.4.

TABLE 5.4: Peak TKE values for the different cases.

R_{ref}	$F_{\alpha 0 h 0}$	AC_{nw}	AC
0.2100	0.0783	0.1295	0.0830

One of the reason for this might be the smaller separation bubble in the latter case. The combined effects of incoming wakes and roughness are manifested in the slightly higher turbulent kinetic energy for case AC compared to $F_{\alpha 0 h 0}$.

Figure 5.14 shows the turbulent kinetic energy production, P, contours over the blade's suction surface for the four cases.

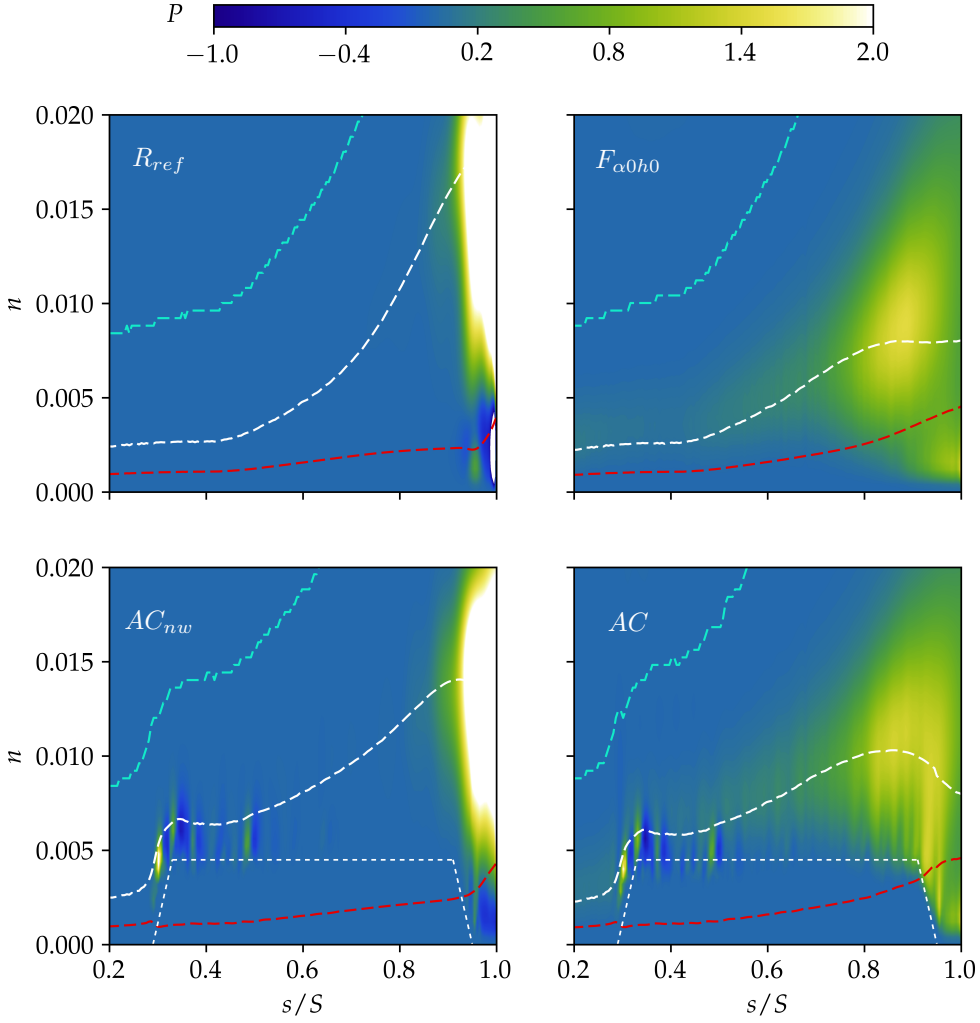

FIGURE 5.14: Contour plots of the production of the turbulent kinetic energy, P.

The production of turbulent kinetic energy is part of the turbulent kinetic energy transport equation and is defined by

$$P = -\overline{\rho}\widetilde{u_i''u_j''}\frac{\partial \tilde{u}_i}{\partial x_j}, \tag{5.6}$$

where $\widetilde{u_i''u_j''}$ are the Reynolds stresses. P remains zero for most of the blade for the reference case, owing to the absence of incoming wakes, disturbances and the long laminar boundary layer. Shortly before the trailing edge, when the shear flow over the large separation bubble begins to transition, the production of TKE rapidly increases. A very similar behaviour is seen for case AC_{nw}. However, for both roughness cases at the start of the as-cast patches, at the height of δ^*, small spots of P are evident, which rapidly switch between positive and negative values. This explains the observed TKE spots and the presence of negative P explains why the growth to larger TKE regions was prevented.

When looking at case $F_{\alpha 0 h 0}$, the production of turbulent kinetic energy is slightly elevated along the blade surface at the height of the displacement thickness due to the incoming wakes. The same can be seen for the case with the added roughness, AC. There is a slight, but visible combined effect of the incoming wakes and the roughness on P. However, this effect is only marginal and not sufficient for triggering earlier transition.

5.2.3.2 Effect of Added As-cast Roughness on the Loss Mechanisms

In this section the effect on the different loss mechanisms of the low-pressure turbine cascade is addressed. In order to do so, the LPT cascade and blade losses are quantified by four different measures, which were already introduced in chapter 4. As a reminder, these are, firstly, the mixed-out losses (Prasad 2005), which are defined by

$$\omega_M = \frac{p_{t,1,M} - p_{t,2,M}}{p_{t,1,M} - p_{2,M}}, \tag{5.7}$$

where $p_{t,1,M}$ and $p_{t,2,M}$ are the mixed out total pressures at measurement planes 1 and 2 shown in figure 5.1. Then, secondly, the bar wake distortion losses, ω_{wake}, through the blade passage, which are obtained by excluding the wake of the blade. These were shown to be significant at the reduced frequency, $F_{red} = 0.6$, used in this work (Michelassi et al. 2016). Thirdly, the Denton losses (Denton 1993)are considered. These are sometimes also denoted as profile or control volume losses and are defined by

$$\zeta = \frac{C_{pb}(\delta^*_{TE} + t_{TE})}{P_{blade}\cos\alpha_2} + \frac{2\theta_{TE}}{P_{blade}\cos\alpha_2} + \left(\frac{\delta^*_{TE} + t_{TE}}{P_{blade}\cos\alpha_2}\right)^2, \tag{5.8}$$

based on the base pressure coefficient C_{pb}, the displacement thickness, δ^*_{TE}, and the momentum thickness, Θ_{TE}, at the trailing edge with thickness t_{TE}. Lastly, the total pressure losses are considered, given by

$$\Omega = \frac{p_{t,1} - p(y)_{t,2}}{p_{t,1} - p_2}, \tag{5.9}$$

which shows the changes of total pressure before and after the blade along the pitchwise direction. For brevity and overview purposes in the following sections, the different loss terms are denoted by the letters A–F, see table 5.5.

TABLE 5.5: Loss terms, descriptions and abbreviations.

Base pressure contribution	Momentum thickness contribution	Displacement thickness contribution	Overall Denton loss	Mixed-out loss	Wake distortion loss
A	B	C	D	E	F
$\frac{C_{pb}(\delta^*_{TE}+t_{TE})}{P_{blade}\cos\alpha_2}$	$\frac{2\theta_{TE}}{P_{blade}\cos\alpha_2}$	$\left(\frac{\delta^*_{TE}+t_{TE}}{P_{blade}\cos\alpha_2}\right)^2$	ζ	ω_M	ω_{wake}

Figure 5.15 shows the Denton loss, D, and its respective loss contribution terms, A–C, as well as the mixed-out losses ω_M and ω_{wake}.

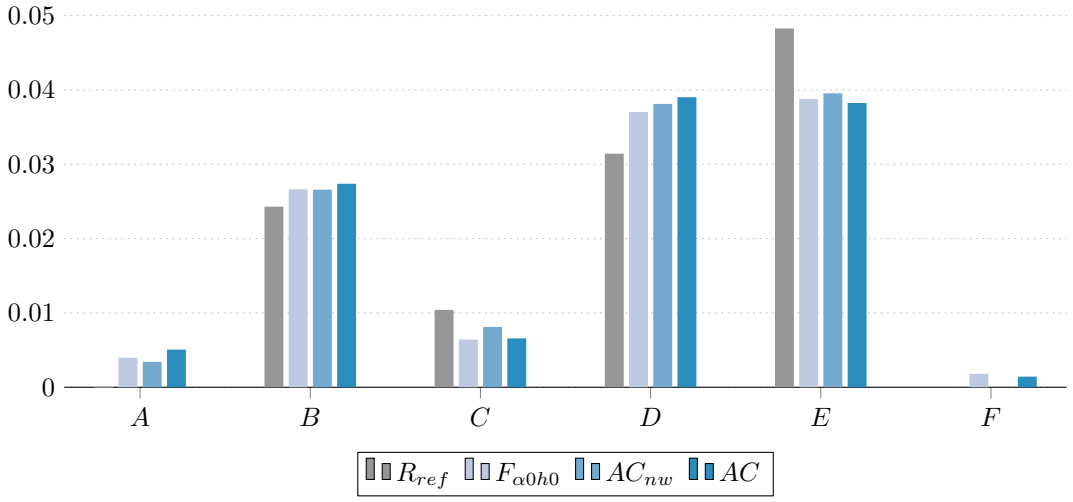

FIGURE 5.15: Denton losses with its respective contribution terms (A–D) and the overall mixed-out as well as wake distortion losses (E,F).

Firstly, the profile losses for the four cases are analysed. As can be observed, the Denton loss, ζ (D), is lowest for the reference case. By adding incoming wakes the profile loss increases, as already discussed in chapter 4. For the added as-cast patch case without the upstream bars the loss further slightly increases. The combination of both the roughness and the wakes results in the highest Denton loss. When looking at the different loss contributions the pictures becomes clearer. The base pressure contribution, A, rises with rising disturbances of the flow environment, see figure 5.12. The same is true for the momentum thickness contribution, B. A very important point to remember, however, is that due to the higher effective blade thicknesses, or rather the bump, for the roughness cases, the momentum thickness is affected. This might explain why the momentum thickness loss contribution, B, is the same between $F_{\alpha 0 h 0}$ and AC_{nw}. The differences for the loss contributions based on the displacement thickness, C, can be solely attributed to the presence and size of the separation bubble. Based on the fact that $F_{\alpha 0 h 0}$ and AC reveal the same

value, it can be argued that the added as-cast patch on top of the blade does not have a direct impact on C, as long as there is no separation bubble and the incoming wakes are dominant.

The mixed-out losses, E, show a different trend compared to the profile losses, D. The highest generated overall loss is by far due to the large separation bubble in case R_{ref}. Interestingly, the same trend as seen for the displacement thickness contribution, C, is present, indicating that for the chosen cases δ^* is the primary parameter determining the overall low-pressure turbine losses. This shows and emphasises again the important benefits of incoming wakes preventing the formation of laminar flow separation and separation bubbles, see chapter 4. The additional wake distortion losses, F, are lower than the additional losses due to the separation bubbles.

Figure 5.16 shows the total pressure losses, Ω, extracted at measurement plane 2 along the pitchwise direction. As can be observed, the losses for each case differ widely.

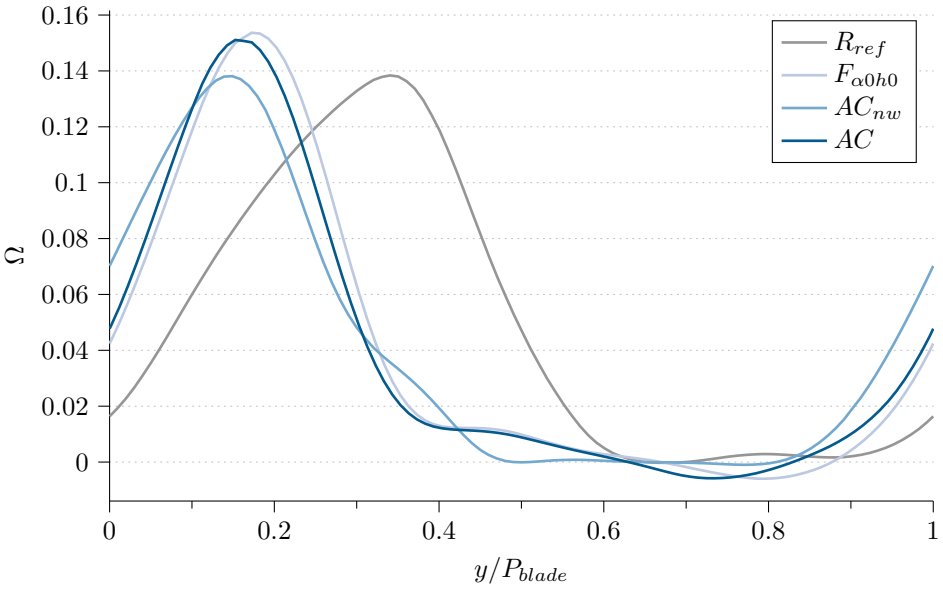

FIGURE 5.16: Total pressure loss profiles, Ω, for the reference, the $F_{\alpha 0h0}$ and the roughness cases.

A wide blade wake and a strong flow deflection for case R_{ref} are apparent, further explaining the high overall losses. Case $F_{\alpha 0h0}$ reveals the highest peak loss followed by AC, which shows a slightly lower peak for Ω and a weaker flow deflection, resulting in a decreased ω_M. For the added as-cast patch case without incoming wakes the peak losses are similar to the reference case, but the flow deflection is markedly reduced, which is due to the smaller separation bubble size and the added roughness patch. The reason for the higher mixed-out loss, E, compared to the incoming wake cases is the noticeably wider blade wake profile.

5.2.3.3 Instantaneous Flow Field Analysis for the As-cast Roughness Patch

In order to further investigate the combined effect of the incoming wakes and the as-cast surface roughness patch, instantaneous flow data at different time instants for case AC are shown in figure 5.17. Contours of the tangential velocity, U_t, taken at a distance of $h/c = 5.3 \cdot 10^{-3}$ above the blade surface in the x/c and y/c plane at different time instants are presented. The two black

low velocity spots at around $x/c = 0.18$ show the distinct roughness peaks that could be seen in the height map in figure 5.3, reflecting the previously mentioned mirroring and distribution of the scaled as-cast patches in section 5.2.1 is apparent. Further downstream, at around $x/c = 0.35$, two more peaks can be seen.

The first striking observation to be made is the highly uneven onset of transition across the whole span between $t/T = 0.08$ – 0.49, which is the time range between wake passings. This is caused by the high and low velocity streaks, denoted by the dashed white ellipses, behind and between the mentioned roughness peaks upstream, respectively. Rao et al. (2014b) also observed streaks emerging from roughness peaks, however, as opposed to streaks induced by free-stream turbulence they were "steady and fixed". The fact that this is not seen in the case of the low-pressure turbine cascade is due to the periodic nature and the dominant incoming wake structures. Furthermore, the apparent streak at $y/c = 0.2$ in the first time instants causes a partial transition further downstream, which is followed by a calmed region, indicated by the lower velocity region.

At time instant $t/T = 0.24$ small streaks behind the two roughness peaks emerge, which start growing and causing a large transition region at $x/c \approx 0.6$ in between the wake passings. Here, the turbulent region, which moves further downstream, is followed by a large calmed region. The observed erratic values for P along the blade at the height of the displacement thickness, after $s/S \approx 0.5$ in figure 5.14 for case AC, can be explained by these emerging streaks. Moreover, due to the additional turbulent regions between the wake passings the slightly higher momentum loss contribution compared to $F_{\alpha 0 h 0}$ can be clarified, even though the effect on the overall loss is small.

The incoming wake at time instant $t/T = 0.57$, denoted by the white long-dash ellipse, can be observed as well. Wake-induced streaks are visible and transition occurs at around $x/c \approx 0.5$. However, the calming effect due to the roughness induced streaks seems to be resilient enough to prevent the generation of streaks induced by the incoming wake, indicated by the enclosed low velocity region at $t/T = 0.89$ and 0.97.

Iso-surfaces of the Q-criterion coloured by the spanwise velocity component, w, over the blade in a top view position are shown at the same time instants in figure 5.18. Large flow structures are observed at the beginning of the as-cast patch. However, a rather stationary behaviour is apparent and the structures do not convect past the mid-section of the blade and remain in the higher adverse pressure gradient region. This also explains the noticeable turbulent kinetic energy production spots in figure 5.14.

Furthermore, distinct vortices and the transition behaviour are more visible and clear in the Q iso-surfaces. Especially the small vortices emerging from the roughness peaks are evident, which cause the large transition region in the aft section of the blade. The incoming wake generates somewhat larger vortices, but only outside the observed calmed region.

Based on the fact that the roughness induces transition between the wake passings, it can be concluded that the as-cast patch must have an equivalent sand-grain roughness Reynolds number somewhere around $Re_{k_s,\infty} \approx 120$. This explains the dominant effect of the incoming wakes.

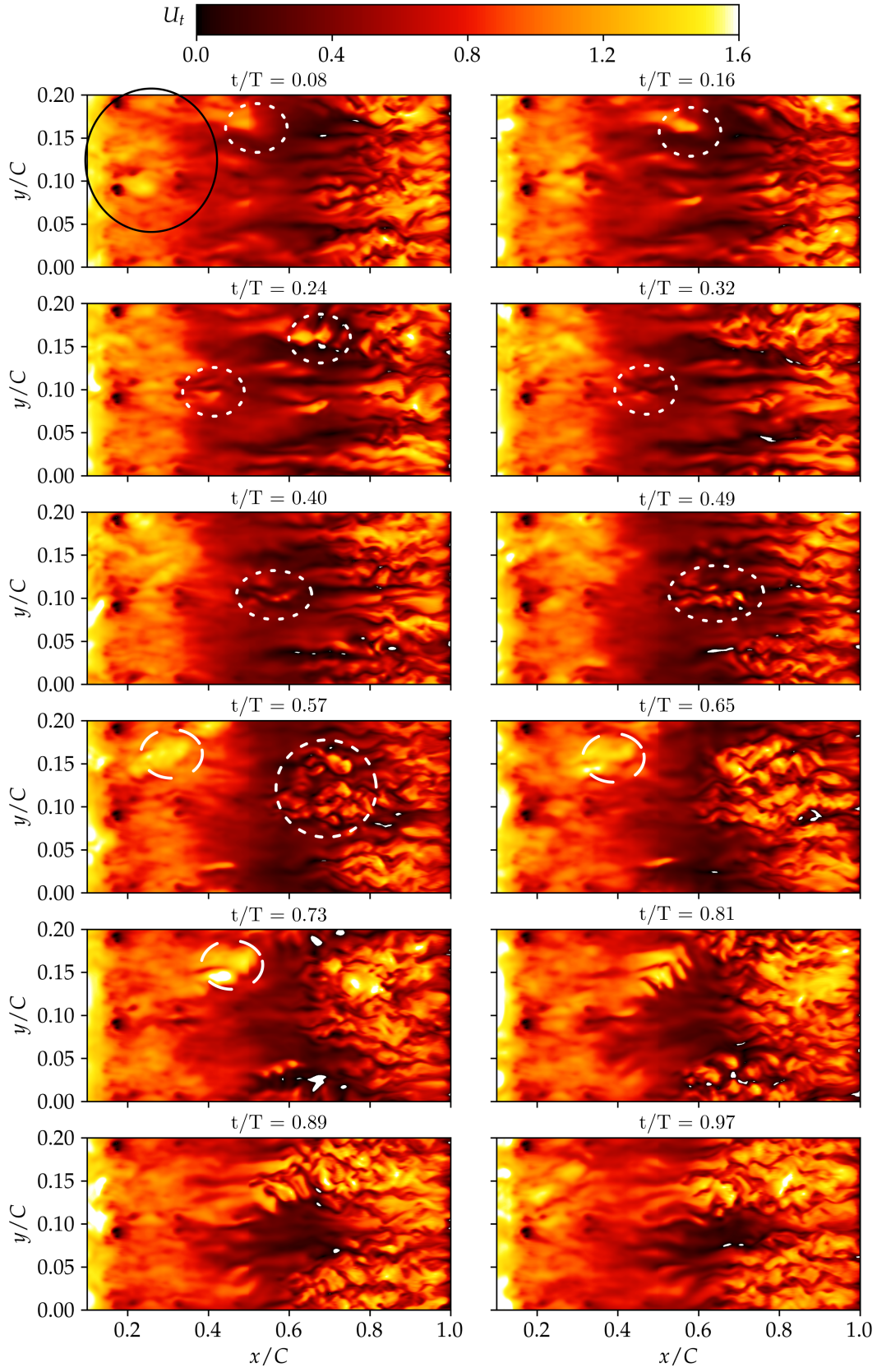

FIGURE 5.17: Contour plot of the tangential velocity, U_t, along the $z-y$ plane extracted slightly above the highest roughness peak, $h/c = 5.3 \cdot 10^{-3}$. The formation and development of streaks due to the roughness peaks is apparent.

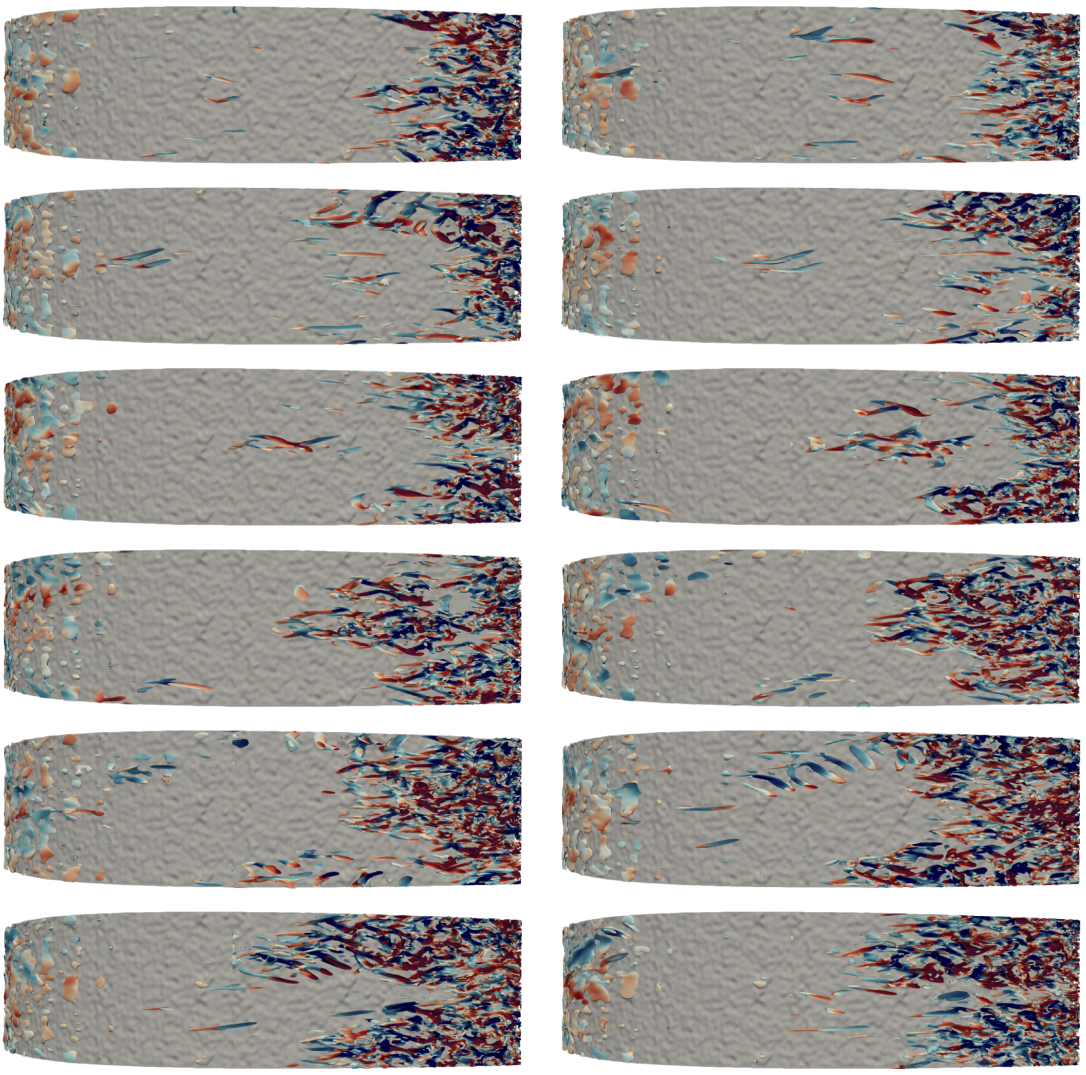

FIGURE 5.18: Perspective top view of the turbine blade with as-cast patch. The iso-surfaces of the Q-criterion ($Q = 1000$) are coloured by the spanwise velocity component, $-0.3 < w < 0.3$.

5.3 Modelled Surface Roughness with the Parametric Forcing Approach

As already mentioned in the previous chapter, another approach to represent surface roughness is the usage of a surface roughness model, see section 2.2.3. In contrast to the complex and computationally costly low-pressure turbine cascade simulation with fully represented rough surfaces, the parametric forcing allows for a significantly lower number of grid points. Hence, a greater number of simulations is possible in order to investigate roughness effects on the low-pressure turbine. The main goal of this section is the analysis of different rough surfaces, expressed in terms of different combinations of roughness densities α_i and heights h as well as lengths l along the blade surface. This was done in order to answer the following questions:

- Can a simple roughness model, namely the Parametric Forcing Approach, be used for transitional cascade flows?
- What are the effects of surface roughness on the blade's boundary layer and the overall loss mechanisms.

Ten different parameter combinations, given in table 5.6, were simulated.

TABLE 5.6: Roughness density and height parameters of the conducted simulations. The mean roughness height to chord length ratio, h/c, the roughness height to chord length ratio, k/c, and the roughness Reynolds numbers Re_k and $Re_{k,\infty}$ are given as well.

Case	α	h^+	h/c $[\cdot 10^{-4}]$	k/c	Re_k	$Re_{k,\infty}{}^{\dagger}$
$F_{\alpha 0 h 0}$	0.0	0.0	0.0	0.0	0.0	0
$F_{\alpha 4 h 15}$	4.0	94.0	15.0	0.003	190	300
$F_{\alpha 6 h 15}$	6.0	94.0	15.0	0.003	190	300
$F_{\alpha 6 h 15,Aft}$	6.0	94.0	15.0	0.003	190	300
$F_{\alpha 6 h 15,LE}$	6.0	94.0	15.0	0.003	190	300
$F_{\alpha 8 h 15}$	8.0	94.0	15.0	0.003	190	300
$F_{\alpha 10 h 15}$	10.0	94.0	15.0	0.003	190	300
$F_{\alpha 10 h 5.4}$	10.0	34.0	5.4	0.00108	30	100
$F_{\alpha 10 h 30}$	10.0	188.0	30.0	0.006	560	600
$F_{\alpha 10 h 50}$	10.0	314.0	50.0	0.01	1000	1000

Compared to the channel cases, the roughness density α is now given for the tangential direction along the blade surface. An important point to note is that, as already mentioned in the earlier chapter, the x-component - or rather the tangential component - of the roughness density α_x is the most significant, whereas the densities in the other two directions only have almost no effect. Hence, in the following the given density values are denoted by α, where $\alpha = \alpha_x$ and $\alpha_y = \alpha_z = 0$. This can be thought of as a representation of $2D$ or $3D$ ribs, as demonstrated by Busse and Sandham (2012); see also section 3.3. Owing to the simplicity of $2D$ and $3D$ ribs, they were used to model surface roughness within DNS studies in order to investigate the effects in turbulent flows (Tsikata and Tachie 2013). Furthermore, higher roughness density values ($\alpha/geq4$) were chosen, because insufficient form drag and blockage effects were observed for lower values in the turbulent channel flow simulations.

The height parameter, h, denotes the mean roughness height in wall-normal direction from the blade surface. For all of the simulations the box profile (figure 5.19)

$$F(z,h) = \begin{cases} 1, & \text{if } z \leq \eta(h) \\ 0, & \text{if } z > \eta(h) \end{cases} \tag{5.10}$$

was used, with $\eta(h) = 2h$ - determined by equation 2.33. This means that the top of the box profile roughness is located at $2h$.

The range of roughness heights and hence the resulting roughness Reynolds numbers, Re_k, was chosen for two reasons. Firstly, the roughness model can be tested for the admissible roughness

height, $k_{adm.}$[‡]. As long as the roughness does not exceed this threshold, there is no influence on the boundary layer. As stated in section 5.2.3, the admissible roughness height for the simulation setup is $k_{adm.} \leq 1.0 \cdot 10^{-3}$ and is valid for the turbulent boundary layer part.

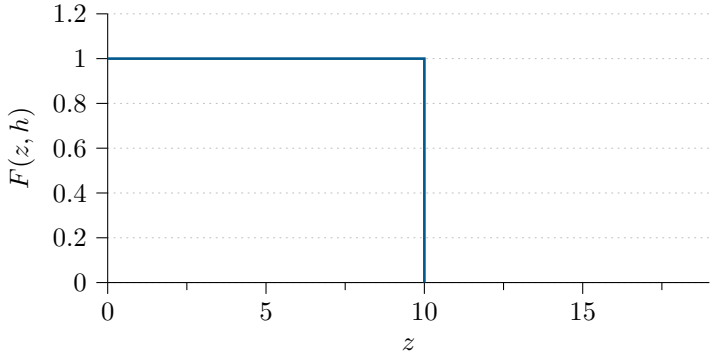

FIGURE 5.19: The box profile form function, $F(z,h)$, that was used for the low-pressure turbine simulations.

Furthermore, k can be imagined to have the same total height as the box profile, i.e. $2h$. This is consistent with other studies (Klebanoff et al. 1992; Rao et al. 2017; Redford et al. 2010), where the height of a single roughness element was equated with the roughness height, k. Case $F_{\alpha 10h5.4}$ has a mean roughness height of $h = 5.4{\cdot}10^{-4}$ and hence a roughness height of $k = 2h = 1.08{\cdot}10^{-3}$, which is right on the admissible threshold. The other cases have roughness heights well above this threshold and are expected to trigger transition to varying degrees, as well as showing an impact on the turbulent boundary layer.

Secondly, another transition parameter, namely the roughness Reynolds number,

$$Re_k = \frac{U_k k}{\nu_k}, \tag{5.11}$$

can be investigated, where U_k and ν_k are the tangential velocity and the kinematic viscosity at roughness height k for a laminar case without roughness (Klebanoff et al. 1992). An important point to remember is that this definition of the roughness Reynolds number is different to that used in section 5.2.3, which was based on the free stream velocity, U_∞, rather than U_k and on the equivalent sandgrain roughness, k_s, rather than k. Redford et al. (2010) conducted direct numerical simulations of a single roughness element in a compressible flat plate boundary layer and found that transition occurs for $Re_k > 300$ for incompressible flows. However, the critical Reynolds number heavily depends on the flow environment. It increases for increasing Mach numbers (Redford et al. 2010), but decreases when free-stream turbulence is present (Tani 1969) as well as for adverse pressure gradients (Tsikata and Tachie 2013). This criterion was chosen because of the sudden change between the smooth and rough surface for the forcing model and thus is expected to act in a similar way to the single roughness elements. With the chosen modelled roughness heights ranging from $Re_k = 30 - 1000$, see table 5.6, this will be examined.

In figure 5.20 (top), the length over which the forcing terms were applied is depicted. For eight out of the ten cases the roughness force was applied between $s_1/S = 0.31$ and $s_3/S = 0.94$, covering around 63.32% of the blade's suction surface, as this is the critical region where roughness

[‡]For the forcing model $k_{adm.}$ is based on k rather than k_s ($k_{s,adm.}$)

affects the boundary layer the most (Bons 2010; Rao et al. 2014b). Additionally, the case $F_{\alpha 6h15,LE}$ (fig. 5.20; bottom right) was simulated in order to see the effect of a roughness patch covering almost the whole suction surface. The patch starts at around $s_1/S = 0.01$ and ends at $s_3/S = 0.94$, resulting in a coverage of 93.47% of the suction surface. As the T106A blade has a strong curvature until about $s_2/S = 0.5$, another case, $F_{\alpha 6h15,Aft}$ (fig. 5.20; bottom left), was simulated, where the roughness force starts slightly after half way ($s_1/S = 0.52$) of the suction surface. The end point is the same as for the other cases, leading to a patch length of 42.71%. In this region the curvature effects are only minimal.

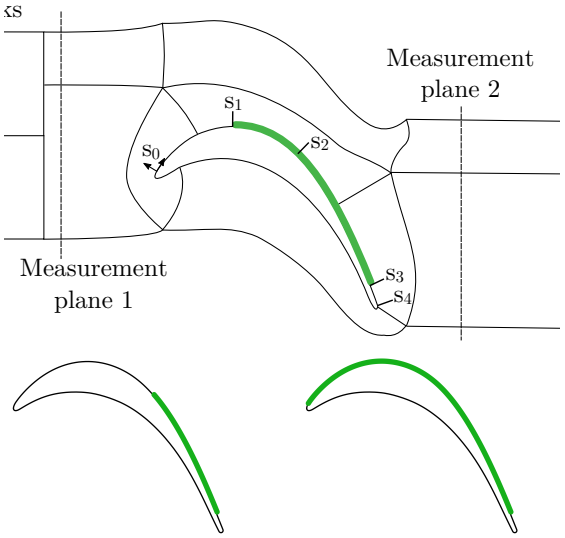

FIGURE 5.20: Blade coverage of the applied parametric forcing terms for the different cases (top). On the bottom left and right the special cases $F_{\alpha 6h15,Aft}$ and $F_{\alpha 6h15,LE}$, respectively, are depicted, for which a different patch length was chosen.

In the following, results and discussion of the ten simulations are presented, where the effects on the boundary layer and the loss mechanisms are investigated. The different cases are split up into three distinct groups. Firstly, the influence of different roughness densities at a constant roughness height is examined. After that the focus is on varying roughness heights at a constant roughness density. Then, for a fixed pair of roughness density and height the effect of roughness patch length is analysed.

5.3.1 Effect of different Roughness Parameters on the Boundary Layer

In this subsection the effect of the varying roughness parameters, namely the density, the height and the lengths, on the boundary layer are investigated. The simulation setup and conditions are the same ones given in section 5.1.

5.3.1.1 Varying Roughness Densities, α, at constant Roughness Height, $h = 15$

The effects of different roughness densities at a constant roughness height are investigated in the following section. In the earlier section 5.2 the as-cast roughness patch was introduced, having

a roughness height of $h/c = 4.7 \cdot 10^{-4}$. It was shown that, due to the low roughness to boundary layer height ratio, there was only a low impact on the boundary layer and the losses. Thus, in order to get a clearer picture regarding the implications of the surface roughness model, the height for the following simulations was increased to $h/c = 15 \cdot 10^{-4}$, elevating the roughness height to $k = 3.0 \cdot 10^{-3}$, which is above the admissible roughness height $k_{adm.} = 1.0 \cdot 10^{-3}$. Furthermore, the roughness Reynolds number for this case is $Re_k = 190$, which is below the critical roughness Reynolds number threshold $Re_k = 300$. Hence, it is expected that the sharp edge imposed at the beginning of the forcing region does not cause transition itself, but only the roughness along the blade's suction surface due to the exceeded admissible roughness height. Even though it does not present a representative roughness height for manufactured blades, valuable research insights can be gained.

Figure 5.21 shows the development of the displacement thickness, δ^*, and momentum thickness, Θ, as well as

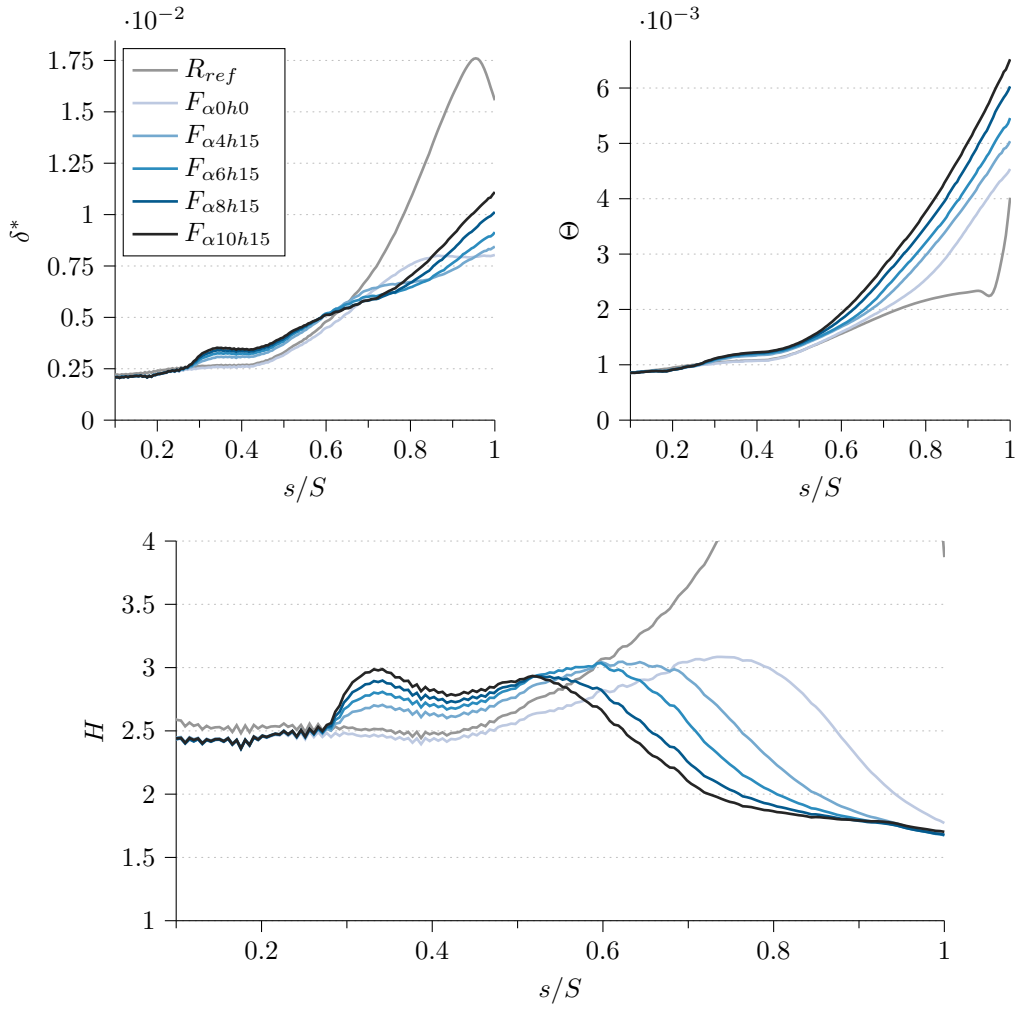

FIGURE 5.21: The displacement, δ^*, and momentum thickness, Θ, as well as the shape factor, H, along the blade surface.

the shape factor, $H = \delta^*/\Theta$, in order to get a clearer picture on the influence of the varying roughness densities on the boundary layer. As already observed in the previous contour plot,

δ^* rapidly and considerably increases for the reference case, R_{ref}, due to the large separation bubble, whereas the momentum thickness remains low until the point of laminar to turbulent transition. As a result, a strong increase of the shape factor, H, is seen. For case $F_{\alpha 0 h 0}$ the displacement thickness increases until a fully turbulent boundary layer (TBL) is achieved and remains constant afterwards. In contrast, once the TBL is established, the momentum thickness rapidly increases due to the incoming wakes, which was already discussed in chapter 4. The shape factor values for the laminar (around $H = 2.5$) and turbulent boundary layer (around $H = 1.6 - 1.8$) match the ones given by Rao et al. (2014a).

Things become more interesting when looking at the different roughness cases. In the laminar boundary layer region before the start of the roughness patches, all but the reference case coincide, confirming two important points. Firstly, the cases are statistically converged and secondly, the sudden jump between no roughness and roughness does not impact the upstream laminar boundary layer. Furthermore, the roughness does not seem to have a large influence on the development of the displacement and momentum thickness of the laminar boundary layer, which is in line with the findings of Stripf et al. (2009) as well as the ones in section 5.2.1. Both remain fairly constant over the range $s/S = 0.35 - 0.55$, which is more evident when looking at the shape factor, H. However, a slight offset in this region for increasing roughness densities can be seen.

Once the transition point is reached, both δ^* and Θ increase for increasing α values, which again is in line with Stripf et al. (2009). An important point to note is that the growth of momentum thickness is more rapid compared to the growth of the displacement thickness, which is revealed by the shape factor, H. After the roughness patch ends at $s_3/S = 0.94$, the shape factors coincide for all roughness cases and start to level off.

In order to further investigate the onset of transition for the different roughness parameters, the maximum turbulence intensity, Tu_{max}, along the blade surface is used, defined by

$$Tu_{max} = \sqrt{\left\langle \widetilde{u'u'} \right\rangle + \left\langle \widetilde{v'v'} \right\rangle + \left\langle \widetilde{w'w'} \right\rangle}\Bigg|_{max} . \tag{5.12}$$

Figure 5.22 shows the results for the different roughness densities at constant roughness height.

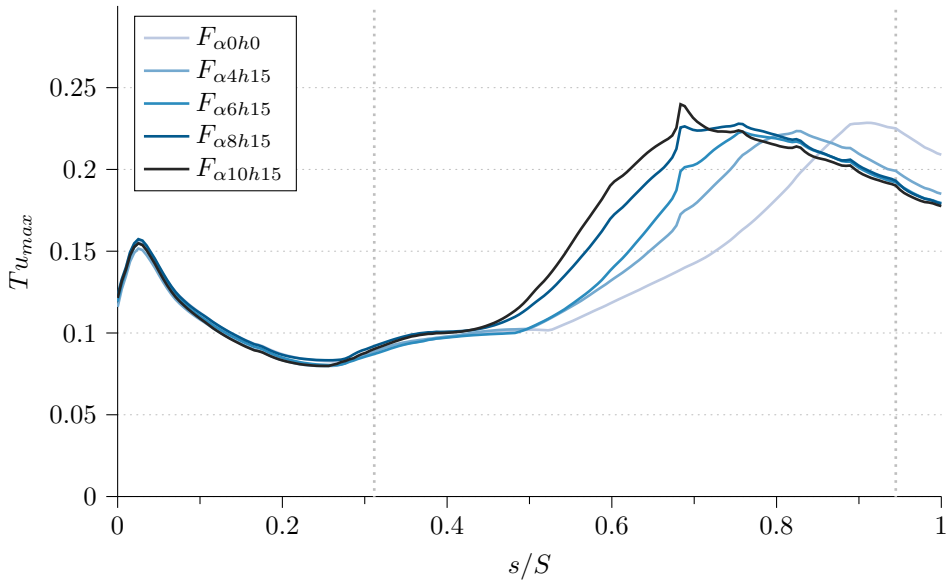

FIGURE 5.22: Onset of transition, indicated by a rapid increase of the maximum turbulence intensity, Tu_{max}, for the different roughness densities at constant roughness height $h = 15 \cdot 10^{-4}$.

The start and end of the roughness patch is denoted by the dotted grey lines. As can be seen, by increasing the density value of the modelled roughness the transition point moves upstream. Furthermore, the rate of transition, based on the inclination of the slopes, is higher for higher values of α. It is apparent from this plot again that the added roughness force does not have an effect on the laminar boundary layer, apart from the transition onset, before and after the start of the roughness patch. This was already observed in chapter 5 for the channel cases with the parametric forcing, where there was only a minimal effect on ΔU^+. However, in case of the low-pressure turbine it can be argued that the deficiency of the forcing model to impact the laminar boundary layer does not play the most important role, because the effect of roughness in this region is considered to be small anyway, as stated by Stripf et al. (2009).

5.3.1.2 Varying Roughness Heights, h, at constant Roughness Density, $\alpha = 10$

In this section the effects of different roughness heights at constant roughness density, $\alpha = 10$, are investigated. The structure and result presentation is similar to the previous section. The forcing model is examined with respect to the admissible roughness height threshold $k_{adm.} < 1.0 \cdot 10^{-3}$ as well as the critical roughness Reynolds number $Re_k > 300$. As already observed for the cases with $Re_k = 190$ in the previous chapter, the sudden jump due to the roughness force did not cause transition. For this reason two cases with higher roughness Reynolds numbers were simulated, with $Re_k = 560$ and $Re_k = 1000$. The relatively high density value, $\alpha = 10$, was chosen because of the profound effect it has on both the onset of transition and the development of the turbulent boundary layer. Thus, a more reliable picture for case $F_{\alpha 10h5.4}$ is expected, where the roughness height $k = 1.08 \cdot 10^{-3}$ is right on the important and widely used admissible roughness height threshold, $k_{adm.}$.

Figure 5.23 shows the velocity contours, the edge of the boundary layer (black dashed) and the displacement thickness, δ^* (white dashed), on the suction surface of the turbine blade.

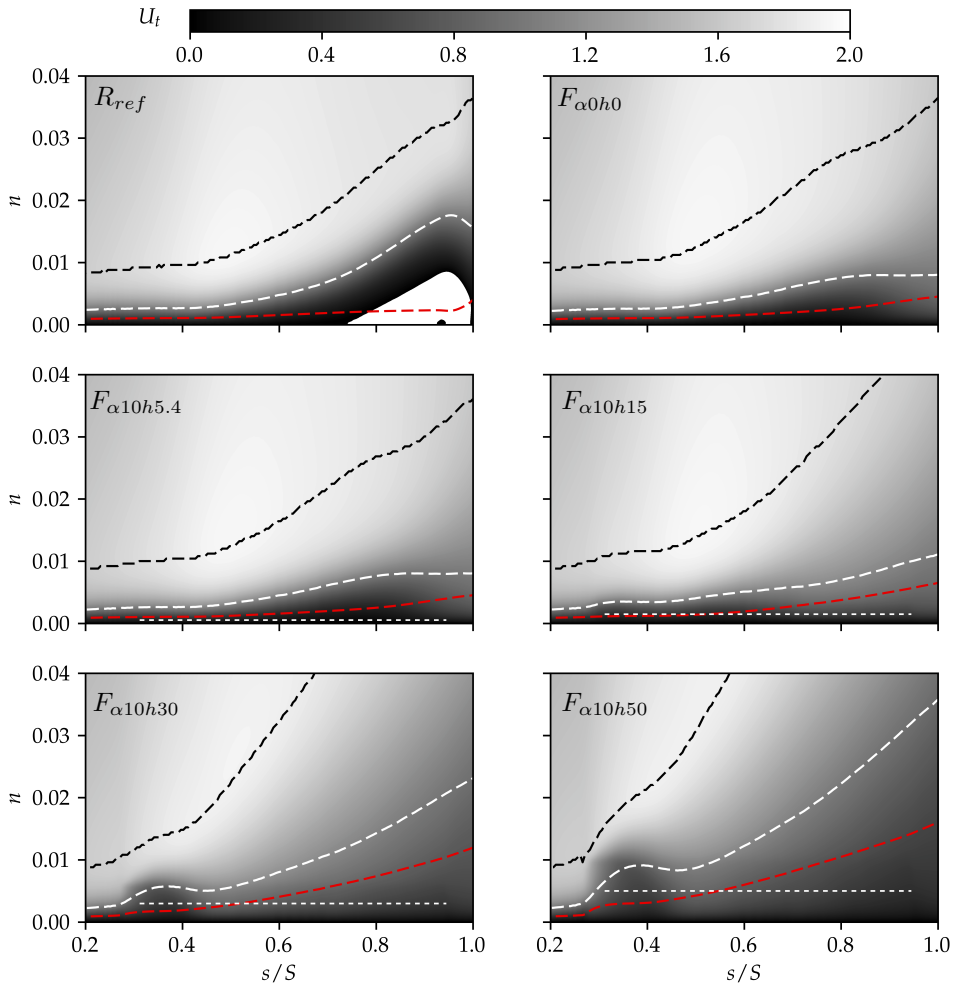

FIGURE 5.23: The tangential velocity, U_t, contour plots along the blade suction surface for different roughness heights at constant roughness density are shown.

To determine δ^*, the tangential flow velocity, U_t, was extracted as a function of the wall normal direction. Due to the pronounced wake regions in the boundary layer profiles, the first derivative of the tangential velocity in the wall normal direction, $\partial U_t/\partial n$, was used to determine the boundary layer edge. The edge of the boundary layer is denoted by the position where the derivative is minimal, i.e. $\min(\partial U_t/\partial n)$, or crosses a given value

$$\min\left(\frac{\partial U_t}{\partial n}\right) < \epsilon = 0.01 \left.\frac{\partial U_t}{\partial n}\right|_{wall}. \tag{5.13}$$

Cases $F_{\alpha 0h0}$ and $F_{\alpha 10h5.4}$ look very similar in terms of the velocity contours and the boundary layer displacement and momentum thickness, which gives a first hint that the roughness with height $k = 1.08 \cdot 10^{-3}$ does not have a strong impact. When the roughness height is tripled ($F_{\alpha 10h15}$) a clear effect on the boundary layer can be observed. For heights higher than that, i.e. cases $F_{\alpha 10h30}$ and $F_{\alpha 10h50}$, dramatic changes occur. A low velocity region at the beginning

of the roughness area is apparent and a sudden deflection of the boundary layer is seen, which results in a rapid increase in displacement and momentum thickness.

In order to get a clearer picture of the boundary layer development, the displacement thickness, δ^*, and momentum thickness, Θ, as well as the shape factor, H, along the suction surface are shown in figure 5.24.

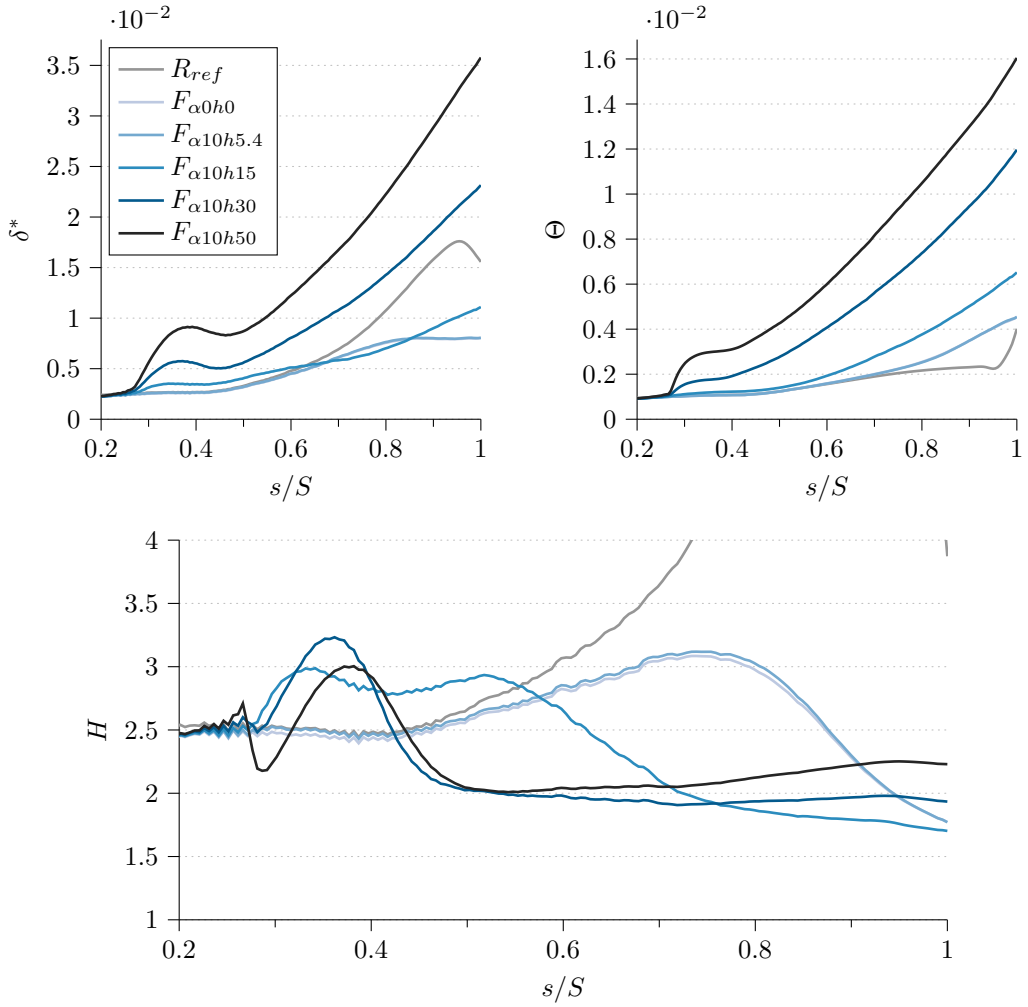

FIGURE 5.24: The displacement, δ^*, and momentum thickness, Θ, as well as the shape factor, H, along the blade surface.

The first thing to notice is that the cases $F_{\alpha 0h0}$ and $F_{\alpha 10h5.4}$ - with $k = 1.08 \cdot 10^{-3}$ and thus only marginally higher than $k_{adm.} < 1.0 \cdot 10^{-3}$ - show almost the same behaviour and only a slight difference in the shape factor curve can be observed. Any further increase in roughness height is now expected to have a stronger effect on the boundary layer.

Increasing the roughness heights above the admissible level leads to strong increases in both the displacement and momentum thickness. For case $F_{\alpha 10h30}$ the change in shape factor from around 2.5 to well above 3 at the beginning of the rough region indicates a stronger influence on the displacement rather than the momentum thickness. After the peak and when transition occurred H decreases to a value of about 1.9, which is common for low-pressure turbine blades as already mentioned. The picture is different for case $F_{\alpha 10h50}$, where a steep drop of H before the

start of the forcing region is apparent, i.e. the roughness has a strong influence on Θ upstream. Right at the start of the roughness region, the shape factor increases again, as observed for case $F_{\alpha 10h30}$, and then decreases to about 2.0 at $s/S \approx 0.5$. Towards the trailing edge of the blade H slowly goes up to a value of 2.2, which means that at this high roughness height the influence on the displacement thickness is stronger than on the momentum thickness.

The onset of transition for the different roughness heights at a constant roughness density is shown in figure 5.25.

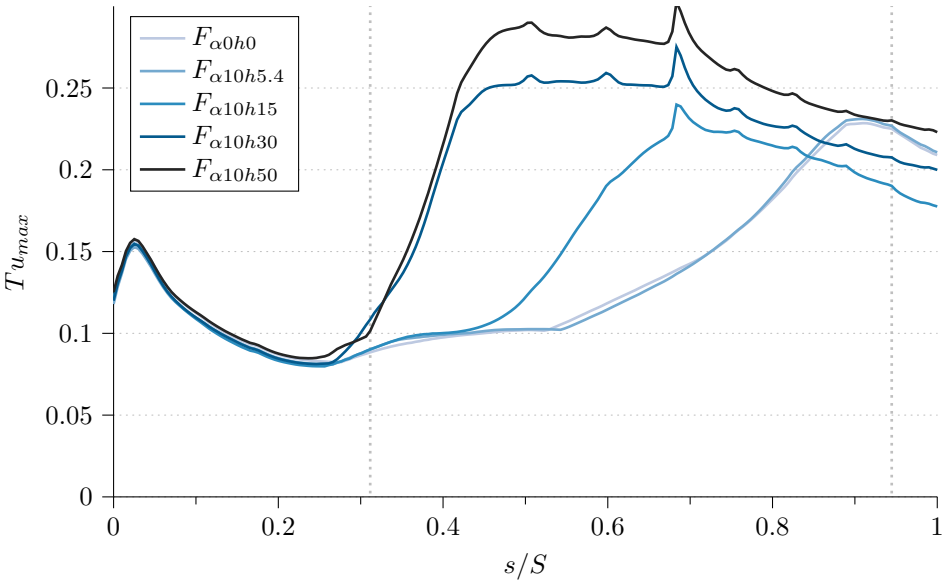

FIGURE 5.25: The maximum turbulence levels, Tu_{max}, along the blade surface for the different roughness height cases. Strongly increasing values indicate the onset of transition.

The slope and start of transition for the case without roughness and the case with the minimum roughness height are almost identical, which also confirms the admissible roughness height assumption. For case $F_{\alpha 10h5.4}$ the transition point is shifted marginally downstream compared to $F_{\alpha 0h0}$. By tripling the minimum height, for case $F_{\alpha 10h15}$ a considerable change of the transition onset can be observed. For the two cases with the highest roughness heights ($Re_k = 560$ and 1000) transition starts immediately at the beginning of the forcing region. This is consistent with a roughness Reynolds number threshold, $Re_k > 300$ (or $Re_{k_s,\infty} > 600$ (Bons 2010)), after which transition due to a roughness element is induced. As seen in the velocity contour and the boundary layer thickness plots, the start of the roughness region for these two cases indeed appears to act like a single roughness element.

To further examine the change in boundary layer development for $Re_k > 300$, instantaneous z-vorticity contours, ω_z, of cases $F_{\alpha 10h15}$, $F_{\alpha 10h30}$ and $F_{\alpha 10h50}$ are shown in figure 5.26.

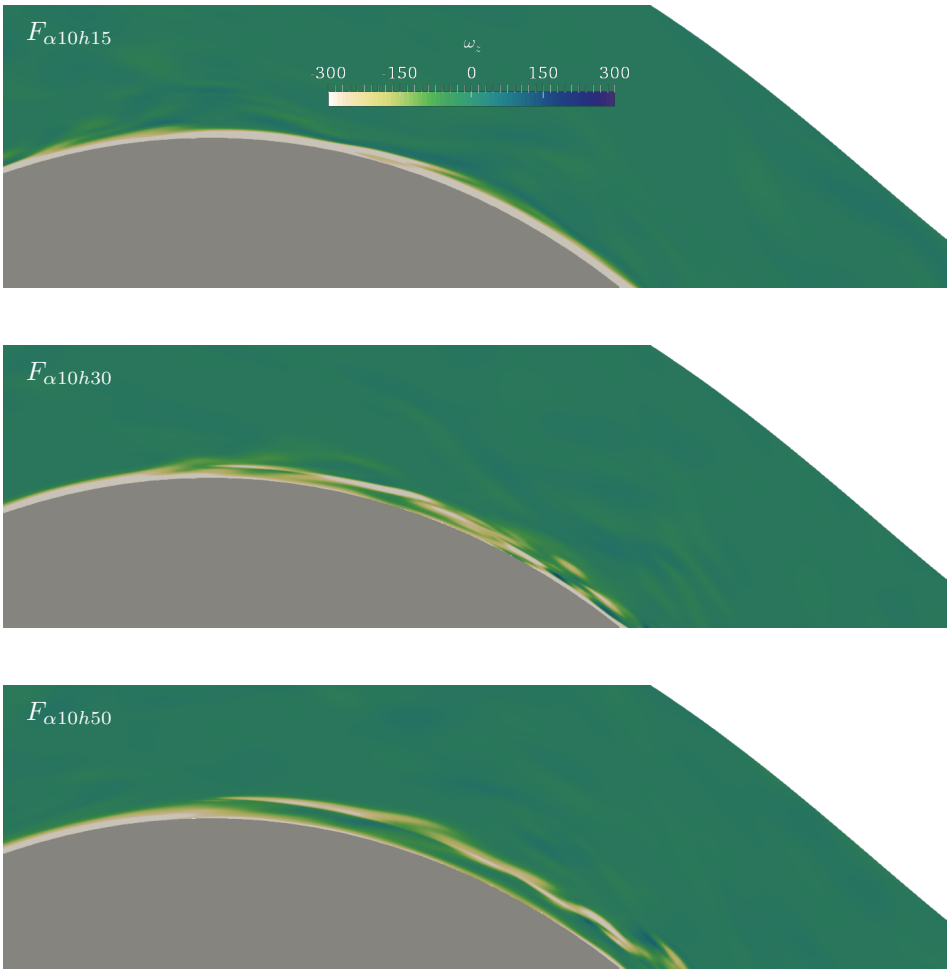

FIGURE 5.26: Instantaneous z-vorticity contours, ω_z, $(-300 \leq \omega_z \leq 300)$ for different roughness heights. For cases with $Re_k > 300$ a detached shear layer is evident.

As can be seen, for case $F_{\alpha 10h15}$ there is no apparent disturbance in the transition region from a smooth to a rough surface. However, when the critical roughness Reynolds number threshold is crossed, a short detached shear layer emerges at the start of the forcing region, which then immediately transitions. The effect is strongest for the highest roughness height case. The appearance of a detached shear layer was also observed in the simulations of Rao et al. (2017) for $Re_k = 400$, whereas for $Re_k = 800$ sudden transition shortly after the roughness element occurred. It can be concluded that the sudden transition from smooth to rough surface in terms of the roughness model does not impact the boundary layer as long as $Re_k < 300$ is maintained. This allows for specific roughness patch placements on the suction surface if necessary.

In this section the existence of both the admissible roughness height, $k_{adm.} < 1.0 \cdot 10^{-3}$, as well as the critical roughness Reynolds number threshold $Re_k = 300$ was confirmed with the parametric forcing approach simulations, increasing the confidence in the viability and reliability of this simple forcing model for linear low-pressure turbine cascade simulations.

5.3.1.3 Varying Roughness Lengths, l, at constant Roughness Density, $\alpha = 6$ and Height, $h = 15$

As mentioned in the last section, when maintaining roughness Reynolds numbers below the threshold $Re_k < 300$, the sudden change between smooth and rough surface does not cause transition. This allows roughness patches to be placed at different positions on the blade's suction surface in order to further investigate the boundary layer development. In this section three different roughness patch lengths are investigated. In addition to case $F_{\alpha 6h15}$, which was already introduced above, cases $F_{\alpha 6h15,aft}$ and $F_{\alpha 6h15,LE}$ were simulated, see also table 5.6 and figure 5.20. The forcing region for $F_{\alpha 6h15,aft}$ starts after half of the suction surface length, $s/S = 0.5$, and thus mainly acts in the low adverse pressure gradient part of the blade passage. For case $F_{\alpha 6h15,LE}$ a roughness patch covering almost the whole suction surface was used.

The height $h = 15$ was chosen, so that the roughness Reynolds number $Re_k = 190$ is slightly less than the critical value $Re_{k,crit.} = 300$. The roughness density, $\alpha = 6$, is in the medium range and showed a noticeable effect on the onset of transition and the turbulent boundary layer. The aim is to gain more insights of the roughness model effect on the laminar boundary layer around the leading edge as well as the influence on the transition onset and the TBL in a lower adverse pressure gradient region.

Figure 5.27 presents the development of the displacement and momentum thickness as well as the shape factor. For comparison purposes, case $F_{\alpha 0h0}$ is shown too. Case $F_{\alpha 6h15,LE}$ shows an elevated displacement and momentum thickness starting from the leading edge compared to the other cases, owing to the added roughness in this region. At the start of the roughness patch of $F_{\alpha 6h15}$ this difference is minimised for δ^* and both cases coincide until about $s/S = 0.7$. After that the slopes diverge with case $F_{\alpha 6h15,LE}$ showing the largest displacement thickness. The momentum thickness is higher along the whole suction surface, as can also be seen in the shape factor plot. The change in H when transition occurs is less dramatic in case $F_{\alpha 6h15,LE}$. Compared to the no roughness case, $F_{\alpha 0h0}$, this means that the transition process induced by the incoming wakes is calmer and less rapid.

When comparing cases $F_{\alpha 6h15,aft}$ and $F_{\alpha 6h15}$ it can be observed that the sudden jump in displacement and momentum thickness due to the change from smooth to rough surface is not present. In fact the boundary layer values are very similar to the no roughness case values until earlier transition is induced, starting at around $s/S \approx 0.51$. Towards the trailing edge, all cases converge to similar shape factors of $H = 1.6 - 1.8$.

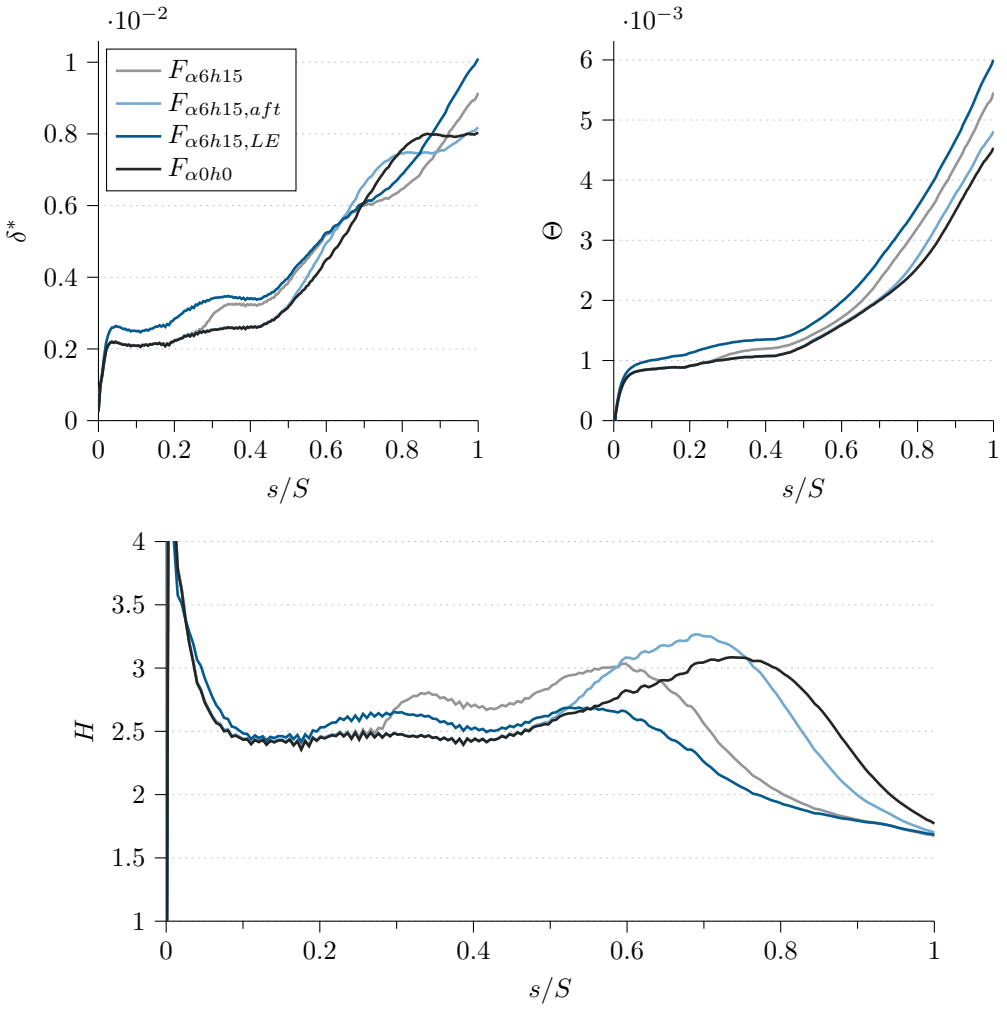

FIGURE 5.27: The displacement, δ^*, and momentum thickness, Θ, as well as the shape factor, H, along the blade surface, s/S

The maximum turbulence level along the suction surface for the different cases is shown in figure 5.28. The onset of transition is only slightly shifted upstream for the roughness patch covering the whole blade compared to case $F_{\alpha 6h15}$. However, as already noted, the transition process is less sudden and rapid, indicated by the smaller inclination of the slope starting at about $s/S \approx 0.48$, as well as calmer, indicated by the lower levels of maximum turbulence. Furthermore, the roughness forcing in the laminar region around the leading edge has an effect on the boundary layer. Given the only slight shift of the transition position, this is probably due to the fact that the blade itself is slightly thicker because of the roughness patch. This was also the reason for the higher displacement and momentum thicknesses.

Transition for cases $F_{\alpha 0h0}$ and $F_{\alpha 6h15,aft}$ start at the same position, but the rate is increased by the roughness. Even though $F_{\alpha 6h15}$ and $F_{\alpha 6h15,aft}$ have the same roughness parameters, the transition rate for case $F_{\alpha 6h15}$ is higher. As the roughness patch for the latter case starts further upstream in a higher adverse pressure region, a possible explanation might be the combined effects of roughness and higher APG, as also observed by Tsikata and Tachie (2013).

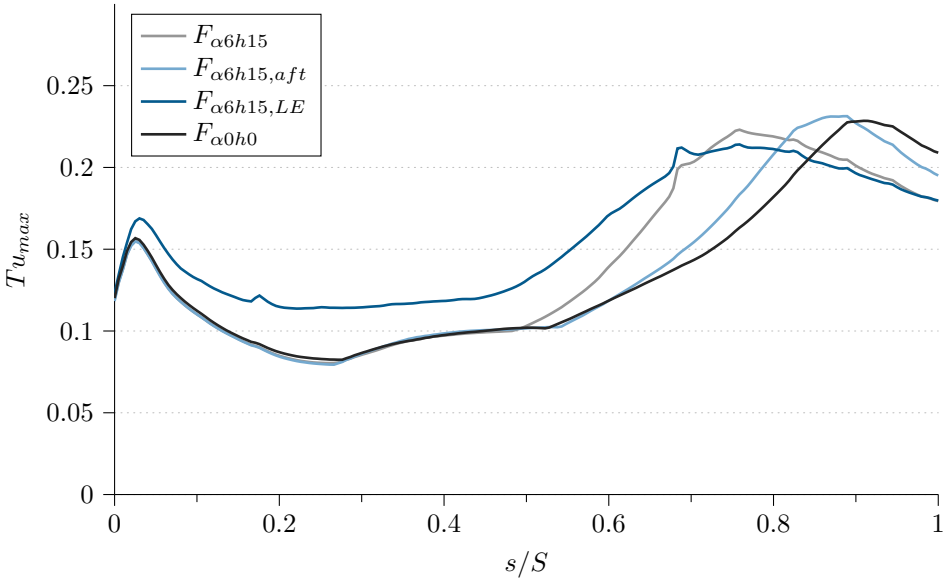

FIGURE 5.28: Onset of transition indicated by the maximum turbulence levels, Tu_{max}.

In conclusion, some significant findings have been found in this section. Firstly, the transition position is barely affected by the patch extending to the leading edge compared to case $F_{\alpha 6h15}$. Secondly, the shortened transition length due to the roughness effect, when comparing $F_{\alpha 0h0}$ and $F_{\alpha 6h15,aft}$, whose onset of transition position is the same, but a fully turbulent boundary layer is achieved first by $F_{\alpha 6h15,aft}$. Thirdly, the shortening of the transition length due to the combined effects of roughness and adverse pressure gradient, when comparing $F_{\alpha 6h15}$ and $F_{\alpha 6h15,aft}$. Both cases have the same roughness parameters, but are placed in different APG regions. Case $F_{\alpha 6h15}$, being exposed to higher gradients, showed a more rapid transition process.

5.3.2 Effect of different Roughness Parameters on the Loss Mechanisms

Having dealt with the effect of roughness on the state and development of the boundary layer, the focus of this section is on the loss mechanisms. The structure follows the same as above, starting with the analysis of varying roughness densities at constant roughness height, followed by the roughness height variation and ending with the different forcing patch lengths.

5.3.2.1 Varying Roughness Densities, α, at constant Roughness Height, $h = 15$

In this subsection the effects on the loss mechanisms for varying roughness densities at constant roughness height, $h = 15$, are investigated. The Denton, mixed-out and wake distortion losses (A–F) are presented in figure 5.29.

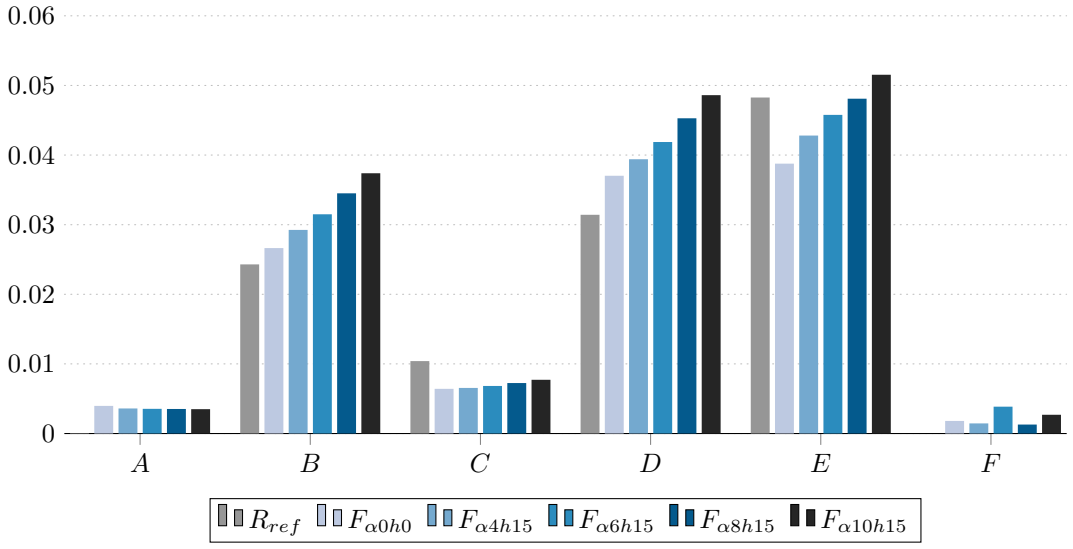

FIGURE 5.29: Denton losses and the respective loss contribution terms (A–D) and the overall mixed-out as well as wake distortion losses (E,F).

Firstly, the profile losses and its different terms are examined. As can be seen, the overall Denton losses, D, increase for increasing α values as well as for the addition of incoming wakes - compared R_{ref} and $F_{\alpha 0h0}$. That is due to the earlier onset of transition, exposing the turbulent boundary layer to the roughness for a longer period of time as well as to denser roughness patches, resulting in higher momentum thicknesses. This is apparent when looking at the momentum loss term, B, which shows exactly the mentioned trend. As already observed in the shape factor plots, the displacement thickness plays a less dominant role towards the trailing edge, which is also true for the loss contribution, C. The reference case, R_{ref}, however, reveals a much higher influence for term C due to the large separation bubble, whereas term A, the base pressure contribution, is negative. The reason for the negative value is a second separation bubble right behind the trailing edge, as noted in chapter 4. Because of this, ζ (D) is low compared to the other cases.

The mixed-out losses, E, have the same trend as the profile losses, but are slightly higher due to the mixing out of the incoming wakes, ω_{wake} (F), within and after the blade passage. There is no apparent reason for the different wake distortion losses, which show a rather random behaviour, appearing to be independent of the roughness effects. Owing to the large separation bubble in the reference case, the mixed-out losses are relatively high when compared to the larger roughness density values.

The total pressure losses extracted at measurement plane 2 along the pitchwise direction for the varying roughness densities are given in figure 5.30.

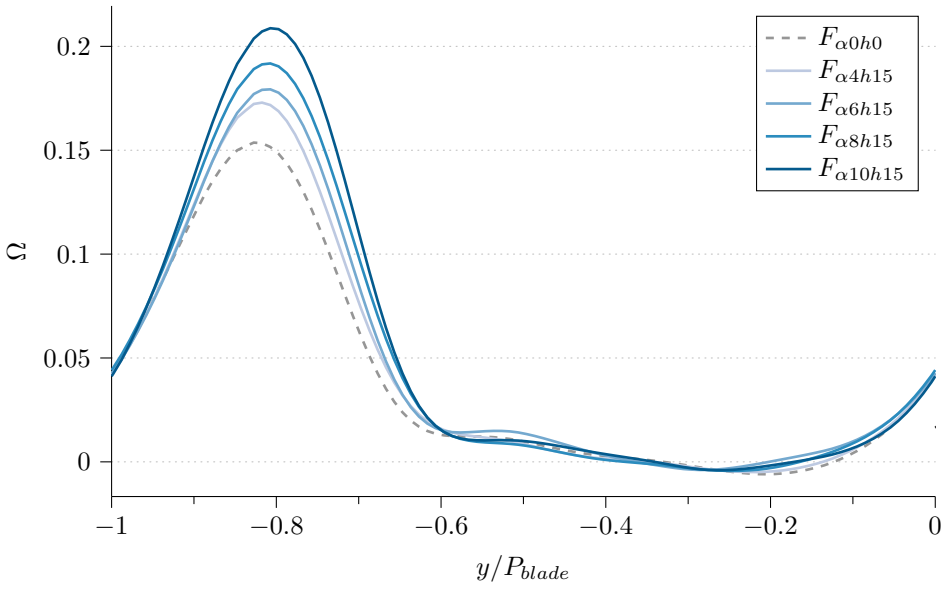

FIGURE 5.30: Total pressure loss profiles, Ω, for different roughness densities at constant height $h = 15 \cdot 10^{-4}$.

As can be observed, the total pressure losses in the blade wake increase for increasing density values. Furthermore, owing to the roughness a slight flow deflection is evident, indicated by the slight shift of the profile peaks in positive pitchwise direction. Interestingly, in the blade passage region a small bump in the $F_{\alpha 6h15}$ profile can be seen, which is in line with the high wake distortion loss for that case.

To summarise, a clear positive correlation between the different roughness densities, α, and the four loss measures was observed.

5.3.2.2 Varying Roughness Heights, h, at constant Roughness Density, $\alpha = 10$

Figure 5.31 shows the different losses for the different roughness heights, h, at constant roughness density, $\alpha = 10$. Looking at the overall profile losses, D, a rapid increase for increasing roughness heights above the admissible roughness height $k_{adm.}/c > 1.0 \cdot 10^{-3}$ can be observed. As already mentioned, the reason for this is in particular due to the higher momentum thicknesses, caused by the longer exposure times to the roughness patches and the extreme roughness heights. The momentum thickness loss term, B, dramatically increases. Furthermore, the loss contribution of the displacement thickness, C, also plays a more pronounced role once the critical roughness Reynolds number threshold, $Re_k \approx 300$, is exceeded, i.e. for cases $F_{\alpha 10h30}$ and $F_{\alpha 10h50}$. Interestingly, the base pressure term, A, slightly decreases for increasing h values, but only have a marginal effect on the overall Denton loss. The results for the no roughness and the minimum roughness case are identical for the profile loss terms, giving confidence in the validity of the admissible roughness height threshold when using the forcing model.

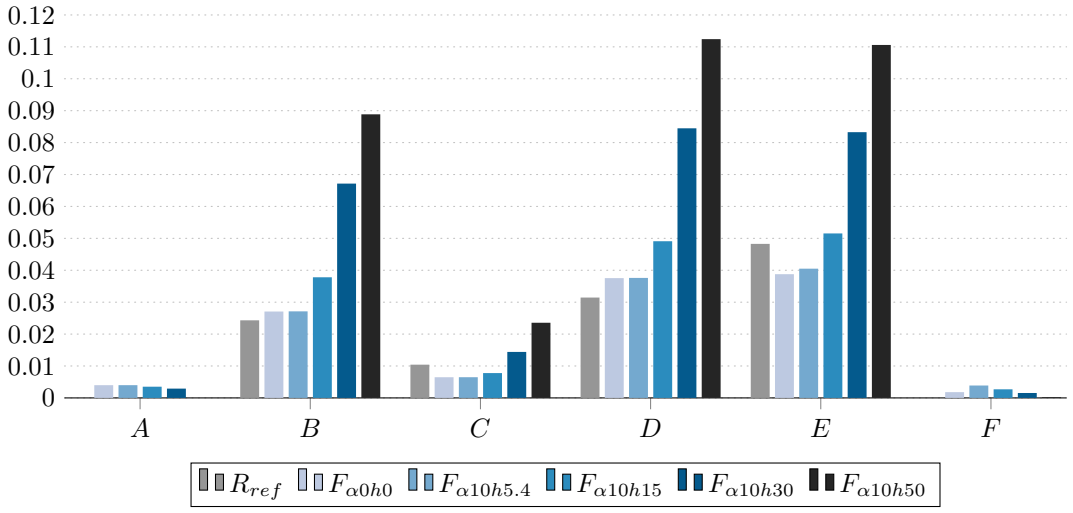

FIGURE 5.31: Denton losses and the respective loss contribution terms (A–D) and the overall mixed-out as well as wake distortion losses (E,F).

Again, the mixed-out losses (E) follow the same trend as the profile losses (D). Compared, they are slightly elevated for cases $F_{\alpha 0h0}$, $F_{\alpha 10h5.4}$ and $F_{\alpha 10h15}$ due to the mixing out of the incoming wakes (F). The reason for the higher ω_M for $F_{\alpha 10h5.4}$ compared to $F_{\alpha 0h0}$ is the augmented wake distortion loss. Hence, even though the profile losses are the same, the added roughness seems to effect the wakes passing through the blade passage.

For the two highest roughness cases, however, the mixed-out loss is lower than the profile loss. Moreover, the wake distortion losses decrease as well. This might be an indication for a mixing effect between the passing wakes and the thick turbulent boundary layers. The TKE production is very high for these cases (see figure C.9, which means an energy transfer between the flow in the passage towards the blade surface. Additionally, after the blade, the blade wake and the bar wakes seem to merge, resulting in a further reduction of the bar wake mixing effects.

Figure 5.32 shows the total pressure loss for the different roughness heights. As already observed for the Denton and mixed-out losses, the roughness height has a significant effect on the total pressure losses. A very strong deflection due to the extreme forcing model heights can be seen, causing the observed shift of the blade wake loss peaks in the positive pitchwise direction. Furthermore, the rapid widening of the blade wake for increasing roughness heights results in a decrease of the blade passage region. This is a confirmation for the mentioned merging effect between the blade and the bar wakes, leading to the lower wake distortion losses, ω_{wake}. The profiles for cases $F_{\alpha 0h0}$ and $F_{\alpha 10h5.4}$ are very similar.

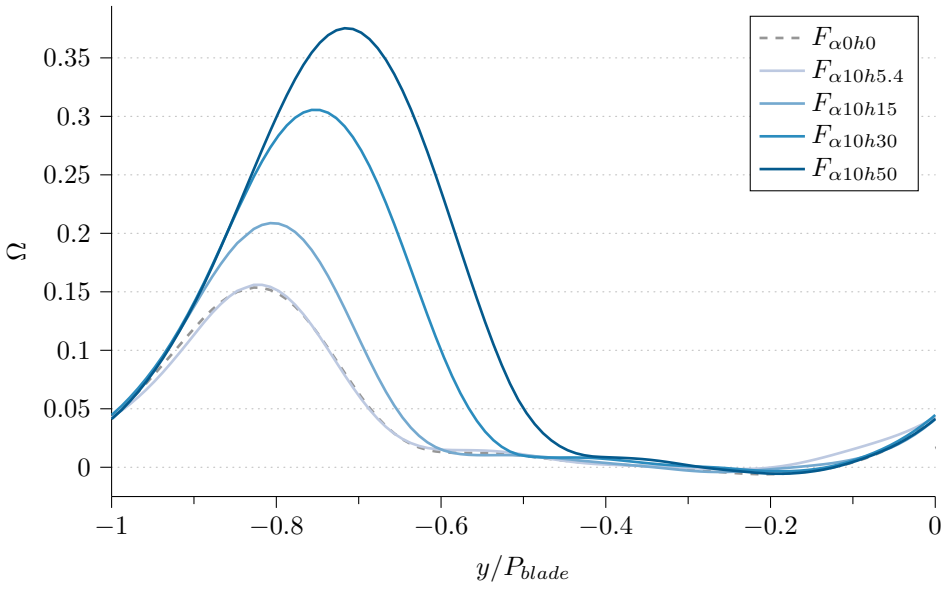

FIGURE 5.32: Total pressure loss profiles, Ω, for different roughness heights at constant roughness density $\alpha = 10$.

5.3.2.3 Varying Roughness Lengths, l, at constant Roughness Density, $\alpha = 6$ and Height, $h = 15$

In this section the investigation of roughness effects on the loss mechanisms is completed by looking at different roughness patch lengths. Proceeding in the same way as above, the profile loss and its respective terms (A-D) as well as the mixed-out and wake distortion losses are depicted in the bar graph in figure 5.33.

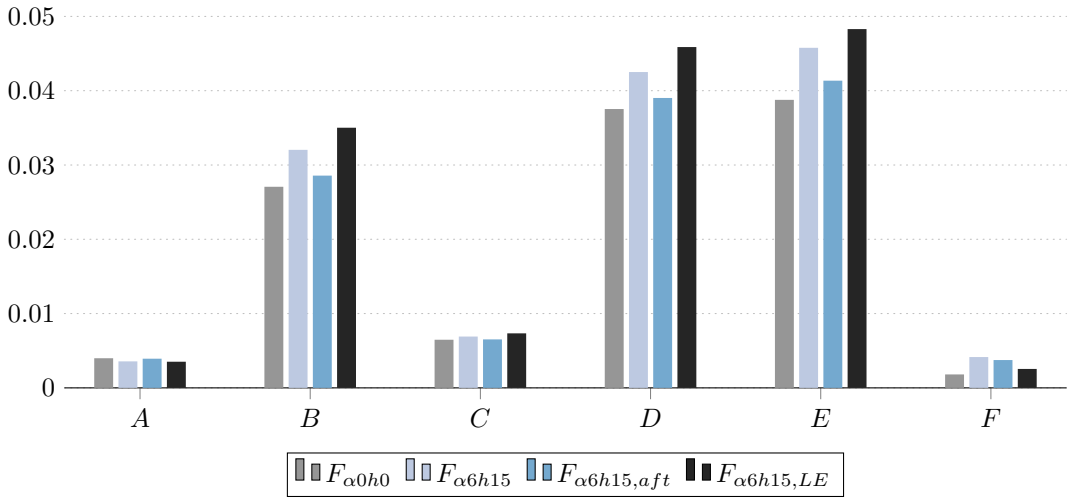

FIGURE 5.33: Denton losses and the respective loss contribution terms (A–D) and the overall mixed-out as well as wake distortion losses (E,F).

As can be observed, the roughness patch covering almost the whole blade suction surface, $F_{\alpha 6h15,LE}$, generates the highest Denton loss, D. This was to be expected given the slightly

earlier transition and hence longer exposure of the turbulent boundary layer to roughness. In contrast, the shortest patch, $F_{\alpha 6h15,aft}$, results in the lowest profile loss. For all cases the base pressure and displacement thickness contributions, A and C, respectively, only show slight differences, whereas the main profile loss contribution can be attributed to the momentum thickness.

The same can be observed for the mixed-out losses, which again are slightly higher compared to ζ owing to the bar wake mixing effects. Interestingly, $F_{\alpha 6h15,LE}$ shows the lowest wake distortion loss, F, of the roughness cases. A possible explanation for this might be the mixing of the bar wakes within the passage with the boundary layer due to the roughness. In figure C.12 an elevated TKE production along the blade suction surface was apparent and thus resulting in energy transfer from the mean flow to the smaller scales, generated slightly above the long roughness patch. Hence, the bar wakes are weakened leading to the observed lower wake distortion losses at measurement plane 2. However, ω_{wake} is still higher than for the no roughness case.

By comparing cases $F_{\alpha 0h0}$ and $F_{\alpha 6h15,aft}$, which have the same transition onset position, higher losses are generated due to the added roughness, as was to be expected.

The total pressure loss profiles in figure 5.34 show the same trend as the mixed-out losses.

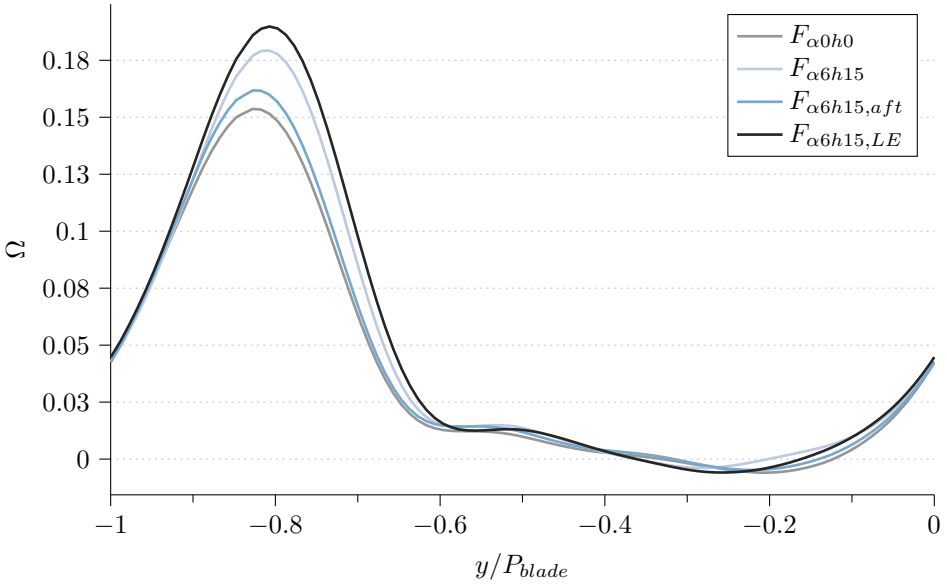

FIGURE 5.34: Total pressure loss profiles, Ω, for different roughness patch lengths.

$F_{\alpha 6h15,LE}$ has the highest profile peak and a slight widening of the blade wake can be seen, probably generated by both the roughness effects on the boundary layer itself and the bar wake mixing within the blade passage, which in turn is also caused by the presence of roughness. As the patch shortens, the total pressure losses decrease, with $F_{\alpha 0h0}$ having the lowest peak. Moreover, the deflection of the blade wakes due to the roughness forcing is evident as well.

5.4 Summary

In total 14 different large eddy simulations of the low-pressure turbine cascade were carried out in order to investigate the effects of roughness on boundary layer transition and losses.

A roughness model and an immersed boundary method were incorporated to simulate different roughness surface conditions. The sufficiency of the chosen grid for the as-cast and forcing model roughness patch simulations was tested by means of a grid convergence study.

It was shown that the admissible roughness height, $k_{s,adm.} = 1.0 \cdot 10^{-3}$, and hence the critical roughness Reynolds number, $Re_{k_s,\infty} \approx 120$ (Bons 2010), was not exceeded for the as-cast roughness patch in case AC_{nw}, as no observable earlier transition was induced compared to the reference case. Furthermore, even though the roughness was present, the boundary layer followed the laminar trend seen for R_{ref}. However, the large separation bubble was reduced due to the patch, leading to a lower overall loss. Interestingly, the added roughness increased the momentum loss contribution of the total profile loss, ζ. Neither did the added roughness cause immediate transition at the beginning of the patch.

The turbulence levels along the blade revealed that the incoming wakes were much more dominant than the roughness. Hence, only a small interaction effect of wakes and roughness were observed. This was mainly seen in the higher profile loss, as the as-cast patch increased the momentum loss contribution, caused by additional turbulent streaks and transition between wake passings. The overall loss, however, was higher for the case without roughness due to slightly higher wake distortion losses.

Another aim was to investigate the suitability and behaviour of the roughness model in cascade simulations. The computational cost with such a model can be greatly reduced compared to full roughness representations with immersed boundary methods. It was shown that the model was capable of altering the onset of transition and affecting the turbulent boundary layer, whereas the laminar boundary layer was not affected, which is in line with findings in the literature, e.g. Stripf et al. (2009). The model also behaved well regarding the admissible roughness height and the critical roughness Reynolds number. For the lowest height case, with a roughness height that is the same as the calculated admissible roughness height, no transition was induced. In case $F_{\alpha 10 h15}$ the $k_{adm.}$ was exceeded, but the critical roughness Reynolds number was below the critical value, $Re_k < 300$. Earlier transition was induced, but the sudden change between smooth and rough blade, i.e. a bump or single roughness element, at the start of the forcing region did not cause immediate transition. For the cases with critical roughness Reynolds number above $Re_k > 300$ immediate transition was observed. Larger modelled roughness heights and density values led to higher profile and overall losses.

Based on the results it can be concluded that the parametric forcing approach is a promising method to incorporate roughness in linear low-pressure turbine simulations in a more cost-effective way than full roughness simulations. The findings also demonstrate the capabilities of the simple and easily implementable roughness model in producing the same trends as other more costly methods.

Chapter 6

Summary and Outlook

6.1 Summary and Conclusions

The low-pressure turbine in a jet engine is typically responsible for driving the fan, which gives a large amount of thrust for the aeroplane. They make up 20-30% of the total jet engine weight and are exposed to a highly unsteady and disturbed flow environment. Hence, low-pressure turbines play an integral part in design process, where numerical flow simulations play an important role. In industry mainly the Reynolds Averaged Navier-Stokes (RANS) equations are used and serve as a design tool for prototypes. However, in order to get deeper insights into the flow mechanisms direct numerical simulations (DNS) and large eddy simulations (LES) are increasingly used. The aim of this work was to numerically investigate a linear low-pressure turbine cascade by means of large eddy simulations in order to further the understanding of flow phenomena.

The main focus was on two important aspects regarding turbine flows. Firstly, the unsteady incoming wakes, which affect in particular the sensitive boundary layer on the suction side of the blade that is prone to separation due to the high loading blades and hence strong adverse pressure gradients. The effect of the incoming wakes is dependent on the wake mixing prior to the turbine blade. Wake mixing is a function of the flow coefficient, Φ, the reduced frequency, F_{red}, as well as the gap size between the stator and the rotor. The latter is a particularly important design parameter, as it not only affects the turbine flow itself, but also the overall size and weight, which influences the economical side of a jet engine (Pichler et al. 2018). Within this work different incoming wake profiles, characterised by their velocity deficit and turbulent kinetic energy, were investigated. One of the main objectives was to find out the relation between the velocity deficit and the turbulent kinetic energy of bars with different drag coefficients, based on the statement of Halstead et al. (1997a). Furthermore, what are the effects of different wakes on the boundary layer of the blade and the overall losses of the turbine? It was also examined whether simple bars, by using the Magnus effect, show similar trends to a full turbine stage regarding different gap sizes.

Secondly, surface roughness effects were considered. During a life cycle of a turbine the blades become rougher due to the harsh environment the turbine operates in. The overall trend is that roughness negatively affects the efficiency and overall performance of a low-pressure turbine.

Furthermore, numerical simulations of roughness on actual low-pressure turbine blades still pose a difficulty in terms of computational power. This is especially problematic during the design phase of an engine. In order to reduce the computational cost it is common to investigate roughness in simple channel flows or by using simple and 'artificial' roughness elements. Another possibility is the use of transition or roughness models, where the wall boundary functions are altered based on empirical data. However, in order to get a better understanding of roughness effects in an actual linear low-pressure turbine cascade, two different approaches were used within this work. An immersed boundary method was employed to fully resolve a real rough surface on a turbine blade, which was computationally expensive. Much more suitable for the design process was the parametric forcing approach (PFA) (Busse and Sandham 2012), where additional forcing terms were added to the momentum and energy equations to account for the form drag and blockage of roughness. The question whether a simple roughness model (PFA) can be used for transitional cascade flows was addressed. Moreover, the feasibility of carrying out large eddy simulations of a real surface roughness patch, represented by an immersed boundary method, on a turbine blade with periodically incoming wakes was tested. By means of a parameter study with the PFA and the fully resolved roughness the effects of surface roughness on the blade's boundary layer and loss mechanisms were investigated.

The parametric forcing approach had not been implemented into the flow solver prior to this work and had only been tested for incompressible and turbulent channel flows. For this reason the implementation and validation of the PFA for different flow problems was part of this study. Moreover, the boundary data immersion method (BDIM) (Maertens and Weymouth 2013; Schlanderer and Sandberg 2018; Schlanderer et al. 2017; Weymouth and Yue 2011) was only capable of dealing with two-dimensional geometries and three-dimensional geometries that did not have any spanwise variations. Hence, it had to be extended to be able to simulate complex three-dimensional geometries like surface roughness.

Before moving to the numerical investigation of the linear low-pressure turbine cascade, the validity and suitability of the two approaches were examined by means of turbulent channel flow simulations in chapter 5. Firstly, a simulation of a turbulent channel flow at $Re_\tau = 180$ with smooth walls was carried out in order to test the computational setup and to obtain reference values for the normalisation of the rough channel solutions. It was shown that the results compared well to the common reference cases in the literature (Kim et al. 1987; Vreman and Kuerten 2014).

The extended boundary data immersion method for complex geometries was then validated and investigated by using turbulent channel flows with wavy and grit blasted walls at a friction Reynolds number of $Re_\tau = 180$. Comparing the streamwise wavy wall flow with the boundary data immersion method to a bodyfitted grid case showed very good agreements. The confidence in the validity and suitability of the BDIM was further established by the grit blasted case, where the results matched well with the results of Thakkar et al. (2017b). Hence, it could be concluded that the extension was successful and could later be used for the roughness simulations in the low-pressure turbine.

As to the compressible formulation of the roughness forcing model, a good agreement with the results of Busse and Sandham (2012) was observed. The differences could be mainly attributed to the inherently different flow solvers. Furthermore, the model had to be tested for the suitability

of laminar-turbulent transition in channel flow, which had not been tested prior to this work. The test was needed owing to the transitional state of the boundary layer of the turbine blade and the importance of transition induced by roughness on the turbine performance (Stripf et al. 2009). A transition study in turbulent channel flow at $Re_\tau = 80$ showed the transition capability of the forcing approach. The resulting roughness density value of $\alpha = 0.015$, matching the transition behaviour of the grit blasted walls in Thakkar et al. (2017b), was then used for a comparison with real roughness turbulent channel flow at $Re_\tau = 180$. The real rough surfaces, grit blasted walls, were represented by the boundary data immersion method. It was shown that the forcing model only had a marginal effect on the flow in the centre of the channel due to the low roughness density value leading to insufficient form drag and blockage effects. Hence, it was concluded that for the linear low-pressure turbine simulations higher roughness density values, $\alpha \geq 1$, had to be used to ensure that the boundary layer on the blade was effect. Even though this made the comparison with a real rough surface difficult, valuable insights during the design process in terms of transition and boundary layer development could be gained.

In chapter 4 it was shown that rotating bars were able to generate wakes with a certain level of asymmetry and circulation, which is characteristic for blade wakes. Furthermore, the results of Halstead et al. (1997a) could be confirmed. They stated that the wake strength is more important for the incoming wake characterisation than the velocity deficit. Non-rotating bars, which are commonly used in the literature (Engber and Fottner 1995; Ladwig and Fottner 1993; Michelassi et al. 2003, 2015; Pfeil and Eifler 1976), cause wakes with turbulent kinetic energy levels that are markedly higher compared to an actual blade wake and lead to a different wake-blade interaction behaviour.

Furthermore, the effects of three different incoming wake profiles on the blade's boundary layer and the loss mechanisms of the low-pressure turbine were investigated. The wakes differed in strength, indicated by the turbulent kinetic energy, representing varying stator-rotor gap sizes, which is an important design parameter (Pichler et al. 2018). The time-averaged statistics for the clean reference case without any disturbances exposed a large separation bubble in the aft region of the blade, whereas with incoming wakes the size could be considerably reduced and even suppressed. Only the weakest incoming wakes were not able to fully prevent the formation of a separation bubble. In the phase-averaged statistics, however, all cases revealed an intermittent separation bubble during one bar passing period, varying in size depending on the strength of the incoming wake. The wakes with the highest TKE levels, representing the smallest gap size, almost completely prevented laminar separation, which was in line with Pichler et al. (2018), who simulated two full stages with different stator-rotor distances. The much smaller separation bubble was due to the stronger wake boundary-layer interaction and thus the positive effects of earlier transition, and calmed regions were more pronounced. Moreover, it was found that combined effects of wake mixing and separation bubble size influenced the overall loss generation. Even though the change in separation bubble size in the case of the strongest wakes was only marginal, the wake mixing diminished this positive effect and resulted in overall higher losses compared to the case with the largest separation bubble and weakest wakes. Hence, it is paramount to characterise the wake generating bars based on the turbulent kinetic energy levels rather than the velocity deficit.

In chapter 5 the effects of surface roughness on boundary layer transition and losses in a linear low-pressure turbine cascade were investigated. In order to represent the rough surfaces, two

approaches were incorporated, namely the parametric forcing approach and the boundary data immersion method, which fully resolved a real as-cast roughness patch on the turbine blade. The suitability of both approaches for roughness simulations had been confirmed in a prior chapter. The study comprised 14 different large eddy simulations, including a parameter study for the PFA and two fully resolved as-cast surface roughness patch cases.

For the as-cast simulations it was shown that the chosen roughness levels did not exceed the critical roughness Reynolds number, $Re_{k_s,\infty} \approx 120$ (Bons 2010) and hence earlier roughness induced transition was not apparent. This was further confirmed by the as-cast case without incoming wakes, which showed a similar laminar boundary layer trend as the clean reference case without disturbances and surface roughness. A reduction of the large separation bubble, however, was observed, having a beneficial effect on the overall turbine losses. Moreover, it was evident that the incoming wakes had a larger effect on the boundary layer than the roughness and it was shown that there was only a small combined effect between the as-cast patch and the impinging wakes. The combined effect resulted in a higher Denton (profile) loss due to an increased momentum thickness loss contribution, that could be attributed to the presence of the rough surface. Between the wake passings, additional low and high velocity streaks and vortices emerging from the roughness peaks were observed in a series of instant time snapshots of the flow field slightly above the as-cast patch, leading to the additional loss effect.

The computational cost of roughness simulations could be decreased by means of a forcing model, enabling the conduction of a parameter study. Different roughness densities, roughness heights and roughness patch lengths were simulated in order to obtain deeper insights into the effects of roughness on turbine flows. As noted in chapter 5, higher roughness densities had to be used for the turbine cascade simulations compared to the values obtained in the transition study with grit blasted walls. The fully turbulent channel flow results exposed an insufficient roughness form drag and blockage effect, showing no influence on the roughness function ΔU^+. With the higher roughness density values it was shown that the model was capable of altering the onset of transition and affecting the turbulent boundary layer, whereas the laminar boundary layer was not affected, which was in line with findings in the literature, e.g. Stripf et al. (2009). Furthermore, the model showed good behaviour regarding the admissible roughness height, $k_{adm.}$, and the critical roughness Reynolds number, Re_k. Especially case $F_{\alpha 10 h 15}$ demonstrated the viability of the forcing model, which exceeded $k_{adm.}$, but was below $Re_k < 300$. Earlier transition was induced by the presence of the additional forcing, but the sudden change between the smooth and rough blade region, imposing a bump or single roughness element, at the start of the forcing region did not cause immediate transition, which happened for the cases with $Re_k \geq 560$. It was also demonstrated that increasing roughness densities and heights increased the profile and overall losses, which was in line with the surface roughness literature (see section 1.2.3). Hence, it was concluded that the parametric forcing model presented a promising model for the low-pressure turbine design process.

6.2 Main Achievements

A summary of the main achievements of this work is given in this section.

- It was shown that the commonly used non-rotating wake generating bars have markedly higher turbulence levels compared to an actual blade wake. Hence, rather than using the wake velocity deficit to characterise wake generating bars, as proposed by Pfeil and Eifler (1976), the strength of the wakes, indicated by the turbulent kinetic energy, should be used in the turbine design process. Using the Magnus effect is an easy approach in order to control and vary the wake profiles.

- By using the Magnus effect for the wake generating bars it was possible to imitate different stator-rotor gap sizes, posing a computationally effective means to conduct parameter studies without the need to generate and change new meshes, which might introduce errors. The results compared well to the gap size study of a full stage of Pichler et al. (2018).

- By employing a simple roughness model, namely the parametric forcing approach (Busse and Sandham 2012), the computational costs were able to be reduced compared to fully resolved roughness cases, allowing for a roughness parameter study.

- Based on the roughness parameter study in the linear low-pressure turbine cascade it was shown that the forcing model behaves well regarding the admissible roughness height, $k_{adm.}$, and the critical roughness Reynolds number, Re_k. Furthermore, the same behaviour as fully resolved rough surfaces were observed. Hence, it was possible to simulate transitional cascade flows with the roughness model, which renders the PFA a valuable approach for parameter studies during the turbine design stage in order to gain first insights into the effects of roughness.

- Large eddy simulations of a linear low-pressure turbine cascade with a fully resolved as-cast roughness patch on the blade's suction surface were carried out. The extended boundary data immersion method for complex geometries was able to successfully represent the as-cast roughness. The simulation showed the combined effect of incoming wakes and surface roughness, leading to higher profile losses due to additional turbulent streaks and vortices during the wake passing cycle, which emerge from the distinct roughness peaks of the as-cast patch.

6.3 Future Work

During this work it was not possible to address all the emerging questions. Hence, some ideas and suggestions for future work are outlined in this section.

As noted in chapter 5 the obtained roughness density values in the transition study were too low in order to have an effect on the turbulent channel flow at friction Reynolds number $Re_\tau = 180$. This was due to the only marginal blocking effect of the forcing model. Hence, it is recommended to test the modified parametric forcing approach proposed by Forooghi et al. (2018), who used an additional linear forcing term to account for viscous drag effects, and run further parameter studies in laminar-turbulent channel flows. Furthermore, it is still not clear how the box shape function height, $2h$, and the domain dimensions should be chosen when comparing to a real roughness case. More simulations with different domain heights need to be carried out to further investigate the form drag and blockage effects of the forcing model.

The first order formulation of the extended boundary data immersion method was used for the roughness simulations. Implementing the second order formulation (Schlanderer et al. 2017) for the complex geometry treatment should result in more accurate flow solutions, allowing for a better assessment of the roughness effects in the vicinity of the surface. This might also remove the differences in the Reynolds stresses observed in the grit blasted channel flow simulations in section 3.2.2.

Regarding the surface roughness simulations in the linear low-pressure turbine cascade several things might be worth considering. So far the roughness patch was merely mapped onto part of the blade surface. In order to further investigate the effects of roughness on the laminar boundary layer of the turbine blade, an as-cast roughness patch covering the whole suction surface, and even the pressure surface, is recommended. This might also clarify the combined effects of roughness with strong surface curvature and favourable pressure gradients. Moreover, the used roughness patches increased the effective blade thickness, making it difficult to draw conclusions between smooth and rough blade simulation cases. Hence, a thinner blade or cavity needs to be used in order to align the roughness mean height with the original T106 blade surface, similar to the grit blasted channel flow case. Following the example of Thakkar et al. (2017b), a set of different rough surface geometries could be simulated to further enhance the understanding of roughness effects. This would also make it possible to narrow down the vast range of equivalent sand-grain roughness correlations for turbomachinery applications, as noted by Bons (2010), and give manufacturers more reliable roughness manufacturing and maintenance thresholds.

Another point worth investigating might be the combined effect of different incoming wake profiles and surface roughness, similar to the investigation in chapter 4. However, in order to keep things more simple and computationally less costly the imposition of wake profiles as inlet conditions is suggested, rather than simulating upstream bars. Especially when one is not particularly concerned with the potential effect between the stator and the rotor (Hodson and Howell 2005b; Korakianitis 1993; Pichler et al. 2018).

Appendix A

Rotating Cylinder

A.1 Literature Review

Even though a rotating cylinder is a very basic case it is still extensively investigated. Rao et al. (2014a) presented a review of the past and present research of the wake transition of rotating cylinders. In figure A.1 different wake states for different Reynolds numbers and rotation rates α are shown (Rao et al. 2014a). The rotation rate α is defined as follows

$$\alpha = \frac{\omega D}{2U_\infty}, \tag{A.1}$$

where ω, D and U_∞ are the angular velocity, the cylinder diameter and the freestream velocity, respectively. There are two main flow states, namely the 'Shedding' and the 'Steady' state that depend on the rotation rate. In the steady state there is no wake shedding and the flow is completely time independent. Furthermore, Mittal and Kumar (2003) and Pralits et al. (2010) observed two modes in the steady state, 'Mode I' and 'Mode II', characterising the shape and structure of the cylinder wakes. In 'Mode I' the wake "forms a 'tail-like' structure", whereas in 'Mode II' "the shear layers wrap around the rotating cylinder" (see fig. 1.6) (Rao et al. 2014a). In the 'Mode I' shedding region (Rao et al. 2014a) a van Kármán vortex street is generated. 'Mode II' shedding is characterised by a single-sided vortex that is shed by the cylinder (Rao et al. 2014a). As can also be noticed, for certain Reynolds numbers and rotation rates the wake can reach a completely steady state where no vortex is shed. The steady states and the shedding modes I and II are characterised as two-dimensional modes. In contrast to that, modes A-F' are three-dimensional modes that grow on the two-dimensional modes and are unstable to perturbations in the spanwise direction.

Mittal and Kumar (2003) carried out two-dimensional DNS simulations of a rotating cylinder at Reynolds number $Re = 200$ and various rotation rates. As can be seen in figure A.2 fairly high lift coefficients C_L can be achieved.

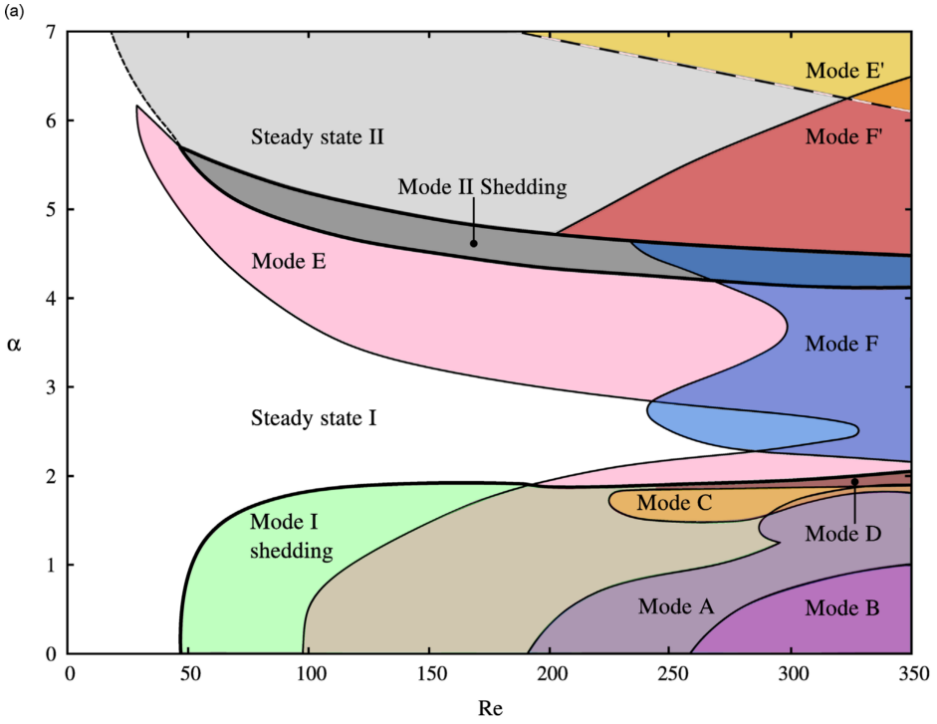

FIGURE A.1: Wake state and instability mode regions for different Reynolds numbers and rotation rates (Rao et al. 2014a).

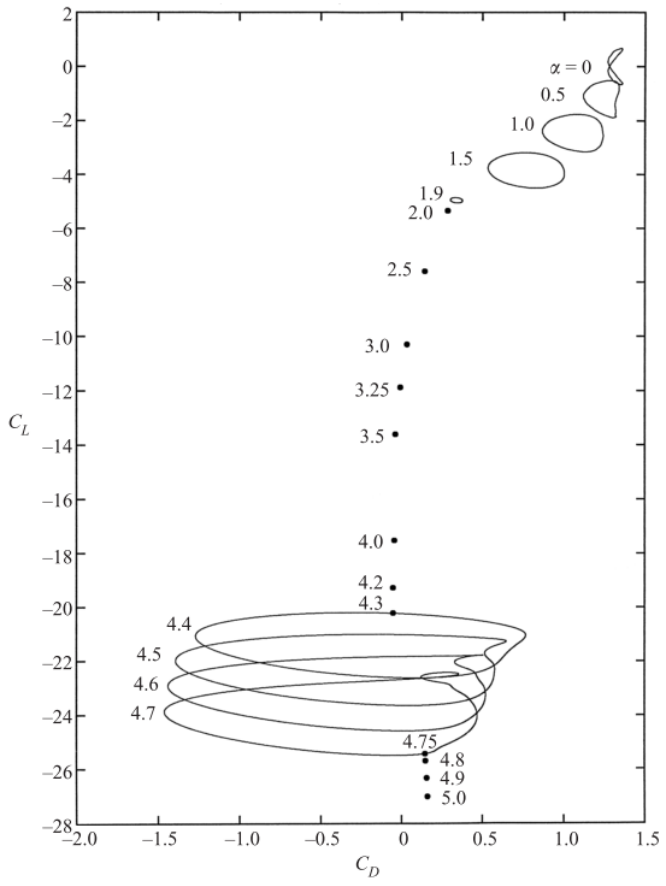

FIGURE A.2: C_L and C_D of a rotating Cylinder for varying rotation rates α; reproduced from Mittal and Kumar (2003)

In the rotation rate region for $0 < \alpha < 1.9$ mode I shedding occurs. After that the flow reaches a steady state until a rotation rate of $\alpha = 4.3$. A smaller region of mode II shedding is followed by a second steady state area. However, the focus in this work is to mimic blade wakes and thus rotation rates in the mode I shedding region will be chosen.

A.2 Further Validation Cases

As already mentioned, in this work moving bars are used to generate the periodically incoming wakes in the linear cascade simulations. The aim is to represent the bars by the boundary data immersion method (see section 2.2.2) on a Cartesian grid rather than a body-fitted mesh. This simplifies the mesh generation and additionally reduces the required number of blocks and thus characteristic interfaces.

In the following subsections three validation cases are presented. Additionally, a BDIM validation case in a linear LPT setup is given in section 4.1.1. Compressible DNS simulations at a Reynolds number $Re = 200$ and rotation rates $\alpha = 0.0, 0.5$ and 4.8 were carried out. Time dependent data was captured at 360 points around the cylinder with an offset of one smoothing region thickness of ϵ from the actual wall boundary. Furthermore, a bilinear interpolation was used to obtain the flow values at the 360 capturing points. For the comparison the drag and lift coefficients C_D and C_L, respectively, are used which are defined as follows:

$$\begin{aligned} C_D &= C_{D,p} + C_{D,f} = \frac{F_{D,p} + F_{D,f}}{0.5\rho_\infty U_\infty^2 D}, \\ C_L &= C_{L,p} + C_{L,f} = \frac{F_{L,p} + F_{L,f}}{0.5\rho_\infty U_\infty^2 D}. \end{aligned} \tag{A.2}$$

where ρ_∞ is the free stream density, U_∞ is the free stream velocity and D denotes the cylinder diameter. The pressure and friction contributions to the drag coefficient $C_{D,p}$ and $C_{D,f}$, as well as the contributions to the lift coefficient $C_{L,p}$ and $C_{L,f}$ are calculated by the pressure and friction forces pointing into the respective direction. These forces are defined by

$$\begin{aligned} F_{D,p} &= \oint_{\Gamma_b} (p \cdot \mathbf{n}_x) ds, F_{D,f} = \oint_{\Gamma_b} (\tau_w \cdot \mathbf{n}_x) ds, \\ F_{L,p} &= \oint_{\Gamma_b} (p \cdot \mathbf{n}_y) ds \text{ and } F_{L,f} = \oint_{\Gamma_b} (\tau_w \cdot \mathbf{n}_y) ds. \end{aligned} \tag{A.3}$$

Here p, τ_w, $\mathbf{n}_x$ and $\mathbf{n}_y$ are the surface pressure, the skin friction, the normal surface vector in the streamwise and in the pitchwise direction, respectively.

In the following the test cases and the results are discussed.

A.2.1 Flow Past a Circular Cylinder

For the non-rotating cylinder a grid convergence study is conducted and a comparison between values found in the literature and the obtained results is made.

The flow domain and grid is depicted in figure A.3. The domain and cylinder size was chosen according to the incompressible simulations done by Maertens and Weymouth (2013). Characteristic inflow (red line), non-reflecting boundary (green) and non-reflecting outflow (blue) conditions were used which are mentioned in section 2.2.4. A zoomed view of the cylinder region shows a uniform Cartesian grid which is stretched towards the boundaries.

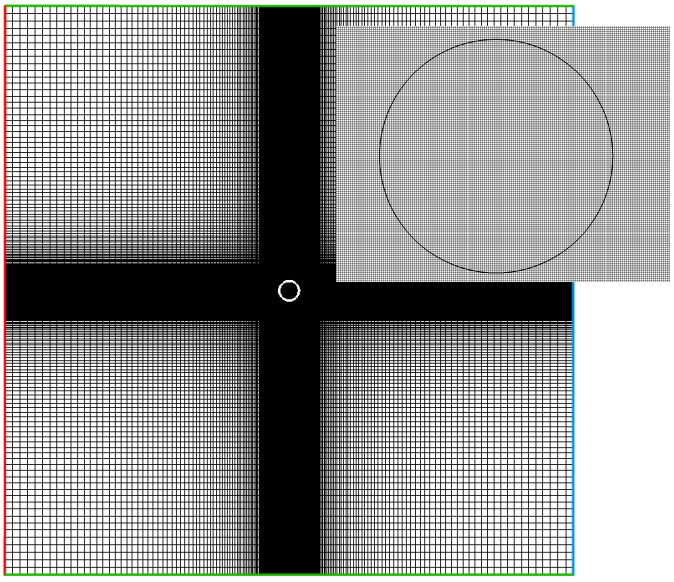

FIGURE A.3: Domain and grid of the non-rotating cylinder case 2NR120. The size is $29D \times 29D$ and the cylinder has a diameter of size D. The red line denotes the soft characteristic inlet condition mentioned in subsection 2.2.4; the blue and green lines are characteristic outlet conditions.

Several simulations with different cylinder resolutions and Mach numbers were carried out and a summary is listed in table A.1. For the grids 1NR120 and 2NR120 the second-order BDIM approach, indicated by '(2nd)', was used as well. The cylinder is resolved by $\mathrm{D}/\Delta x$ grid points along its diameter. Even though the flow at a Mach number of $M = 0.2$ can be considered as incompressible, two additional simulations at $M = 0.1$ were run in order to examine compressibility effects.

TABLE A.1: Summary of non-rotating cylinder cases at $Re = 100$

Grid	Points	$\mathrm{D}/\Delta x$	Mach number M
1NR120 (2nd)	145,161	120	0.1
2NR80	103,041	80	0.2
2NR120 (2nd)	145,161	120	0.2
2NR200	251,001	200	0.2

Grid Convergence:

For the grid convergence study three different grids are used where the cylinder is resolved by $D/\Delta x = 80, 120$ and 200 points across its diameter. The simulations were carried out at Mach

number $M = 0.2$ and the first-order BDIM approach was applied. The drag coefficient C_D and its pressure and friction contribution $C_{D,p}$ and $C_{D,f}$, respectively, are shown in figure A.4.

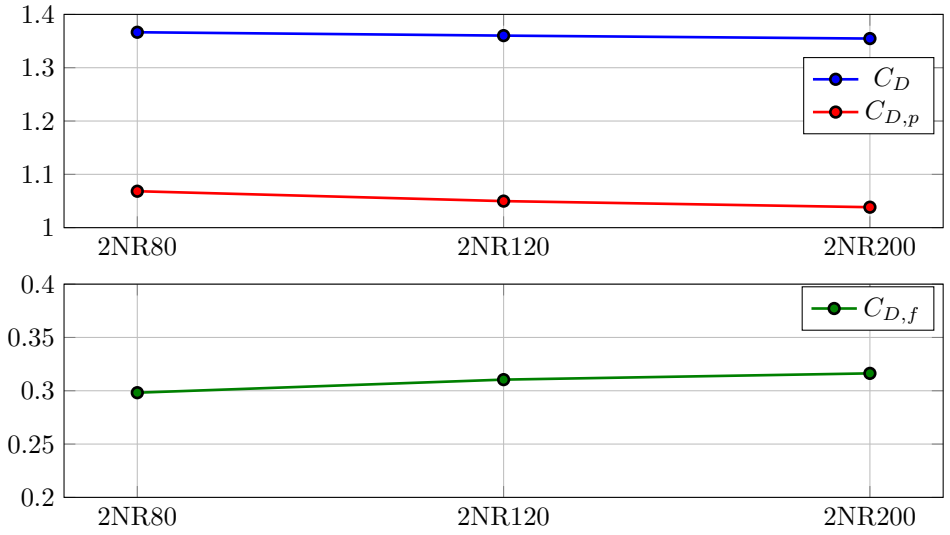

FIGURE A.4: Overall drag coefficient as well as pressure and friction contribution for different grid resolutions.

As can be seen C_D remains almost constant for all three cylinder resolutions. This is due to the decreasing pressure and increasing friction contribution that do not show a converged state even for the highest chosen resolution. As the 2NR200 grid consists already of about 250,000 points in the 2D plane, the BDIM approach might not be feasible for 3D simulations where an accurate prediction of the drag, and especially its pressure and friction contributions, is necessary.

Validation:

For a comparison of the obtained data, the results from Maertens and Weymouth (2013) are used which validated the BDIM in their flow solver with other numerical and experimental data. In contrast to the bilinear interpolation that was used within this work to extract data at the points close to the BDIM boundary, they used a one-sided direct informed kernel (DIK) method, which is derived in Weymouth (2008). Even though the xNR120 grid is not fully converged, as shown in the last section, it was used for the comparison as it matches the cylinder resolution of the case in Maertens and Weymouth (2013). Simulations with the first- and second-order BDIM approach and two different Mach numbers $M = 0.1$ and 0.2 were carried out. The results are shown in tables A.2 and A.3.

TABLE A.2: Comparison of drag and lift coefficient with Maertens and Weymouth (2013). Kernel half-width $\epsilon = 2\Delta x$ and cylinder resolution $D = 120\Delta x$

Source	C_D	C_L
2NR120 1st	1.36 ± 0.010	± 0.327
1NR120 1st	1.35 ± 0.007	± 0.340
2NR120 2nd	1.34 ± 0.008	± 0.314
1NR120 2nd	1.32 ± 0.008	± 0.320
Maertens and Weymouth (2013) 1st	1.31 ± 0.009	± 0.321
Maertens and Weymouth (2013) 2nd	1.31 ± 0.009	± 0.313

In the table A.2 the total drag C_D and the total lift C_L coefficients are compared. As can be seen, both total coefficients compare well with the reference data. However, by choosing the second-order approach and decreasing the Mach number, C_D decreases slightly and matches values from the literature more closely. Moreover, a decrease in Mach number also results in a slightly higher amplitude of the lift coefficient.

Table A.3 shows the friction and pressure contributions to the lift and drag coefficient. Again, the first-order BDIM approach results in slightly higher values. What can also be seen from this table is, that decreasing the Mach number causes an increase in the friction contribution to the drag and a decrease in the pressure contribution.

TABLE A.3: Results of the friction and pressure contribution to the drag and lift coefficient. Comparison with Maertens and Weymouth (2013). Kernel half-width $\epsilon = 2\Delta x$ and cylinder resolution $D = 120\Delta x$

Source	C_{Df}	C_{Dp}	C_{Lf}	C_{Lp}
2NR120 1st	0.31 ± 0.0009	1.05 ± 0.0096	± 0.037	± 0.296
1NR120 1st	0.32 ± 0.0006	1.03 ± 0.0067	± 0.039	± 0.307
2NR120 2nd	0.30 ± 0.0006	1.04 ± 0.0080	± 0.035	± 0.287
1NR120 2nd	0.30 ± 0.0008	1.02 ± 0.0071	± 0.034	± 0.292
Maertens and Weymouth (2013) 1st	0.30 ± 0.0008	1.01 ± 0.0085	± 0.035	± 0.292
Maertens and Weymouth (2013) 2nd	0.30 ± 0.0007	1.00 ± 0.0081	± 0.034	± 0.285

A.2.2 Flow Past a Slowly Rotating Cylinder

The domain size for the rotating cylinder cases is $60D \times 60D$ and the boundary conditions are the same as for the non-rotating case.

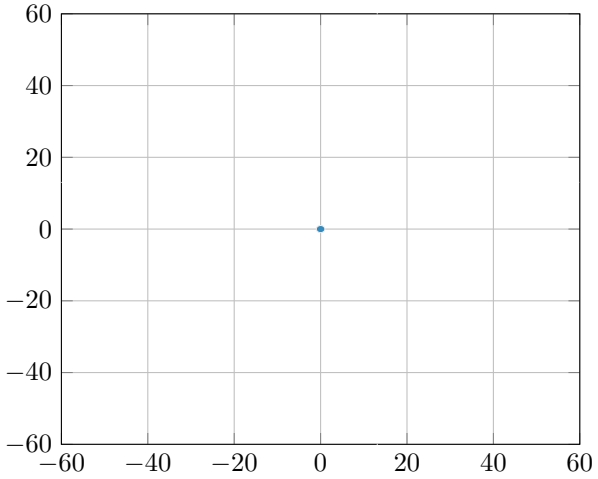

FIGURE A.5: Domain of the rotating cylinder cases. The size is $60D \times 60D$ and the cylinder has a diameter of size D.

A summary of the simulations at the low rotation rate is listed in table A.4. Four different cylinder resolutions at a Reynolds number of $Re = 200$ and Mach number $M = 0.1$ were used. The extension 'B' denotes the cases where a bigger domain size of $150D \times 150D$ was used.

TABLE A.4: Summary of rotating cylinder cases with rotating rate $\alpha = 0.5$ and $Re = 200$

Grid	Points	D/Δx	Mach number M
1NR60	70,531	60	0.1
1NR60 2nd	70,531	60	0.1
1NR120	126,511	120	0.1
1NR200	267,841	200	0.1
1NR300	446,641	300	0.1
1NR300B	521,451	300	0.1
1NR300B 2nd	521,451	300	0.1

Grid Convergence and Validation: Figure A.6 shows the grid convergence of the total drag coefficient C_D and its pressure and friction contribution $C_{D,p}$ and $C_{D,f}$, respectively.

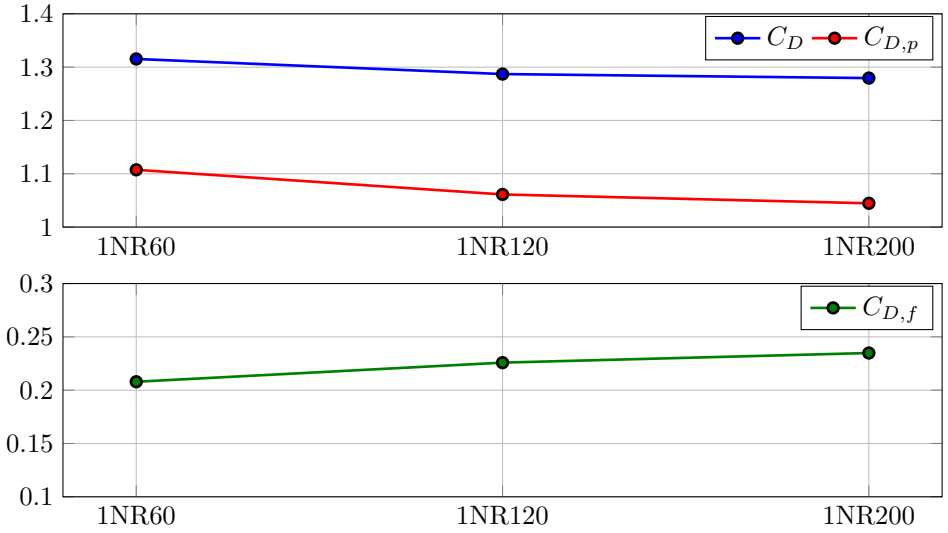

FIGURE A.6: Convergence of the drag coefficient and its pressure and friction contribution parts.

A similar convergence behaviour to that in the non-rotating case can be seen. The overall drag changes only slightly on account of the contrary trend of the pressure and friction parts. The lift coefficient C_L and its parts show the same pattern, as can be observed in figure A.7. An important point to note is that the rotating cylinder at this rate already creates a fairly high lift coefficient.

The slightly slower convergence rate, compared to the non-rotating case, may be due to both the additional rotation and the higher Reynolds number and thus a less resolved boundary layer by the BDIM approach.

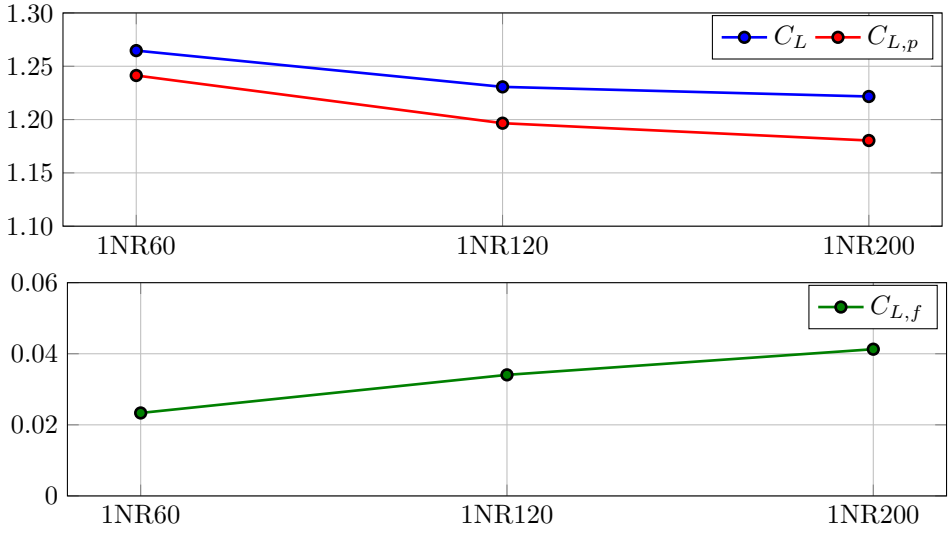

FIGURE A.7: Convergence of the lift coefficient and its pressure and friction contribution parts.

The $C_L - C_D$ plot in figure A.8 shows one complete shedding cycle. As can be seen, the lowest resolved case with the first order BDIM framework over-predicts the drag coefficient, whereas

with the second order enhancement an under-prediction of both, the drag and the lift coefficient is apparent. By increasing the domain size for the highest cylinder resolution there is only a slight change in the result. When the second order BDIM is used, a very good fit with the incompressible DNS results of Mittal and Kumar (2003) is achieved. It can be concluded that a sufficient resolution is needed in order for the second order method to perform better than the first order BDIM.

The values of the lift coefficient and the shape of all three refinement levels compare fairly well with the data from the literature. However, the drag is slightly off, which is a general problem already mentioned in the literature. Rao et al. (2013) compared results for three different rotation rates $\alpha = 1, 2$ and 3 with Mittal and Kumar (2003) and Padrino and Joseph (2006). All three obtain lift coefficients that compare quite well, but have large discrepancies in the drag coefficient. Martín-Alcántara et al. (2015) simulated rotating cylinders with the CFD solver OpenFOAM® and noticed a large discrepancy in the drag coefficient for $\alpha = 3.0$ compared to Mittal and Kumar (2003), whereas the lift coefficients agree very well.

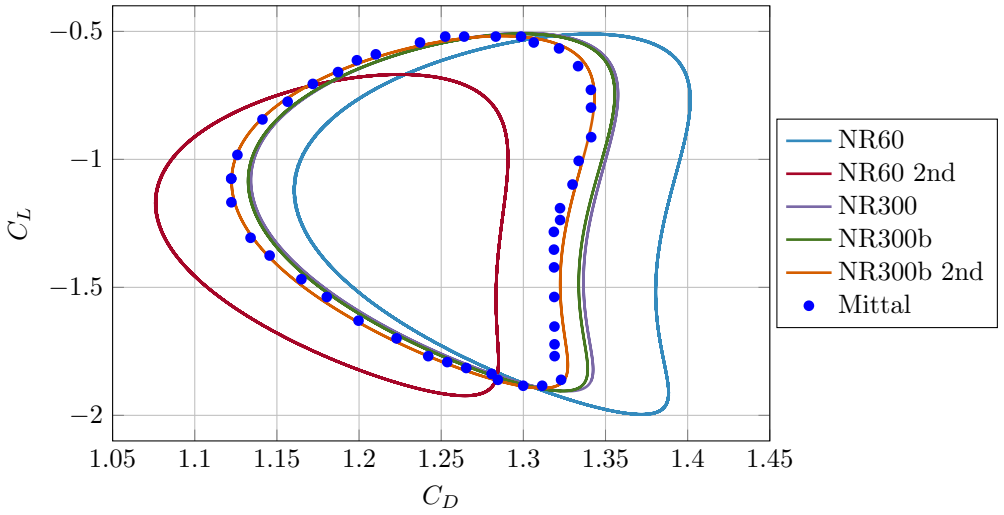

FIGURE A.8: Comparison of the drag and lift coefficients with Mittal and Kumar (2003)

A.2.3 Flow Past a Fast Rotating Cylinder

A high rotation rate of $\alpha = 4.8$ was chosen to test the capabilities of the BDIM approach. At this rate the flow reaches a steady state and the streamlines wrap around the body and the stagnation point (black dot) moves away from the cylinder boundary, as can be seen in figure A.9. In total, nine different cases were simulated which are summarised in table A.5. For the grid convergence study 5 different cylinder resolutions are compared. The highest resolved grid reaches almost one million cell points in the 2D plane. A comparison is drawn between the data obtained by the BDIM and the results from Mittal and Kumar (2003). Furthermore, the influence of the Mach number on the drag and lift coefficient is investigated.

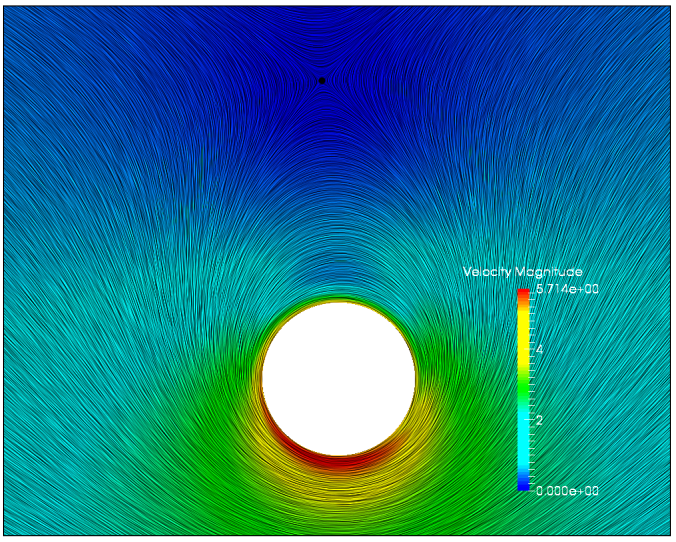

FIGURE A.9: Streamlines and velocity magnitude contour of rotating cylinder with rotation rate $\alpha = 4.8$. The black dot denotes the stagnation point.

TABLE A.5: Summary of rotating cylinder cases with rotating rate $\alpha = 4.8$ and $Re = 200$

Grid	Points	D/Δx	Mach number M
03NR60	70,531	60	0.03
03NR120 (2nd)	126,511	120	0.03
03NR200	267,841	200	0.03
03NR350	551,425	350	0.03
03NR500	939,241	500	0.03
01NR60	70,531	60	0.01
02NR60	70,531	60	0.02
03NR60	70,531	60	0.03

Grid Convergence:

The results of the grid convergence of the rotating cylinder with high rotation rate is shown in figure A.10. The total drag and lift coefficients and their pressure and friction contributions are plotted for 5 different levels of resolution. As can be seen, both the drag and the lift values are not fully converged even for the most resolved grid with almost one million grid points. Similar to the previous cases, the friction contribution is underestimated and the pressure contribution is overestimated for coarser cylinder resolutions. This can be observed in particular for the lift coefficients. A reason for this might be due to the data capturing, which is done at a distance of one smoothing region length ϵ away from the actual body surface. As a consequence, the boundary layer is not properly captured and resolved. An indicator for this could also be the results obtained by the second-order BDIM approach denoted by the squares for the 03NR120 case. As already mentioned in section 2.2.2, the second-order approach tries to tackle the velocity gradient discontinuity at the boundary. Especially for the lift coefficients the difference between the first- and second-order approach is apparent.

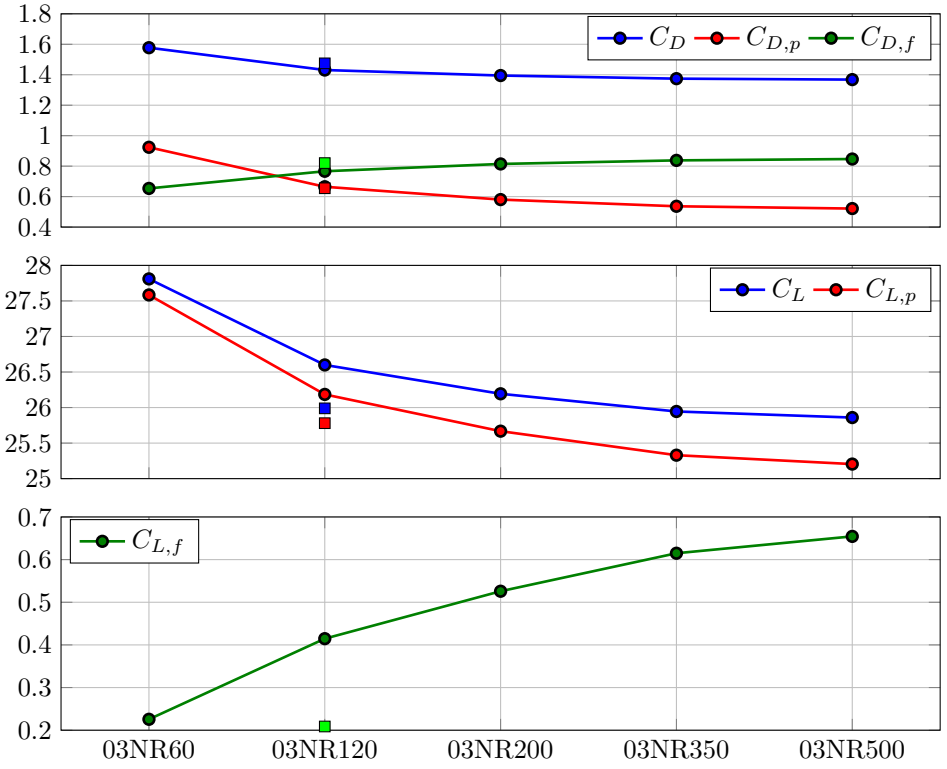

FIGURE A.10: Convergence of the drag and lift coefficients and their pressure and friction contribution parts. The squares denote the results with the second-order BDIM approach.

Validation:

As before, the results are compared with the data from Mittal and Kumar (2003) and the comparison can be seen in table A.6. The drag and lift coefficients of both the coarsest and the finest grid are listed. A large discrepancy in the drag coefficient C_D is apparent. Even for the finest grid the value is an order of magnitude off compared to the results obtained from the literature. However, the lift coefficient C_L compares fairly well. As already mentioned earlier, the drag coefficient seems to give different results for different flow solving methods used throughout the literature. These differences increase as the rotation increases. Martín-Alcántara et al. (2015) found in their simulations that the domain size plays an important role. They noticed a large change of the drag coefficient when they increased the radius of their circular domain from $30R$ to $100R$. The value of C_D dropped from above 0.5 to under 0.2 and by further increasing the radius to $250R$ it reached approximately a value of 0.1. Thus, as the chosen domain size in this work lies in the range where marked changes are present, further simulations with a bigger domain have to be done. Additionally, a control volume approach is used in order to calculate the total drag C_D and the total lift C_L by the momentum exchange. The results obtained by this approach match the ones gathered at the boundary of the body. This gives confidence in the simple bilinear interpolation method used for the data-capturing.

TABLE A.6: Comparison

Grid	C_D	C_L
03NR60	1.58	27.81
03NR500	1.37	25.86
Mittal and Kumar (2003)	0.15	25.70

As the previously mentioned results in the literature were all obtained using the incompressible Navier-Stokes equations, simulations at three different Mach numbers were carried out in order to investigate the influence of possible compressibility effects. The coarsest grid xNR60 was used and the results are shown in figures A.11 and A.12. As can be seen, by decreasing the Mach number the drag slightly decreases and the lift slightly increases. As far as the drag is concerned, only the friction contribution changes and the pressure contribution stays constant. In the case of the lift, both contributions change. It can be concluded that, even though the local Mach number in the vicinity of the rotating body is lower than 0.3, compressibility effects occur.

In figure A.13 the distribution of the pressure coefficient C_P, which is defined as follows

$$C_P = \frac{p - p_\infty}{0.5\rho_\infty U_\infty^2}, \tag{A.4}$$

along the cylinder surface is shown. The coefficient is fairly low on the bottom part of the cylinder, where the highest flow velocity is reached, compared to the top part, where the flow is slowed down. This explains the high lift forces achieved by the fast rotating cylinder.

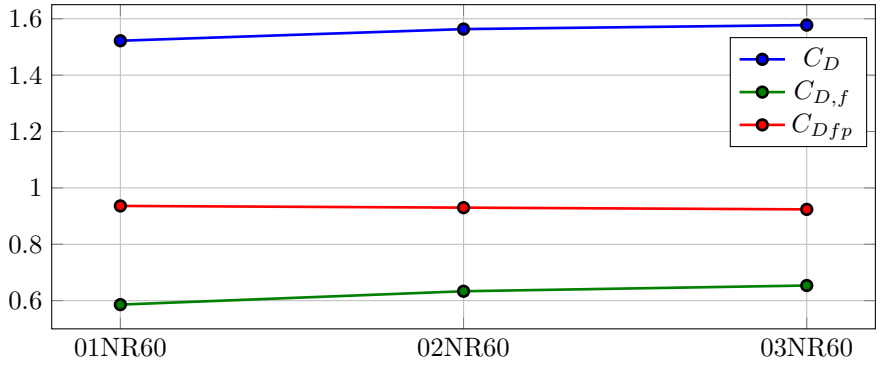

FIGURE A.11: Influence of Mach number variation on C_D for cases xNR60.

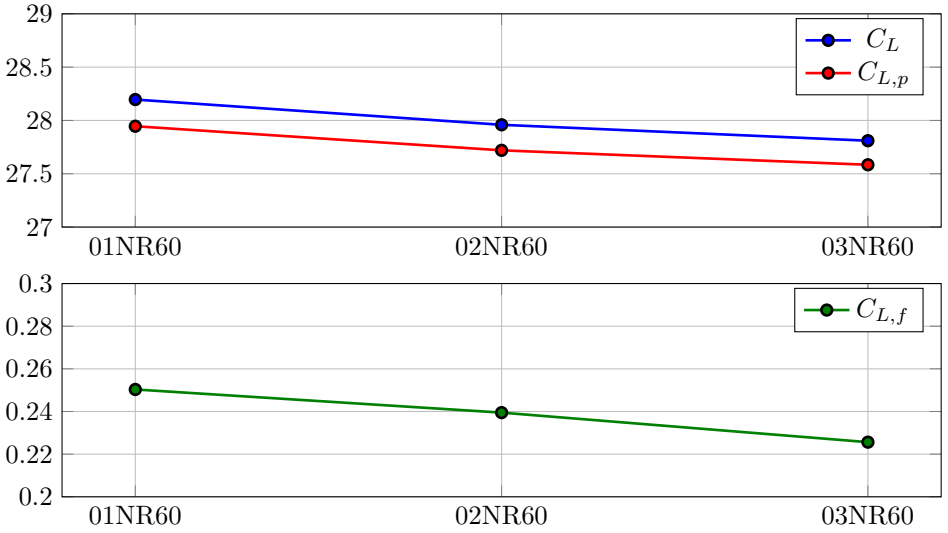

FIGURE A.12: Influence of Mach number variation on C_L for cases xNR60.

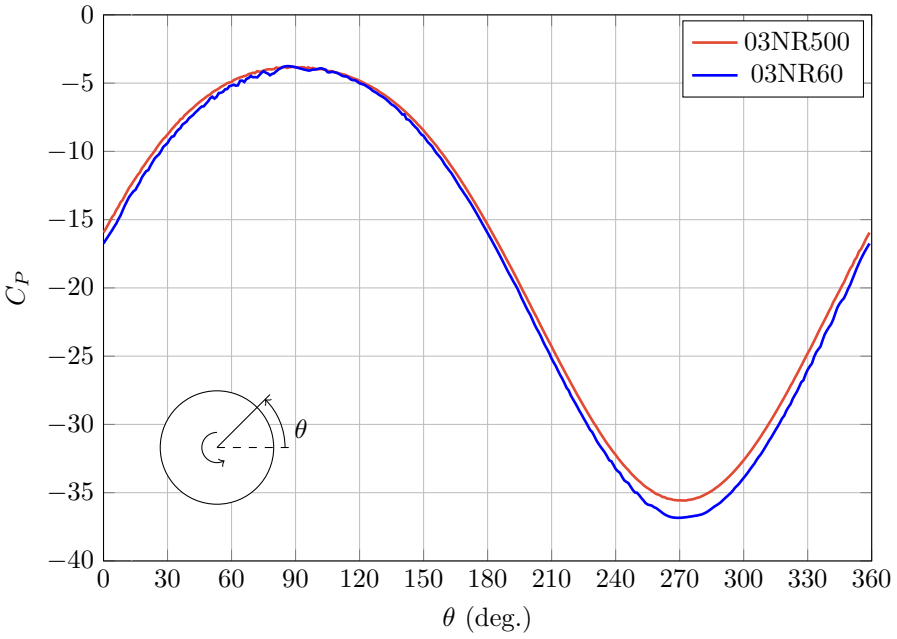

FIGURE A.13: Pressure coefficient C_P distribution on cylinder surface of coarsest and finest grid.

The main purpose of this work is to investigate the potential effects created due to the lift of a rotating cylinder on the LPT cascade. The results for the lift show that they match the data taken from the literature for all three cases $\alpha = 0.0, 0.5$ and 4.8 fairly well. This gives confidence in the suitability of the BDIM approach as wake generates in the linear LPT cascade.

Appendix B

Influence of different Wake Profiles on the linear Low-Pressure Turbine Cascade

Figure B.1 shows the velocity contours, the edge of the boundary layer (black dashed) and the displacement thickness, δ^* (white dashed), on the suction surface of the turbine blade.

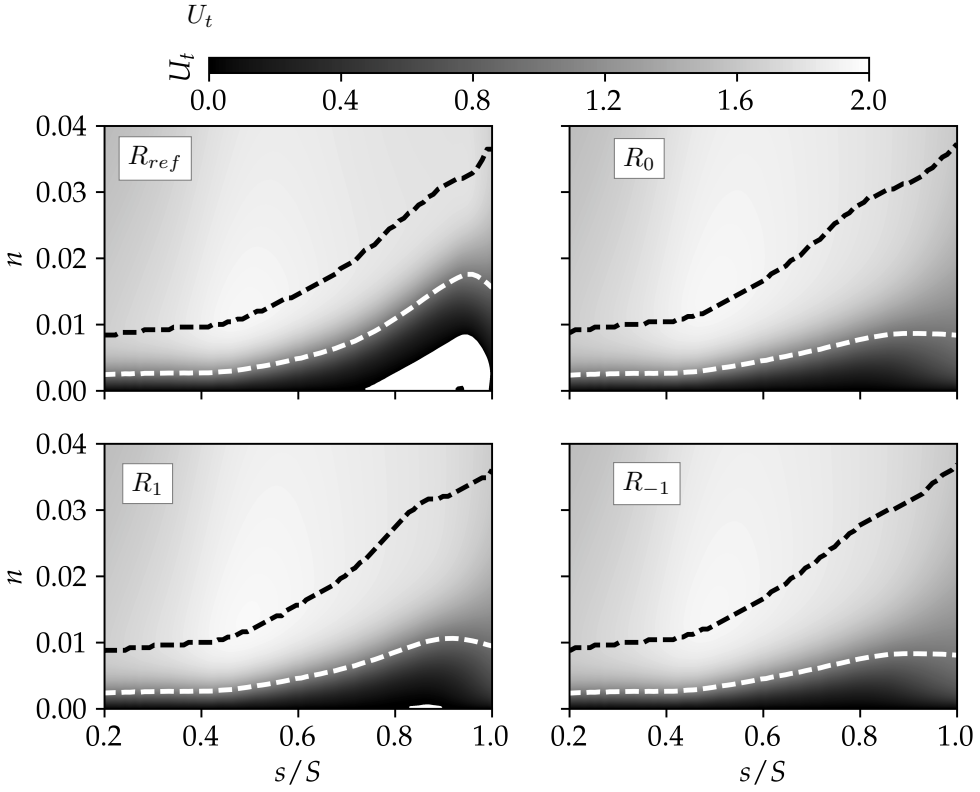

FIGURE B.1: Velocity contours, edge of the boundary layer (black dashed line) and displacement thickness, δ^*, (white dashed line) along the suction surface for the non-rotating bar case R_0, the counter-clockwise rotating bar case R_1, the clockwise rotating bar case R_{-1} and the reference case R_{ref} without bars.

The most striking feature that can be observed is the length of the separation bubble for the reference case and its wall-normal extension into the blade passage. The boundary layer remains laminar until the top of the bubble, then transitions and closes the separation shortly before the trailing edge. The cases R_0 and R_{-1} show very similar contours. A small separation bubble for case R_1 can also be observed. The most apparent differences can be observed in the thickening of the displacement thickness for cases R_{ref} and R_1 due to the separation bubbles.

Appendix C

Influence of Surface Roughness in a linear Low-Pressure Turbine Cascade

C.1 Grid Convergence of the LES Simulations with the As-cast Surface Roughness

In this section further plots concerning the grid convergence study (see sec. 5.2.2) of the as-cast roughness patch simulations are presented.

Figure C.1 shows the different spanwise roughness resolutions for AC_{nw} and $AC_{c,nw}$.

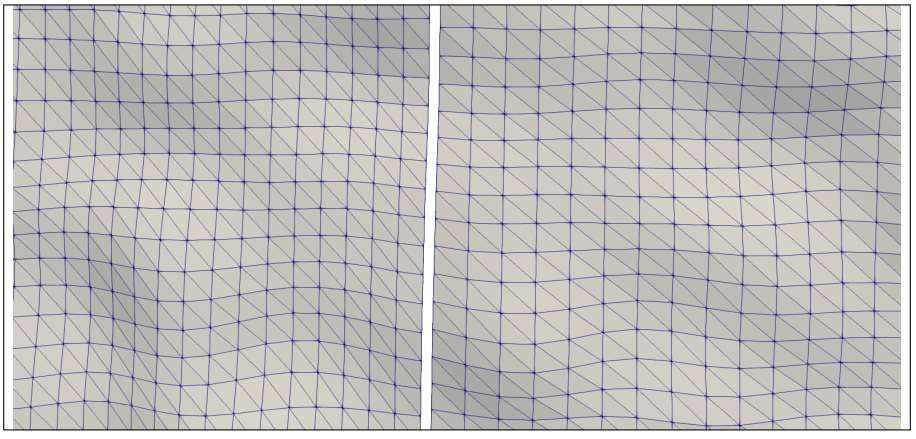

FIGURE C.1: Comparison between the spanwise roughness resolution for cases AC_{nw} (left) and $AC_{c,nw}$ (right). The spanwise cell size of the finer case, AC_{nw}, is around 75% compared to the coarser case.

Figures C.2 to C.4 show the tangential velocity, U_t, the turbulent kinetic energy, TKE, and the turbulent kinetic energy production, P, contours along the blade suction surface, s/S.

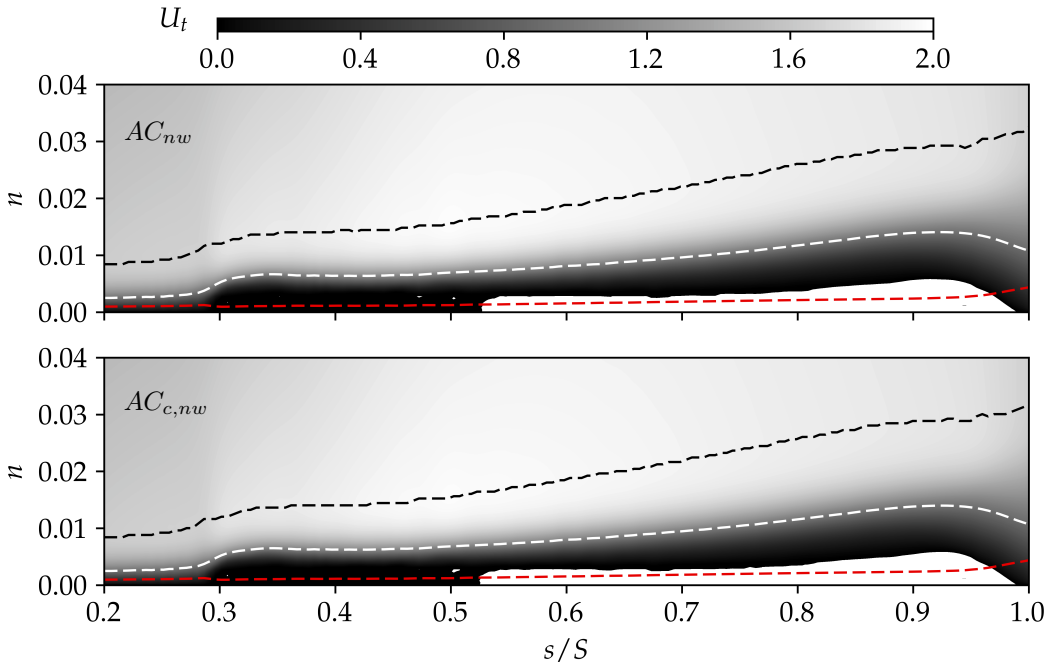

FIGURE C.2: Tangential velocity, U_t, contours along the blade suction surface, s/S. The dashed black, white and red lines depict The boundary layer edge, the displacement thickness, δ^*, and the momentum thickness, Θ, are denoted by the dashed black, white and red lines, respectively.

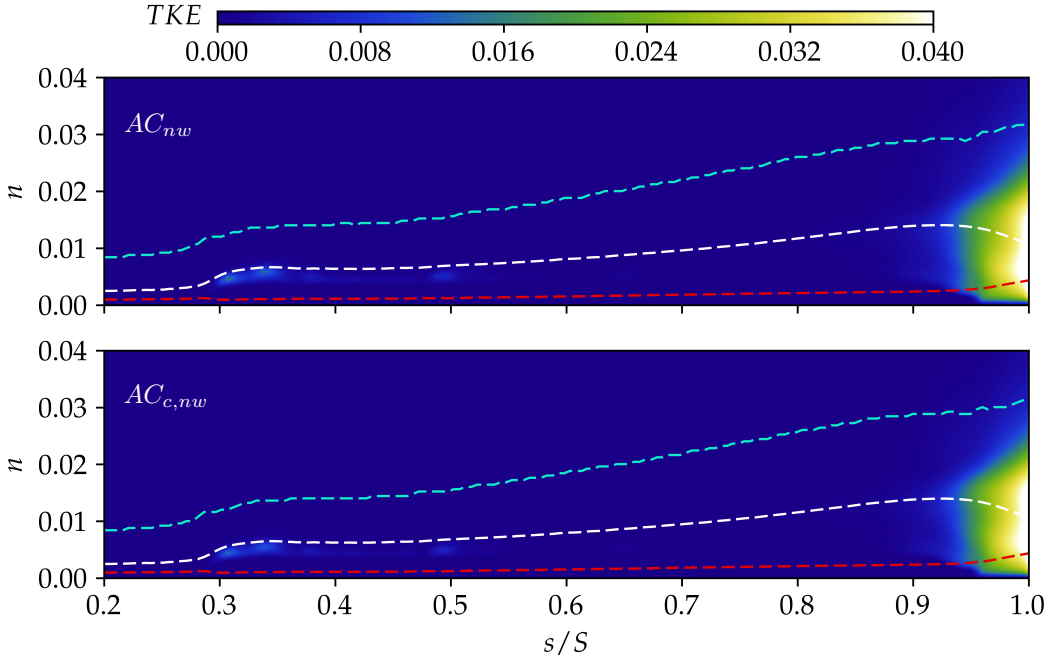

FIGURE C.3: Turbulent kinetic energy, TKE, contours along the blade suction surface, s/S.

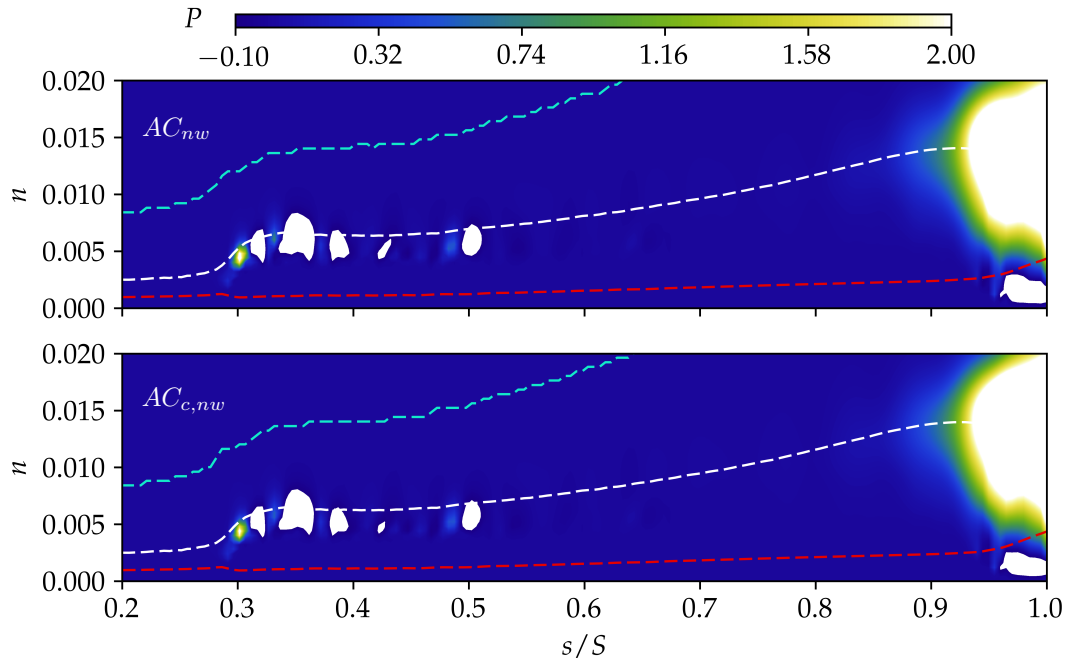

FIGURE C.4: Production of turbulent kinetic energy, P, contours along the blade suction surface, s/S.

The normalised wall normal distance is denoted by n. Furthermore, the dashed black, white and red lines depict the boundary layer edge, the displacement thickness, δ^*, and the momentum thickness, Θ, respectively. The white tangential velocity, U_t, regions indicate velocity values ≤ 0.0.

Almost identical flow features can be observed in all contour plots. The negative velocity region only shows marginal differences. In both cases the small TKE spots between $s/S = 0.3-0.34$ are captured. Furthermore, the same erratic turbulent kinetic energy production behaviour ranging from $s/S = 0.3$ to 0.55 can be seen for AC_{nw} and $AC_{c,nw}$, which gives confidence in the chosen grid resolution.

C.2 Modelled Surface Roughness with the Parametric Forcing Approach

C.2.1 Varying Roughness Densities, α, at constant Roughness Height, $h = 15$

In figure C.5 contour plots of the time-averaged and normalised tangential velocity, U_t, for the reference case, R_{ref}, - no bars and no roughness - and the varying roughness density cases are depicted.

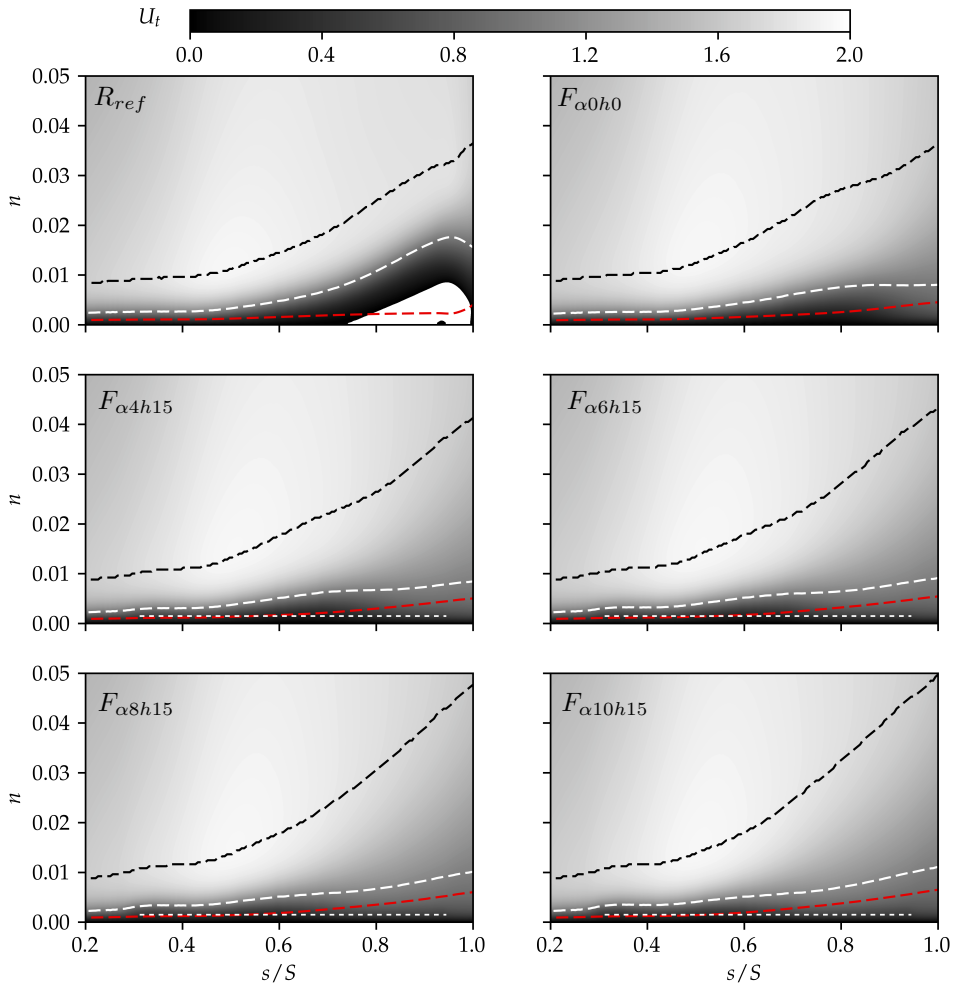

FIGURE C.5: Contour plots of normalised tangential velocity, U_t, along the blade suction surface for different roughness densities at constant roughness height.

The contours are plotted along the suction surface, s/S, and the wall normal distance, n, which is normalised by the chord length, c. The thick black, white and red dashed lines show the boundary layer edge, the displacement thickness, δ^*, and the momentum thickness, Θ, respectively, whereas the thin dashed white line represents the height, h, as well as the start and end point of the roughness forcing term.

As can be observed, for all cases but the reference one, R_{ref}, the separation bubble is suppressed and the contours reveal a fairly similar velocity profile, with a peak velocity of $U_t \approx 1.8$ at around $s/S \approx 0.5$ (s_2/S) and $n \approx 0.01$. Furthermore, by increasing the roughness densities the boundary layer thickness increases once the transition to a turbulent boundary layer occurrs.

Figure C.6 shows the turbulent kinetic energy, TKE, contour plots for the different roughness densities at constant roughness height.

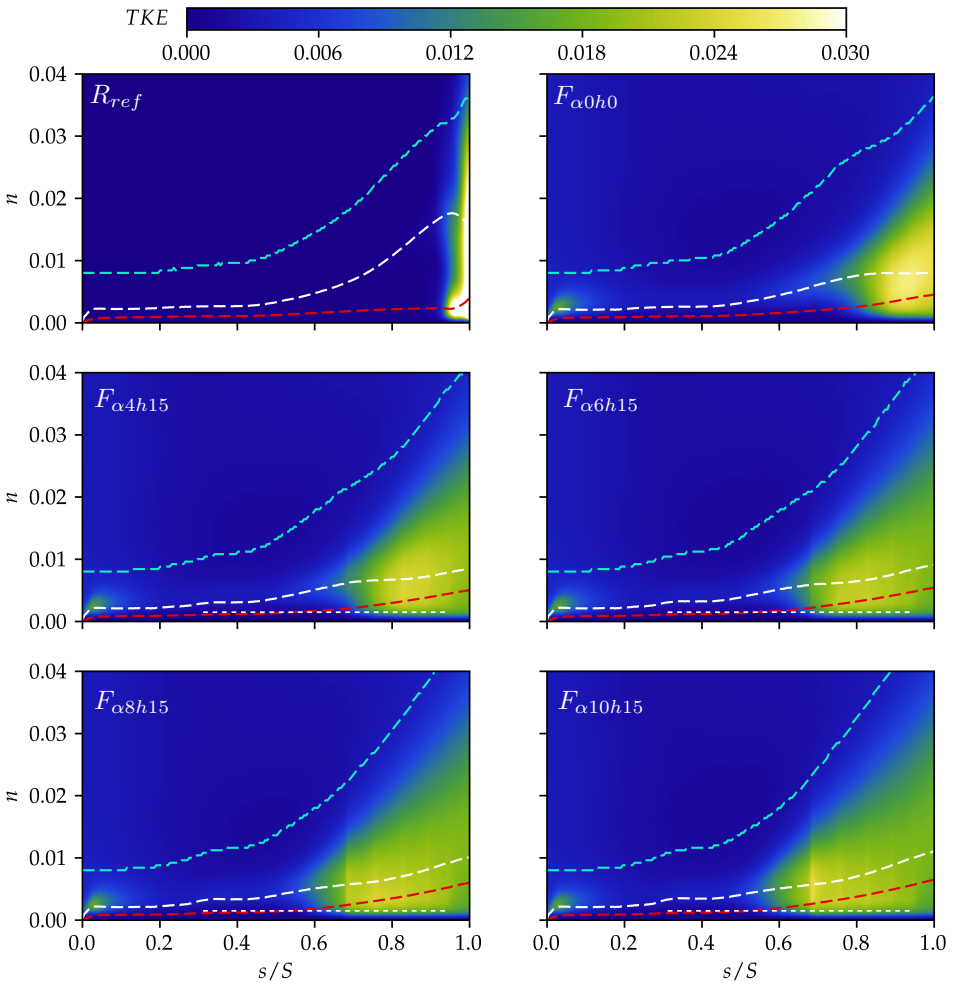

FIGURE C.6: Contour plots of the normalised turbulent kinetic energy, TKE, along the blade suction surface.

As one would expect, for the reference case the TKE remains minimal along the blade and only rapidly increases once the laminar separated shear layer has fully transitioned, leading to a reattachment. For increasing roughness densities three things can be observed. Firstly, the upstream shift of the transition point is apparent. Secondly, the peak TKE location follows this trend. Thirdly, the transition point and peak TKE location shift allow for larger elevated turbulent kinetic energy regions for higher α values, which leads to the observed increase in momentum thickness. However, the peak TKE drops by about 5% between cases $F_{\alpha 0h0}$ and $F_{\alpha 6h15}$ and then reaches its maximum for $F_{\alpha 10h15}$; see table C.1.

TABLE C.1: Peak TKE values for the different roughness density cases.

R_{ref}	$F_{\alpha 0h0}$	$F_{\alpha 4h15}$	$F_{\alpha 6h15}$	$F_{\alpha 8h15}$	$F_{\alpha 10h15}$
0.2100	0.0783	0.0751	0.0747	0.0782	0.0864

The decrease might be explained by the slight blocking effect (form drag increase) due to the added roughness forcing, which was already discussed in chapter 5. For the highest density value this blocking effect is overshadowed, leading to an enhancement of the velocity fluctuations rather than a damping.

In figure C.7 contour plots of the TKE production P for the different cases are shown.

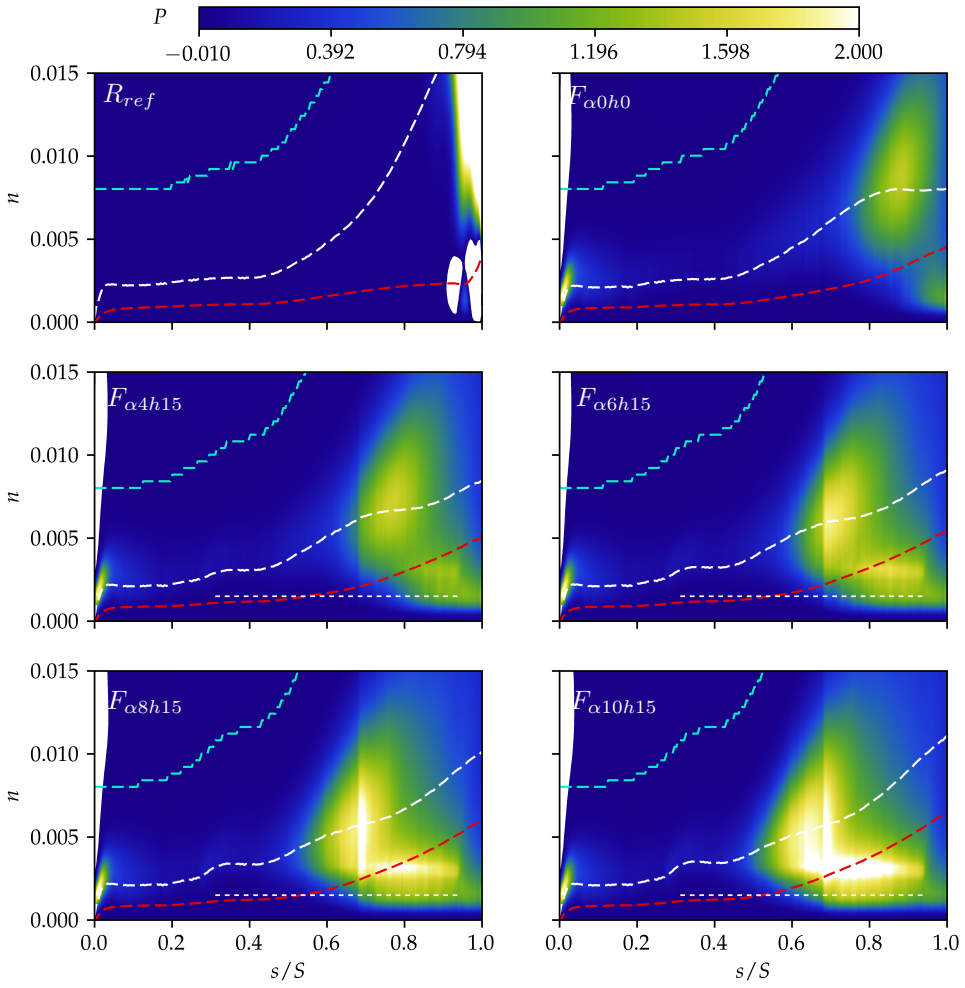

FIGURE C.7: Contour plots of the production of turbulent kinetic energy, P, along the blade suction surface.

Small spots with high P values can be observed at the leading edge within the boundary layer for all but the reference case, which is due to the missing incoming wakes. Furthermore, white regions denote negative TKE production and hence indicate energy transfer towards the mean flow.

Moving further along the blade's suction surface P remains fairly low until the transition point occurs, where a sudden increase of TKE production can be observed. These spots occur right before the high TKE spots shown in figure C.6. The increase of production of turbulent kinetic

energy is at the height of the displacement thickness, δ^*, and not directly at the roughness, which was also observed by Tsikata and Tachie (2013). For increasing roughness densities the high regions of P move upstream and increase the production values. Moreover, an L-shape form is apparent, which explains the observed wedge-like increase of TKE as well as the thickening of the momentum rather than the displacement thickness. This was also shown by the dominance of momentum growth expressed by the decrease of the shape factor, H, once transition has occurred. Owing to the suppression of the separation bubble, the extreme TKE production observed for the reference case is prevented.

The results are in line with Stripf et al. (2009), who stated that roughness has no effect on the laminar boundary layer, but on the onset of transition and the turbulent boundary layer. The fluctuations prior to transition were not affected by the different roughness density values. However, for increasing α values the transition location and the turbulent boundary layer were changed.

C.2.1.1 Varying Roughness Heights, h, at constant Roughness Density, $\alpha = 10$

Figure C.8 shows the turbulent kinetic energy, TKE, contour plots.

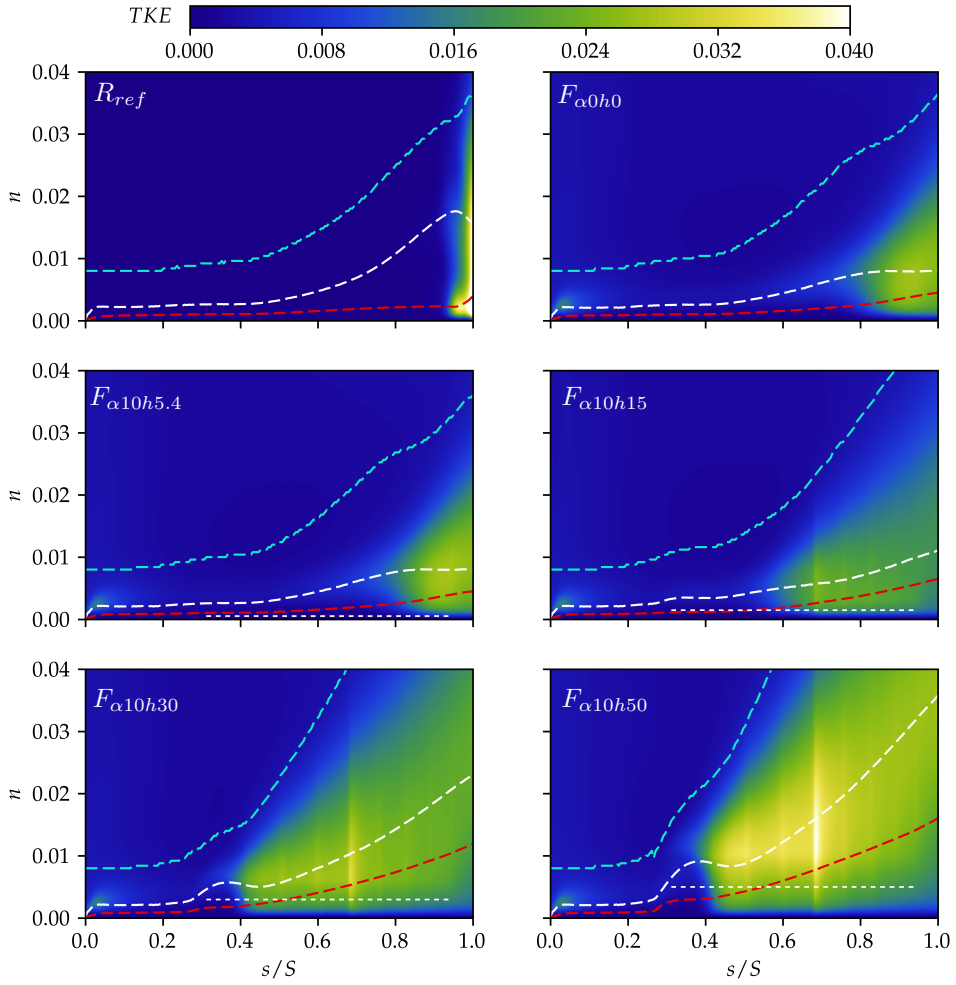

FIGURE C.8: Contour plots of normalised turbulent kinetic energy, TKE, along the blade suction surface for different roughness heights at constant roughness density.

Again, there are no observable differences between the cases with no roughness and the smallest roughness height apart from a slightly higher peak TKE value, see table C.2.

TABLE C.2: Peak TKE values for the different roughness height cases.

R_{ref}	$F_{\alpha 0h0}$	$F_{\alpha 10h5.4}$	$F_{\alpha 10h15}$	$F_{\alpha 10h30}$	$F_{\alpha 10h50}$
0.2100	0.0783	0.0801	0.0864	0.1130	0.1366

By further increasing the height both the location of the peak TKE as well as the peak TKE value itself substantially change. Moreover, the elevated TKE region increases considerably in a wedge-like shape.

Looking at the turbulent kinetic energy production in figure C.9, large values of P for cases $F_{\alpha 10h30}$ and $F_{\alpha 10h50}$ can be observed right after transition occurred.

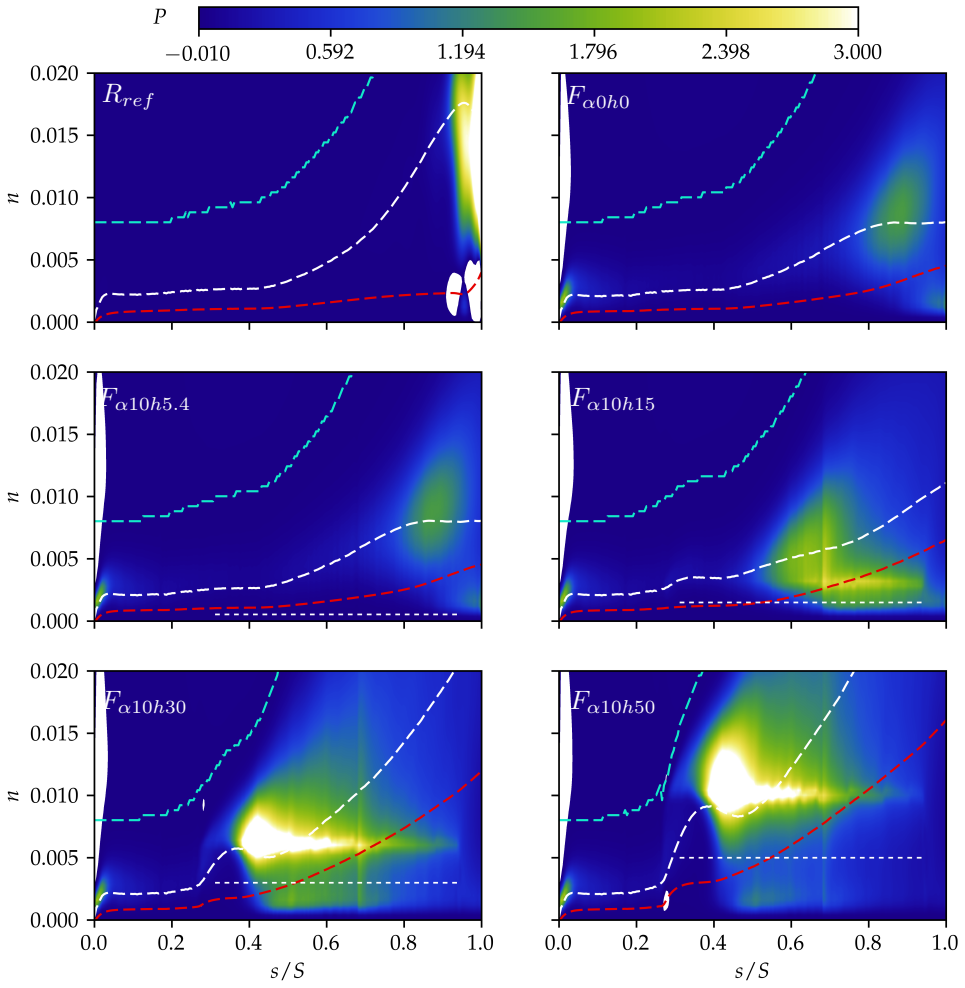

FIGURE C.9: Turbulent kinetic energy production, P, contour plots along the blade suction surface.

The high production regions are slightly above the displacement thickness height, fairly distant from the roughness, indicating the sudden transition in the shear layer. Interestingly, a small negative TKE production spot is located directly before the start of the forcing region for case $F_{\alpha 10h50}$ very close to the wall, where the steep drop of the shape factor was seen.

C.2.1.2 Varying Roughness Lengths, l, at constant Roughness Density, $\alpha = 6$ and Height, $h = 15$

Figure C.10 shows the velocity contours along the blade's suction surface from the leading to the trailing edge of the different roughness patch length cases.

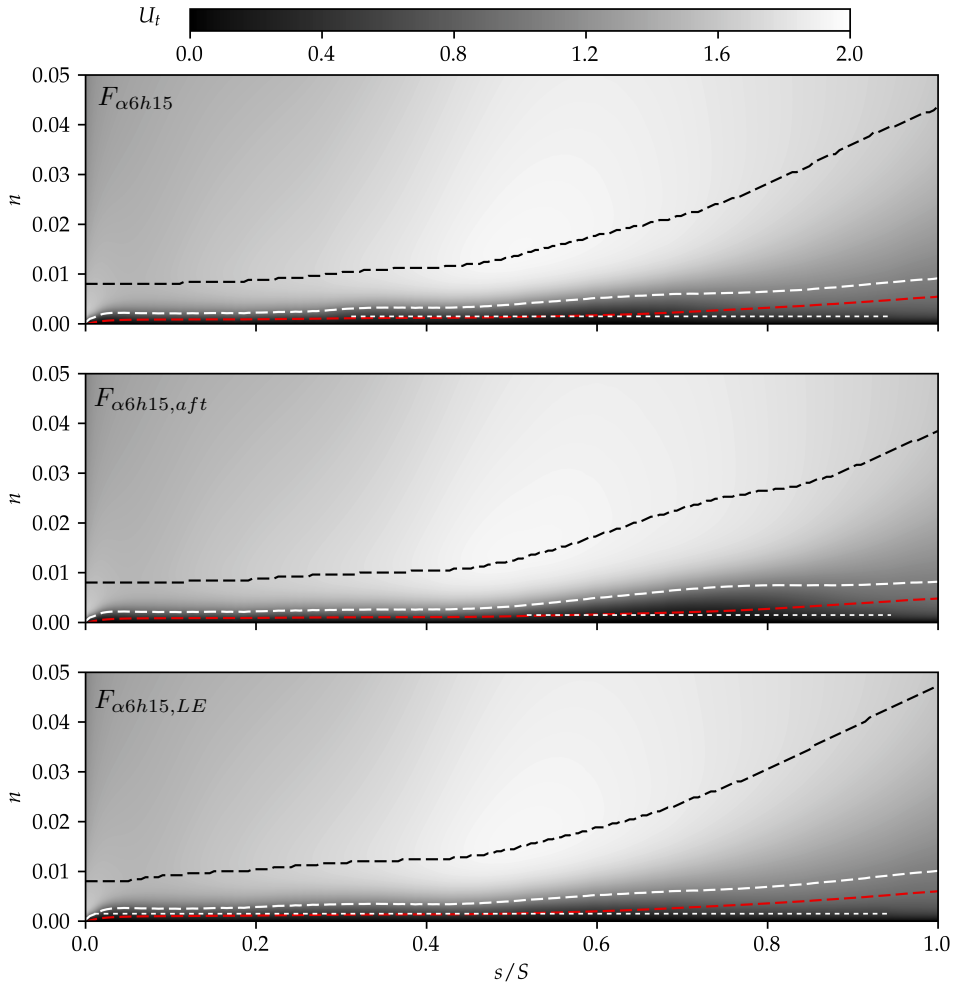

FIGURE C.10: Tangential velocity, U_t, contour plots along the blade suction surface for the different roughness patch length cases.

The velocity field outside the boundary layer is similar for all cases. In case of $F_{\alpha 6h15,LE}$ a slightly increased boundary layer thickness can be observed, which can probably be attributed to the turbulent boundary layer being exposed to roughness for a longer distance. A bump in the displacement thickness and boundary layer edge between $s/S = 0.6 - 0.8$ for case $F_{\alpha 6h15,aft}$ is apparent, too.

The TKE contours for the three cases are presented in figure C.11.

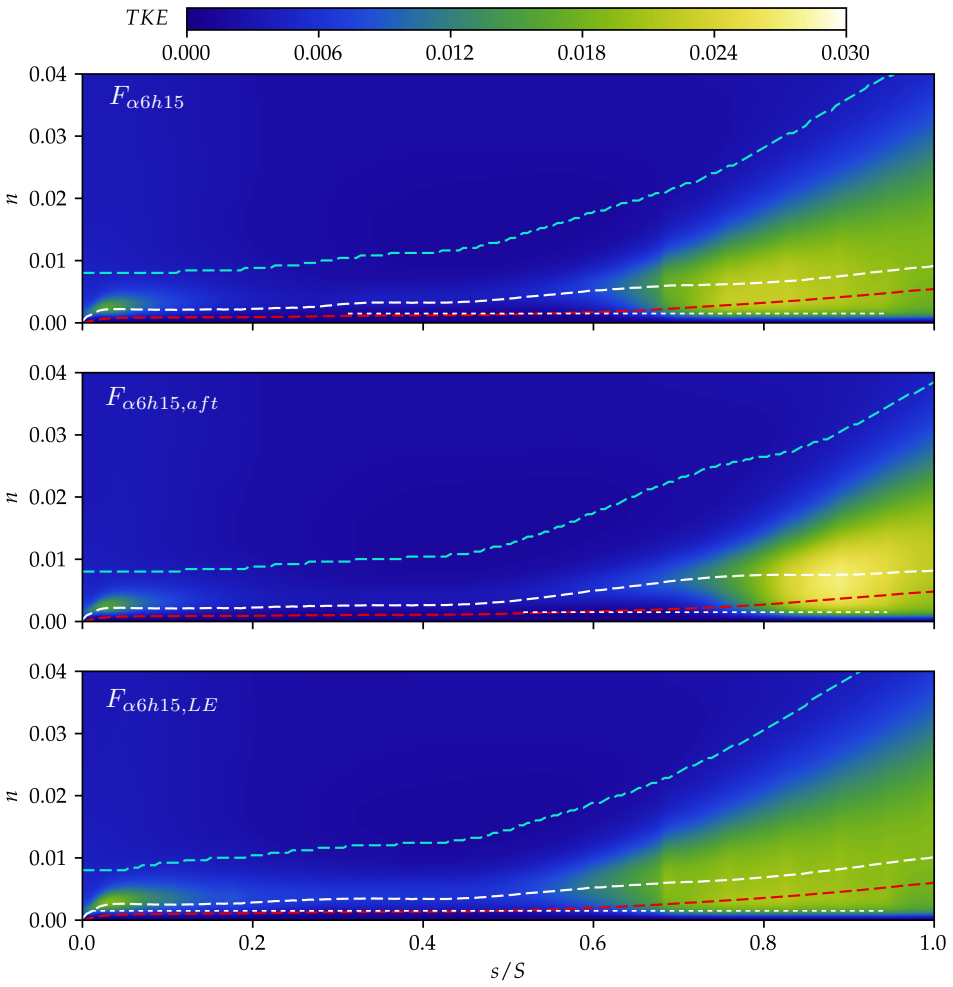

FIGURE C.11: Normalised TKE contour plots over the blade's suction surface.

The most apparent differences that can be observed are the different onset of transition positions, marked by the tip of the wedge-like TKE regions. Furthermore, the highest TKE values are achieved by the shortest roughness patch, whereas the full length surface roughness generates the lowest turbulent kinetic energy levels, see table C.3.

TABLE C.3: Peak TKE values for the different roughness patch length cases.

$F_{\alpha 6h15}$	$F_{\alpha 6h15,aft}$	$F_{\alpha 6h15,LE}$
0.0747	0.0803	0.0687

The contour plots of turbulent kinetic energy production, P, see figure C.12, reveal the same behaviour as the TKE contour plots.

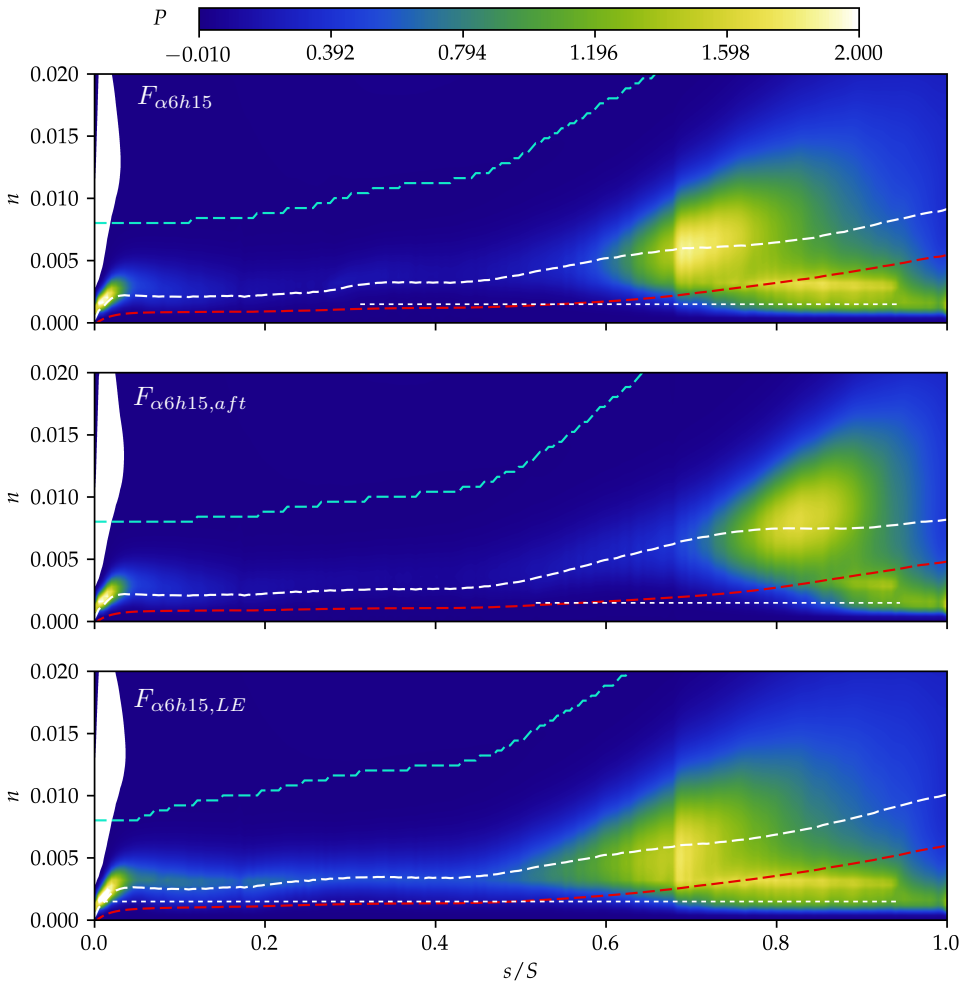

FIGURE C.12: Turbulent kinetic energy production, P, contour plots along the blade surface.

Interestingly, for case $F_{\alpha 6h15,LE}$ elevated TKE production values along the whole suction surface at the displacement thickness height, δ^*, are evident. This explains the slightly earlier onset of transition, compared to $F_{\alpha 6h15}$, and the smoother and less rapid transition process.

References

Aainsqatsi, K. (2008). *Turbofan operation.* URL: `https://en.wikipedia.org/wiki/Jet_engine#/media/File:Turbofan_operation_lbp.svg` (visited on 08/2015).

Anderson, W. and C. Meneveau (2010). "A large-eddy simulation model for boundary-layer flow over surfaces with horizontally resolved but vertically unresolved roughness elements". In: *Boundary-layer meteorology* 137.3, pp. 397–415.

Bechlars, P. (Nov. 2015). "Comprehensive characterisation of turbulence dynamics with emphasis on wall-bounded flows". PhD thesis. University of Southampton.

Bechlars, P. and R. Sandberg (2017). "Evolution of the velocity gradient tensor invariant dynamics in a turbulent boundary layer". In: *Journal of Fluid Mechanics* 815, pp. 223–242.

Bhaganagar, K., J. Kim, and G. Coleman (2004). "Effect of roughness on wall-bounded turbulence". In: *Flow, turbulence and combustion* 72.2-4, pp. 463–492.

Blair, M. F. (1992). "An experimental study of heat transfer in a large-scale turbine rotor passage". In: *ASME 1992 International Gas Turbine and Aeroengine Congress and Exposition.* American Society of Mechanical Engineers, V004T09A012–V004T09A012.

Bons, J. P. (2010). "A review of surface roughness effects in gas turbines". In: *Journal of turbomachinery* 132.2, p. 021004.

Bons, J. P. et al. (2001). "The Many Faces of Turbine Surface Roughness". In: *Turbo Expo: Power for Land, Sea, and Air* 3.

Boyle, R. and R. Senyitko (2003). "Measurements and predictions of surface roughness effects on the turbine vane aerodynamics". In: *ASME Turbo Expo 2003, collocated with the 2003 International Joint Power Generation Conference.* American Society of Mechanical Engineers, pp. 291–303.

Busse, A. and N. D. Sandham (2012). "Parametric forcing approach to rough-wall turbulent channel flow". In: *Journal of Fluid Mechanics* 712, pp. 169–202.

Busse, A., M. Lützner, and N. D. Sandham (2015). "Direct numerical simulation of turbulent flow over a rough surface based on a surface scan". In: *Computers & Fluids* 116, pp. 129–147.

Chan, L. et al. (2015). "A systematic investigation of roughness height and wavelength in turbulent pipe flow in the transitionally rough regime". In: *Journal of Fluid Mechanics* 771, pp. 743–777.

Choi, H., P. Moin, and J. Kim (1993). "Direct numerical simulation of turbulent flow over riblets". In: *Journal of fluid mechanics* 255, pp. 503–539.

Chung, D. et al. (June 2015). "A fast direct numerical simulation method for characterising hydraulic roughness". In: *Journal of Fluid Mechanics* 773, pp. 418–431.

Cobley, K. et al. (1997). "Design of new three stage low pressure turbine for BMW Rolls-Royce BR715 engine". In: *International Gas Turbine and Aeroengine Congress and Exhibition* 97.

Coleman, H., B. Hodge, and R. Taylor (1984). "A re-evaluation of Schlichting's surface roughness experiment". In: *Journal of Fluids Engineering* 106.1, pp. 60–65.

Coull, J. D. and H. P. Hodson (2011). "Unsteady boundary-layer transition in low-pressure turbines". English. In: *Journal of Fluid Mechanics* 681.1, pp. 370–410.

Coull, J. D., R. L. Thomas, and H. P. Hodson (2010). "Velocity distributions for low pressure turbines". In: *Journal of Turbomachinery* 132.4, p. 041006.

Cui, J., V. C. Patel, and C.-L. Lin (2003). "Prediction of turbulent flow over rough surfaces using a force field in large eddy simulation". In: *Journal of fluids engineering* 125.1, pp. 2–9.

Denton, J. D. (1993). "The 1993 IGTI Scholar Lecture: Loss mechanisms in turbomachines". In: *Journal of Turbomachinery* 115.4, p. 621.

Ducros, F., F. Nicoud, and T. Poinsot (1999). "Wall-adapting local eddy-viscosity models for simulations in complex geometries". In:

Engber, M. and L. Fottner (1995). "The effect of Incoming Wakes in Boundary Layer Transition". In: *Loss Mechanisms and Unsteady Flows in Turbomachines*. Derby.

Feindt, E. G. (1957). "Untersuchungen über die Abhängigkeit des Umschlages laminar-turbulent von der Oberflächenrauhigkeit und der Druckverteilung". PhD thesis. Technische Hochschule Carolo-Wilhelmina zu Braunschweig.

Fiala, A. and E. Kügeler (2011). "Roughness modeling for turbomachinery". In: *ASME 2011 Turbo Expo: Turbine Technical Conference and Exposition*. American Society of Mechanical Engineers, pp. 595–607.

Flores, O. and J. Jimenez (2006). "Effect of wall-boundary disturbances on turbulent channel flows". In: *Journal of Fluid Mechanics* 566, pp. 357–376.

Forooghi, P. et al. (2017). "Toward a universal roughness correlation". In: *Journal of Fluids Engineering* 139.12, p. 121201.

Forooghi, P. et al. (2018). "A modified parametric forcing approach for modelling of roughness". In: *International Journal of Heat and Fluid Flow* 71, pp. 200–209.

Galiano, S. S. (Dec. 2016). "Fluid-structure interaction of membrane aerofoils at low Reynolds numbers". PhD thesis. University of Southampton.

Goldstein, D., R. Handler, and L. Sirovich (1993a). "Modeling a No-Slip Flow Boundary with an External Force Field". In: *Journal of Computational Physics* 105.2, pp. 354–366.

Goldstein, D., R. Handler, and L. Sirovich (1993b). "Modeling a no-slip flow boundary with an external force field". In: *Journal of Computational Physics* 105.2, pp. 354–366.

Gross, A. and H. F. Fasel (Dec. 2008). "Multi-block Poisson grid generator for cascade simulations". In: *Mathematics and Computers in Simulation* 79.3, pp. 416–428.

Guy, R. D. and D. A. Hartenstine (2010). "On the Accuracy of Direct Forcing Immersed Boundary Methods with Projection Methods". In: *J. Comput. Phys.* 229.7, pp. 2479–2496.

Halstead, D. E. (1997). "Flowfield unsteadiness and turbulence in multistage low pressure turbines". In: *Conf. Boundary layer transition in turbomachines*, pp. 7–10.

Halstead, D. et al. (1997a). "Boundary Layer Development in Axial Compressors and Turbines: Part 2 of 4 - Compressors". In: *Journal of turbomachinery* 119.3, pp. 426–444.

Halstead, D. et al. (1997b). "Boundary Layer Development in Axial Compressors and Turbines: Part 3 of 4 - LP Turbines". In: *Journal of Turbomachinery* 119.2, pp. 225–237.

Hama, F. R. (1954). "Boundary layer characteristics for smooth and rough surfaces". In: *Trans. Soc. Nav. Arch. Marine Engrs.* 62, pp. 333–358.

Hammer, F., N. D. Sandham, and R. D. Sandberg (2018a). "Large Eddy Simulations of a Low-Pressure Turbine: Roughness Modeling and the Effects on Boundary Layer Transition and Losses". In: *ASME Turbo Expo 2018: Turbomachinery Technical Conference and Exposition*. American Society of Mechanical Engineers, V02BT41A014–V02BT41A014.

Hammer, F., N. D. Sandham, and R. D. Sandberg (2018b). "The Influence of Different Wake Profiles on Losses in a Low Pressure Turbine Cascade". In: *International Journal of Turbomachinery, Propulsion and Power* 3.2, p. 10.

Harbecke, U. G., W. Riess, and J. R. Seume (2002). "The Effect of Milling Process Induced Coarse Surface Texture on Aerodynamic Turbine Profile Losses". In: *ASME Turbo Expo 2002: Power for Land, Sea, and Air*. American Society of Mechanical Engineers, pp. 81–88.

Hodson, H. P. and R. J. Howell (2005a). "Bladerow interactions, transition, and high-lift aerofoils in low-pressure turbines". In: *Annu. Rev. Fluid Mech.* 37, pp. 71–98.

Hodson, H. P. and R. J. Howell (2005b). "The role of transition in high-lift low-pressure turbines for aeroengines". In: *Progress in Aerospace Sciences* 41.6, pp. 419–454.

Hummel et al. (2005). "Surface roughness effects on turbine blade aerodynamics". In: *Journal of Turbomachinery* 127.3, pp. 453–461.

Jiménez, J. (2004). "Turbulent Flows over Rough Walls". In: *Annual Review of Fluid Mechanics* 36.1, pp. 173–196.

Johnstone, R., L. Chen, and R. D. Sandberg (2015). "A sliding characteristic interface condition for direct numerical simulations". In: *Computers & Fluids* 107, pp. 165–177.

Joo, J., G. Medic, and O. Sharma (2016). "Large-Eddy Simulation Investigation of Impact of Roughness on Flow in a Low-Pressure Turbine". In: pp. 1–12.

Kármán, v. T. (2013). "On the mechanism of the drag a moving body experiences in a fluid". In: *P. Aerosp. Sci.* 59, pp. 13–15.

Kennedy, C. a., M. H. Carpenter, and R. M. Lewis (2000). "Low-storage, explicit Runge-Kutta schemes for the compressible Navier-Stokes equations". In: *Applied Numerical Mathematics* 35.3, pp. 177–219.

Kennedy, C. A. and A. Gruber (2008). "Reduced aliasing formulations of the convective terms within the Navier-Stokes equations for a compressible fluid". In: *Journal of Computational Physics* 227.3, pp. 1676–1700.

Kim, J. W. and D. J. Lee (2000). "Generalized characteristic boundary conditions for computational aeroacoustics". In: 38.11, pp. 2040–2049.

Kim, J. W. and D. J. Lee (2003). "Characteristic interface conditions for multi-block high-order computation on singular structured grid". In: 41.12.

Kim, J. W. and R. D. Sandberg (2012). "Efficient parallel computing with a compact finite difference scheme". In: *Computers & Fluids* 58, pp. 70–87.

Kim, J., P. Moin, and R. Moser (1987). "Turbulence statistics in fully developed channel flow at low Reynolds number". In: *Journal of Fluid Mechanics*.

Kind, R. J., P. J. Serjak, and M. W. Abbott (1996). "Measurements and prediction of the effects of surface roughness on profile losses and deviation in a turbine cascade". In: *ASME 1996 International Gas Turbine and Aeroengine Congress and Exhibition*. American Society of Mechanical Engineers, V001T01A067–V001T01A067.

Klebanoff, P. S., W. G. Cleveland, and K. D. Tidstrom (Apr. 1992). "On the evolution of a turbulent boundary layer induced by a three-dimensional roughness element". In: *Journal of Fluid Mechanics* 237, p. 101.

Korakianitis, T. (1993). "On the Propagation of Viscous Wakes and Potential Flow in Axial-Turbine Cascades". In: *Journal of Turbomachinery*.

Ladwig, M. and L. Fottner (1993). "Experimental investigations of the influence of incoming wakes on the losses of a linear turbine cascade". In: *ASME 1993 International Gas Turbine and Aeroengine Congress and Exposition*. American Society of Mechanical Engineers, V03CT17A055–V03CT17A055.

Lam, K. and Y. F. Lin (2009). "Effects of wavelength and amplitude of a wavy cylinder in cross-flow at low Reynolds numbers". In: *Journal of Fluid Mechanics* 620.2009, p. 195.

Leggett, J. (Apr. 2018). "Detailed investigation of loss prediction of an axial compressor cascade at of-design conditions in the presence of incident free-stream disturbances using large eddy simulations". PhD thesis. University of Southampton.

Leggett, J. et al. (2018). "Loss Prediction in an Axial Compressor Cascade at Off-Design Incidences With Free Stream Disturbances Using Large Eddy Simulation". In: *Journal of Turbomachinery* 140.7, p. 071005.

Leonardi, S., P. Orlandi, and R. A. Antonia (2007). "Properties of d-and k-type roughness in a turbulent channel flow". In: *Physics of Fluids* 19.12, p. 125101.

Leonardi, S. et al. (2003). "Direct numerical simulations of turbulent channel flow with transverse square bars on one wall". In: *Journal of Fluid Mechanics* 491, pp. 229–238.

Licari, A. M. and K. T. Christensen (2011). "Modeling Cumulative Surface Damage and Assessing its Impact on Wall Turbulence". In: *AIAA Journal* 49.10, pp. 2305–2320.

Liu, X. and W. Rodi (1994). "Surface pressure and heat transfer measurements in a turbine cascade with unsteady oncoming wakes". In: *Exp. Fluids* 17, pp. 171–178.

Maertens, A. P. and G. D. Weymouth (2013). "Accurate Cartesian-grid simulations of near-body flows at intermediate Reynolds numbers". In: *submitted to Computer Methods in Applied Mechanics and Engineering* 283, pp. 106–129.

Martín-Alcántara, A., E. Sanmiguel-Rojas, and R. Fernandez-Feria (2015). "On the development of lift and drag in a rotating and translating cylinder". In: *Journal of Fluids and Structures* 54, pp. 868–885.

McIlroy, H. M., R. S. Budwig, and D. M. McEligot (2003). "Scaling of Turbine Blade Roughness for Model Studies". In: *ASME 2003 International Mechanical Engineering Congress and Exposition*. American Society of Mechanical Engineers, pp. 99–105.

Meyer, R. X. (1958). "The Effect of Wakes on the Transient Pressure and Velocity Distributions in Turbomachines". In: *ASME* 80, pp. 1544–1552.

Michelassi, V., J. G. Wissink, and W. Rodi (2003). "DNS of separating, low Reynolds number flow in a turbine cascade with incoming wakes". In: *International Journal of Heat and Fluid Flow* 69, pp. 295–330.

Michelassi, V. et al. (2015). "Compressible Direct Numerical Simulation of Low-Pressure Turbines-Part II: Effect of Inflow Disturbances". In: *Journal of Turbomachinery* 137.7, p. 071005.

Michelassi, V. et al. (2016). "High-Fidelity Simulations of Low-Pressure Turbines: Effect of Flow Coefficient and Reduced Frequency on Losses". In: *Journal of Turbomachinery* 138.11.

Mittal, R. and G. Iaccarino (2005). "Immersed Boundary Methods". In: *Annual Review of Fluid Mechanics* 37, pp. 239–261.

Mittal, S. and B. Kumar (2003). "Flow past a rotating cylinder". In: *Journal of Fluid Mechanics* 476, pp. 303–334.

Moin, P. (2010). *Fundamentals of Engineering Numerical Analysis*.

Montomoli, F., H. Hodson, and F. Haselbach (2010). "Effect of roughness and unsteadiness on the performance of a new low pressure turbine blade at low Reynolds numbers". In: *Journal of Turbomachinery* 132.3, p. 031018.

Nicoud, F. and F. Ducros (1999). "Subgrid-Scale Stress Modelling Based on the Square of the Velocity Gradient Tensor". In: *Flow, Turbulence and Combustion* 62.3, pp. 183–200.

Nikuradse, J. (1933). *Strömungsgesetze in rauhen Rohren: mit 13 Zahlentafeln*. VDI-Verlag.

Otero, J. J., A. S. Sharma, and R. D. Sandberg (2017). "Compressible Invariant Solutions In Open Cavity Flows". In: *arXiv preprint arXiv:1710.03060*.

Otero, J. (May 2017). "Development and application of an adjoint-based optimal flow control framework for compressible direct numerical simulations". PhD thesis. University of Southampton.

Padrino, J. C. and D. D. Joseph (2006). "Numerical study of the steady-state uniform flow past a rotating cylinder". In: *Journal of Fluid Mechanics* 557, p. 191.

Perry, A. E., W. H. Schofield, and P. N. Joubert (1969). "Rough wall turbulent boundary layers". In: *Journal of Fluid Mechanics* 37.2, pp. 383–413.

Peskin, C. S. (Oct. 1972). "Flow Patterns Around Heart Valves: A Numerical Method". In: *Journal of Computational Physics* 10, pp. 252–271.

Peskin, C. S. (2002). "The immersed boundary method". In: *Acta Numerica* 11, pp. 479–517.

Pfeil, H. and J. Eifler (1976). "Turbulenzverhältnisse hinter rotierenden Zylindergittern". In: *Forschung im Ingenieurwesen* 42.1, pp. 27–32.

Pichler, R. (Mar. 2016). "Investigations on turbulence in low pressure turbines based on direct numerical simulations". PhD thesis. University of Southampton.

Pichler, R. et al. (2018). "Highly Resolved Large Eddy Simulation Study of Gap Size Effect on Low-Pressure Turbine Stage". In: *Journal of Turbomachinery* 140.2, p. 021003.

Pralits, J. O., L. Brandt, and F. Giannetti (2010). "Instability and sensitivity of the flow around a rotating circular cylinder". In: *Journal of Fluid Mechanics* 650, pp. 513–536.

Prandtl, L. (1925). "Magnuseffekt und Windkraftschiff". In: *Die Naturwissenschaften* Dreizehnte.Heft 6, pp. 93–108.

Prasad, A. (2005). "Calculation of the Mixed-Out State in Turbomachine Flows". In: *Journal of Turbomachinery* 127.3.

Rao, A. et al. (2013). "Three-dimensionality in the wake of a rapidly rotating cylinder in uniform flow". In: *Journal of Fluid Mechanics* 730, pp. 379–391.

Rao, A. et al. (2014a). "A review of rotating cylinder wake transitions". In: *Journal of Fluids and Structures*, pp. 1–13.

Rao, N., V. Paul, and P. Durbin (2017). "Distributed Roughness Effects on Transitional and Turbulent Boundary Layers". In: *Flow, Turbulence and Combustion*.

Rao, N. et al. (2014b). "Large eddy simulations in turbines: influence of roughness and free-stream turbulence". In: *Flow, Turbulence and Combustion* 92.1-2, pp. 543–561.

Redford, J. A., N. D. Sandham, and G. T. Roberts (2010). "Roughness-induced transition of compressible laminar boundary layers". en. In: *Seventh IUTAM Symposium on Laminar-Turbulent Transition*. Ed. by P. Schlatter and D. S. Henningson. Vol. 18. Dordrecht: Springer Netherlands, pp. 337–342.

Roberts, S. K. and M. I. Yaras (Feb. 2005). "Boundary-Layer Transition Affected by Surface Roughness and Free-Stream Turbulence". In: *Journal of Fluids Engineering* 127.3, pp. 449–457.

Rutledge, J. L., D. Robertson, and D. G. Bogard (2006). "Degradation of film cooling performance on a turbine vane suction side due to surface roughness". In: *Journal of turbomachinery* 128.3, pp. 547–554.

Sandberg, R. D., R. Pichler, and L. Chen (2012). "Assessing the sensitivity of Turbine Cascade Flow to Inflow Disturbances using Direct Numerical Simulation". In: *Isuaaat 13*.

Sandberg, R. D. et al. (2015). "Compressible Direct Numerical Simulation of Low-Pressure Turbines: Part I – Methodology". In: *Journal of Turbomachinery* 137.5.

Sarkar, S. (2009). "Influence of wake structure on unsteady flow in a low pressure turbine blade passage". In: *Journal of turbomachinery* 131.4, p. 041016.

Schlanderer, S. and R. Sandberg (2018). "Boundary Data Immersion Method for DNS of aero-vibro-acoustic systems". In: *Direct and Large-Eddy Simulation X*. Springer, pp. 425–431.

Schlanderer, S. C., G. D. Weymouth, and R. D. Sandberg (2017). "The boundary data immersion method for compressible flows with application to aeroacoustics". In: *Journal of Computational Physics* 333, pp. 440–461.

Schlichting, H. (1936). "Experimentelle Untersuchungen zum Rauhigkeitsproblem". In: *Ingenieur-Archiv* 7.1, pp. 1–34.

Schlichting, H. and K. Gersten (2006). *Grenzschicht-theorie*. Springer-Verlag.

Schoepplein, M. et al. (2018). "Application of an evolutionary algorithm to LES modeling of turbulent transport in premixed flames". In: *Journal of Computational Physics*.

Senocak, I. et al. (2015). "An Immersed Boundary Geometric Preprocessor for Arbitrarily Complex Terrain and Geometry". In: *Journal of Atmospheric and Oceanic Technology* 32.11, pp. 2075–2087.

Serrano-Galiano, S., N. D. Sandham, and R. D. Sandberg (2018). "Fluid–structure coupling mechanism and its aerodynamic effect on membrane aerofoils". In: *Journal of Fluid Mechanics* 848, pp. 1127–1156.

Smith, L. H. (1966). "Wake Dispersion in Turbomachines". In: *Journal of Basic Engineering* 88.3.

Stadtmüller, P. (2001). "Investigation of wake-induced tansition on the LP turbine cascade T106A-EIZ." DFG-Verbundprojekt Fo 136/11, Version 1.1. Germany.

Stieger, R. D. and H. P. Hodson (2005). "The Unsteady Development of a Turbulent Wake Through a Downstream Low-Pressure Turbine Blade Passage". In: *Journal of Turbomachinery* 127.2, p. 388.

Stripf, M., A. Schulz, and S. Wittig (2004). "Surface roughness effects on external heat transfer of a HP turbine vane". In: *ASME Turbo Expo 2004: Power for Land, Sea, and Air*. American Society of Mechanical Engineers, pp. 1–10.

Stripf, M. et al. (2009). "Extended Models for Transitional Rough Wall Boundary Layers With Heat Transfer - Part I: Model Formulations". In: *Journal of Turbomachinery* 131.3, p. 031016.

Sunday, D. (2001). *Intersection of a ray/segment with a triangle*. URL: `http://www.geomalgorithms.com/a06-_intersect-2.html#Segment-Triangle` (visited on 07/2016).

Tani, I. (1969). "Boundary-Layer Transition". In: *Annual Review of Fluid Mechanics* 1.1, pp. 169–196.

Taylor, R., H. Coleman, and B. Hodge (1985). "Prediction of turbulent rough-wall skin friction using a discrete element approach". In: *Journal of Fluids Engineering* 107.2, pp. 251–257.

Thakkar, M. (Oct. 2017). "Investigation of turbulent flow over irregular rough surfaces using direct numerical simulations". PhD thesis. University of Southampton.

Thakkar, M. N., A. Busse, and N. Sandham (2017a). *Dataset for "Investigation of turbulent flow over irregular rough surfaces using direct numerical simulations"*.

Thakkar, M., A. Busse, and N. Sandham (2017b). "Surface correlations of hydrodynamic drag for transitionally rough engineering surfaces". In: *Journal of Turbulence* 18.2, pp. 138–169.

Tseng, Y.-H. and J. H. Ferziger (2003). "A ghost-cell immersed boundary method for flow in complex geometry". In: *Journal of computational physics* 192.2, pp. 593–623.

Tsikata, J. M. and M. F. Tachie (2013). "Adverse pressure gradient turbulent flows over rough walls". In: *International Journal of Heat and Fluid Flow* 39. Publisher: Elsevier Inc. ISBN: 0142727X, pp. 127–145.

Tucker, P. (2013). "Trends in turbomachinery turbulence treatments". In: *Progress in Aerospace Sciences* 63, pp. 1–32.

Vera, M. et al. (2007). "Separation and transition control on an aft-loaded ultra-high-lift LP turbine blade at low Reynolds numbers: high-speed validation". In: *Journal of turbomachinery* 129.2, pp. 340–347.

Vreman, A. W. and J. G. M. Kuerten (2014). "Comparison of direct numerical simulation databases of turbulent channel flow at $Re_\tau = 180$". In: *Physics of Fluids* 26.1, p. 015102.

Weatheritt, J. (Nov. 2015). "The development of data driven approaches to further turbulence closures". PhD thesis. University of Southampton.

Weymouth, G. D. (2008). "Physics and learning based computational models for breaking bow waves based on new boundary immersion approaches". PhD thesis. Department of Mechanical Engineering, Massachusetts Institute of Technology.

Weymouth, G. D. and D. K. P. Yue (2011). "Boundary data immersion method for Cartesian-grid simulations of fluid-body interaction problems". In: *Journal of Computational Physics* 230.16, pp. 6233–6247.

Wheeler, A. P. et al. (2016). "Direct numerical simulations of a high-pressure turbine vane". In: *Journal of Turbomachinery* 138.7, p. 071003.

White, F. and I. Corfield (2006). *Viscous Fluid Flow*. Vol. 3. New York: McGraw-Hill.

Wu, X. and P. A. Durbin (2001). "Evidence of longitudinal vortices evolved from distorted wakes in a turbine passage". In: *Journal of Fluid Mechanics* 446, pp. 199–228.

Wu, X. et al. (1999). "Simulation of boundary layer transition induced by periodically passing wakes". In: *Journal of Fluid Mechanics* 398, pp. 109–153.